BEYOND-THE-DIPOLE EFFECTS IN STRONG-FIELD PHOTOIONIZATION USING SHORT INTENSE LASER PULSES

DISSERTATION

zur Erlangung des akademischen Grades

Doctor rerum naturalium
(Dr. rer. nat.)
im Fach: Physik
Spezialisierung: Theoretische Physik
eingereicht an der
Mathematisch-Naturwissenschaftlichen Fakultät
Humboldt-Universität zu Berlin

von
M.Sc. Eric Ouma Jobunga

Präsidentin der Humboldt-Universität zu Berlin:
Prof. Dr.-Ing. habil. Dr. Sabine Kunst

Dekan der Mathematisch-Naturwissenschaftlichen Fakultät:
Prof. Dr. Elmar Kulke

Gutachter:
1. Prof. Dr. Alejandro Saenz
2. Prof. Dr. Mikhail Ivanov
3. Prof. Henri Bachau

Tag der mündlichen Prüfung: 03.11.2016

Selbständigkeitserklärung

Ich erkläre, dass ich die vorliegende Arbeit selbständig und nur unter Verwendung der angegebenen Literatur und Hilfsmittel angefertigt habe.

Berlin, den 01.09.2016 Eric Ouma Jobunga

Acknowledgement

I am filled with deep gratitude towards **Prof. Dr. Alejandro Saenz** who not only gave me an opportunity to undertake my Ph.D studies in his Modern Optics research group at the Humboldt University-Berlin but also encouraged, supported, and challenged me in every front in this academic undertaking. I am glad to have been mentored by him as I walked through the jungle of the research field with many hurdles along the way.

I am also greatly indebted to the entire team of the Modern Optics research group, both past and present members, for their support towards this academic milestone. I do appreciate the benefit I derived from this team through their direct or indirect contributions by way of discussions, code development and improvement, as well as the team building spirit. I extend my sincere gratitude to **Prof. Morten Førre** of the University of Bergen in Norway for accepting to benchmark with us and also for supplying us with data whenever he was called upon.

To my friends in and out of Berlin, I accept the significant role you played in my social well-being and for that I am grateful. Without you, life would have been boring and even the research would have been much of a daunting task. The moral support provided by my brothers, sisters, and other relatives as I struggled in this academic endeavour is also acknowledged.

There is no better way to express my gratitude to the sacrifice made by my wife **Jacqueline** to have accepted to live with an unavailable husband, and my children **Samuel Edward**, **Faith Winfrey**, and **Hilary Henry** to have lived with an absentee Dad during my scholarship period. It was truly difficult and painful to miss the comfort of this wonderful family. To my mum **Monica** and my Dad **Edward**, I dedicate this honour to you even in your absentia. I know you would have loved to see the fruits of your labour but you chose to harken to a higher calling.

Finally, I thank God for filling my mind with deep insights and revelations into the hidden aspects of my research that would not have been obvious. In deed the Almighty God, the creator of the heavens and earth and everything in them, is in control over all situations and nothing puzzles Him.

Abstract

The development of free-electron lasers and new generation light sources is enabling the realisation of high intensities and short pulse durations exceeding the currently attainable $\sim 10^{23}$ W cm^{-2} and attosecond time scale limits. These extreme laser limits should make it possible to unravel new science which is not yet feasible at the current laser parameter regimes. The very high intensity of radiation sources and the short pulse duration is anticipated to enhance imaging of tiny structures with very high resolution, filming of ultra-fast processes, and studying matter under extreme conditions. Besides the new frontiers likely to be unfolded, significant challenges exist in the theoretical simulation of these non-linear processes. In the weak-field intensity regime, the electric dipole approximation has been quite successful in describing the light-matter interaction dynamics reproducing many of the experimentally observed features. But at the unprecedented intensities and x-ray wavelengths produced by the new light sources, the electric dipole approximation is likely to break down. The role of higher multipole-order terms in the interaction Hamiltonian, associated with the radiation pressure, is then expected to become important in the accurate description of the interaction dynamics.

This study extends the solution of the non-relativistic time dependent Schrödinger equation for a single active electron system interacting with short intense laser pulses beyond the standard dipole approximation. This is realized using both the Taylor and the Rayleigh plane-wave multipole expansion series of the spatial retardation term. The inclusion of higher multipole-order terms of the interaction is expected to increase the validity and accuracy of the calculated observables relative to the experimental measurements. In addition, it is shown that for equivalent laser parameters the Rayleigh multipole expansion series is more accurate and efficient in numerical convergence. The investigated non-dipole effects manifest in both differential and total ionization probabilities in form of the increased ion yields, the distorted above-threshold-ionization structure, and asymmetry of the photoelectron angular distribution in both polarization and propagation directions. The non-dipole effects are seen to increase with intensity, wavelength, and pulse duration. The results for hydrogen as well as helium atom are presented in this study. A new model potential for helium, and any other two-electron atomic system, yielding reasonably accurate results within the frozen core approximation is also developed.

Zusammenfassung

Die Entwicklung Freier-Elektronen-Laser und einer neuen Generation von Strahlungsquellen erlaubt die Realisierung hoher Intensitäten und kurzer Pulsdauern über die derzeit erreichbaren $\sim 10^{23}$ W cm^{-2} und Attosekunden Zeitskalen hinausgehend. Diese extremen Laserparameter sollten den Zugang zu neuen physikalischen Regimes schaffen, welche über die derzeit realisierten Regimes hinausgehen. Die sehr hohen Intensitäten der Strahlungsquellen sowie die kurzen Pulsdauern sollten das Abbilden kleinster Strukturen mit sehr hoher Auflösung, filmen ultraschneller Prozesse und studieren von Materie unter Extrembedingungen ermöglichen. Neben den sich durch die experimentellen Entwicklungen ergebenden Möglichkeiten gibt es signifikante Herausforderungen bei der theoretischen Simulation dieser nicht-linearen Prozesse. Im Regime niedriger Laserintensitäten war bisher die Dipolnäherung recht erfolgreich bei der Beschreibung der durch die Licht-Materie-Wechselwirkung erzeugten Dynamik, wodurch viele experimentell beobachtete Resultate reproduziert werden konnten. Bei den durch die neuen Strahlungsqullen erzeugten bisher unerreichten Intensitäten und Rönten-Wellenlängen kann die Dipolnäherung allerdings zusammenbrechen. Höhere Multipol-Wechselwirkungen, die mit dem Strahlungsdruck assoziiert werden, sollten dann erwartungsgemäß wichtig zur genauen Beschreibung der Wechselwirkungsdynamiken werden.

In dieser Arbeit wird eine Methode zur Lösung der nichtrelativistischen zeitabhängigen Schrödingergleichung zur Beschreibung von Systemen mit einem einzelnen aktiven Elektron, das mit einem Laserfeld wechselwirkt, über die Dipolnäherung hinausgehend erweitert. Dabei wird sowohl die Taylor- als auch die Rayleight-Multipol-entwicklung des Retardierungsterms ebener Wellen verwendet. Es wird erwartet, dass die Berücksichtigung höherer Ordnungen der Multipolwechselwirkung zu einer erhöhten Genauigkeit und Richtigkeit der Resultate führen. Weiterhin wird gezeigt, dass die Rayleigh-Multipolentwicklung für gleiche Laserparameter genauer ist und schneller zur Konvergenz der numerischen Rechnung führt. Die nicht-Dipoleffekte spiegeln is sowohl in den differentiellen als auch den totalen Ionisierungswahrscheinlichkeiten in Form von erhöhten Ionisierungsausbeuten, verzerrten ATI Strukturen und einer Asymmetrie in der Photoelektronenwinkelverteilung in der Polarisations und Propagationsrichtung wider. Es wird beobachtet, dass die nicht-Dipoleffekte mit der Intensität, Wellenlänge und Pulsdauer zunehmen. Es werden Ergebnisse sowohl für das Wasserstoffatom als auch das Heliumatom gezeigt. Zusätzlich wurde ein neues Modellpotential für Helium (oder ein beliebiges anderes atomares System mit zwei Elektronen) entwickelt, welches sinnvolle Ergebnisse im Rahmen der Näherung eines eingefrorenen Elektronenrumpfes liefert.

List of Publications

- Jobunga, E. O., Khosravi, E., and Saenz, A. The lowest-order spatial-phase retardation effects in strong-field ionization of hydrogen atoms. *To be submitted.*
- Jobunga, E. O. and Saenz, A. Comparison of the spatial-phase retardation effects between Taylor and Rayleigh plane-wave series approximations . *To be submitted.*
- E. Jobunga, J. Okumu, and C. S. Singh. Electron-impact excitation of the lowest autoionizing state of potassium using a distorted-wave method. *J. phys: Conf. Ser.* **388**, 042031, (2012).
- E. Jobunga, J. Okumu, and C. S. Singh. Excitation cross-section evaluation for the lowest autoionizing state of potassium. *African Review of Physics* **7**, 001, (2012).
- E. Jobunga, J. Okumu, and C. S. Singh. Electron-impact excitation of the lowest autoionizing state of alkalis using a distorted-wave method. *VDM Verlag publishers, Germany.* (2010).
- E. Jobunga, J. Okumu, and C. S. Singh. Electron-impact excitation of the lowest autoionizing state of sodium using a distorted-wave method. *African Journal of Science and Technology*, Vol. **11/2**, 24 (2010).

Contents

1 Introduction

The development of free-electron lasers and new generation light sources [1] is enabling the realisation of high precision experiments investigating various non-linear processes in the dynamics of atoms, molecules, ions, and solid clusters interacting with laser pulses with intensities in the order of $\sim 10^{23}$ W cm^{-2} and durations in the attosecond time scale respectively [2].

The Free-electron Lasers (FLASH) in Hamburg (Germany) can produce 13.7 nm optimal wavelength accompanied by 4.6 nm in the 3^{rd} harmonic and, 2.75 nm in the 5^{th} harmonic with the pulse duration in the region of 10 fs and peak powers of 10 GW [3]. The X-ray Free Electron Laser (XFEL) in Hamburg (Germany) is expected to be operational by 2017 with the super-radiance output in the $4.7-0.05$nm spectral range[1].

The Linac Coherent Laser Source (LCLS) in Stanford (USA) and Spring-8 Angstrom Compact free-electron Laser (SACLA) [4] in Harima (Japan) produce tunable femtosecond x-ray sources with $1 - 0.1$ nm spectral range in the self amplified spontaneous emission (SASE) radiation mode [1]. The Spring-8 Compact SASE Source (SCSS) in Riken (Japan) produces FEL in the region of 49 nm.

The FERMI at Elettra in Trieste (Italy) are free-electron lasers which produce radiation in the XUV ($100 - 10$ nm) spectral range with peak powers in the region of $\sim$ 1GW . The European Synchroton Radiation Facility (ESRF) in Grenoble (France) is a prominent x-ray research centre producing $1 - 100$ keV beam lines with an intensity of the order 10^{21} Wcm^{-2} [5].

The European Laser Infrastructure (ELI) which is a trio of cutting-edge high power optical laser laboratories in Czech Republic, Hungary, and Romania is also an on-going project expected to be operational by 2018. The ELI project is designed to push the current intensity and pulse duration limits into the zettawatt (10^{21} Wcm^{-2}) peak intensity and zeptosecond (10^{-21} s) pulse limits [6]. Figure 1.1 shows an intensity map for the current and targeted laser peak intensities and the fundamental science they are expected to address.

These extreme laser limits should make it possible to unravel new science which are not yet feasible at the current laser parameter regimes. The very high intensity of radiation sources and the short pulse duration shall enhance imaging of tiny structures with very high resolution, filming of ultra-fast processes, and studying matter under extreme conditions. The possible areas of application would include fundamental research in quantum electrodynamics, medical research, materials science and development [4], amongst others.

It is already recognized that two special kinds of light have changed the landscape of research [7]. The advanced visible-spectrum optical lasers has contributed immensely in ultrafast processes, new materials development, telecommunications advancement and

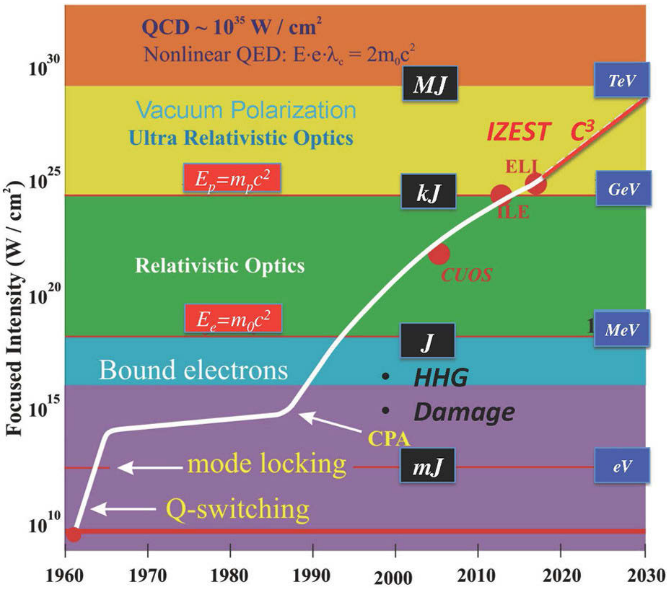

Figure 1.1: (An extract from ref.[6]). Intensity evolution since the first laser demonstration in 1960, with the different regimes of optics and electrodynamics . Red part of line represents the regime addressed by the proposed International Center for Zetta- and Exawatt Science and Technology (IZEST). Black boxes (joules) indicate typical laser energies. Blue boxes (electron volts) indicate typical particle energies. QCD: Quantum chromodynamics. QED: Quantum electrodynamics. E: Electric field. e : Electron charge. λ_c : Compton wavelength. m_0 : Electron mass. c : Speed of light. E_p : Proton energy. m_p : Proton mass. E_e: Electron energy. $C3$: Cascaded conversion compression. ELI: Extreme Light Infrastructure. ILE: Institut de la Lumiére Extrême. CUOS: Center for Ultrafast Optical Science. HHG: High harmonic generation. CPA: Chirped pulse amplification.

many others. The intense x-rays produced at synchrotons have made it possible to image new structures and otherwise invisible parts of matter enabling huge leaps in biochemistry, pharmacology, and material science.

Imaging the ultra-fast processes as an example requires the use of extremely short pulses in the order of an attosecond pulse duration in order to capture the dynamics of an electron in an atom or molecule with a typical orbiting time-scales of about 100 as [2, 8]. Such ultra-short pulses can be generated using the high-harmonic generation (HHG) process where a photo-ionized electron returns and recollides with the parent ion producing very high energetic radiation when the driving field reverses its direction in the second-half cylce [9]. The HHG process has also been successfully applied in molecular orbital tomography [10] based on the idea that the HHG signal contains information about the ionizing and the recombining system.

Besides being the backbone of processes like HHG, photoionization is in itself very interesting and applicable in pump-probe experiments . The pump-probe experiments involve two or more pulses where the pump pulse may polarize and induce dynamics within the system and the probe pulse would photoionize the system. The photoelectron angular or energy distributions of the photoionized wave packet reveals crucial information of the system [11].

Based on the intensity of the laser fields, academic disciplines investigating both theoretically and experimentally the various aspects of light-matter interactions are already established. These disciplines cover all the laser field regimes: weak-field, strong-field, plasma, and extremely high intensity laser field regimes. Theoretical studies employ models that are based on the classical solutions to the Newton's or Maxwell's equation, or on the semi-classical and/or semi-relativistic quantum mechanical solution of the Schrödinger and Pauli equations or on the full relativistic solution of the Dirac equation.

In the weak-field and perturbative strong-field regimes, the electric dipole approximation has been quite successful in describing the light-matter interaction reproducing many of the experimentally observed features with the exception of extremely short wavelengths where the dipole approximation is not valid any more. But at unprecedented intensities and x-ray wavelengths introduced by the current generation light sources, the dipole approximation is theoretically anticipated to break down and the role of higher multipole-order terms is expected [12, 13] to contribute actively in the interaction dynamics.

Going beyond the dipole approximation in simulating the laser-matter interaction dynamics not only provides a higher degree of validity but also shows the limits of using the dipole approximation. However, certain key challenges have to be addressed in launching beyond dipole approximation in the interaction dynamics. First, the very nice cylindrical symmetry property, where the projection quantum number m is conserved, is broken. The cylindrical symmetry is predominantly used in the dipole approximation for treating atomic interactions with radiations whose electric field vector is linearly polarized along the z axis. This has a consequence of stretching the computational capacity by requiring very large storage space and very long durations in the calculations especially in the time propagation routines. This makes calculations going beyond the dipole to be feasible only for very short wavelengths and lower photoelectron energies, requiring relatively smaller box radii and significantly smaller basis sizes. Second, the numerical implementation of the several interactions that come into play is quite a non-trivial task requiring a deeper insight into the interaction dynamics.

This challenging path of tackling the non-dipole interactions is the theme of this thesis. The aim was to start with the simplest interactions for a single hydrogen-like electron system coupling with the radiation field. The overall goal here is to have a very clear understanding of the effects of the interaction while eliminating the role of multi-electron systems in the dynamics. The work involved extending the code that was originally developed by Yulian Vvanne [14] to solve the Time-Dependent Schrödinger Equation (TDSE) for one-electron systems interacting with strong-field radiation within the dipole approximation. A spectral expansion employing B splines basis-set is used in the evaluation of the radial solutions of the time-independent Schrödinger equation. The radiation gauge was found to be quite convenient and reliable for the numerical implementation, making use of the known efficiency of velocity gauge [15–17].

The extended BEYDIP code allows two parallel pathways of expanding the spatial phase retardation term ($e^{i\mathbf{k}\cdot\mathbf{r}}$). One employs the Taylor multipole expansion series and the other employs an equivalent Rayleigh plane-wave multipole expansion series which make use of the spherical Bessel functions in the multipole expansion [18–20]. In the comparison of the two approaches, it is found that the Rayleigh series perform better despite the fact that the Taylor expansion offer some convenience if implemented up to the quadrupole term.

The calculations involving higher multipole-order terms are limited essentially to the short-wavelength low photoelectron energy domain where the computational capacity is feasible except in special cases employing the spherical Bessel functions where it is possible to extract spatial effects while utilizing the cylindrical symmetry. In principle, the numerical implementation discussed in this work permits the evaluation of the non-relativistic time-dependent Schrödinger equation to any multipole-order with the only restriction being the computational limits imposed by the computers and the data storage capacity. In this work, the results calculated from the 0^{th} up to the 3^{rd} multipole-order terms of the interaction Hamiltonian are reported.

This thesis is organized as follows. In chapter 1 a brief introduction and motivation for doing this work is presented. This is followed by chapter 2 which tracks the developments in strong-field physics from the days when the concept of atomic photoinization was conceptualized. Chapter 3 describes the theoretical framework for non-dipole interactions, the method used and the details of numerical procedure employed in this work. The results and discussion are presented from chapter 4 up to chapter 7. Chapter 8 presents a summary and conclusion based on the findings.

2 Strong Field Photoionization

Atoms, molecules, and ions interacting with light, depending on the strength of the radiation field, may remain unaffected if the interaction is elastic, or be excited to higher energy levels of their bound states or continuum states in the case of inelastic interaction. For excitation to the continuum states, the system is ionized by loosing one or more of its electrons to the unbound states. The effect of the light field may also lead to photoassociation if two or more atoms coalesce to form molecules, photodissociation when the reverse process of disintegrating molecules occurs, or stimulated emission of radiation where light of a given frequency induces an excited system to release some energy as the excited electrons relax to the ground state or to lower energy excited states.

The interaction process can be classified as weak-field if the Coulombic binding potential due to the nuclear field is much greater than that of the optical field. If the interaction potential due to the optical field is greater, then the process can be considered as strong-field. The strength of the optical field is usually rated in terms of the radiation intensity or frequency. In this definition of a weak field process, the effect of the optical field can be regarded as a weak perturbation on the atomic (or molecular or ionic) potential and the use of perturbative methods to analyse the effect of the radiation is justified. On the other hand, perturbation theory is invalid in a strong-field process and consequently the radiative effects can only be described accurately with non-perturbative methods.

The natural starting point for a discussion of photoionization in atoms and molecules is the discovery of the photoelectric effect by Hertz in 1881 [21, 22] and the quantum mechanical interpretation of this effect was first presented by Einstein in his famous article in 1905 [23]. In the article, the Einstein's law for photoelectric effect relating the kinetic energy of photoelectrons emitted from a metal surface to the frequency of the electromagnetic radiation and to Planck's constant, is established.

Prior to the production of intense coherent radiation from lasers, ionization of matter due to its interaction with light was predominantly weak field and it could be adequately described by the Einstein's law for photoelectric effect [24]. The law is strictly concerned with the absorption of a single photon during a transition from a discrete level to a continuum. The possibility of multiphoton transitions were first predicted by Göppert-Mayer in 1931 [24–26] and were first observed at radiofrequencies by Hughes and Grabner in 1950 [24, 27]. The study of multiphoton transitions became practically feasible with the development of intense laser sources in the 1960s. Two-photon absorption was first observed in a crystal [28], and in cesium [29]. Likewise, multiphoton ionization was first observed in the experiments of Hall, Robinson, and Branscomb involving a ruby laser and negative halogen ions [30] and subsequently from rare gases by Voronov and Delone

[31] and Agostini and co-workers [32, 33].

Keldysh [34] in his work in 1964 studied the theory of ionization dynamics of matter under intense radiation fields. He set a criteria, defined by the so called adiabaticity or Keldysh parameter ($\gamma = \sqrt{I_p/2U_p}$), to distinguish between the different ionization mechanisms. The broader classification includes the multiphoton ionization regime if $\gamma > 1$ and tunneling ionization regime if $\gamma \ll 1$. The term I_p refers to the ionization potential of the system which is the minimum energy necessary to release a bound electron to the continuum states of the system. $U_p = e^2E_0^2/4m\omega^2$ on the other hand refers to the ponderomotive potential (or energy) of the electromagnetic radiation, where E_0 is the magnitude of the peak electric field of the radiation, e and m are the electronic charge and mass respectively, and ω is the radiation frequency. Figure 2.1 shows a schematic representation of the various ionization regimes as classified by the Keldysh parameter. The quasistatic regimes can be further split into tunneling and over-the-barrier ionization regimes, where as multiphoton regime broadly comprises the resonant and non-resonant multiphoton processes as well as above-the-threshold ionization regimes. The lowest-order perturbation theory (LOPT) regime is valid at relatively lower strong-field intensities and in the region where the contribution of resonant processes involving the intermediate states is negligible. Outside the LOPT regime, higher orders of perturbation theory or a direct numerical solution of the TDSE should be applied for accurate treatment of the strong-field interactions.

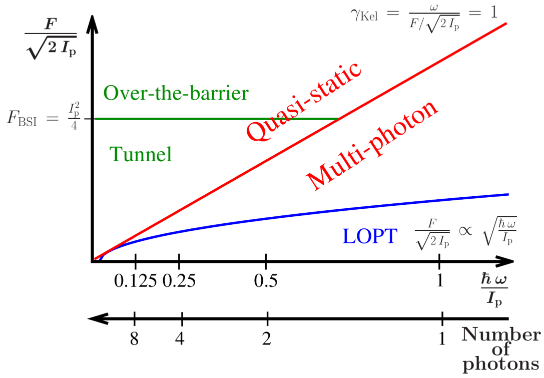

Figure 2.1: (An extract from ref.[35]). A schematic representation of the ionization regimes. A scaled field strength as a function of scaled photon energy is shown. The solid red line shows $\gamma_{Kel} = 1$, which divides the region into multiphoton and quasi-static regimes. The quasi-static regime is further divided into the tunnel and over-the-barrier (or barrier suppression) ionization regimes.

Similar but slightly different approaches in the theory of multiphoton atomic ionization, based on the calculation of the transition matrix elements from an initial discrete bound state of the system to a final state described by the Volkov wavefunction, were also developed by Faisal [36] and Reiss [37]. These approaches are generally consolidated together and referred to as Keldysh-Faisal-Reiss (KFR) theory. Reiss subsequently developed the so-called Strong field approximation (SFA) [38], which is generally seen as a modification of the KFR model [39].

With the current technology, it is now possible to produce laser fields with unprecedented intensities [40]. With such high intense fields, strong-field effects such as multiphoton ionization, above-the-threshold ionization, non-dipole effects, spin and other relativistic effects may have quite a significant contribution to the light-matter interactions. A brief description of some of the strong-field effects are presented in the following section.

2.1 Multiphoton Ionization

Multiphoton ionization occurs if a system (atom, molecule or an ion) is ionized by an electromagnetic field of frequency ω when at least n photons are absorbed in order to overcome the ionization potential I_p of the system, n being the smallest integer larger than $I_p/\hbar\omega$. In the weak field, all ejected electrons have energy $n\hbar\omega - I_p$. In a strong field, more than n photons may be absorbed and the energy spectrum of the ejected electrons consists of peaks at energies $(n+k)\hbar\omega - I_p$ corresponding to ionization after $n+k$ photons [41] where k is the number of excess photons absorbed. These ionization mechanisms are illustrated by figure 2.2.

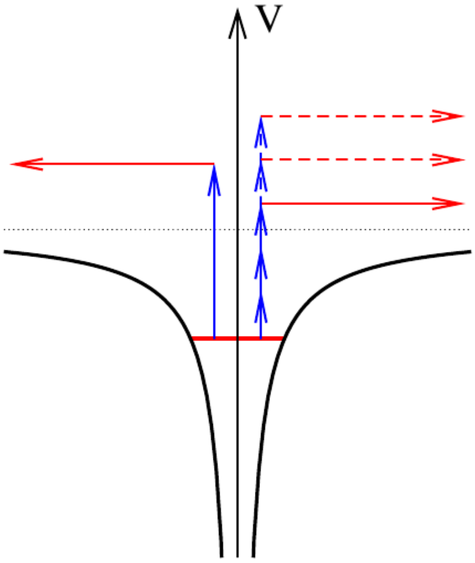

Figure 2.2: (An extract from ref.[14]). A schematic representation of the single photon, multiphoton, and above-the-threshold ionization. Each arrow represents a photon and the length of the arrow represents the magnitude of the photon energy. On the left side of the Coulomb potential, only one photon is sufficient for ionization while on the right side, many photons are coupled with virtual states in order to ionize as illustrated by the red solid arrows. Excess photons may also be absorbed in the above-the-threshold ionization as shown by the red broken arrows.

If the laser intensities are not too large, the ionization probabilities can be calculated by perturbation theory applied at the minimum non-vanishing order. The probability of ejecting an electron after absorption of $n+k$ photons is proportional to I^{n+k} where I is the laser field intensity. If the first peak of the electron energy spectrum is much higher than the others, the ionization probability would still be proportional to I^n. This agrees with experimental results of noble gases irradiated by intensities upto 10^{15} W cm^2 [42] supporting the validity of perturbation theory applied at the minimum non-vanishing order.

2.1.1 Resonant Multiphoton Ionization (REMPI)

Resonant processes occurs if, instead of the virtual states shown in figure 2.2, one or more excited bound states serve as an intermediate state. The final bound states would correspond to resonant excitation while the final continuum or autoionizing states would correspond to resonant ionization [43]. This simply means that absorption of multiple photons with a total energy equal to the excitation energy of any bound state may lead to an electron being excited first to the resonant bound state before being finally ionized. Ionization or excitation from low radiation intensity is predominantly resonant and the probability of the multiphoton processes is very low and this is in agreement with the lowest order perturbation theory (LOPT). But in intense radiation fields, the atomic states exhibit ac-Stark shifts and broadening. Resonant ionization in very intense laser fields where the ac-Stark shifts of the states become comparable with the photon energy was first observed in the experiment of Freeman *et al.* [44]. Resonant population of AC-Stark-shifted Rydberg levels of an atom with an integer number of laser photons leads to resonant enhancement of the ionization yield, and results in the appearence of sub-structures within the low-energy above-threshold-ionization (ATI) peaks, known as Freeman resonances [44, 45]. Since high-lying Rydberg levels experience ponderomotive shifts that are very similar of the ponderomotive shift of the ionization continuum, the position of these resonant features in the photoelectron energy spectrum is independent of the temporal and spatial profile of the laser puse, including the peak laser intensity, and depends only on the photon energy and the number of photons absorbed [45].

2.1.2 Non-resonant Multiphoton Ionization

Non-resonant ionization is supposed to occur if the excitation energies of the intermediate states with proper parities are far detuned from multiples of the photon energy $N\hbar\omega$ [43]. Usually at non-resonant intensities the ionization probability is lower whereas resonant ionization is characterized by a strong electron signal at a definite electron energy at the resonance intensity. The non-resonant multiphoton ionization is characterized by intensity dependent peak shifting [46] implying that non-resonant processes may become resonant and vice versa as the laser intensity is changed [47].

2.2 Above Threshold Ionization

This is one of the most interesting effects in the investigation of multiphoton ionization (MPI) of atoms, molecules or ions by intense laser light. In this process, the system (atom, molecule or ion) absorbs one or more photons above the minimum number required to overcome the ionization potential [44, 48]. This effect has been extensibly discussed in the previous decades [33, 49, 50]. The relevant photoelectron energy spectrum consists in equally spaced intensity dependent peaks whose amplitudes decrease monotonically. The separation between the peaks is equal to a single photon energy.

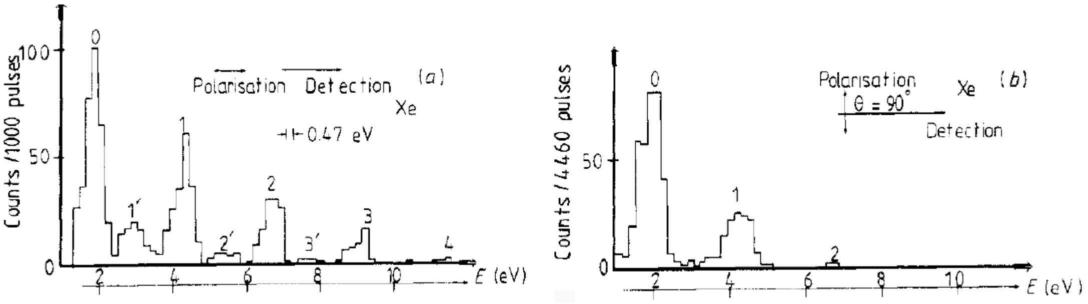

Figure 2.3: (An extract from ref. [51]). Angle and spin resolved ATI photoelectron energy spectrum for xenon atoms. The laser polarization (a) parallel ($\theta = 0°$), (b) perpendicular ($\theta = 90°$) to the detection angle. The peaks are labelled according to the value of spin S with a prime for the $P_{1/2}$ configuration.

Figure 2.3 shows the angle and spin resolved ATI peaks of the photoelectrons resulting from the experimental measurement of the ionization of xenon atoms [51]. A radiation of photon energy 2.34 eV corresponding to six-photon ionization of the xenon atoms was used in this experiment. The photoelectrons were collected parallel and perpendicular to the polarization of the electric field vector of the laser. The peaks are labelled by the number of photons absorbed above the minimum necessary for ionization. The 0^{th} peak corresponds to the threshold number of photons necessary for multiphoton ionization. The number of peaks beyond the 0^{th} corresponds to the extra photons absorbed, beyond the minimum, for the ATI process. A prime is used in the figure to label the peaks originating from the ${}^2P_{1/2}$ core configuration.

The above-threshold-ionization (ATI) distribution is consistent with the classical picture. The distribution has a first cut-off energy at $2\,U_p$ followed by a flat plateau which emerges at $2\,U_p$ and extends up to a second cut-off energy of $10\,U_p$ [52]. The $2\,U_p$ cut-off is a result of direct electrons while the plateau and the $10\,U_p$ cut-off are effects of backscattering of the ionized electrons off the core [9].

For intense picosecond and subpicosecond pulses, it is known that the low-energy ATI peaks break up into a series of narrow lines. The origin of these structures is ascribed to resonances induced by the field [44]. A system in an intense low-frequency radiation field experiences an ionization potential (I_p) increase of U_p.

There have been some key challenges in the experimental measurement of the ATI process. First, it is almost impossible to measure an instantaneous intensity in Fourier-limited pulses currently available and the intensity generated by the spikes of multimode nanosecond laser pulses can only be estimated [53]. In order to solve this problem, many experimentalists opt to reference the intensity used in any given experiment relative to the saturation intensity of the MPI process under study [53]. This permits a comparison among different experiments after correcting pulse length differences when they are measurable.

Second, the effect of space charge also poses a serious difficulty in ATI experiments [54]. The MPI process creates a plasma of ions with thermal velocities and electrons whose velocity is determined by the energy that they have gained in the interaction. Some of the electrons released in the ATI process leave the interaction volume much faster than others, leaving behind them a net positive charge that can deviate or trap slower electrons, leading to changes in the electron spectra [41]. These changes are of the same nature as the suppression of low-energy electron peaks and the magnitude of the effect depends on the spreading of the spectrum. Space charge effects are reduced by working with as few ionization events as possible in the interaction volume and using a highly efficient technique for collecting electrons [54]. This consequently leads to the problem of obtaining small ionization signals at high intensities. which is done by decreasing the atomic density as much as possible, taking ionization of background gases into account, and reducing the interaction volume.

2.2.1 Intensity Dependence of ATI

It has been shown in many theoretical and experimental studies that when the laser intensity is increased beyond the threshold necessary for observing the multiphoton ionization, more and more ATI electron peaks appear as a consequence of the electrons with very high kinetic energies [53]. The different ATI peaks for these high intense radiations tend to have comparable orders of magnitude. Observations and interpretations of ATI can be viewed on the basis of the perturbative character of the process. If the laser intensity is increased but not exceeding the perturbative intensity limits, ATI appears first as a correction to the normal multiphoton ionization (MPI) process. Additional peaks in the photoelectron energy spectrum then appear acting as an experimental signature of the ATI process. The effect of these additional peaks remain as a small contribution to the total ionization yield. The amplitudes of the additional peaks decrease with the increase in the order of the process. At the lower energy end of the spectrum, one may observe the disappearance (suppression) of low-energy electron peaks and the intensity dependences of the rates which strongly deviate from the lowest-order perturbation theory (LOPT) predictions [55]. The peak suppression feature is explained to be a consequence of the ponderomotively shifted binding energy leading to an increase in the number of photons required for photoionization. This is the basis of channel switching (also called channel closing) effect discussed in the following section.

2.2.2 Wavelength Dependence of ATI

The measurement of photoelectron spectra at a limited range of laser intensities and at a fixed wavelength (usually 800 nm) is commonly used in ATI studies. However, the measurement of wavelength-dependent ATI photoelectron spectra may open up features that may be invisible for a fixed wavelength. For example, Rottke *et al.* [43] observed channel switching from a 6- to 7-photon resonant ionization in Xe by varying the laser wavelength between 592 nm and 616 nm and measuring the energy and angle resolved photoelectron distributions. Channel switching effects have also been observed in the measurements of $2D$ photoelectron momentum spectra resulting from the ATI of Xe and Ar in a wide range of wavelengths in between 600 nm and 800 nm [45]. Also, Kaminski *et al.* [56] observed the transition between resonant and non-resonant ionization channels and identified the excited states involved in the ionization process by varying both the wavelength between $500 - 650$ nm and the intensity between $10^{12} - 10^{13}$ Wcm^{-2} and measuring the corresponding photoelectron energy and angular distributions.

2.2.3 Pulse Length Dependence of ATI

Above-threshold-ionization processes have quite distinctive features depending on the pulse duration. A photoelectron emitted in intense radiation would have its launching kinetic energy reduced by the ponderomotive energy, although a sufficiently long pulse would compensate this lost energy as it accelerates within the optical field due to the raised ionization potential. This means that for sufficiently long pulses, a photoelectron converts the ponderomotive energy into kinetic energy as it exits from the interaction volume making it virtually impossible to observe the effects of the I_p shift on the energy spectra in the long-pulse ATI experiments. The pulse length therefore dictates the fraction of the kinetic energy recovered as an electron accelerates in the ponderomotive field when it exits the interaction volume. Consequently, the ATI processes can be classified into short and long pulse regimes. An ATI experiment is considered to be in the long-pulse regime if the duration of the ionizing radiation is long compared to the time it takes a photoelectron to leave the interaction volume [44]. Otherwise the experiment is considered to be in the short pulse regime.

In the short pulse regime, there is not enough time for the photoelectron to accelerate before the pulse leaves. Thus in the limit of very short pulse duration, the photoelectron energy spectrum records the actual photoelectron energies and angular distributions at the moment of ionization [44]. In the experimental studies in the long-pulse regime, it has been shown that the number [46, 49] and the intensity of the peaks in the electron spectra [53, 57, 58], their angular distributions [59], and the peak widths [53] all depend upon the intensity of the ionizing radiation, but the recorded electron energies are nearly independent of intensity [44]. This independence arises from the fact that there exists a nearly complete cancellation of the ponderomotive energy by the gain in kinetic energy of the electron from ponderomotive acceleration as it leaves the interaction volume [60]. In the short-pulse regime, where the duration of the ionizing laser pulse (typically $\tau_{\text{pulse}} < 1$ ps) is shorter than the time it takes a photoelectron to leave the interaction volume, the absolute position of the ATI peaks in the photoelectron energy spectrum depends on the the value of the ponderomotive energy U_p [61] and consequently on the laser intensity [45].

2.3 Tunneling Ionization

Tunneling ionization can be explained using the fact that when an electric field is applied to an atom (or any system) the symmetric atomic potential is deformed creating a barrier through which an electron can tunnel. Figure 2.4 illustrates the bending of the Coulomb potential by an applied field leading to tunneling and over-the-barrier ionization. Various theoretical models have been developed ranging from the Wentzel-Kramers-Brillouin (WKB) quasi-classical approximation [62–64], Landau-Lifshitz [65], Peremolov-Popov-Terent'ev (PPT) [66–68], to Ammosov-Delone-Krainov (ADK) [69] to estimate the tunneling ionization rates.

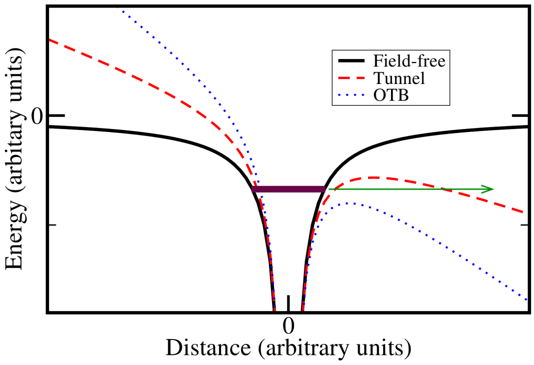

Figure 2.4: (An extract from ref.[35]). A pictorial representation of tunnel and over-the-barrier ionization. The black curves represent the field-free Coulomb potential. The Coulomb potential is modified by the applied field as shown by the red curve. The tunnelling process is illustrated by the green arrow. If the field exceeds a critical value, the Coulomb potential is excessively deformed as shown by the blue dotted lines and the tunnelling process is transformed to over-the- barrier ionization.

2.4 Over-the-Barrier Ionization

If the radiation field is too strong, the Coulomb potential barrier is completely suppressed as shown in figure 2.4 leading to an over-the-barrier (OTB) ionization, alternatively called the barrier-suppression ionization (BSI). Such strong fields cause the perturbed energy of the initial atomic state to exceed the maximum of the effective potential barrier thereby freeing the bound electrons [70]. Barrier-suppression ionization is a classical threshold effect since the effective potential is zero at the onset of OTB. OTB was first studied by Augst *et al.* [71] who used a neodymium laser with 1.053 μm wavelength and radiation intensity ranging from $10^{13} - 10^{16}$ Wcm^{-2}. Depending on the laser focus location, the ionization was sometimes tunneling and at other times barrier-suppression. In contrast to tunneling, in OTB the electric field amplitude F_0 exceeds a critical value $F_{\mathrm{OTB}} = I_p^2/4Z$ [72] which is necessary in order to permit the bound electron, with the ionization potential I_p and charge of the atomic core Z, to escape without tunneling.

2.5 Low- and Very Low-Energy Structures

These are characteristic spike-like structures, similar to the ATI peaks but at very low electron energies, which become prominent in the photoelectron energy distribution of atoms and molecules irradiated with intense mid-infrared laser wavelengths in the deep tunneling regime and are observable in all atoms and molecules [73–75]. The low-energy structures (LES) are classified to span the $1-20$ eV regime [73] in the photoelectron energy spectrum (PES) while the very low-energy structures (VLES) occur below 1 eV [52]. (V)LES are considered as the low energy features of ATI usually contrasted to plateaux in the same ATI which are high energy features emanating from the rescattering of ionized electrons. Investigation of the physical origin of these structures is still a subject of scientific debate with suggestions pointing the effect to be a consequence of the long-range Coulomb interaction in the tunneling regime [52, 74] although reference [76] concludes that LES exists in principle for any potential as long as there is scattering.

2.6 Stabilization

Stabilization refers to a decrease in or saturation of the total ionization yield of an atom or molecule as the laser intensity increases [77]. Atomic stabilization is fundamentally a non-perturbative concept meaning that it arises at the laser parameter regimes beyond the limits of perturbation theory. The lowest-order perturbation theory (LOPT) predicts that multiphoton ionization rates that steadily increase with intensity while a direct non-perturbative treatment of the Schrödinger equation establishes that the LOPT-predicted increase in ionization levels off at some intensity, and the reverse trend sets in resulting into lower ionization yields at a higher intensity. Stabilization can generally be classified into two categories: Quasistationary (adiabatic) stabilization which refers to the stabilization which scales with the magnitude of the optical field and dynamic stabilization which refers to the stabilization emanating from the temporal aspects of the pulse. Although stabilization is prominently known for strong-field interactions where the photon energy is comparable to the atomic potential [78], the possibility of stabilization at low frequencies has been experimentally realized and explained to be a consequence of frustrated tunnelling ionization [79]. The Kramers-Henneberger (KH) frame, the moving coordinates frame of a free electron responding to the laser field, is a natural choice to discuss stabilization. In this frame, the ground-state wave function of the system splits into two non-overlapping peaks and the system becomes stabilized against ionization when the laser frequency is much higher than the bound state frequency of the system [80].

2.7 High-Harmonic Generation

High-harmonic generation (HHG) [81] is the production of strong coherent energetic beams of light when a lower-frequency coherent optical fields interact with atoms, molecules, ions, or clusters. The origin of the HHG is explained by the Corkum's three step model [9]. First, electron wavepackets are launched by strong-field ionization. The acceleration of the ejected electrons follows, and then their re-collision with their parent ions gives rise to coherent radiation with frequencies which are integral multiples of the driving frequency. Such radiation can be used to provide detailed information about electronic structure [10], to probe the dynamics of atoms in molecules [82], and to image the spreading of free and bound electron wavepackets in the generated ionic species [83]. HHG, just like ATI, is a consequence of non-linear response of matter to intense laser fields. The production of harmonics is apparently dominant in the multiphoton regime but declines in strength as intensities exceed the critical value for the barrier-suppression ionization regime [84].

2.8 Non-Dipole Effects

The dipole approximation in relative coordinates assumes that the spatial extent of an electron wavepacket from the centre of mass is very small in comparison to the wavelength of radiation interacting with the system and therefore the retardation term $e^{i\mathbf{k}\cdot\mathbf{r}}$ can be approximated to unity. This assumption may be justified in cases where the wavelength of the radiation is long and satisfies the inequality condition $r \ll \lambda$ or where the intensity of the radiation is low and hence the excursion radius is assumed to be negligibly small. Interestingly, this approximation has been quite successful in reproducing several dynamical features in light-matter interactions leading to its wider applicability even in cases where the stated assumptions may not be valid. Figure 2.5 shows an illustration of the wavelength-intensity parameter space illustrating the limits of the expected validity of the dipole approximation (dipole oasis) [85] in strong-field physics. The tunnel oasis region is depicted as a sub-space of the dipole oasis where the concept of tunnelling may be valid.

The parameter $z_f = 2U_p/mc^2 = 1$ in figure 2.5 demarcates the line where strong relativistic effects are expected. The parameter $\beta_0 = U_p/2mc\omega = 1$ a.u. marks the beginning of the region where the contribution of the magnetic field would be important in treating laser-matter dynamics. Non-dipole effects can alternatively be assessed by considering the momentum and energy of a motion induced by radiation pressure [86]. The kinetic energy corresponding to this momentum is given in non-relativistic form as $KE_{\text{radp}} = U_p^2/2mc^2 = 0.5$ a.u. The low-frequency dipole approximation limit therefore arise from the constraints evaluated by examining radiation pressure effects in terms of displacements due to the magnetic component of the laser field or directly from the kinetic energy due to radiation pressure effects. On the other hand, the high frequency (upper dipole) limit for which the dipole approximation is applicable was already defined by Göppert-Meyer [26] as $\lambda \geq 1$ a.u.

While most theoretical strong-field studies have been concentrated on the spatially independent dipole approximation, there have been some previous efforts to incorporate the non-dipole effects in intense laser fields dating back to more than two decades [12, 13, 87]. The results of these non-dipole effects, although for different laser parameters, have been quite diverse, some reporting a breakdown of the dipole approximation [12, 13, 88, 89], some observing new structures in the photoelectron angular distribution[90–92], and others predicting negligible contribution of these effects [93, 94]. The relative contribution of the non-dipole $\mathbf{A}^2(\mathbf{r}, t)$ in comparison to the non-dipole $\mathbf{A}(\mathbf{r}, t) \cdot \mathbf{p}$ at different wavelengths and field amplitudes has also been a subject of conflicting viewpoints. One group finds the former to be dominant [90, 91, 95] while the

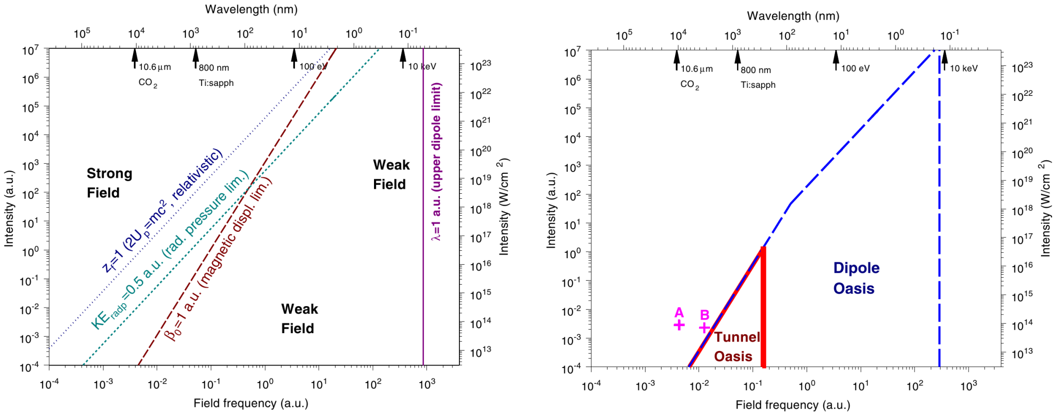

Figure 2.5: (An extract from [85]). Left: Illustration of the wavelength-intensity parameter space in strong-field ionization scaling limits, taking the magnetic field component into account. Right: The area where the dipole approximation is considered as valid (dipole oasis) is depicted as the region enclosed by the blue dashed line. The well-known short-wavelength (upper dipole) limit arises for wavelengths on the order of the atomic scale, i.e., for $\lambda = 1$ a.u.. The long-wavelength limit arises due to the laser magnetic field component, and is characterized by the ratio $U_p/2\omega c = 1$ a.u. [85].

other finds the latter to be dominant [92, 93, 96]. Note that for reasons of computational convenience, Bugacov, Pont, and Shakeshaft [12] were the first to ignore the contribution of the non-dipole $\mathbf{A}(\mathbf{r}, t) \cdot \mathbf{p}$ interaction. They justified the approximation by reasoning that a considerable computer time was demanded when carrying out calculations at very high intensities, a fact which is confirmed in this study. Besides the controversy surrounding the non-dipole effects, their contribution in reducing the stabilization of atoms in intense short wavelength fields was first pointed out by Katsouleas and Mori [97] and subsequently confirmed [13, 91, 98, 99]. Incorporating the magnetic field component in the interaction dynamics and the relativistic mass shift have been found to be comparable and each of these effects lead to a decrease in plateau height and a shift of the cut-off energy of the ATI spectrum to lower energies [100]. Also, the non-dipole effects have also been found to enhance low- and very low-energy structures prevalent in strong-field photoionization of atoms and molecules [91]. At higher radiation intensities, the magnetic field induced drift in the propagation direction prevents the electron from exactly revisiting the ionic core and consequently reduces the rescattering probability [101, 102]. This has a direct consequence on the high-harmonic generation, non-sequential photoionization, and above the threshold ionization processes which depend on the rescattering probability.

Although diverse theoretical approaches have been used to analyze these strong-field effects, one of the things that many researchers have employed in common is the use of the Taylor approximation of the retardation term $e^{i\mathbf{k}\cdot\mathbf{r}}$ [18] to include the non-dipole effects. It is well known that this approximation may not be quite reliable at lower multipole orders especially for short wavelength radiation but inclusion of many orders may also be quite expensive computationally. Therefore, the need for a better expansion for this retardation term has been an open question. The Rayleigh multipole expansion of the plane wave retardation term using the spherical Bessel functions and spherical harmonics [20, 103]may provide a useful alternative to the Taylor expansion when employed. Bugacov, Pont, and Shakeshaft [12] already noted that the use of this multipole expansion may be more accurate, although they preferred Taylor expansion in their work because of the convenience of evaluating the transition matrix elements.

In this study, the non-dipole effects are evaluated in the ionization dynamics of atoms interacting with intense field short duration laser pulses. This is done by first comparing the expansions of the spatial retardation term using both the Rayleigh and the Taylor plane-wave expansion series. The use of the Rayleigh plane-wave multipole expansion, which employs the regular spherical Bessel functions, is found to be more accurate and efficient in computational time. The Rayleigh expansion also incorporates the contribution of higher-order terms which are quite expensive to obtain if the Taylor expansion is employed. Besides, it is found that for the laser parameters employed in our calculations, the effect of non-dipole $\mathbf{A}(\mathbf{r},t)\cdot\mathbf{p}$ interaction is dominant over that of $\mathbf{A}^2(\mathbf{r},t)$ interaction. This is in line with the quantum predictions that the paramagnetic contribution of the magnetic field component is more dominant over the diamagnetic contribution [18].

3 Non-relativistic Solutions of the TDSE

In atomic structure studies as well as the response of the atomic, molecular, and ionic systems to an external electromagnetic field, the computational aspects are among the most crucial [104]. The basic processes in the electromagnetic field-matter interactions may lead to excitation, ionization, or elastic scattering of the target system with the latter leaving the state of the system unchanged. The advent of strong laser fields has lead to a lot of investigations focussing on photoionization processes. In strong-field interactions, one or more photon transitions have a significant contribution to ionization. The basic photoionization process concerns an atomic, molecular, or ionic system in a bound eigenstate (usually in ground state) irradiated by a strong electromagnetic field leaving it in final states belonging to the continuous spectrum. The field-matter interactions can be described quantum mechanically by solving the time-dependent Schrödinger equation (TDSE) in the non-relativistic regime if the electron spin contributions are not significant. In the relativistic regime, the interactions can be described by the time dependent Dirac equation (TDDE). In this study, the interaction process using the radiation (Coulomb's) gauge treatment is described but with the possibility of transforming to the conventional length and velocity gauges. The spatial phase retardation term $e^{(i\mathbf{k}\cdot\mathbf{r})}$ in the vector potential describing the interaction process is expanded to include the contribution of the higher-order non-dipole terms. The numerical framework employed in the beyond-the-dipole solution of the TDSE is described in this section. The chapter begins by giving a brief outline of some of the relevant mathematical concepts implicitly or explicitly embedded in the implementation as well as other alternative theoretical methods.

3.1 Mathematical Framework

In this subsection, some of the underlying fundamental mathematical concepts necessary in the understanding of our implementation are highlighted. These include the discussion of B splines [14, 105–107], Legendre and associated Legendre polynomials, spherical harmonics, spherical Bessel functions [103], and a method for solving ordinary differential equations. The spectral method adopted in this study to solve the field-free Schrödinger equation for a single electron system in a central potential using B splines is specifically discussed.

3.1.1 B Spline Basis Sets

B splines are defined as piecewise polynomials and are originally introduced by deBoor [105]. Because of their interesting properties, their use in theoretical atomic physics to construct finite basis sets is gaining prominence over the use of global basis sets such as Gaussian or Slater-type orbitals. A better understanding of B splines and their use in atomic physics is discussed in detail in the review articles [106, 107] and Yulian Vanne's PhD thesis [14]. B splines offer the following advantages. First, the banded nature of the matrices to be diagonalized allows for the generation of very large basis sets with no complication from linear dependence. Second, the flexibility to choose the radial grid points between which the B splines are defined can allow accurate description of the bound or continuum states. This is done by either selecting a dense exponential or geometric spacing between the knot points for the bound states, and a linear sparse spacing for the continuum states. Third, the code involved is relatively simple and the related integrals, comprising only polynomials, can be evaluated to machine accuracy with Gaussian integration. These make B splines to be accurate and easy to set up finite basis set with wide utility. B splines were first used in atomic physics by Shore [108] up to cubic order.

In the construction of B spline basis set, the number n of the basis-set elements and the order k of the B splines is pre-determined. As prescribed by deBoor [105], the finite interval $[0, R_{\text{max}}]$ is divided into segments. The end points of such segments are given by the knot sequence

$$\{t_i\}, i = 1, 2, \cdots, n + k. \tag{3.1}$$

The B splines $B_{i,k}(r)$ of the order k are defined recursively on this knot sequence by the relations

$$B_{i,1}(r) = \begin{cases} 1, & t_i \leq r < t_{i+1} \\ 0, & \text{otherwise} \end{cases} \tag{3.2}$$

and

$$B_{i,k}(r) = \frac{r - t_i}{t_{i+k-1} - t_i} B_{i,k-1}(r) + \frac{t_{i+k} - r}{t_{i+k} - t_{i+1}} B_{i+1,k-1}(r). \tag{3.3}$$

The function $B_{i,k}(r)$ is a piecewise polynomial of degree $k - 1$ with a non-vanishing value inside the interval $t_i \leq r < t_{i+k}$ and a vanishing value outside the interval. Efficient FORTRAN codes which evaluate these functions and their derivatives already exist in many numerical libraries. The sum of all the non-vanishing B splines at any point r is unity. The set of B splines of order k on the knot sequence $\{t_i\}$ forms a complete basis for piecewise polynomials of degree $k - 1$ on the interval spanned by the knot sequence. The knots defining the B spline grid have k-fold multiplicity at the end of the points 0 and r_{max}. That is, $t_1 = t_2 = \cdots = t_k = 0$ and $t_{1+k} = t_{2+k} = \cdots = t_{n+k} = r_{max}$ at 0 and at r_{max} respectively. The multiple knot sequences at the end points require the use of the limiting forms of the B spline recursive relation. For $k > 1$ at the end points, the B splines are conditioned to vanish with only the $B_{1,k}(r)$ and $B_{n,k}(r)$ having unitary values at 0 and at r_{max} respectively. The boundary conditions can then be set based on the end point behaviour of the B spline functions. The knot sequence $\{t_{i=k,\cdots,n}\}$ can be arbitrarily chosen provided that they increase monotonically. In the implementation in this study, the use of a combination of a geometrically and a linearly

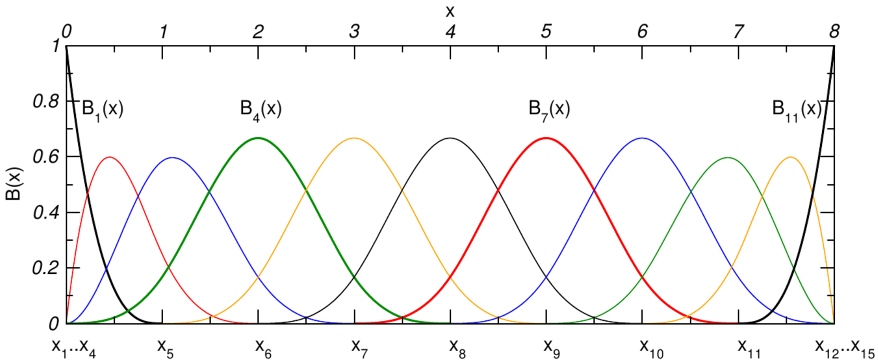

Figure 3.1: (An extract from Vanne [14]). Full sets of 11 B splines of order $k = 4$ defined for the knot sequence $\{x_i\} = \{0, 0, 0, 0, 1, 2, 3, 4, 5, 6, 7, 8, 8, 8, 8\}$.

increasing knot sequence is preferred in order to have a good description of both the bound and continuum states [14].

Figure 3.1 shows 4th order B splines spread over a linear knot sequence with the end points each having multiplicities of four. It can can be seen that between any two successive breakpoints, marking an interval, there are four non-zero B splines corresponding to the order. Since B spline functions are k^{th} order polynomials, evaluating their derivatives is rather straight forward and results in no singularities which may cause computational challenges. The first derivative is of order $k-1$, the second derivative is of order $k-2$, and the n^{th} derivative is of order $k-n$ provided that $n < k-1$. In general, the following points give a summary of the properties of B splines that we have taken advantage of in our spectral implementation.

- The 1st derivative of a B spline $B_i(r)$ can also be expanded recursively as

$$\frac{dB_i^k}{dr}(r) = \frac{k-1}{t_{i+k-1} - t_i} B_i^{k-1}(r) - \frac{k-1}{t_{i+k} - t_{i+1}} B_{i+1}^{k-1}(r) \tag{3.4}$$

- $B_i(r) \neq 0$ for $j = i_k + 1, \cdots, i$ or in other words $B_i(r) \neq 0$ for $r \epsilon (t_i, t_{i+k})$ meaning that between any consecutive breakpoint sequence, there are exactly k non-zero B splines.

- Any function $f(r)$ can be expanded as a linear combination of B splines as

$$f(r) = \sum_{j=1}^{n} c_j B_j(r) = \sum_{j=i-k+1}^{i} c_j B_j(r) \quad \text{for } r \ \epsilon \ [t_i, t_{i+1}]. \tag{3.5}$$

  This shows that one always has only k terms contributing and therefore only a minimal number of operations is needed. B splines are therefore non-negative with minimal support. The expansion coefficients of any arbitrary function f are close to the function values at the breakpoints. This means that wild oscillations in the coefficients are avoided, cancellation errors are minimized, and numerical stability is enhanced.

- The sum $\sum_j B_j(r) = 1$ over the interval $[t_i, t_{i+k-1}]$, hence B spline basis sets are normalized.

- B splines are discontinuous at the end points. That is, $B_1(r) = 1$, $B_n(r) = 1$, and $B_j(r) = 0$ at $r = a$ or $r = R_{max}$ for any $1 < j < n$. This is useful in implementing the boundary conditions.

- The product of B splines $B_i(r)B_j(r) = 0$ for $|i - j| \geq k$. This shows that every B spline overlaps with a limited number of other B splines. The sparsity property B spline basis set matrices is embedded in this limited overlap number of B splines.

- The integral $\langle B_i(r)B'_j(r)\rangle = -\langle B'_i(r)B_j(r)\rangle$ where $B'_j(r) = dB_j(r)/dr$. This integral relation can be easily verified using integration by parts and the boundary conditions imposed on the B splines.

- Likewise, the integral $\langle B_i(r)B''_j(r)\rangle = -\langle B'_i(r)B'_j(r)\rangle$ where $B''_j(r) = dB'_j(r)/dr$.

In approximating analytic functions, higher-order B splines, typically $k = 7 - 10$, are highly recommended because of their compatibility with numerical stability and round-off errors [107]. The error can be estimated using the relation

$$\varepsilon =\sim \frac{h_j^k}{k!} |D^k f(r_j)| \tag{3.6}$$

where h_j is the width of the interval I_j, $r_j \epsilon I_j$, and D^k is the k^{th} derivative of a function . The advantage here is that the error can be controlled here by the step size.

3.1.2 Legendre Polynomials

The Legendre's differential equation has the form [103]

$$(1 - x^2)y'' - 2xy' + l(l + 1)y = 0 \tag{3.7}$$

where y'' and y' are the second and the first derivatives of the variable y with respect to x respectively and l can in principle be any real number. The equation has three regular points, at $x = -1, 1, \infty$. Equation (3.7) is usually arrived at in numerous physical situations, particularly in problems having axial symmetry involving the ∇^2 operator if they are expressed in spherical polar co-ordinates. In normal usage the variable x in the Legendre's equation is the cosine of the polar angle, and thus $-1 \leq x \leq 1$. In such physical situations, the parameter l takes integer values $l = 0, 1, 2, \cdots$ representing the orbital angular quantum numbers.

Like many other second order ordinary differential equations, the Legendre equation has a power-series solution,

$$y = \sum_{l=0}^{\infty} a_l\, x^l, \tag{3.8}$$

with the coefficients a_l satisfying the recurrence relation

$$a_{l+2} = \frac{[l(l+1) - l(l+1)]}{(l+1)(l+2)}\, a_l \;=\; 0. \tag{3.9}$$

From this recurrence relation, one can clearly see that the summation in the power series solution only contains two terms, $y = a_0 y_0(x) + a_1 y_1(x)$, while the other terms vanish. This reduces the general solution of the Legendre's equation (3.7) to the form

$$y(x) = c_1 P_l(x) + c_2 Q_l(x) \tag{3.10}$$

where $P_l(x)$ and $Q_l(x)$ are the normalized forms of $y_0(x)$ and $y_1(x)$ referred to as the Legendre polynomial of the first kind and Legendre polynomial of the second kind respectively. $P_l(x)$ is usually a finite polynomial of order l and so it converges for all x where as $Q_l(x)$ is an infinite series that converges for only $|x| < 1$. The physical situations considered in this work require the solution of the Legendre equation $y(x)$ to be regular at $x = \pm 1$ which corresponds to $\theta = 0$ or $\theta = \pi$ polar angles in the case of $+$ and $-$ values of x respectively. This requires a polynomial solution and therefore l has to be an integer and the coefficient c_2 of the Legendre polynomial of the second kind $Q_l(x)$ has to vanish since $Q_l(x)$ is singular at $x = \pm 1$. This reduces the solution of the Legendre equation in the case of our interest to be simply a multiple of the relevant Legendre polynomial $P_l(x)$. The first few Legendre polynomials can be written as

$$\begin{aligned} P_0(x) &= 1 \\ P_1(x) &= x \\ P_2(x) &= \frac{1}{2}(3x^2 - 1) \\ P_3(x) &= \frac{1}{2}(5x^2 - 3x) \end{aligned} \tag{3.11}$$

The Legendre polynomials can be generated using the Rodrigues' formula

$$P_l(x) = \frac{1}{2^l\, l!} \frac{d^l}{dx^l}(x^2 - 1)^l \tag{3.12}$$

and they have the following properties:

- They have a simple recurrence relation

  $$(l+1)P_{l+1}(x) = (21+1)xP_l(x) - lP_{l-1}(x) \tag{3.13}$$

  which makes it easy to generate higher order Legendre polynomials as long as the first two are specified.

- They satisfy the normalization condition

  $$\frac{2l+1}{2} \int_{-1}^{1} P_l(x)\, P_l(x)\, dx = 1 \tag{3.14}$$

- They are mutually orthogonal to each other, that is,

$$\int_{-1}^{1} P_l(x)\, P_k(x)\, dx = 0, \quad \text{if } l \neq k. \tag{3.15}$$

- The orthogonality and normalization conditions satisfied by these polynomials makes it possible to express any reasonable function $f(x)$

$$f(x) = \sum_{l=0}^{\infty} a_l\, P_l(x) \tag{3.16}$$

  in the interval $|x| < 1$ as an infinite sum of the Legendre polynomials where the coefficients are given by

$$a_l = \frac{2l+1}{2} \int_{-1}^{1} f(x)\, P_l(x)\, dx \tag{3.17}$$

3.1.3 Associated Legendre Functions

The associated Legendre equation has the form [103]

$$(1-x^2)y'' - 2xy' + [l(l+1) - \frac{m^2}{1-x^2}]y = 0 \tag{3.18}$$

which has three singular points at $x = -1, 1, \infty$. It reduces to the Legendre equation (3.7) when $m = 0$. This equation also occurs in physical situations involving the operator ∇^2, if expressed in spherical polar co-ordinates. In such cases, $-l \leq m \leq l$ and m is restricted to integer values. As with the case of the Legendre equation, in normal use the variable x is the cosine of the polar angle in spherical polar co-ordinates. Any solution of equation (3.18) is called an associated Legendre function.

The solutions $y_{|m|}(x)$ to the associated Legendre equations can be derived from the known solutions of the Legendre equation $u(x)$ using the relationship

$$y_{|m|}(x) = (1-x^2)^{\frac{|m|}{2}} \frac{d^{|m|}u(x)}{dx^{|m|}}. \tag{3.19}$$

For the physical situations we are interested in, l and m are both integers and the general solution to equation (3.18) is denoted by

$$y_{|m|}(x) = c_1 P_l^m(x) + c_2 Q_l^m(x) \tag{3.20}$$

where $P_l^m(x)$ and $Q_l^m(x)$ are the associated Legendre functions of the first and second kind respectively. For non-negative m values, the associated Legendre functions are related to the ordinary Legendre functions for integer l by

$$\begin{aligned} P_l^m(x) &= (1-x^2)^{\frac{|m|}{2}} \frac{d^{|m|} P_l(x)}{dx^{|m|}} \\ Q_l^m(x) &= (1-x^2)^{\frac{|m|}{2}} \frac{d^{|m|} Q_l(x)}{dx^{|m|}} \end{aligned} \tag{3.21}$$

Just like the $Q_l(x)$, the $Q_l^m(x)$ are singular at $x = \pm 1$ and therefore their coefficients have to vanish in the cases of our interest. Some of the associated Legendre polynomials are given by

$$\begin{aligned} P_1^1(x) &= (1-x)^{\frac{1}{2}} \\ P_2^1(x) &= 3x\,(1-x)^{\frac{1}{2}} \\ P_2^2(x) &= 3x\,(1-x^2) \end{aligned} \tag{3.22}$$

The associated Legendre polynomials

- are mutually orthogonal over the interval $-1 \leq x \leq 1$, that is,

$$\begin{aligned} &\int_{-1}^{1} P_l^m(x)\, P_k^m(x)\, dx = 0 \quad \text{if } l \neq k \\ &\int_{-1}^{1} P_l^m(x)\, P_l^k(x)\, (1-x^2)^{-1}\, dx = 0 \quad \text{if } |m| \neq |k| \end{aligned} \tag{3.23}$$

- satisfy the normalization conditions

$$\begin{aligned} I_{l,m} &= \int_{-1}^{1} P_l^m(x)\, P_l^m(x)\, dx = \frac{2}{2l+1} \frac{(l+m)!}{(l-m)!} \\ I_{l,m} &= \int_{-1}^{1} P_l^m(x)\, P_l^m(x)\, (1-x^2)^{-1}\, dx = \frac{(l+m)!}{m(l-m)!} \end{aligned} \tag{3.24}$$

- have a wide range of recurrence relations

$$\begin{aligned} &P_l^{m+1}(x) = \frac{2mx}{(1-x^2)^{\frac{1}{2}}} P_l^m(x) + [m(m-1) - l(l+1)] P_l^{m-1}(x), \\ &(2l+1) x P_l^m(x) = (l+m) P_{l-1}^m(x) + (l-m+1) P_{l+1}^m(x), \\ &(2l+1)(1-x^2)^{\frac{1}{2}} P_l^m(x) = P_{l+1}^{m+1}(x) - P_{l-1}^{m+1}(x), \\ &2(1-x^2)^{\frac{1}{2}} \frac{dP_l^m(x)}{dx} = P_l^{m+1}(x) - (l+m)(l-m+1) P_l^{m-1}(x) \end{aligned} \tag{3.25}$$

  due to the presence of the two indices, l and m.

3.1.4 Spherical Harmonics

Usually if physical problems are expressed in spherical polar co-ordinates, a solution

$$y(\mathbf{r}) = R(r)\,\Theta(\theta)\,\Phi(\phi) \tag{3.26}$$

separable in the three co-ordinates r, θ, and ϕ may be assumed for spherically symmetric potentials. In principle, the angular parts, $\Pi(\Omega) = \Theta(\theta)\,\Phi(\phi)$, can be evaluated together by expressing them as a linear combination of spherical harmonics, $Y_l^m(\theta,\phi)$ [1], defined as

$$Y_l^m(\Omega) = (-1)^m \left[\frac{2l+1(l-m)!}{4\pi(l+m)!}\right]^{\frac{1}{2}} P_l^m(\cos\theta)\,\exp(im\phi) \tag{3.27}$$

where $\Omega = (\theta, \phi)$ denote a solid angle and l and m are the orbital and projection angular momentum quantum numbers and $P_l^m(\cos\theta)$ are the associated Legendre polynomials.

Spherical harmonics have unique properties that are quite useful in solving problems in atomic physics. These properties include:

- the symmetry relation

$$Y_l^{-m}(\theta,\phi) = (-1)^m Y_l^{m*}(\theta,\phi) \tag{3.28}$$

  where the asterisk denotes complex conjugation

- the ortho-normality relation

$$\int_{-1}^{1}\int_{0}^{2\pi} Y_l^{m*}(\theta,\phi) Y_{l'}^{'m}(\theta,\phi)\, d\phi\, d(\cos\theta) = \delta_{ll'}\,\delta_{mm'} \tag{3.29}$$

- the closure relation

$$\sum_{l,m} Y_l^m(\Omega)\, Y_l^{m*}(\Omega') = \delta(\Omega - \Omega') \tag{3.30}$$

  where $\delta(\Omega - \Omega')$ is a Dirac delta function with a zero value if $\Omega \neq \Omega'$.

- the reduction relation

$$\sum_{l,m} Y_l^m(\Omega)\, Y_l^{m*}(\Omega') = \sum_{l} \frac{2l+1}{4\pi}\, P_l(\cos\theta) \tag{3.31}$$

  where θ is the overlap angle between the two solid angles

- the integral relation

$$\begin{aligned} &\int_{-1}^{1}\int_{0}^{2\pi} Y_l^{m*}(\theta,\phi) Y_k^{\mu}(\theta,\phi) Y_{l'}^{'m}(\theta,\phi)\, d\phi\, d(\cos\theta) \\ &\qquad = \frac{(2l+1)(2k+1)(2l'+1)}{4\pi} \begin{pmatrix} l & k & l' \\ m & \mu & m' \end{pmatrix} \begin{pmatrix} l & k & l' \\ 0 & 0 & 0 \end{pmatrix} \end{aligned} \tag{3.32}$$

---

[1] Different conventions for defining the spherical harmonics exist.

where the brackets denote the Wigner-3j symbols. These can equivalently be expressed using the Clebsch-Gordan coefficients [20].

3.1.5 Spherical Bessel Functions

The Spherical Bessel functions are obtained from the solutions of the Helmholtz' equation, $(\nabla^2 + k^2) = 0$, in spherical polar co-ordinates [103]. For solutions that are finite on the polar axis, the radial part $R(r)$ of the solution must satisfy the equation

$$r^2 R'' + 2rR' + \left[k^2 r^2 - l(l+1)\right] R = 0 \tag{3.33}$$

where l is an integer and the primes denote the derivatives with respect to r. This equation looks very much like Bessel's equation and can in fact be reduced to it by writing $R(r) = r^{-\frac{1}{2}} S(r)$, in which case $S(r)$ satisfies

$$r^2 S'' + rS' + \left[k^2 r^2 - (l + \frac{1}{2})^2\right] S = 0. \tag{3.34}$$

With a further change of variable $x = kr$ and letting $y(x) = S(kr)$, one obtains

$$x^2 y'' + xy' + \left[x^2 - (l + \frac{1}{2})^2\right] y = 0 \tag{3.35}$$

which is a Bessel's equation of order $l + \frac{1}{2}$ with the general solutions of the form, $J_{l+\frac{1}{2}}(x)$ and $Y_{l+\frac{1}{2}}(x)$. These solutions are known as ordinary Bessel functions of the first and second kind, respectively.

The general solution of equation (3.33) can therefore be written as

$$R(r) = r^{-\frac{1}{2}} \left[c_1 J_{l+\frac{1}{2}}(kr) + c_2 Y_{l+\frac{1}{2}}(kr)\right] \tag{3.36}$$

where c_1 and c_2 are constants that have to be determined from the boundary conditions imposed on the solutions. In particular, for solutions that are finite at the origin, we require that $c_2 = 0$. The functions, $x^{-\frac{1}{2}} J_{l+\frac{1}{2}}(x)$ and $x^{-\frac{1}{2}} Y_{l+\frac{1}{2}}(x)$, when suitably normalized, are called the spherical Bessel functions of the first and second kind respectively. They are expressed in terms of the corresponding ordinary Bessel functions as

$$\begin{aligned} j_l(x) &= \sqrt{\frac{\pi}{2x}}\, J_{l+\frac{1}{2}}(x) \\ \eta_l(x) &= \sqrt{\frac{\pi}{2x}}\, Y_{l+\frac{1}{2}}(x). \end{aligned} \tag{3.37}$$

The first two spherical Bessel functions of each kind are given by:

$$\begin{aligned} j_0(x) &= \frac{\sin x}{x} \\ \eta_0(x) &= -\frac{\cos x}{x} \\ j_1(x) &= \frac{\sin x}{x^2} - \frac{\cos x}{x} \\ \eta_1(x) &= -\frac{\cos x}{x^2} - \frac{\sin x}{x} \end{aligned} \tag{3.38}$$

In general, spherical Bessel functions:

- of any order l can be obtained from the zeroth order function term using

$$f_l(x) = (-1)^l \, x^l \left(\frac{1}{x} \frac{\mathrm{d}}{\mathrm{d}x} \right)^l f_0(x) \tag{3.39}$$

  where $f_l(x)$ denotes $j_l(x)$ or $\eta_l(x)$.

- satisfy the recurrence relations

$$\begin{aligned} \frac{\mathrm{d}}{\mathrm{d}x}[x^l \, j_l(x)] &= x^l \, j_{l-1}(x) \\ j_{l-1}(x) + j_{l+1}(x) &= \frac{2l}{x} \, j_l(x) \end{aligned} \tag{3.40}$$

- can be expanded in the power series [109, 110]

$$j_l(x) = x^l \sum_{n=0}^{\infty} \frac{(-1)^n \, x^{2n}}{2^n \, n!(2n+2l+1)!!} \tag{3.41}$$

3.1.6 Solution of Field-Free Schrödinger Equation using B splines

In solving the TDSE, a spectral approach is followed in which the field-free Schrödinger equation is first solved to generate the corresponding eigenvalues and eigenvectors. The eigenvalues correspond to the system's energy for the corresponding state vector. The obtained state vectors are then used in evaluating time-independent transition matrix elements which are subsequently used, together with the eigenvalues, in the time propagation process. In this section, the method of using B splines to obtain the eigenvalues and vector [14, 106] is explained. The discussion is confined to a one-electron system with a central binding potential.

The Schrödinger equation for a one-electron system in the absence of any external fields can be written as

$$\left[-\frac{1}{2}\nabla^2 + V(r) \right] \Psi(\mathbf{r}) = E \, \Psi(\mathbf{r}) \tag{3.42}$$

where the first term on the left is the kinetic energy of the electron, $V(r)$ is the central binding potential of the electron, $\Psi(\mathbf{r})$ is the electron's wavefunction, and E is the total energy of the electron. The bracketed term on the left hand side constitute the Hamiltonian operator of the system.

A spectral expansion of the total wavefunction

$$\Psi(\mathbf{r}) = \sum_{nlm} c_{nlm}\, \psi_{nlm}(\mathbf{r}) \tag{3.43}$$

is considered, where $\psi_{nlm}(\mathbf{r})$ is the wavefunction of a particular symmetry defined by the principal quantum number n, orbital angular momentum quantum number l, projection angular momentum quantum number m, and having a unique energy E_{nlm}. The coefficient c_{nlm} is a weighting function for the distribution and it takes unity value if the electron is known to occupy a definite eigenstate and the other states remain unoccupied and zero otherwise. Usually, the states with different m quantum numbers but same l quantum number, in the absence of magnetic fields, have the same energy value and they are referred to as degenerate states.

Each wavefunction $\psi_{nlm}(\mathbf{r})$ can be conveniently written as product

$$\psi_{nlm}(\mathbf{r}) = R_{nl}(r)\, Y_l^m(\theta, \phi) \tag{3.44}$$

of the radial part $R_{nl}(r)$ and the angular part in spherical harmonics $Y_l^m(\theta, \phi)$. The radial part can further be expanded in a finite number of B spline functions B_i of a predetermined order k

$$R_{nl}(r) = \frac{P_{nl}(r)}{r} = \sum_{i=2}^{n_r-1} \rho_i^{nl} \frac{B_i}{r} \tag{3.45}$$

where ρ_i^{nl} are the weighting functions of each B spline for a particular value of n and l. The subscript k has been omitted from $B_{i,k}$ for notational simplicity. The first and the last B splines are removed to be consistent with the boundary conditions requirement. P_{nl} are solutions to the reduced radial Schrödinger equation

$$\left[-\frac{1}{2}\left(\frac{\mathrm{d}^2}{\mathrm{d}r^2} - \frac{l(l+1)}{r^2}\right) - \frac{Z}{r}\right] P_{nl} = E_{nl} P_{nl} \tag{3.46}$$

with an explicit hydrogenic Coulomb potential $-Z/r$ considered.

If the total wavefunction in equation (3.42) is considered to be from a definite single quantum state and the inner product is taken , the angular part reduces to unity due to the orthonormality condition of the spherical harmonics. The radial part of equation (3.45), in the B spline expansion, takes the form

$$\begin{aligned} S = \sum_{i,j} \rho_i \rho_j \int_0^{r_{\max}} \mathrm{d}r \left[-\frac{1}{2}\left(B_j(r)\frac{\mathrm{d}^2}{\mathrm{d}r^2}B_i(r)\right) + B_j(r)\left(-\frac{Z}{r} + \frac{l(l+1)}{2r^2}\right)B_i(r)\right] \\ - \epsilon_{nl} \sum_{i,j} \rho_i \rho_j \int_0^{r_{\max}} \mathrm{d}r\; B_j(r) B_i(r) \end{aligned} \tag{3.47}$$

where the inner product has been expressed in an equivalent variational equation which can be minimized using the condition $\delta S = 0$. In this case ϵ_{nl} plays the role of a Lagrange multiplier introduced to ensure that the normalization constraint

$$\int_0^{r_{\max}} |P_{nl}(r)|^2 = 1 \tag{3.48}$$

for a given cylindrical symmetry n, l is satisfied. The variational principle $\delta S = 0$, together with the constraints $\delta P_{nl}(0) = 0$ and $\delta P_{nl}(r_{\max}) = 0$, lead to the solution of the radial Schrödinger equation for $P_{nl}(r)$.

The action S in equation (3.47) is quadratic in ρ_i. A system of linear equations for the expansion coefficients can be obtained by taking a partial derivative

$$\frac{\partial S}{\partial \rho_i} = 0, \qquad i = 2, \cdots, n_r - 1. \tag{3.49}$$

The resulting equations can be written in the form of a $(n_r - 2) \times (n_r - 2)$ symmetric generalized eigenvalue equation

$$\mathbf{HC} = \epsilon \mathbf{SC} \tag{3.50}$$

where $\mathbf{C}$ is the vector of expansion coefficients

$$\mathbf{C} = (\rho_2, \rho_3, \cdots, \rho_{n-1}) \tag{3.51}$$

and the matrices $\mathbf{H}$ and $\mathbf{S}$ are given by

$$\begin{aligned} \mathbf{H}_{i,j} &= \int_0^{r_{max}} \mathrm{d}r \left[-\frac{1}{2} \left(B_j(r) \frac{\mathrm{d}^2}{\mathrm{d}r^2} B_i(r) \right) + B_j(r) \left(-\frac{Z}{r} + \frac{l(l+1)}{2r^2} \right) B_i(r) \right] \\ \mathbf{S}_{i,j} &= \int_0^{r_{max}} \mathrm{d}r \, B_j(r) \, B_i(r). \end{aligned} \tag{3.52}$$

The first part of $\mathbf{H}_{i,j}$ can be further simplified using the derivative property of B splines, $\langle B_j | B_i'' \rangle = -\langle B_j' | B_i' \rangle$. The primes denote derivatives in this case. Since the product of $B_i(r)$ and $B_j(r)$ are non-vanishing only when i and j differ by the B splines order k or less, the matrices $\mathbf{H}$ and $\mathbf{S}$ are sparse and diagonally dominant banded matrices. The solution to the eigenvalue problem of such matrices is numerically stable. Standard fortran routines can be used to solve this eigenvalue problem numerically with $n_r - 2$ eigenvalues and $n_r - 2$ eigenvectors as the output results. Gaussian integration of order $2k$ allows the evaluation of the matrix elements of $\mathbf{H}$ and $\mathbf{S}$ to machine accuracy with an exception of matrix elements of the Coulomb potential with $1/r$ dependence which are solved to a reasonable accuracy. The resulting eigen vectors are orthonormalised for every l symmetry.

The quality of the generated eigenvalues and the eigenvectors, and the numerical stability, depend on several tunable parameters used in the B spline basis set. Vanne [14] performed a systematic study of these tunable parameters and found that the quality and numerical stability scales with the box size r_{max}, the order of the B splines k, the number of the B splines s, the breakpoint sequence used, and the density of the B splines, $s/r_{\max}$. The ground state and some lowly lying excited states can be accurately reproduced even with a smaller box radius but this accuracy is reduced for highly excited and continuum states because of the induced box confinement and the incompleteness of the basis set. The box induced inaccuracies can be reduced by increasing the box radius $r_{\max}$, using B splines of order $7-10$, employing a geometrically progressive break point sequence for accurate description of both bound and continuum states, and increasing the density of states $s/r_{\max} > 1$ for a reliable treatment of photoionization processes.

3.2 Gauge Invariance and Gauge Transformation

An interesting feature in the description of the electromagnetic field is the fact that the field strengths are derivable from the potentials but to a certain extent, the potentials can be chosen freely without changing the field strengths [111].

This means that the vector potential ($\mathbf{A}(\mathbf{r},t)$) and the scalar potential ($\phi(\mathbf{r},t)$) can in principle be expressed in any other gauge provided the following gauge-transformation conditions are satisfied,

$$\mathbf{A}'(\mathbf{r},t) = \mathbf{A}(\mathbf{r},t) - \nabla\chi(\mathbf{r},t) \tag{3.53}$$

$$\phi'(\mathbf{r},t) = \phi(\mathbf{r},t) + \frac{\partial}{\partial t}\chi(\mathbf{r},t) \tag{3.54}$$

and the wave function is correspondingly transformed to

$$\Psi'(\mathbf{r},t) = T_R\Psi(\mathbf{r},t) = e^{\frac{i}{\hbar c}\chi(\mathbf{r},t)}\Psi(\mathbf{r},t) \tag{3.55}$$

where $\mathbf{T_R}$ is the transformation and $\chi(\mathbf{r},t)$ is the gauge function which is usually an arbitrary function of r and t.

3.2.1 Generalised Gauge TDSE

If an N-electron system is exposed to intense laser pulse, the TDSE is formulated in the X-gauge [14] by

$$\left\{ i\frac{\partial}{\partial t} - H_X(t) \right\} \mid \Psi_X(t)\rangle = 0 \tag{3.56}$$

where the total Hamiltonian H_X is a partition of a field-free part H_0 and a system-field interaction part V_X given by

$$H_X \ = \ H_0 \ + \ V_X \tag{3.57}$$

The field-free Hamiltonian H_0 is system dependent and it is given for an N-electron system, assuming an infinitely massive nuclei, by

$$H_0 \ = \ -\frac{1}{2}\sum_{j}^{N}\nabla_j^2 - \sum_{j<k}^{N}\left\{ \frac{1}{r_j} - \frac{1}{\mathbf{r}_{jk}} \right\} \tag{3.58}$$

The first term on the right of this equation is the electronic kinetic energy operator of the j^{th} electron and the other terms are the electronic potential energy operators due to the electron-nucleus interaction and the electron-electron interaction respectively

The field-system interaction in the X gauge V_X is given by

$$V_X \;=\; \sum_j \mathbf{A}_X(\mathbf{r}_j,t)\,\cdot\,\mathbf{p}_X(j)\;-\;\phi_X(\mathbf{r}_j,t)\;+\;\frac{A_X^2(t)}{2} \tag{3.59}$$

where the magnetic vector potential $\mathbf{A}_X(\mathbf{r},t)$ and the electric scalar potential $\Phi_X(\mathbf{r},t)$ are generally gauge dependent and can be expressed as

$$\begin{aligned} \mathbf{A}_X(t) \;&=\; \mathbf{A}(\mathbf{r}_j,t)\;-\nabla\,\chi(\mathbf{r}_j,t) \\ \Phi_X(r_j,t) \;&=\; [\mathbf{F}(\mathbf{r}_j,t)+\dot{\chi}(\mathbf{r},t)]\,\cdot\,\mathbf{r}_j\;+\;N\dot{\chi}_0(t) \end{aligned} \tag{3.60}$$

Within the single active electron (SAE) approximation, equation (3.56) is solved by expanding the time dependent vector $\mid\Psi_X(\mathbf{r},t)\rangle$ in the basis vectors $\mid\Phi_\alpha(\mathbf{r},t)\rangle$, that is,

$$\mid\,\Psi_X(\mathbf{r},t)\,\rangle\;=\;\sum_\alpha C_\alpha(t)\;\mid\,\Phi_\alpha(\mathbf{r},t)\,\rangle \tag{3.61}$$

where $\mid\Phi_\alpha(\mathbf{r},t)\rangle$ are the solutions of TDSE with the field-free Hamiltonian H_0.

Multiplication of equation (3.56) with $\langle\,\Phi_{\alpha'}(\mathbf{r},t)\;\mid$ for all α' and integration over the electronic co-ordinates yields a system of ordinary differential equations

$$\begin{aligned} &\langle\,\Phi_{\alpha'}(\mathbf{r},t)\;\mid i\,\frac{\partial}{\partial t}-H_X\mid\Psi_X(\mathbf{r},t)\,\rangle=0 \\ &\sum_\alpha\langle\,\Phi_\alpha(t)\;\mid i\,\dot{C}_\alpha(t)\mid\;\Phi_\alpha(\mathbf{r},t)\,\rangle \\ &\qquad-\sum_\alpha C_\alpha(t)\,\langle\,\Phi_{\alpha'}(\mathbf{r},t)\mid H_0+V_X(\mathbf{r},t)\mid\Phi_\alpha(\mathbf{r},t)\,\rangle=0 \end{aligned} \tag{3.62}$$

The above integro-differential equation can be re-written as

$$i\sum_\alpha\dot{C}_\alpha(t)\,\langle\,\Phi_{\alpha'}(\mathbf{r},t)\;\mid\;\Phi_\alpha(\mathbf{r},t)\,\rangle\;=\;\Sigma_\alpha\,C_\alpha(t)\,\langle\,\Phi_{\alpha'}(\mathbf{r},t)\;\mid\;V_X(\mathbf{r},t)\;\mid\;\Phi_\alpha(\mathbf{r},t)\,\rangle. \tag{3.63}$$

If a discretization of the continuum is used, the vectors Φ_α can be renormalized to fulfil the orthonormality condition, $\langle\,\Phi_{\alpha'}\;\mid\;\Phi_\alpha\,\rangle\;=\;\delta_{\alpha'\,\alpha}$, further simplifying the above equation to

$$i\,\dot{C}_{\alpha'}(t)\;=\;\Sigma_\alpha\,C_\alpha(t)\,\langle\,\Phi_{\alpha'}(\mathbf{r},t)\;\mid\;V_X(\mathbf{r},t)\;\mid\;\Phi_\alpha(\mathbf{r},t)\,\rangle. \tag{3.64}$$

From this general gauge treatment of the TDSE, the usual length(L) and velocity(V) forms of the Lorenz gauge are obtainable by choosing appropriately the arbitrary function $\chi(\mathbf{r},t)$ and the new Hamiltonian H_X under the gauge transform becomes

$$H_X=e^{\frac{-ie\chi}{\hbar c}}\,[H_R]\,e^{\frac{ie\chi}{\hbar c}} \tag{3.65}$$

with H_R being the Hamiltonian operator in radiation gauge. Under these transformations, the interaction Hamiltonians H_I in the usual length and velocity gauge dipole approximations respectively become

$$H_I^l = -e\mathbf{r} \cdot \mathbf{E}(t) \tag{3.66}$$

and

$$H_I^v = \frac{ie\hbar}{\mu c}\mathbf{A} \cdot \nabla + \frac{e^2}{2\mu c^2}A^2(t) \tag{3.67}$$

where $\mathbf{E}(t)$ is the electric field component of the electromagnetic radiation and $\mathbf{A}(t)$ is the vector potential describing the electromagnetic radiation. These two quantities are related by

$$\mathbf{E}(t) = -\frac{1}{c}\frac{\partial \mathbf{A}(t)}{\partial t} \tag{3.68}$$

From this point on, only atomic units are used unless it is explicitly specified otherwise. The radiation-gauge whose boundary conditions require the scalar potential $\phi(r)$ and the divergence of the vector potential $\mathbf{A}$ to vanish is the preferred gauge. With the boundary conditions, the vector potential satisfies the general wave equation and hence it can be expressed in terms of plane waves

$$\mathbf{A}(t) = A_0\, f(t)\, \hat{\varepsilon}\, \exp[i(\omega t - \mathbf{k} \cdot \mathbf{r} + \delta)] + c.c. \tag{3.69}$$

with *c.c.* denoting complex conjugation. In this equation, $A_0 = E_0/\omega$ is the magnitude of the vector potential expressed in terms of the peak electric field strength E_0 divided by the field frequency ω, $f(t)$ is the carrier envelope pulse envelope, and $\mathbf{k}$ is the radiation momentum whose magnitude $k = 2\pi/\lambda$. The modifications introduced by the spatial retardation terms $e^{\pm i\mathbf{k}\cdot\mathbf{r}}$ in equation (3.69) are investigated in this study.

3.3 Strong Field Theories

In this section, a brief overview of some of the theoretical approaches used in the solution of the TDSE is discussed. The numerical TDSE solution used to incorporate the beyond-the-dipole effects is also introduced here and subsequently discussed in detail in the sections that follow.

3.3.1 Landau-Lifshitz Theory

Landau and Lifshitz [112] solved the Schrödinger equation for a hydrogen atom in a quasi-static field using parabolic co-ordinates. In these co-ordinates, the symmetry of the effective potential as well as the degeneracy of the eigenstates of the system are removed. They derived the tunnel ionization rate as

$$\Gamma_{LL} = 4\,\frac{(2\mid \varepsilon_0 \mid)^{5/2}}{F}\exp\left(-\frac{2(2\mid \varepsilon_0 \mid)^{3/2}}{3\,F}\right) \tag{3.70}$$

where ε_0 is the ionization potential of the hydrogen atom in its ground state and F is the quasi-static field strength. The rate can be generalized to other hydrogenic systems using $\varepsilon_0 = -Z^2/2$.

3.3.2 KFR/SFA Theories

Keldysh-Faisal-Reiss (KFR), also known as strong-field approximation (SFA), theories are very similar in nature although developed at different times. Keldysh in his seminal paper [34] on strong-field ionization pioneered the work by providing a unified picture of the ionization process for multiphoton and tunneling regimes. With the discovery of the above-threshold-ionization (ATI) [32], Faisal [36] and Reiss [37] formulated a theory closely related to Keldysh but in the velocity gauge.

The KFR/SFA ionization probability amplitude is given by

$$a_p(t) = -i \int^t \mathrm{d}t'\, e^{-iS(t,t',\mathbf{p})} \left\langle \phi_V\left(\mathbf{p} + \mathbf{A}(t')\right) \middle| V(t') \middle| \phi_i \right\rangle \tag{3.71}$$

where ϕ_i is the initial bound state, ϕ_V is a Volkov (dressed) state of a free-electron in a radiation field, $V(t')$ is the interaction Hamiltonian at the time of birth of the free-electron, and the action integral $S(t, t', \mathbf{p})$ is defined as

$$S(t, t', \mathbf{p}) = \frac{1}{2} \int_{t'}^{t} \mathrm{d}\tau [\mathbf{p} + \mathbf{A}(\tau)]^2 + I_p(\tau - t'). \tag{3.72}$$

In general, the KFR theories ignore the effect of the laser fields in the initial state. The effect of resonant transitions is also not included in these theories.

3.3.3 PPT Theory

The work of Keldysh [34] was closely followed by a detailed analytical solution of the TDSE derived by Peremolov, Popov, and Terent'ev (PPT) [66]. They calculated the total rate of multiphoton ionization from a state in a laser field for linear polarization to be

$$\begin{aligned} \Gamma_{\mathrm{PPT}} = {} & |C_{n^*l^*}|^2 \sqrt{\frac{6}{\pi}}\, f_{lm}\, E_i \left(\frac{2(2E_i)^{\frac{3}{2}}}{F} \right)^{2n^* - |m| - \frac{3}{2}} \\ & \times (1+\gamma)^{2|\frac{m}{2}| + \frac{3}{4}}\, A_m(\omega, \gamma) \exp\left(-\frac{2(2E_i)^{\frac{3}{2}}}{F}\, g(\gamma) \right) \end{aligned} \tag{3.73}$$

where:

$$
\begin{aligned}
n^* &= \frac{Z}{\sqrt{2E_i}} \\
\gamma &= \frac{\omega(\sqrt{2E_i})}{F} \\
l^* &= n^* - 1 \\
f_{lm} &= \frac{(2l+1)(l+|m|)!}{2^{|m|}|m|!(l-|m|)!} \\
g(\gamma) &= \frac{3}{2\gamma}\left[1+\frac{1}{2\gamma^2}\sinh^{-1}(\gamma)-\frac{\sqrt{1+\gamma^2}}{2\gamma}\right] \\
A_m(\omega,\gamma) &= \frac{4}{3\pi}\frac{1}{|m|!}\frac{\gamma^2}{1+\gamma^2}\sum_{n-\nu}^{\infty}\omega_m \times \sqrt{\frac{2\gamma}{1+\gamma^2}(n-\nu)e^{-(n-\nu)\alpha(\gamma)}} \\
\omega_m(x) &= e^{-x^2}\int_0^x (x^2-y^2)^m e^{y^2}\mathrm{d}y \\
\alpha(\gamma) &= 2(\sinh^{-1}(\gamma)-\frac{\gamma}{\sqrt{1+\gamma^2}}) \\
\nu &= \frac{E_i}{\omega}(1+\frac{1}{2\gamma^2})
\end{aligned}
\tag{3.74}
$$

and E_i is bound state energy corresponding to the i^{th} state, Z is the charge state, γ is the Keldysh parameter, and n, l and m are the quantum numbers specifying the state of the system.

3.3.4 ADK Theory

Ammosov, Delone, and Krainov (ADK) [69] imposed a limiting condition $\gamma \to 0$ on the PPT formula to obtain a more popular relation that is valid only in the quasi-static tunneling (QST) limit. With this limit, the total rate of multiphoton ionization reduces to

$$
\Gamma_{\text{ADK}} = |C_{n^*l^*}|^2\sqrt{\frac{6}{\pi}}\, f_{lm}\, E_i \left(\frac{2(2E_i)^{\frac{3}{2}}}{F}\right)^{2n^*-|m|-\frac{3}{2}} \times \exp\left[-\frac{2(2E_i)^{\frac{3}{2}}}{F}\right] \tag{3.75}
$$

with the terms as defined in equation (3.74).

3.3.5 Lowest-order Perturbation Theory (LOPT)

In perturbation theory, the evolution operator in the TDSE can be expanded in the Dyson series [113] as

$$
U_I(t) = 1 - \frac{i}{\hbar}\int_0^t \mathrm{d}t'\, V_I(t') + \left(\frac{-i}{\hbar}\right)^2 \int_0^t \mathrm{d}t' \int_0^{t'} \mathrm{d}t''\, V_I(t')\, V_I(t'') + 0(V^3). \tag{3.76}
$$

The lowest-order term (LOPT) in the expansion of the transition amplitude for $\alpha \neq \alpha'$ is

$$\begin{aligned}
-\frac{i}{\hbar}\int_0^t & \mathrm{d}t' \, \langle \alpha' \mid V_I(t') \mid \alpha \rangle \\
&= -\frac{i}{\hbar}\int_0^t \mathrm{d}t' \, \langle \alpha' e^{\frac{iH_0 t'}{\hbar}} \mid V_I(t') \mid e^{\frac{iH_0 t'}{\hbar}} \alpha \rangle \\
&= -\frac{i}{\hbar}\int_0^t \mathrm{d}t' \, e^{\frac{-i(E_\alpha - E_{\alpha'})t'}{\hbar}} \langle \alpha' \mid V_I(t') \mid \alpha \rangle \\
&= \frac{[\exp \frac{-i(E_\alpha - E_{\alpha'})t}{\hbar} - 1]}{E_\alpha - E_{\alpha'}} V_{\alpha\alpha'}.
\end{aligned} \tag{3.77}$$

The transition probability is then defined as

$$P(\alpha \rightarrow \alpha') = \frac{[4\sin^2 \frac{\Delta E t}{2\hbar}]}{(\Delta E)^2} |V_{\alpha\alpha'}|^2 \tag{3.78}$$

where $\Delta E = E_\alpha - E_{\alpha'}$ and the LOPT transition rate is

$$\Gamma(\alpha \rightarrow \alpha') = \lim_{t \rightarrow +\infty} \frac{[4\sin^2 \frac{\Delta E t}{2\hbar}]}{t(\Delta E)^2} |V_{\alpha\alpha'}|^2 \tag{3.79}$$

where $\alpha = \{n, l, m\}$ represents a set of quantum numbers defining an eigenstate of a system.

3.3.6 Numerical TDSE

The above methods are quite useful in providing a clear and intuitive picture of the interaction processes. But when an accurate quantitative description is desirable, then one has to directly solve the TDSE numerically. In the perturbative regime, the interpretation of the numerical TDSE results is rather easy but beyond the limits of the lowest-order perturbation theory (LOPT), the interpretation of the results is quite a challenging task. The accuracy of the numerical TDSE results is limited by the order of the multipole expansion used in transition matrices. In most cases, the dipole approximation has been employed to describe the interaction processes. This approximation may not be valid if very short wavelengths are used and/or if the peak electric field strength of the radiation field is very large. In this study, the validity of the dipole approximation in the strong-field processes is tested and the effects of the non-dipole interactions in the photoionization dynamics are discussed.

Different approaches for solving the TDSE exist even within the single-active-electron (SAE) approximation. The solution of the non-relativistic TDSE using a spectral method employing B splines used in this study is restricted to the SAE approximation. The discussion is centred on the hydrogen atom but with some extension to the helium atom.

3.4 The TDSE in Radiation and Length Gauge

The total Hamiltonian for a quantum system can be written as a sum of the field-free Hamiltonian H_0 and an interaction Hamiltonian H_I. The field-free Hamiltonian for a system with several electrons can be written as

$$H_0 = \sum_{j,k}^{N} \frac{1}{2\mu} p_j^2 + V(r_j, r_k) \tag{3.80}$$

where the first term in the summation gives the kinetic energy and the second term gives the potential energy of the j^{th} electron respectively. The potential energy term can be fully expressed as

$$V(r_j, r_k) = -\frac{Z}{r_j} + \frac{1}{r_{jk}}. \tag{3.81}$$

Here, the first term of the equation is the attractive Coulomb interaction between the j^{th} electron and the nucleus whose atomic number is Z while the second term is the repulsive Coulomb interaction between any pair of the interacting electrons. By considering the motion of a single active electron and freezing the other electrons in their respective ground-state configurations, the field-free Hamiltonian can be approximated by a SAE model with a central potential $V_{\text{eff}}(r)$ obtained by using mean-field approaches to minimize the electron-electron interaction terms.

A non-relativistic single-active-electron system interacting with a radiation field in the non-depletion mode [2], can be described using the semi-classical time dependent Schrödinger equation in the minimal coupling formalism [111]

$$-i\frac{\partial \Psi(\mathbf{r},t)}{\partial t} = \frac{1}{2m}[(\mathbf{p} - \frac{q}{c}\mathbf{A})^2 - \Phi(\mathbf{r},t) + V(r)]\Psi(\mathbf{r},t). \tag{3.82}$$

In the SAE model, the interaction Hamiltonian H_I would be similar to that of the hydrogen atom and therefore it can be expressed in any of the different gauges provided that the gauge invariance conditions are satisfied. For example, in Radiation gauge it can take the form

$$H_I = \mathbf{A} \cdot \mathbf{p} + \frac{A^2}{2} \tag{3.83}$$

with the Coulomb gauge conditions specified as

$$\nabla \cdot \mathbf{A} = 0; \qquad \Phi = 0. \tag{3.84}$$

In length gauge, the scalar function $\chi = \mathbf{A}(\mathbf{r},t) \cdot \mathbf{r}$ is used in transforming both the vector and scalar potentials, and the wave function from the radiation gauge.

From vector analysis, one can show easily that

$$\nabla \chi(\mathbf{r},t) = \mathbf{A}(\mathbf{r},t) + \mathbf{r}\nabla \cdot \mathbf{A}(\mathbf{r},t) + i(\mathbf{L} \times \mathbf{A}) \tag{3.85}$$

---

[2] The number of photons in the radiation field is assumed to be in excess and can not be depleted.

yielding the corresponding vector and the scalar potentials in length gauge as

$$\begin{aligned} \mathbf{A}_L &= \mathbf{A} - \nabla(\mathbf{A}\cdot\mathbf{r}) = -i\mathbf{L}\times\mathbf{A}; \\ \Phi_L &= \mathbf{F}\cdot\mathbf{r}. \end{aligned} \tag{3.86}$$

3.4.1 Transformation to Length Gauge

The semi-classical Hamiltonian in a new gauge can be written in terms of the corresponding vector $\mathbf{A}'$ and scalar $\Phi'(r)$ potentials as

$$\begin{aligned} H &= \frac{1}{2m}[\mathbf{p} - q\mathbf{A}']^2 + V(r) + \Phi'(r) \\ &= \frac{1}{2m}[\mathbf{p}^2 - q\mathbf{p}\cdot\mathbf{A}' - q\mathbf{A}'\cdot\mathbf{p} + q^2\mathbf{A}'^2] + V(r) + \Phi'(r) \\ &= H_0 + \frac{1}{2m}[-q\mathbf{p}\cdot\mathbf{A}' - q\mathbf{A}'\cdot\mathbf{p} + q^2\mathbf{A}'^2] + \Phi'(r) \end{aligned} \tag{3.87}$$

where H_0 is the field-free Hamiltonian. Considering the explicit form of the length-gauge vector potential already shown in equation(3.86) and expanding it further, yields

$$\begin{aligned} \mathbf{A}_L &= -i\,\mathbf{L}\times\mathbf{A} \\ &= -\hbar\,(\mathbf{r}\times\nabla\times\mathbf{A}) \\ &= -\hbar\,(\hat{x}z\partial_x A_z + \hat{y}z\partial_y A_z - \hat{z}[x\partial_x A_z + y\partial_y A_z]) \end{aligned} \tag{3.88}$$

where the case of a linear polarized radiation field is considered with its electric field component pointing in the $+z$ direction. Making appropriate substitutions for this vector potential in the equation for the semi-classical Hamiltonian above, the first interaction Hamiltonian term can be re-written as,

$$\begin{aligned} -\frac{q\mathbf{p}\cdot\mathbf{A}_L}{2m} &= \frac{i\hbar^2 e}{2m}\,\nabla\cdot(\hat{x}z\partial_x A_z + \hat{y}z\partial_y A_z - \hat{z}[x\partial_x A_z + y\partial_y A_z]) \\ &= \frac{i\hbar^2 e}{2m}\,(z\partial_{xx}A_z + z\partial_{yy}A_z - x\partial_{zx}A_z - y\partial_{zy}A_z) \\ &= \frac{i\hbar^2 e}{2m}\,(z\partial_{xx}A_z + z\partial_{yy}A_z + z\partial_{zz}A_z - z\partial_{zz}A_z - x\partial_{xz}A_z - y\partial_{yz}A_z) \\ &= \frac{i\hbar^2 e}{2m}\,z\,\nabla^2 A_z \\ &= -\frac{i\hbar^2\omega^2 e}{2mc^2}\,z\,A_z \end{aligned} \tag{3.89}$$

having made use of the Coulomb gauge condition $\nabla\cdot\mathbf{A} = 0$ and noting that the vector potential $\mathbf{A}$ satisfies the Maxwell's wave equation, that is,

$$\nabla^2\mathbf{A} = \frac{1}{c^2}\frac{\partial^2}{\partial t^2}\mathbf{A} = -\frac{\omega^2}{c^2}\,\mathbf{A} \tag{3.90}$$

Likewise, the second term of the interaction Hamiltonian is expressed as

$$\begin{aligned} -\frac{q\,\mathbf{A}_L\cdot\mathbf{p}}{2m} &= \frac{i\hbar^2 e}{2m}\left(\hat{x}z\partial_x A_z + \hat{y}z\partial_y A_z - \hat{z}[x\partial_x A_z + y\partial_y A_z]\right)\cdot\nabla \\ &= \frac{i\hbar^2 e}{2m}\left(z\partial_x A_z\partial_x + z\partial_y A_z\partial_y - [x\partial_x A_z + y\partial_y A_z]\partial_z\right) \\ &= \frac{i\hbar^2 e}{2m}\left(\partial_x A_z\right)(z\partial_x - x\partial_z) \\ &= \frac{\hbar e}{2m}\left(\partial_x A_z\right)L_y \end{aligned} \tag{3.91}$$

having explicitly considered the radiation propagation direction to be the $+x$ direction. The third interaction term can also be expressed as

$$\begin{aligned} \frac{q^2\mathbf{A}_L^2}{2m} &= \frac{\hbar^2 e^2}{2m}(\hat{x}z\partial_x A_z + \hat{y}z\partial_y A_z - \hat{z}[x\partial_x A_z + y\partial_y A_z])^2 \\ &= \frac{\hbar^2 e^2}{2m}\left\{(z\partial_x A_z)^2 + (z\partial_y A_z)^2 + [x\partial_x A_z + y\partial_y A_z]^2\right\} \\ &= \frac{\hbar^2 e^2}{2m}\left\{(z\partial_x A_z)^2 + (x\partial_x A_z)^2\right\} \\ &= \frac{\hbar^2 e^2}{2m}\left(\partial_x A_z\right)^2[z^2 + x^2] \end{aligned} \tag{3.92}$$

The last interaction term incorporated by the gauge transformation of the scalar potential is given by

$$\begin{aligned} \Phi_L &= \partial_t(\mathbf{A}(\mathbf{r},t)\cdot\mathbf{r}) = (\partial_t\mathbf{A}(\mathbf{r},t)\cdot\mathbf{r}) \\ &= \mathbf{F}(\mathbf{r},t)\cdot\mathbf{r} = -\mathbf{E}(\mathbf{r},t)\cdot\mathbf{r} \end{aligned} \tag{3.93}$$

The full length-gauge interaction Hamiltonian put together in the conventional Cartesian co-ordinates can be written as

$$H_I^l = -Ez - \frac{i\hbar^2\omega^2 e}{2mc^2}\,zA_z + \frac{\hbar e}{2m}\left(\partial_x A_z\right)L_y + \frac{\hbar^2 e^2}{2m}\left(\partial_x A_z\right)^2\left[z^2 + x^2\right] \tag{3.94}$$

The first term gives the dominant contribution to the interaction Hamiltonian, the second is an intensity and wavelength dependent relativistic correction term, while the third and the fourth are the explicit contributions of the paramagnetic and diamagnetic fields respectively, with $B = \partial_x A_z$ as the magnitude of the magnetic field strength. In the weak-field and long-wavelength regimes, the magnetic and relativistic contributions can be ignored without any significant effect on the reliability of the Hamiltonian. But in the strong-field regime, the magnetic and the relativistic contributions may not be negligible. It is evident that the relativistic correction provided by the second term in equation (3.94) has the same selection rules as the first term which yields the leading contribution. It can therefore provide additional corrections to the dipole spectrum in the strong-field regime.

3.4.2 Implicit-Energy Solution of the TDSE

The TDSE, with the Hamiltonian separated into two parts, can be expressed as

$$i\hbar\frac{\partial}{\partial t}\,\Psi(\mathbf{r},t) = [H_0 + H_I]\,\Psi \tag{3.95}$$

where Ψ is the total wavefunction of the system, H_0 is the field-free Hamiltonian, and H_I is the interaction Hamiltonian in any gauge provided the gauge conditions are fulfilled.

The total wavefunction is expanded as a linear combination of field-free states $\Phi_\alpha(\mathbf{r})$ as

$$\Psi_{\mathbf{r},t} = \sum_\alpha C_\alpha(t)\,\phi_\alpha(\mathbf{r}) \tag{3.96}$$

In this case, the time dependence of the field-free wavefunctions is implicitly included in the expansion coefficients $C_\alpha(t)$. Substituting this expansion in the TDSE and taking the inner product using $\phi_{\alpha'}$, one obtains

$$\sum_\alpha \langle\,\phi_{\alpha'}\;\mid i\hbar\frac{\partial}{\partial t}C_\alpha(t)\phi(\mathbf{r})\,\rangle = \sum_\alpha [C_\alpha(t)\langle\,\phi_{\alpha'}\;\mid H_0\mid\phi_\alpha\,\rangle + C_\alpha(t)\langle\,\phi_{\alpha'}\;\mid H_I\mid\phi_\alpha\,\rangle]. \tag{3.97}$$

If evaluated on both sides, this equation reduces to the following system of coupled integro -differential equations

$$i\hbar\,\dot{C}_{\alpha'} = C_{\alpha'}(t)E_{\alpha'} + \sum_\alpha C_\alpha(t)\,\langle\,\phi_{\alpha'}\;\mid\;H_I\;\mid\;\phi_\alpha\,\rangle \tag{3.98}$$

This system of equations yields temporally and spatially coupled integral equations which can be solved numerically in the radiation, length or velocity gauges by substituting a suitable form of the interaction Hamiltonian H_I together with the corresponding gauge transformed wavefunctions. That is,

$$\dot{C}_{\alpha'}(t) = -\frac{i}{\hbar}\,[C_{\alpha'}(t)E_{\alpha'} + \sum_\alpha C_\alpha(t)\langle\,\phi_{\alpha'}\;\mid H_I\mid\phi_\alpha\,\rangle] \tag{3.99}$$

In the radiation gauge, the above equations can be written as

$$\dot{C}_{\alpha'}(t) = -\frac{i}{\hbar}\,[C_{\alpha'}(t)E_{\alpha'} + \sum_\alpha C_\alpha(t)\,\langle\,\phi_{\alpha'}\mid\;\mathbf{A}\cdot\mathbf{p} + \frac{A^2}{2}\;\mid\phi_\alpha\,\rangle] \tag{3.100}$$

The corresponding equations for velocity gauge would be

$$\dot{C}_{\alpha'}(t) = -\frac{i}{\hbar}\,[C_{\alpha'}(t)E_{\alpha'} + \sum_\alpha C_\alpha(t)\,\langle\,\phi_{\alpha'}\mid\;\mathbf{A}\cdot\mathbf{p}\mid\;\phi_\alpha\rangle] \tag{3.101}$$

where the $\mathbf{A}^2$ term can only be gauged away within the dipole approximation using a phase transformation. As for the length gauge, one has

$$\dot{C}_{\alpha'}(t) = -\frac{i}{\hbar}\,[C_{\alpha'}(t)E_{n'} + \sum_{\alpha} C_{\alpha}(t)\,\langle\, \phi_{\alpha'} \mid H_I^l \mid \phi_{\alpha}^{(l)} \rangle] \tag{3.102}$$

where H_I^l is defined in equation (3.94) and $\phi_{\alpha}^{(l)}$ is the length-gauge basis set.

3.4.3 Explicit-Energy Solution of the TDSE

As an alternative, the time dependence of the wavefunction can be defined by including an explicit energy phase as

$$\Psi_{\mathbf{r},t} = \sum_{\alpha} C_{\alpha}(t)\,\phi_{\alpha}(\mathbf{r})\,e^{-\frac{i}{\hbar}E_{\alpha}t}. \tag{3.103}$$

With this time-dependent phase of the wave function in the TDSE, one obtains the coupled integro-differntial equations

$$\dot{C}_{\alpha'}(t) = -\frac{i}{\hbar}\sum_{\alpha} C_{\alpha}(t)\langle\, \phi_{\alpha'} \mid H_I^{l(v)} \mid \Phi_{\alpha}\,\rangle\, e^{\frac{i}{\hbar}[E'_{\alpha}-E_{\alpha}]t}. \tag{3.104}$$

This set of equations can also be solved using a method similar to the implicit case given by equation (3.99) above. In the following discussions, the explicit form of the coupled equations is employed only for the sake of convenience. The extension to the implicit case is rather similar as long as the contribution of the energy phase in the coupled equations is taken into consideration.

3.4.4 Radiation-Gauge Integro-Differential Equations

The vector potential $\mathbf{A}$ in the radiation gauge satisfies the Maxwell's wave equation whose solution is a plane-wave which is a linear combination of two terms, one corresponding to photon absorption and the other to emission of photons with frequency ω by the target system. The vector potential can be written as

$$\mathbf{A}(\mathbf{r},t) = A_0\, f(t)\,\hat{\varepsilon}\sin[(\omega t - \mathbf{k}\cdot\mathbf{r} + \delta)]. \tag{3.105}$$

As already defined in equation (3.69) above, A_0 is the amplitude of the potential, $f(t)$ is a time-dependent function which describes the pulse shape of the radiation field, $\hat{\varepsilon}$ is a unit vector specifying the direction of the vector potential and it usually corresponds to the direction of the electric field of the radiation. Vectors $\mathbf{k}$ and $\mathbf{r}$ are the photon momentum and radial electron co-ordinate vectors that define the direction of propagation of the radiation and the orientation of the electron with respect to the centre of mass (nucleus in case of atomic target) respectively. The δ is the carrier envelope phase (CEP) shift of the vector potential envelope relative to the carrier.

The explicit case of the system of integro-differential equations (3.104) above in the radiation gauge, with the purely temporal part included, can therefore be written as

$$\begin{aligned}\dot{C}_{\alpha'}(t) = -\frac{i}{\hbar}\sum_{\alpha}\tilde{C}_{\alpha}(t)\,\{\,\langle\,\phi_{\alpha'}\mid[\zeta_1(t)\cos(\mathbf{k}\cdot\mathbf{r})+\zeta_1'(t)\sin(\mathbf{k}\cdot\mathbf{r})]\,\hat{\varepsilon}\cdot\mathbf{p}_c\mid\phi_{\alpha}\,\rangle\\ +\langle\,\phi_{\alpha'}\mid[\zeta_3(t)+\zeta_2(t)\cos(2\mathbf{k}\cdot\mathbf{r})+\zeta_2'(t)\sin(2\mathbf{k}\cdot\mathbf{r})]\mid\phi_{\alpha}\,\rangle\,\}\end{aligned} \tag{3.106}$$

with the time-dependent functions in the interaction Hamiltonian taking the values

$$\begin{aligned}\zeta_1(t) &= A_0 f(t)\sin(\omega t+\delta)\\ \zeta_1'(t) &= -A_0 f(t)\cos(\omega t+\delta)\\ \zeta_2(t) &= -\frac{A_0^2 f^2(t)[\cos(2\omega t+2\delta)]}{4}\\ \zeta_2'(t) &= -\frac{A_0^2 f^2(t)[\sin(2\omega t+2\delta)]}{4}\\ \zeta_3(t) &= \frac{A_0^2 f^2(t)}{4}\end{aligned} \tag{3.107}$$

and

$$\tilde{C}_{\alpha}(t) = \tilde{C}_{\alpha}\,e^{\frac{i}{\hbar}[E_{\alpha'}-E_{\alpha}]\,t} \tag{3.108}$$

3.4.5 Length-Gauge Integro-Differential Equations

In length-gauge, the system of integro-differential equations can be written as

$$\begin{aligned}\dot{C}_{\alpha'}(t) = -\frac{i}{\hbar}\sum_{\alpha}\{\,-\tilde{C}_{\alpha}(t)\,\langle\,\phi_{\alpha'}\mid[\zeta_1(t)\sin(\mathbf{k}\cdot\mathbf{r})-\zeta_1'(t)\cos(\mathbf{k}\cdot\mathbf{r})]\gamma_L'\mid\phi_{\alpha}\,\rangle\\ +C_{\alpha}(t)\times\langle\,\phi_{\alpha'}\mid[\zeta_3(t)-\frac{1}{2}\zeta_2(t)\cos(\mathbf{k}\cdot\mathbf{r})-\frac{1}{2}\zeta_2'(t)\sin(\mathbf{k}\cdot\mathbf{r})]\gamma_L''\mid\phi_{\alpha}\,\rangle\,\}\end{aligned} \tag{3.109}$$

where use has been made of the definitions of the prefactors already outlined in equation (3.107) of the radiation gauge. Also used is the relationship between the momentum vector and angular frequency, that is, $|\mathbf{k}| = \omega/c$ where c is the speed of light. ϕ_{α} is the eigen vector in length-gauge describing the system during the interaction with the radiation field. The coefficients γ_L' and γ_L'' as used in the integro-differential equation

$$\begin{aligned}\gamma_L' &= -\,[\omega z+\frac{ik^2}{2}z+\frac{k}{2}L_y]\\ \gamma_L'' &= \frac{k^2}{2}\,[z^2+x^2]\end{aligned} \tag{3.110}$$

are defined in relation to the corresponding terms in the length-gauge interaction Hamiltonian in equation (3.94). The above integral equations can be separated into parts with one part being spatial and the other being temporal and each can be integrated independently of the other. The evaluation of the space dependent part yields the time independent transition matrix elements M_{ba} that are governed by certain selection criteria stipulated by the symmetry rules of angular momentum. The values of the coefficients $C_{\alpha'}(\tau)$ at the end of the pulse duration τ for any of the gauges can therefore be obtained by performing the above integrations numerically using any reliable time integration routine. The velocity-gauge integro-differential equation incorporating the non-dipole terms takes a similar form to that of radiation gauge and therefore it is not considered here.

3.5 Time-Independent Transition Matrix Elements

The time-dependent transition matrix element between the initial state and the final state of an $N-$electron system can be given in more general terms by

$$T_{\alpha'-\alpha} = -\frac{i}{\hbar}\sum_{j=1}^{N} C_{\alpha}(t)\,\tilde{\zeta}(t)\,\langle\,\psi_{\alpha'}(\mathbf{r}_j,t)\;\mid \tilde{H}_I^j\;\mid\,\psi_{\alpha}(\mathbf{r}_j,t)\,\rangle \tag{3.111}$$

where $\tilde{H}_I^j$ is the spatial part of the interaction Hamiltonian of the j^{th}-electron with the radiation field, often referred to as the transition-matrix operator, $\tilde{\zeta}(t)$ is the time-dependent part of the interaction operator, and is a $C_{\alpha}(t)$ is a time-dependent weighting function whose square yields the probability of occupation of the specific quantum state (α) if the total wavefunction is normalized. The wavefunction ψ_{α} are single-electron orbitals which form part of a many-electron total wavefunction $\Psi_{\alpha'}$. For physical problems involving light-matter interactions, the length- or velocity-gauge transition matrix operators are commonly used. The total wavefunction can be expanded in the form of Slater-type determinants

$$\Psi_{\alpha'} = \frac{1}{\sqrt{N}}[1 - \sum_{1}^{N-1} \hat{P}_{jk}]\,\psi(\mathbf{r}_1)\psi(\mathbf{r}_2)\cdots\psi(\mathbf{r}_N). \tag{3.112}$$

The parity operator $\hat{P}_{jk}$ interchanges the positions of the j^{th} and k^{th} electrons and ensures the total anti-symmetrization of the wavefunction in consistence with the Pauli-exclusion principle.

Within the single-active-electron (SAE) approximation, a many-electron system can be reduced to a single-electron problem by using some mean-field approximations. The multielectron effects are embedded in a model potential derived from such mean-field approximations. In this study, a one-electron system is explicitly considered. An extension to the many-electron problem is possible using the SAE approximation. The two distinct states, ψ_a and ψ_b corresponding to the initial and the final states of the one-electron system respectively, are used in the evaluation of the time-independent transition matrix elements. If the wavefunctions of these distinct orbitals are substituted in the transition matrix equation, one obtains

$$\begin{aligned} T_{ba} &= \frac{i}{\hbar}\, C_a(t)\, \tilde{\zeta}(t)\, \langle \psi_b \mid \tilde{H}_I^j \mid \psi_a \rangle \\ T_{ba} &= \frac{i}{\hbar}\, C_a(t)\, \tilde{\zeta}(t)\; M_{ba} \end{aligned} \tag{3.113}$$

where the time-independent transition matrix element M_{ba} between the two states is

$$M_{ba} = \langle \psi_b \mid \tilde{H}_I^j \mid \psi_a \rangle. \tag{3.114}$$

Depending on the type of interaction and the gauge used, the time-independent transition matrix elements can be symmetric or anti-symmetric upon inversion. For example, the dipole length-gauge interaction matrix elements are symmetric ($M_{ba} = M_{ab}$) whereas the velocity-gauge transition matrix elements within the same dipole interactions are anti-symmetric, that is, ($M_{ba} = -M_{ab}$).

3.5.1 Radiation-Gauge Matrix Elements

The transition matrix for radiation gauge within the SAE approximation can be separated into two parts with part one being

$$\begin{aligned} {}^1T_{\alpha' \leftarrow \alpha} = &-\frac{i}{\hbar}\, C_\alpha(t)\, \zeta_1(t) \langle\, \psi_{\alpha'} \mid \cos(\mathbf{k}\cdot\mathbf{r})\, \hat{\varepsilon}\cdot\mathbf{p}_c \mid \psi_\alpha \,\rangle \\ &- \frac{i}{\hbar}\, C_\alpha(t)\, \zeta_1'(t) \langle\, \psi_{\alpha'} \mid \sin(\mathbf{k}\cdot\mathbf{r})\, \hat{\varepsilon}\cdot\mathbf{p}_c \mid \psi_\alpha \,\rangle \end{aligned} \tag{3.115}$$

and the other part is expressed as

$$\begin{aligned} {}^2T_{\alpha' \leftarrow \alpha} = &-\frac{i}{\hbar}\, C_\alpha(t)\, \zeta_2(t) \langle\, \psi_{\alpha'} \mid \cos(2\mathbf{k}\cdot\mathbf{r}) \mid \psi_\alpha \,\rangle \\ &- \frac{i}{\hbar}\, C_\alpha(t)\, \zeta_2'(t) \langle\, \psi_{\alpha'} \mid \sin(2\mathbf{k}\cdot\mathbf{r}) \mid \psi_\alpha \,\rangle \end{aligned} \tag{3.116}$$

where the trigonometric functions $\cos(\mathbf{k}\cdot\mathbf{r})$, $\sin(\mathbf{k}\cdot\mathbf{r})$, and the corresponding quadratic terms can be approximated using the even and the odd terms of the plane wave expansion series respectively. In the Rayleigh multipole expansion of the plane wave $e^{i\mathbf{k}\cdot\mathbf{r}}$,

$$e^{i\mathbf{k}\cdot\mathbf{r}} = \sum_{l,m}^{\infty} 4\pi\, i^l\, j_l(kr)\, Y_l^{m*}(\hat{k})\, Y_l^m(\hat{r}), \tag{3.117}$$

$j_l(kr)$ are the spherical Bessel functions and Y_l^m are the spherical harmonics [19]. An equivalent formulation in the Taylor expansion series is expressed later for the sake of comparison.

The transition matrices, M_{ba} between the two states, $\alpha = a$ and $\alpha = b$, for the first part, ${}^1T_{b\leftarrow a}$ with the direction of radiation propagation explicitly considered, are expanded in spherical harmonics as

$$M_{ba} = \sum_{l,m}^{\infty} 4\pi\, i^{l'}\, \langle\, \psi_b \mid i^l\, j_l(kr)\, Y_l^{m*}(\hat{k})\, Y_l^m(\hat{r})\, \hat{\varepsilon}\, \cdot\, -i\nabla \mid \psi_a \,\rangle \tag{3.118}$$

or simply,

$$M_{ba} = \sum_{l=0}^{\infty} \sum_{m=-l}^{+l} M_{ba}^{(l,m)} \tag{3.119}$$

where $l' = l$ for even multipole orders and $l' = l - 1$ for the odd multipole orders. The first term of the series obeys the cylindrical symmetry selection rules similar to the dipole approximation matrix elements although it contains higher order corrections. The additional higher multipole-order terms, in the frame of Taylor expansion series, may be seen as corrections to the dipole approximation within the lowest-order Rayleigh expansion. The correspondence between the orders of the Rayleigh and Taylor multipole expansion series is therefore not exact and would yield some discrepancy in results. By considering the explicit propagation direction of the radiation field, the matrix elements above can be reduced to the form

$$M_{ba}^{(l,m)} = 4\pi\, i^{l'}\, Y_l^{m*}(\hat{k}) \sum_{\lambda} \langle\, \psi_b \mid j_l(kr)\, Y_l^m(\hat{r})\, \hat{\varepsilon}_\lambda\, \nabla_\lambda \mid \psi_a \,\rangle. \tag{3.120}$$

In evaluating the derivative $\nabla_\lambda \psi$, the implementation discussed in Bethe and Salpeter (A.37-39) [18] for an electron in $3D$ space is employed. That is,

$$\begin{aligned}\left\{ \frac{\partial}{\partial z} \right\} \{\, f(r)\, Y_{lm}(\hat{r}) \,\} =& \sqrt{\frac{(l+m+1)(l-m+1)}{(2l+3)(2l+1)}}\, Y_{l+1,m} \left\{ \frac{\partial f}{\partial r} - l\frac{f}{r} \right\} \\ &+ \sqrt{\frac{(l+m)(l-m)}{(2l+1)(2l-1)}}\, Y_{l-1,m} \left\{ \frac{\partial f}{\partial r} + (l+1)\frac{f}{r} \right\}\end{aligned} \tag{3.121}$$

$$\begin{aligned}\left\{ \frac{\partial}{\partial x} + i\,\frac{\partial}{\partial y} \right\} \{\, f(r)\, Y_{lm}(\hat{r}) \,\} =& \sqrt{\frac{(l+m+2)(l+m+1)}{(2l+3)(2l+1)}}\, Y_{l+1,m+1} \left\{ \frac{\partial f}{\partial r} - l\frac{f}{r} \right\} \\ &- \sqrt{\frac{(l-m)(l-m-1)}{(2l+1)(2l-1)}}\, Y_{l-1,m+1} \left\{ \frac{\partial f}{\partial r} + (l+1)\frac{f}{r} \right\}\end{aligned} \tag{3.122}$$

$$\begin{aligned}\left\{ \frac{\partial}{\partial x} - i\,\frac{\partial}{\partial y} \right\} \{\, f(r)\, Y_{lm}(\hat{r}) \,\} =& -\sqrt{\frac{(l-m+2)(l-m+1)}{(2l+3)(2l+1)}}\, Y_{l+1,m-1} \left\{ \frac{\partial f}{\partial r} - l\frac{f}{r} \right\} \\ &+ \sqrt{\frac{(l+m)(l+m-1)}{(2l+1)(2l-1)}}\, Y_{l-1,m-1} \left\{ \frac{\partial f}{\partial r} + (l+1)\,\frac{f}{r} \right\}\end{aligned} \tag{3.123}$$

Equation (3.120) can then be separated into radial and angular parts and solved numerically. Usually, one would fix the polarization directions of the electric field vector to be either linear or circular to reduce the complexity of the interactions. Fixing the polarization direction also makes physical sense in that in many cases, the interest is on systems interacting with polarized fields from lasers or other sources. In this study, the radiation is considered to be propagating in the $+x$ direction with its vector potential directed along the $+z$ direction and the magnetic-field vector in the $+y$ direction. Equations (3.121)-(3.123) give the dependence of transition matrix elements on the angular quantum numbers as well as radial co-ordinates. With these considerations, the matrix element can be fully expanded as

$$\begin{aligned}
\sum_{\lambda} \langle\, \psi_b \mid j_l(kr)\, Y_l^0(\hat{r})\, \hat{\varepsilon}_\lambda \nabla_\lambda \mid \psi_a \,\rangle = & \\
& \left[\frac{(l_a+m_a+1)(l_a-m_a+1)}{(2l_a+3)(2l_a+1)}\right]^{\frac{1}{2}} \int \mathrm{d}\Omega\, Y_{l_b}^{m_b^*}(\hat{r})\, Y_l^m(\hat{r})\, Y_{l_a+1}^{m_a}(\hat{r}) \\
& \times \int \mathrm{d}r\, R_b(r)\, j_l(kr) \left[\frac{\partial R_a(r_j)}{\partial r} - l_a \frac{R_a(r)}{r}\right] \\
& + \left[\frac{(l_a+m_a)(l_a-m_a)}{(2l_a+1)(2l_a-1)}\right]^{\frac{1}{2}} \int \mathrm{d}\Omega\, Y_{l_b}^{m_b^*}(\hat{r})\, Y_l^m(\hat{r})\, Y_{l_a-1}^{m_a}(\hat{r}) \\
& \times \int \mathrm{d}r\, R_b(r)\, j_l(kr) \left[\frac{\partial R_a(r)}{\partial r} + (l_a+1)\frac{R_a(r)}{r}\right]
\end{aligned} \tag{3.124}$$

The angular integrals can be simplified further using the angular momentum algebra. In terms of Clebsch-Gordan coefficients, the angular integrals yield

$$\begin{aligned}
\int \mathrm{d}\Omega\, Y_{l_b}^{m_b^*}(\hat{r}) Y_l^m(\hat{r}) Y_{l_a+1}^{m_a}(\hat{r}) =& (-1)^{m_a+1}\left[\frac{(2l_b+1)(2l+1)}{4\pi(2l_a+3)}\right]^{\frac{1}{2}} \\
& \times \langle l_b\, l\, 0\, 0 \mid l_a+1\, 0\rangle\, \langle l_b\, l\, m_b\, m \mid l_a+1\, m_a\rangle \\
\int \mathrm{d}\Omega\, Y_{l_b}^{m_b^*}(\hat{r}) Y_l^m(\hat{r}) Y_{l_a-1}^{m_a}(\hat{r}) =& (-1)^{m_a-1}\left[\frac{(2l_b+1)(2l+1)}{4\pi(2l_a+3)}\right]^{\frac{1}{2}} \\
& \times \langle l_b\, l\, 0\, 0 \mid l_a-1\, 0\rangle\, \langle l_b\, l\, m_b\, m \mid l_a-1\, m_a\rangle.
\end{aligned} \tag{3.125}$$

The transition matrix elements of the second part, ${}^2T_{b\leftarrow a}$ are also evaluated by expanding the term, $e^{2i(\mathbf{k}\cdot\mathbf{r})}$, in spherical harmonics and considering that the photon propagates in the x direction. This yields

$$M_{ba}^{(l,m)} = 4\pi\, i^{l'}\, Y_l^{m^*}(\hat{k})\, \langle\, \psi_b \mid j_l(2kr)\, Y_l^m(\mathbf{r}) \mid \psi_a \,\rangle. \tag{3.126}$$

If the radial and angular parts are separated, the equation reduces to the form

$$M_{ba}^{(l,m)} = 4\pi\, i^{l'}\, Y_l^{m^*}(\hat{k}) \int \mathrm{d}r\, R_b(r)\, R_a(r)\, j_l(2kr) \int \mathrm{d}\Omega\, Y_{l_b}^{m_b^*}(\mathbf{r})\, Y_l^m(\hat{r})\, Y_{l_a}^{m_a}(\hat{r}). \tag{3.127}$$

which can be numerically evaluated. The angular integral for these matrix elements evaluate to

$$\int \mathrm{d}\Omega\, Y_b(\mathbf{r})\, Y_l^m(\hat{r})\, Y_a(\hat{r}) = \sqrt{\left[\frac{(2l_b+1)(2l+1)}{4\pi(2l_a+1)}\right]} \langle l_b\, l\, 0\, 0 \mid l_a\, 0\rangle \, \langle l_b\, l\, m_b\, m \mid l_a\, m_a\rangle. \tag{3.128}$$

3.5.2 Length-Gauge Matrix Elements

The length-gauge transition matrix elements $T_{\alpha'\leftarrow\alpha}$ can be separated into two parts with the first part expressed as

$$^1T_{\alpha'\leftarrow\alpha} = C_\alpha(t)\,\langle\, \psi_{\alpha'} \mid [\zeta_1(t)\sin(\mathbf{k}\cdot\mathbf{r}) - \zeta_1'(t)\cos(\mathbf{k}\cdot\mathbf{r})]\gamma_L' \mid \psi_\alpha\,\rangle \tag{3.129}$$

$$^2T_{\alpha'\leftarrow\alpha} = C_\alpha(t)\langle\, \psi_{\alpha'} \mid [\zeta_3(t) - \frac{1}{2}\zeta_2(t)\cos(\mathbf{k}\cdot\mathbf{r}) - \frac{1}{2}\zeta_2'(t)\sin(\mathbf{k}\cdot\mathbf{r})]\gamma_L'' \mid \psi_\alpha\,\rangle \tag{3.130}$$

where terms ζ_i for $i = \{1, 2, 3\}$ are defined in equation (3.109) and the terms γ_L' and γ_L'' are defined in equation (3.110). The two-parts of the length-gauge transition matrix elements have different selection rules. That means they correspond to different final states if the initial state is the same. One should also note the difference in the time-dependent functions used for the different parts of each transition matrix elements.

The transition matrix elements M_{ba} from state a to state b for the first part,$^1T_{b\leftarrow a}$ corresponds to

$$M_{ba} \;=\; 4\pi \sum_{l=0}^{\infty}\sum_{m=-l}^{l} \langle\, \psi_b \mid i^{l'}\, j_l(kr)\, Y_l^{m^*}(\hat{k})\, Y_l^m(\hat{r})\, \hat{\varepsilon}\, \cdot\, \mathbf{r} \mid \psi_a\,\rangle \tag{3.131}$$

where the Rayleigh multipole expansion has been used and only the terms $\propto z$ and $\propto z^2$ in equations (3.109) and (3.110) are considered for clarity purposes. The primed term is defined as $l' = l$ for even multipole orders and $l' = l - 1$ for odd multipole orders. This matrix element can further be written as a summation of symmetry resolved matrix elements with of the orbital angular momentum quantum number l and the projection quantum number m

$$M_{ba} = \sum_{l=O}^{\infty}\sum_{m=-l}^{+l} M_{ba}^{(l,m)} \tag{3.132}$$

of the radiation field. The first term $l = 0$ yields the lowest multipole order approximation and the higher l values as the non-dipole corrections beyond the lowest order approximation. We expand the transition matrix elements

$$M_{ba}^{(l,m)} = 4\pi\, i^{l'}\,\langle\, \psi_b \mid j_l(kr)\, Y_l^{m^*}(\hat{k})\, Y_l^m(\hat{r})\, \varepsilon\, \cdot\, \mathbf{r} \mid \psi_a\,\rangle \tag{3.133}$$

with the consideration that the radiation field propagates in the x direction. By explicitly considering the direction of $\mathbf{k}$ is known in the function $Y_l^{m*}(\hat{k})$, the matrix elements

$$M_{ba}^{(l,m)} = (4\pi)\, i^{l'}\, Y_l^{m*}(\hat{k})\, \langle\, \psi_b \mid j_l(kr)\, Y_l^{m}\,(\hat{r})\, \hat{\varepsilon} \cdot \mathbf{r} \mid \psi_a \,\rangle. \tag{3.134}$$

can be evaluated. The vectors $\hat{\varepsilon}$ and $\mathbf{r}$ can be expressed in terms of their spherical components ε_q and $\mathbf{r}_q$ where $q = 1, 0, -1$. In terms of cartesian coordinates, the spherical components can be expressed as

$$\begin{aligned} \hat{\varepsilon}_1 &= -\frac{1}{\sqrt{2}}(\hat{\varepsilon}_x + i\hat{\varepsilon}_y) \\ \hat{\varepsilon}_0 &= \hat{\varepsilon}_z \\ \hat{\varepsilon}_{-1} &= \frac{1}{\sqrt{2}}(\hat{\varepsilon}_x - i\hat{\varepsilon}_y) \end{aligned} \tag{3.135}$$

and

$$\begin{aligned} r_1 &= -\frac{1}{\sqrt{2}}(x + iy) = r(\frac{4\pi}{3})^{\frac{1}{2}}\, Y_1^1(\hat{r}) \\ r_0 &= z = r(\frac{4\pi}{3})^{\frac{1}{2}}\, Y_1^0(\hat{r}) \\ r_{-1} &= \frac{1}{\sqrt{2}}(x - iy) = r(\frac{4\pi}{3})^{\frac{1}{2}}\, Y_1^{-1}(\hat{r}) \end{aligned} \tag{3.136}$$

The scalar product $\hat{\varepsilon} \cdot \mathbf{r}$ can then be evaluated in terms the spherical components as

$$\hat{\varepsilon} \cdot \mathbf{r} = \sum_{q=-1}^{1} \hat{\varepsilon}_q\, r_q. \tag{3.137}$$

Substituting this product into the matrix-elements expansion yields

$$M_{ba}^{(l,m)} = (4\pi)\, i^{l'} \sum_q Y_l^{m^*}(\hat{k})\, \langle\, \psi_b \mid j_l(kr)\, r\, Y_l^m(\hat{r})\, Y_1^q(\hat{r}) \mid \psi_a \,\rangle. \tag{3.138}$$

Making use of angular-momentum vector addition algebra,

$$\begin{aligned} Y_{l_1}^{m_1}(\hat{r}_1)\, Y_{l_2}^{m_2}(\hat{r}_2) = &\sum_{L=|l_1-l_2|}^{l_1+l_2} \sum_{M=-L}^{+L} \sqrt{\frac{(2l_1+1)(2l_2+1)}{4\pi(2L+1)}} \\ &\times \langle\, l_1\, l_2\, 0\, 0 \mid L\, 0 \,\rangle \langle\, l_1\, l_2\, m_1\, m_2 \mid L\, M \,\rangle\, Y_L^{M^*}(\hat{r}) \end{aligned} \tag{3.139}$$

leads to a further simplification of the form

$$\begin{aligned} M_{ba}^{(l,m)} = &\sum_{q,L,M} (4\pi)\, i^{l'}\, Y_l^{m*}(\hat{k}) \sqrt{\left[\frac{2l+1}{2L+1}\right]}\, \langle\, l\, 1\, 0\, 0 \mid L\, 0 \,\rangle \\ &\times \langle\, l\, 1\, m\, q \mid L\, M \,\rangle \langle\, \psi_b \mid j_l(kr)\, r\, Y_l^m(\hat{r}) \mid \psi_a \,\rangle. \end{aligned} \tag{3.140}$$

Separating the radial and the angular parts, one obtains the matrix elements

$$\begin{aligned} M_{ba}^{(l,m)} &= (4\pi)\, i^{l'}\, Y_l^{m*}(\hat{k}) \sum_{q,L,M} \sqrt{\left[\frac{2l+1}{2L+1}\right]} \langle\, l\, 1\, 0\, 0 \mid L\, 0\, \rangle \langle\, l\, 1\, m\, q \mid L\, M\, \rangle \\ &\times \int \mathrm{d}r\, r^3\, R_b\, j_l(kr)\, R_a^m \int \mathrm{d}\Omega Y_{l_b}^{m_b^*}(\hat{r})\, Y_l^m(\hat{r})\, Y_{l_a}^{m_a}(\hat{r}) \end{aligned} \tag{3.141}$$

which can be evaluated for any given radiation polarization q. The angular integral when evaluated using the orthonormality conditions of spherical harmonics reduces to

$$\begin{aligned} &\int d\Omega\, Y_{l_b}^{m_b^*}(\hat{r})\, Y_l^m(\hat{r})\, Y_{l_a}^{m_a}(\hat{r}) \\ &\quad = (-1)^{m_a} \left[\frac{(2l_b+1)(2L+1)}{4\pi(2l_a+1)}\right]^{\frac{1}{2}} \langle l_b\, L\, 0\, 0 \mid l_a\, 0\, \rangle \langle l_b\, L\, m_b\, M \mid l_a\, m_a\, \rangle \end{aligned} \tag{3.142}$$

The second part of the length-gauge transition matrix, ${}^2T_{\alpha' \leftarrow \alpha}$, can also be evaluated following a similar procedure as the first part.

3.6 Selection Rules

The transition-matrix elements can be expressed as a product of radial and angular integrals as already shown. The radial integrals are always in principle non-zero while the angular integrals can only be non-zero for certain combinations of (l_b, m_b) and (l_a, m_a) owing to the orthonormality conditions of the spherical harmonics. The non-zero angular integrals obey certain selection rules derived from the algebra of angular momentum. In the case of optical transitions, any particular selection rule depends on the nature of the interaction Hamiltonian, the l and m values of the spherically expanded spatial phase retardation term $e^{i\mathbf{k}\cdot\mathbf{r}}$, and the direction of propagation of the radiation. In this section, the selection rules suitable for describing the multipole transitions are discussed but specifically for cases where the vector potential of the radiation is linearly polarized along the $+z$ direction while its propagation is along the $+x$ direction.

From the expressions of the transition-matrix elements considered in this study, it can be seen that generally the angular integrals take any of the following three forms

$$\int \mathrm{d}\Omega \quad Y_{l_1}^{m_1}(\hat{r})\, Y_{l_2}^{m_2}(\hat{r}) \tag{3.143}$$

$$\int \mathrm{d}\Omega \quad Y_{l_1}^{m_1}(\hat{r})\, L_\lambda\, Y_{l_2}^{m_2}(\hat{r}) \tag{3.144}$$

$$\int \mathrm{d}\Omega \quad Y_{l_1}^{m_1}(\hat{r})\, Y_\lambda^{m_\lambda}(\hat{r})\, Y_{l_2}^{m_2}(\hat{r}) \tag{3.145}$$

where L_λ can be L_z or any of the ladder operators $L_+ = L_x + iL_y$ or $L_- = L_x - iL_y$, and $Y_\lambda^{m_\lambda}$ is a spherical harmonics function with orbital angular momentum quantum number λ and its projection quantum number m_λ.

The integral in equation (3.143) vanishes unless $l_1 = l_2$ and $m_1 = m_2$. Similarly, the ladder operator $L_+(L_-)$ raises (lowers) the projection quantum number m of a state subject to the condition $|m \pm 1| \leq l$ while L_z preserves the projection quantum number of the state. In terms of eigenvalue equations, the operations yield

$$\begin{aligned} L_z Y_l^m(\hat{r}) &= m\hbar Y_l^m(\hat{r}) \\ L_+ Y_l^m(\hat{r}) &= \hbar\sqrt{(l-m)(l+m+1)}Y_l^{m+1}(\hat{r}) \\ L_- Y_l^m(\hat{r}) &= \hbar\sqrt{(l+m)(l-m+1)}Y_l^{m-1}(\hat{r}) \end{aligned} \tag{3.146}$$

with the corresponding eigenvalues. This imposes the conditions $l_1 = l_2$ on orbital angular momentum quantum numbers and $m_1 = m_2$, $m_1 = m_2 + 1$, or $m_1 = m_2 - 1$ on projection angular momentum quantum numbers corresponding to L_z, L_+, or L_- respectively. Otherwise, the integral of the form of equation (3.144) would vanish.

The integral $I(l_1, m_1; \lambda, m_\lambda; l_2, m_2)$ in equation (3.145) can be expressed in terms of the Clebsch-Gordan coefficients as

$$I(l_1, m_1; \lambda, m_\lambda; l_2, m_2) = (-1)^{m_2} [\frac{(2l_1+1)(2\lambda+1)}{4\pi(2l_2+1)}]^{\frac{1}{2}} \langle l_1\, \lambda\, 0\, 0 \mid l_2\, 0 \rangle \langle l_1\, \lambda\, m_1\, m_\lambda \mid l_2\, m_2 \rangle \tag{3.147}$$

From the properties of the Clebsch-Gordan coefficients, the above integral vanishes unless the following two conditions

$$\begin{aligned} l_2 &= l_1 \pm \lambda \\ m_2 &= m_1 + m_\lambda \end{aligned} \tag{3.148}$$

are satisfied. These relations correspond to the orbital angular momentum and the projection quantum number selection rules respectively. The parity requirement that the integrand should be an even function for the integral to be non-vanishing under a co-ordinate transformation $\mathbf{r} = -\mathbf{r}$ corresponding to

$$\begin{aligned} R_{nl}(r)Y_l^m(\theta,\phi) &= R_{nl}(r)Y_l^m(\pi-\theta,\phi+\pi) \\ R_{nl}(r)Y_l^m(\theta,\phi) &= R_{nl}(r)(-1)^l\, Y_l^m(\theta,\phi) \end{aligned} \tag{3.149}$$

introduces a further condition that the sum of the orbital angular momentum quantum numbers should be an even number. This requirement results in a parity selection rule for the angular momentum transitions given by

$$\Delta l' = \begin{cases} -\lambda, -\lambda+1, \lambda-1, \lambda & \text{for } \mathbf{A}\cdot\mathbf{p} \text{ transitions} \\ -\lambda, \lambda, & \text{for } \mathbf{A}\cdot\mathbf{A} \text{ transitions} \end{cases} \tag{3.150}$$

where λ is a positive integer equivalent to the photon angular momentum transferred to the target state. This selection rule goes hand in hand with requirement that the change in the projection quantum number $\Delta m' = m_\lambda$ is such that $-\lambda \leq m_\lambda \leq \lambda$.

In this study, the polarization of the electric field vector has been chosen to be along the $+z$ direction, the magnetic field vector to be along $+y$ direction, and the radiation

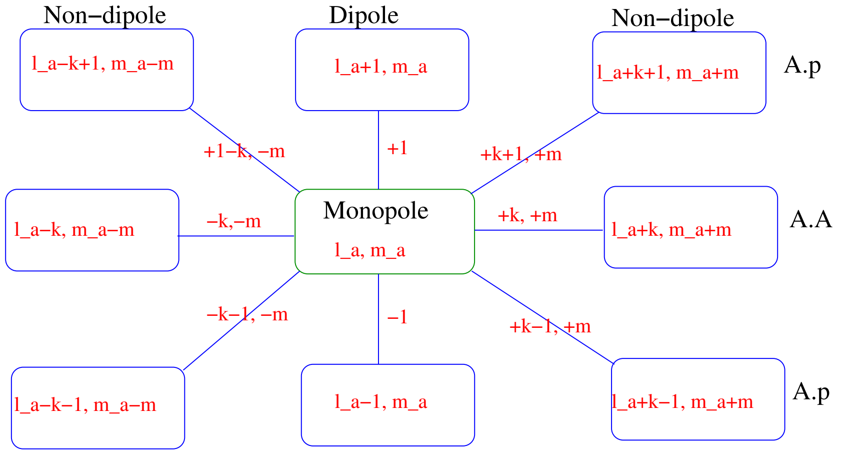

Figure 3.2: Orbital angular momentum selection criteria map for both $\mathbf{A} \cdot \mathbf{p}$ and $\mathbf{A} \cdot \mathbf{A}$ for a k-th order multipole. The lines show possible transitions for the different interactions in the radiation gauge in a system with either the initial or final state angular momentum quantum numbers (l_a, m_a) .

momentum vector to be along the $+x$ direction. The selection rules summarised in Table 3.1 apply for each of the corresponding interaction Hamiltonians.

Gauge	Interaction	Selection Criteria	
Length	$\mathbf{E} \cdot \mathbf{r}$	$\Delta l' = \{-(l+1), -l+1, l-1, (l+1)\}$	$\Delta m' = m$
	$\mathbf{A} \cdot \mathbf{r}$	$\Delta l' = \{-(l+1), -l+1, l-1, (l+1)\}$	$\Delta m' = m$
	$\mathbf{B} \cdot \mathbf{L}$	$\Delta l' = \{-l+1, l-1\}$	$\Delta m' = m$
	$B^2 r^2 - (\mathbf{B} \cdot \mathbf{r})^2$	$\Delta l' = \{-(l+2), -l, l, (l+2)\}$	$\Delta m' = m^*$
Radiation	$\mathbf{A} \cdot \nabla$	$\Delta l' = \{-(l+1), -l+1, l-1, (l+1)\}$	$\Delta m' = m$
	$(\mathbf{A} \cdot \mathbf{A})$	$\Delta l' = \{-l, l\}$	$\Delta m' = m$

Table 3.1: Selection rules defined for any particular order l of the multipole expansion of the exponential retardation term $e^{i\mathbf{k}\cdot\mathbf{r}}$. Here $\Delta l' = |l_a - l_b|$, $\Delta m' = |m_a - m_b|$, and $m^* = \{m, m \pm 2\}$.

The length-gauge interaction Hamiltonians presented in the Table 3.1 are extracted from equation (3.94) where as the radiation gauge interaction Hamiltonians are straight forward. In the table, vectors **E** and **B** correspond to the electric and magnetic field vectors which are the temporal and the spatial derivatives of the vector potential **A** respectively. An additional selection rule is provided in this case by the propagation direction of the radiation field which in this case has been specified to be along the + x direction. This imposes a selection rule in the spherical harmonics such that the transition matrix elements are non-vanishing only for the cases where $Y_l^{m^*}(\hat{k})$ is non-zero. The consideration of the magnetic dipole transitions has been restricted further by an additional selection rule provided by the principal quantum number $\Delta n = 0$ [3] [18] besides the usual angular momentum selection rules $\Delta l = 0$ and $\Delta l = \pm 1$. Figure 3.2 shows the pictorial map of possible transitions enabled by the l-th multipole-order

---

[3] The selection rule is discussed in equation 66.14 in [18]

terms for a system with arbitrary initial angular momenta, l_a and m_a. For the sake of clarity, the multipole-order in the map is defined with the index k as opposed to l. In the calculations presented in the numerical solution of the non-relativistic time dependent Schrödinger equation, both the electric and magnetic transitions have been considered using the radiation gauge. The magnetic dipole transition resulting from the quadrupole $\mathbf{A} \cdot \mathbf{p}$ term of the multipole expansion leads to two orbital angular momentum conserving channels which are completely antisymmetric. On the contrary, the magnetic monopole transition arising from the lowest order $\mathbf{A} \cdot \mathbf{A}$ term is symmetric and the angular momenta are conserved in both l and m. The magnetic monopole transitions in the Rayleigh multipole-order expansion series therefore eliminate the possibility of any forbidden transitions and consequently reduce the lifetime of any possible metastable states.

3.6.1 The Wigner 3j Coefficients

The properties of the spherical harmonics have already been discussed in section 3.1.4. Here the concepts are only revisited for the purpose of discussing the Wigner-3j coefficients which are used in the evaluation of the angular integrals. The spherical harmonics $Y_l^m(\theta,\phi)$ and $Y_l^{-m}(\theta,\phi)$ can be defined in terms of the associated Legendre Polynomials $P_l^m(\cos\theta)$ as

$$Y_l^m(\theta,\phi) = \sqrt{\frac{(2l+1)}{4\pi}\frac{(l-m)!}{(l+m)!}}\, P_l^m(\cos\theta)\, \mathrm{e}^{im\phi} \tag{3.151}$$

and

$$Y_l^{-m}(\theta,\phi) = \sqrt{\frac{(2l+1)}{4\pi}\frac{(l+m)!}{(l-m)!}}\, P_l^{-m}(\cos\theta)\, \mathrm{e}^{-im\phi} \tag{3.152}$$

Since the negative m component of the associated Legendre polynomial P_l^{-m} is related to its corresponding positive component by the relation

$$P_l^{-m}(\cos\theta) = (-1)^m \frac{(l-m)!}{(l+m)!} P_l^m(\cos\theta), \tag{3.153}$$

the negative m component of the spherical harmonic $Y_l^{-m}(\theta,\phi)$ can also be expressed in terms of its positive counterpart as

$$Y_l^{-m}(\theta,\phi) = (-1)^m\, Y_l^{m*}(\theta,\phi). \tag{3.154}$$

The spherical harmonics have orthonormality conditions making them quite useful in evaluating the three dimensional spatial integrals by reducing the problem into radial integrals and angular integrals as already shown in the subsections 3.5.1 and 3.5.2 above. Usually, the angular part is further simplified using the Clebsch Gordan, Racah, or Wigner Coefficients. These coeffficients possess phase relations between themselves and each of them obeys different symmetry properties. The implementation in the BEYDIP code employs the Wigner-3j coefficients in evaluating the angular integrals. The following is an outline of some of the symmetry properties [20]

$$C^{j_1,j_2,j_3}_{m_1,m_2,m_3} = (-1)^{j_1+j_2-j_3}\, C^{j_1,j_2,j_3}_{-m_1,-m_2,-m_3} \tag{3.155}$$

$$C^{j_1,j_2,j_3}_{m_1,m_2,m_3} = (-1)^{j_2+m_2} \sqrt{\frac{2j_3+1}{2j_1+1}}\, C^{j_3,j_2,j_1}_{-m_3,m_2,-m_1} \tag{3.156}$$

satisfied by the Wigner-3j coefficients used in the BEYDIP code. Using the two symmetry properties stated, one can show further that

$$C^{j_3,j_2,j_1}_{m_3,-m_2,m_1} = (-1)^{-j_3+j_1-m_2} \sqrt{\frac{2j_1+1}{2j_3+1}}\, C^{j_1,j_2,j_3}_{m_1,m_2,m_3}. \tag{3.157}$$

Employing the relationship between the Racah coeffficients and the Wigner3j coefficients

$$C^{j_1,j_2,j_3}_{m_1,m_2,m_3} = (-1)^{-j_1+j_2-m_3} \sqrt{2j_3+1} \begin{pmatrix} j_1 & j_2 & j_3 \\ m_1 & m_2 & -m_3 \end{pmatrix} \tag{3.158}$$

on both sides yields an additional property

$$\begin{pmatrix} j_3 & j_2 & j_1 \\ m_3 & -m_2 & m_1 \end{pmatrix} = (-1)^{-m_1-m_2-m_3} \begin{pmatrix} j_1 & j_2 & j_3 \\ -m_1 & m_2 & -m_3 \end{pmatrix} \tag{3.159}$$

of the Wigner3j coefficients. The symmetry relations of the coefficients are quite instrumental in the optimization of computational resources. For example, the number of transition matrix elements can be significantly reduced by just embracing the symmetry relations.

3.7 Numerical Implementation of the Multipole Expansion

A general pulse of electromagnetic radiation can be described using a vector potential of the form [19]

$$\mathbf{A}(\mathbf{r},t) = \int_{\Delta\omega} \mathrm{d}\omega\, \mathrm{A}_0(\omega)\, \hat{\varepsilon}\, [\mathrm{e}^{i(\omega t - \mathbf{k}\cdot\mathbf{r}+\delta)} \pm \mathrm{e}^{-i(\omega t-\mathbf{k}\cdot\mathbf{r}+\delta)}] \tag{3.160}$$

with the carrier frequency ω, the frequency dependent pulse amplitude $\mathrm{A}_0(\omega)$, the wavevector $\mathbf{k}$ whose magnitude is related to the radiation wavelength by $2\pi/\lambda$, and the carrier envelope phase shift δ. From the vector potential $\mathbf{A}(\mathbf{r},t)$ and scalar potential $\phi(\mathbf{r},t)$ describing an electromagnetic field, one can derive the electric and magnetic field vectors which constitute the electromagnetic radiation using the relations

$$\begin{aligned} \mathbf{E} &= -\frac{1}{c}\frac{\partial \mathbf{A}}{\partial t} - \nabla\Phi \\ \mathbf{B} &= \nabla \times \mathbf{A} \end{aligned} \tag{3.161}$$

and the fields satisfy the Maxwell's equations in a region of space with no charge. From the Maxwell's equations, one can adopt the Coulomb gauge conditions $\nabla \cdot \mathbf{A} = 0$ and $\Phi = 0$ as the boundary conditions which the potentials must fulfil. The above expression of the vector potential can be instrumental in describing the photoabsorption and the photoemission processes which occur during the interactions between matter and electromagnetic radiation.

Ideally, the radiation from a laser source is monochromatic and coherent. One therefore needs not to integrate the vector potential over the frequency range $\Delta\omega$. Considering that any interaction process consists of both absorption and emission processes occuring simultaneously, a linear combination of both processes must be considered. The vector potential can therefore be expanded, assuming a symmetric linear combination, as

$$\begin{aligned}\mathbf{A}(\mathbf{r},t) = \frac{1}{2}\mathrm{A}_0\, f(t)\, \hat{\varepsilon}\, [&\cos(\omega t - \mathbf{k}\cdot\mathbf{r} + \delta) + i\sin(\omega t - \mathbf{k}\cdot\mathbf{r} + \delta) \\ &+ \cos(\omega t - \mathbf{k}\cdot\mathbf{r} + \delta) - i\sin(\omega t - \mathbf{k}\cdot\mathbf{r} + \delta)]\end{aligned} \tag{3.162}$$

where factor $\frac{1}{2}$ denotes the random relative probabilities of both absorption and emission processes. The expression simplifies to a real part

$$\mathbf{A}(\mathbf{r},t) = \mathrm{A}_0\, f(t)\, \hat{\varepsilon} \cos(\omega t - \mathbf{k}\cdot\mathbf{r} + \delta) \tag{3.163}$$

for the symmetric linear combination or to an imaginary part

$$\mathbf{A}(\mathbf{r},t) = \mathrm{A}_0\, f(t)\, \hat{\varepsilon} \sin(\omega t - \mathbf{k}\cdot\mathbf{r} + \delta) \tag{3.164}$$

for the antisymmetric linear combination. In the BEYDIP code implementation, the latter form of the vector potential is used but in principle any of the two forms or their linear combination is still appropriate. Further expansion of the trigonometric function in the vector potential using the equivalence relation $\sin(A - B) = \sin A \cos B - \cos A \sin B$ yields

$$\mathbf{A}(\mathbf{r},t) = \mathrm{A}_0\, f(t)\, [\sin(\omega t + \delta)\cos(\mathbf{k}\cdot\mathbf{r}) - \cos(\omega t + \delta)\sin(\mathbf{k}\cdot\mathbf{r})]. \tag{3.165}$$

Similarly, the square of the vector potential considered in this case can be expanded as

$$\begin{aligned}\mathbf{A}^2(\mathbf{r},t) &= \mathrm{A}_0^2\, , f^2(t)\, (\varepsilon\cdot\varepsilon) \sin^2[\omega t - \mathbf{k}\cdot\mathbf{r} + \delta] \\ &= \frac{\mathrm{A}_0^2}{2}\, f^2(t)\, [1 - \cos\{2[\omega t - \mathbf{k}\cdot\mathbf{r} + \delta]\}] \\ &= \frac{\mathrm{A}_0^2}{2}\, f^2(t)\, [1 - \cos(2\omega t + 2\delta)\cos(2\mathbf{k}\cdot\mathbf{r}) - \sin(2\omega t + 2\delta)\sin(2\mathbf{k}\cdot\mathbf{r})].\end{aligned} \tag{3.166}$$

In a reduced notation, the vector potential and its square can be expressed respectively as

$$
\begin{aligned}
\mathbf{A}(\mathbf{r},t) &= \mathrm{A}_1(\mathrm{t})\mathrm{cos}(\mathbf{k}\cdot\mathbf{r}) - \mathrm{A}_2(\mathrm{t})\mathrm{sin}(\mathbf{k}\cdot\mathbf{r}) \\
\mathbf{A}^2(\mathbf{r},t) &= \frac{1}{2}\left[A_3^2(t) + [\mathrm{A}_1^2(\mathrm{t}) - \mathrm{A}_2^2(\mathrm{t})]\mathrm{cos}(2\mathbf{k}\cdot\mathbf{r}) - 2[\mathrm{A}_1(\mathrm{t})\cdot\mathrm{A}_2(\mathrm{t})]\mathrm{sin}(2\mathbf{k}\cdot\mathbf{r})\right]
\end{aligned}
\tag{3.167}
$$

where the $A_{i=1,2,3}$ are defined as

$$
\begin{aligned}
\mathrm{A}_1(\mathrm{t}) &= \mathrm{A}_0\, f(t)\sin(\omega t+\delta) \\
\mathrm{A}_2(\mathrm{t}) &= \mathrm{A}_0\, f(t)\cos(\omega t+\delta) + \frac{\mathrm{A}_0}{\omega}\,\dot{f}(t)\sin(\omega t+\delta) \\
\mathrm{A}_3(\mathrm{t}) &= \mathrm{A}_0\, f(t).
\end{aligned}
\tag{3.168}
$$

The expansion of $\mathbf{A}^2(\mathbf{r},t)$ employed the use of the trigonometric relations $\cos(2A) = \cos^2\!A - \sin^2\!A$ and $\sin(2A) = 2\sin\!A\cos\!A$ in the time-dependent functions. The spatially dependent trigonometric functions, $\sin(\mathbf{k}\cdot\mathbf{r})$ and $\cos(\mathbf{k}\cdot\mathbf{r})$, can then be expressed as

$$
\begin{aligned}
\sin(\mathbf{k}\cdot\mathbf{r}) &= \frac{1}{2i}(e^{i\mathbf{k}\cdot\mathbf{r}} - e^{-i\mathbf{k}\cdot\mathbf{r}}) \\
\cos(\mathbf{k}\cdot\mathbf{r}) &= \frac{1}{2}(e^{i\mathbf{k}\cdot\mathbf{r}} + e^{-i\mathbf{k}\cdot\mathbf{r}}).
\end{aligned}
\tag{3.169}
$$

These trigonometric functions can be expressed further in terms of the Rayleigh multipole expansion of the retardation term $e^{i\mathbf{k}\cdot\mathbf{r}}$ yielding

$$
\begin{aligned}
\sin(\mathbf{k}\cdot\mathbf{r}) &= \sum_{l=1,3,5,\cdots}\ \sum_{m_l=-l}^{+l} 4\pi\, i^{(l-1)}\, j_l(kr)\, Y_l^{m^*}(\hat{k})\, Y_l^m(\hat{r}) \\
\cos(\mathbf{k}\cdot\mathbf{r}) &= \sum_{l=0,2,4,\cdots}\ \sum_{m_l=-l}^{+l} 4\pi\, i^l\, j_l(kr)\, Y_l^{m^*}(\hat{k})\, Y_l^m(\hat{r})
\end{aligned}
\tag{3.170}
$$

the sum of odd terms of the sequence, of products of spherical Bessel functions and spherical harmonics of the same order, for the sine function $\sin(\mathbf{k}\cdot\mathbf{r})$ and the sum of even terms of the sequence for the cosine function $\cos(\mathbf{k}\cdot\mathbf{r})$. An alternative expansion of the trigonometric functions employ the Taylor's series yielding

$$
\begin{aligned}
\sin(\mathbf{k}\cdot\mathbf{r}) &= \sum_{l=1,3,5,\cdots} (-1)^{l-1}\,\frac{(\mathbf{k}\cdot\mathbf{r})^l}{l!} \\
\cos(\mathbf{k}\cdot\mathbf{r}) &= \sum_{l=0,2,4,\cdots} (-1)^{l}\,\frac{(\mathbf{k}\cdot\mathbf{r})^l}{l!}.
\end{aligned}
\tag{3.171}
$$

A similar expansion can also be implemented for $\sin(2\mathbf{k}\cdot\mathbf{r})$ and $\cos(2\mathbf{k}\cdot\mathbf{r})$. With these trigonometric functions in the Taylor's expansion, and considering the polarization and propagation directions to be along the $+z$ and $+x$ axis respectively, the terms in the non-relativistic interaction Hamiltonian up to the octupole terms can be re-written as

$$\begin{aligned}\mathbf{A}\cdot\mathbf{p}+\frac{1}{2}\,\mathbf{A}\cdot\mathbf{A} =& A_1(t)\,p_z - kx\,A_2(t)\,p_z - \frac{k^2x^2}{2}\,A_1(t)\,p_z\\ &+\frac{1}{4}\,A_3^2(t)+\frac{1}{4}\,[A_1^2(t)-A_2^2(t)]\\ &-kx\,[A_1(t)\,A_2(t)]-\frac{k^2x^2}{2}\,[A_1^2(t)-A_2^2(t)]\end{aligned}\tag{3.172}$$

where the first term gives the standard dipole approximation, the second and the third terms give the quadrupole and octupole corrections to the $\mathbf{A}\cdot\mathbf{p}$ term respectively. The fourth and the fifth terms are solely time-independent contribution of $\mathbf{A}^2$ term which can be removed by a phase transformation. The sixth and the seventh terms are the quadrupole and octupole contributions of the $\mathbf{A}^2$ term respectively. In the equivalent Rayleigh multipole series expansion, they become

$$\begin{aligned}&\mathbf{A}\cdot\mathbf{p}+\frac{1}{2}\mathbf{A}\cdot\mathbf{A}\\ &\quad= 4\,\pi\,\{A_1(t)\,j_0(kr)\,[Y_0^{0^*}(\hat{k}_x)\,Y_0^0(\hat{r})]p_z\\ &\qquad+\frac{1}{4}\,A_3^2(t)+\frac{1}{4}\,[A_1^2(t)-A_2^2(t)]\,j_0(2kr)\,[Y_0^{0^*}(\hat{k}_x)\,Y_0^0(\hat{r})]\\ &\qquad-A_2(t)\,j_1(kr)\,[Y_1^{-1^*}(\hat{k}_x)\,Y_1^{-1}(\hat{r})+Y_1^{1^*}(\hat{k}_x)\,Y_1^1(\hat{r})]\,p_z\\ &\qquad-\frac{1}{2}\,[A_1(t)\,A_2(t)]\,j_1(2kr)\,[Y_1^{-1^*}(\hat{k}_x)\,Y_1^{-1}(\hat{r})+Y_1^{1^*}(\hat{k}_x)\,Y_1^1(\hat{r})]\\ &\qquad-A_1(t)\,j_2(kr)\,[Y_2^{-2^*}(\hat{k}_x)\,Y_2^{-2}(\hat{r})+Y_2^{0^*}(\hat{k}_x)\,Y_2^0(\hat{r})+Y_2^{2^*}(\hat{k}_x)\,Y_2^2(\hat{r})]\,p_z\\ &\qquad-\frac{1}{4}\,[A_1^2(t)-A_2^2(t)]\,j_2(kr)\\ &\qquad\times[Y_2^{-2^*}(\hat{k}_x)\,Y_2^{-2}(\hat{r})+Y_2^{0^*}(\hat{k}_x)\,Y_2^0(\hat{r})+Y_2^{2^*}(\hat{k}_x)\,Y_2^2(\hat{r})]\}\end{aligned}\tag{3.173}$$

where the l^{th} order of the spherical Bessel functions $j_l(kr)$ specify the contributions of the corresponding multipole orders. It may be important to note that each of the spherical Bessel functions is a series of infinite order polynomial and their equivalence with the corresponding orders of the Taylor expansions in equation (3.172) is not exact as will be shown in section 4.

Equations (3.172) and (3.173) are the leading equations implemented in this study in going beyond the dipole approximation in the non-relativistic solution of the TDSE. The extension of the equations to include higher multipole-order corrections can be done by increasing the number of terms in the multipole expansion series. The Rayleigh expansion has a structural advantage in the $3D$ solution of the TDSE in that it is already pre-set in the spherical co-ordinates. The Taylor expansion on the other hand requires change of co-ordinates if the spherical co-ordinate system would be advantageous to use. An additional observation in the comparison of the two equations is that in the latter equation, all terms have both spatial and temporal dependence and therefore no term can be ignored on the basis of a phase transformation.

The above expressions are fully implemented in the BEYDIP code using the radiation gauge with the option of choosing either the Taylor or the Rayleigh multipole expansion series option. The transition matrix elements are evaluated up to an arbitrary order n of the multipole interaction terms. The upper limit for any order of implementation may be restricted depending on the desired accuracy and the available computational resources.

3.8 Determination of the Ionization Yield

The non-relativistic dynamics of atoms interacting with a classical electromagnetic field is governed by the time dependent Schrödinger equation

$$i\frac{\partial\Psi(\mathbf{r},t)}{\partial t} = [H_0 + V(t)]\Psi(\mathbf{r},t) \tag{3.174}$$

where H_0 is the field-free Hamiltonian corresponding to the field-free eigen states, $V(t)$ is the radiation gauge interaction potential expressed in terms of momentum operator $\mathbf{p}$ and the vector potential $\mathbf{A}(\mathbf{r},t)$ as

$$V(t) = -q\mathbf{A}\cdot\mathbf{p} + \frac{1}{2}q^2\mathbf{A}^2. \tag{3.175}$$

The the expansion of these interactions up to the 2^{nd} order multipole terms in Taylor and Rayleigh series can be seen in equations (3.172) and (3.173) respectively in the previous section.

The solution of equation (3.174) begins with a diagonalization procedure involving only the field-free Hamiltonian H_0 yielding the eigenvalues and the eigenvectors of the field-free states. This procedure is already discussed in section 3.1.6 using the B splines spectral expansion. In brief, the field-free bound and continuum states of the system are obtained by considering the system (atom) to be confined within a spherical box boundary of radius r_{max}. This leads to a discretization of the continuum spectrum, whereas the bound states remain unmodified if r_{max} is chosen sufficiently large and not too highly excited Rydberg states are considered. Introducing in the region $(0, r_{max})$ a B spline set consisting of $n+2$ spline functions $B_i(r)$ of order k, the radial functions are expanded in B splines as expressed in equation (3.45) but with the first and the last splines removed from the expansion to ensure that the boundary conditions $R(0) = 0$ and $R(r_{max}) = 0$ are satisfied. With this condition, the radial Schrödinger equation is then transformed into the $n \times n$ generalized banded eigenvalue problem with respect to the coefficient vector

$$\mathbf{C} = (\rho_1, \rho_2, \cdots \rho_n) \tag{3.176}$$

which yields n solutions for every orbital quantum number l.

For two coupled atomic states ψ_a and ψ_b characterised by the set of quantum numbers $\alpha = \{n_a, l_a, m_a\}$ and $\alpha' = \{n_b, l_b, m_b\}$ respectively, the time-dependent transition matrix elements

$V_{ba} = \langle\psi_b \mid V(t) \mid \psi_a\rangle$ corresponding to either $\mathbf{A}\cdot\mathbf{p}$ or $\mathbf{A}\cdot\mathbf{A}$ transitions evaluated in radiation gauge can be written as

$$V_{ab} = \sum_{l,m} \sum_{i=1}^{6} V^{i}_{b,a}(t) \tag{3.177}$$

where

$$\begin{aligned}
V^{1}_{b,a}(t) &= \delta_{-m_b,m_a+m}\, \delta_{l_b,l_a+l+1}\, \Omega_1(l_b,m_b,l,m,l_a,m_a)\, I_1(n_b,l_b,k,l,n_a,l_a,t)\\
V^{2}_{b,a}(t) &= \delta_{-m_b,m_a+m}\, \delta_{l_b,l_a-l+1}\, \Omega_1(l_b,m_b,l,m,l_a,m_a)\, I_1(n_b,l_b,k,l,n_a,l_a,t)\\
V^{3}_{b,a}(t) &= \delta_{-m_b,m_a+m}\, \delta_{l_b,l_a+l-1}\, \Omega_2(l_b,m_b,l,m,l_a,m_a)\, I_2(n_b,l_b,k,l,n_a,l_a,t)\\
V^{4}_{b,a}(t) &= \delta_{-m_b,m_a+m}\, \delta_{l_b,l_a-l-1}\, \Omega_2(l_b,m_b,l,m,l_a,m_a)\, I_2(n_b,l_b,k,l,n_a,l_a,t)\\
V^{5}_{b,a}(t) &= \delta_{-m_b,m_a+m}\, \delta_{l_b,l_a+l}\, \Omega_3(l_b,m_b,l,m,l_a,m_a)\, I_3(n_b,l'_b,k,l,n_a,l_a,t)\\
V^{6}_{b,a}(t) &= \delta_{-m_b,m_a+m}\, \delta_{l_b,l_a-l}\, \Omega_3(l_b,m_b,l,m,l_a,m_a)\, I_3(n_b,l_b,k,l,n_a,l_a,t)
\end{aligned} \tag{3.178}$$

where the selection rules are embedded in the Kronecker deltas $\delta_{l,l'}$ and $\delta_{m,m'}$. The evaluation of transition matrix elements in the radiation gauge has already been discussed in section 3.5.1. The first four transitions originate from the $\mathbf{A}\cdot\mathbf{p}$ term while the last two are from the $\mathbf{A}\cdot\mathbf{A}$ term .

The angular integrals evaluated in terms of Wigner-3j symbols are

$$\begin{aligned}
\Omega_1 &= \sum_{m} (-1)^{m_b} \sqrt{\frac{4\pi(2l_b+1)(2l+1)(l_a+m_a+1)(l_a-m_a+1)}{2l_a+1}}\\
&\qquad \times Y^{*}_{l,m}(\hat{k}_x) \begin{pmatrix} l_b & l & l_a+1 \\ -m_b & m & m_a \end{pmatrix} \begin{pmatrix} l_b & l & l_a+1 \\ 0 & 0 & 0 \end{pmatrix}\\
\Omega_2 &= \sum_{m} (-1)^{m_b} \sqrt{\frac{4\pi(2l_b+1)(2l+1)(l_a+m_a)(l_a-m_a)}{2l_a-1}}\\
&\qquad \times Y^{*}_{l,m}(\hat{k}_x) \begin{pmatrix} l_b & l & l_a-1 \\ -m_b & m & m_a \end{pmatrix} \begin{pmatrix} l_b & l & l_a-1 \\ 0 & 0 & 0 \end{pmatrix}\\
\Omega_3 &= \sum_{m} (-1)^{m_b} \sqrt{4\pi(2l_b+1)(2l+1)(2l_a+1)}\\
&\qquad \times Y^{*}_{l,m}(\hat{k}_x) \begin{pmatrix} l_b & l & l_a \\ -m_b & m & m_a \end{pmatrix} \begin{pmatrix} l_b & l & l_a \\ 0 & 0 & 0 \end{pmatrix}
\end{aligned} \tag{3.179}$$

and the radial integrals are described by

$$\begin{aligned}
I_1(t) &= -i^{\hat{l}+1}\, A_l(t) \int \mathrm{d}r\, [R_{n_b,l_b}(r)\, j_l(kr)(\frac{\partial R_{n_a,l_a}(r)}{\partial r} - l_a \frac{R_{n_a,l_a}(r)}{r})]\\
I_2(t) &= -i^{\hat{l}+1}\, A_l(t) \int \mathrm{d}r [R_{n_b,l_b}(r)\, j_l(kr)(\frac{\partial R_{n_a,l_a}(r)}{\partial r} + (l_a+1)\frac{R_{n_a,l_a}(r)}{r})]\\
I_3(t) &= i^{\hat{l}}\, \frac{A^{sq}_{l}(t)}{2} \int \mathrm{d}r\, [R_{n_b,l_b}(r)\, j_l(2kr)\, R_{n_a,l_a}(r)]
\end{aligned} \tag{3.180}$$

with $\hat{l} = l$, $A_l(t) = A_1(t)$, $A_l^{sq}(t) = [A_1^2(t) - A_2^2(t)]/2$ whenever l is even or with $\hat{l} = l - 1$, $A_l(t) = -A_2(t)$, $A_l^{sq}(t) = -[A_1(t) \cdot A_2(t)]$ whenever l is odd. The time-dependent functions $A_{i=1,2,3}$ are defined in equation (3.168).

The TDSE in equation (3.174), with the substitution of equation (3.175) into it, reduces to a system of coupled first order ordinary differential equations.

$$i\dot{C}_\alpha(t) = C_\alpha\,(t)E_\alpha + \sum_{\alpha'} C_{\alpha'}(t)\,V_{\alpha\alpha'}(t) + \sum_{\alpha''} C_{\alpha''}(t)\,V_{\alpha\alpha''}(t) \tag{3.181}$$

which are integrated numerically using a variable-order, variable-step Adams solver [114]. The ionization yield, after the pulse, is then obtained by summing over all the continuum states

$$Y_{ion} = \sum_{\alpha, E_\alpha > E_{ion}} \mid C_\alpha(\frac{\tau}{2}) \mid^2 \tag{3.182}$$

where E_{ion} is the ionization potential.

3.9 Probability Distributions

Besides the total ionization yield, the energy or angle resolved photoelectron distributions can also be extracted from the wave packet at the end of the laser pulse. The method described here follows the outline of reference [93, 115]. The most detailed energy and angular distribution is given by the formula

$$P(E, \Omega) = k\,|A(E, \Omega)|^2 \tag{3.183}$$

where $\Omega = \mathbf{k}/k$ is the direction of the asymptotic momentum $\mathbf{k}$ of the photoelectron of energy $E = k^2/2$. The photoionization amplitude $A(E, \Omega)$ is obtained by projecting the wave function at the end of the pulse onto the incoming continuum solutions,$u^{(-)}(\mathbf{k}, \mathbf{r})$, as

$$A(E, \Omega) = \langle u^{(-)} | \Psi(t = +\tau/2) \rangle. \tag{3.184}$$

The functions $u^{(-)}(\mathbf{k}, \mathbf{r})$ can be expanded in partial waves,

$$u^{(-)}(\mathbf{k}, \mathbf{r}) = \frac{4\pi}{(2\pi)^{3/2}} \sum_{l=0}^{\infty} \sum_{m=-l}^{l} i^l\, e^{-i\delta_l}\, Y_l^{m^*}(\Omega) \times \frac{\chi_l(k, r)}{r} Y_l^m(\hat{r}) \tag{3.185}$$

where the radial eigenfunction χ_l has the asymptotic behaviour (for $r \to \infty$)

$$\lim_{r \to +\infty} \chi_l(k, r) \approx \frac{1}{k} \sin\left[kr - \frac{l\pi}{2} + \delta_c(k, r) + \delta_l(k)\right]. \tag{3.186}$$

The phase $\delta_c(k, r)$ is the logarithmic term inherent to the Coulomb potential and $\delta_l(k)$

is the Coulomb phase shift. For the amplitude $A(E,\Omega)$, one obtains the expansion

$$A(E,\Omega) = \sum_{l=0}^{\infty} \sum_{m=-l}^{l} A_{l,m}(k)\, Y_l^m(\Omega) \tag{3.187}$$

where

$$A_{l,m}(k) = \frac{4\pi}{(2\pi)^{3/2}}\, i^l\, e^{-i\delta_l} \sum_n c_n^{(l,m)}(t = \frac{+\tau}{2})\, I_{nl}(k) \tag{3.188}$$

and

$$I_{nl}(k) \equiv \int_0^{r_{\max}} \chi_l(k,r)\, R_{nl}(r) \mathrm{d}r. \tag{3.189}$$

with R_{nl} being basis set radial states used in the spectral expansion of the wave packet Ψ. For the numerical evaluation of the radial integral $I_{nl}(k)$, at an energy E not too close to the eigenvalue E_{nl}, one can use the formula

$$I_{nl}(k) = \frac{\chi_l(k, r_{\max})}{k - k_{nl}} \frac{R'_{nl}(r_{\max})}{k + k_{nl}} \tag{3.190}$$

derived from the Wronskian theorem attached to the radial Schrödinger equation. In equation (3.190), $k_{nl} = \sqrt{2E_{nl}}$ and $R'_{nl}(r_{\max}) = (\mathrm{d}R_{nl}/\mathrm{d}r)|_{r=r_{\max}}$.

3.9.1 Photoelectron Angular Distribution (PAD)

The photoelectron angular distribution (PAD) can be determined by integrating the function $P(E,\Omega)$

$$P(\Omega) = \int |A(E,\Omega)|^2 \mathrm{d}E \tag{3.191}$$

with respect to all possible photoelectron energies. In order to reproduce the dependence of ionization probability on the azimuthal angle analogous to the experimental observations [116–118], the amplitude $A_{l,m}(k)$ is modified in equation (3.187) by including the prefactor $\cos(m\phi/2)$ for the cases where $m \neq 0$ and using the alternative density of states formulation

$$P(\Omega) = \sum_{l,m,E_\alpha > E_{ion}} |A_{l,m}(E_\alpha) Y_l^m(\Omega)|^2 / \Delta E. \tag{3.192}$$

where $\Delta E = (E_{n+1,l} - E_{n-1,l})/2$. Given the normalization of the function $u^{(-)}(\mathbf{k},\mathbf{r})$ to unity, the coefficient $1/\Delta E$ corresponds to the density of the discretized state [93].

It is common in many cases to estimate the electron angular probability distribution by [118, 119]

$$\frac{\mathrm{d}P}{\mathrm{d}\Omega} = \frac{P_{\mathrm{tot}}}{4\pi} \left[1 + \frac{\beta}{2}(3\cos^2\theta - 1) + (\delta + \gamma\cos^2\theta)\,\sin\theta\,\cos\phi\right] \tag{3.193}$$

where θ and ϕ are the polar and azimuthal angles respectively, β, δ, and γ are the dipole, electric quadrupole, and magnetic dipole asymmetry parameters, respectively, and P_{tot}

is the total ionization probability. The PADs when measured accurately can be used to provide stringent tests for theoretical calculations [116].

3.9.2 Photoelectron Energy Spectrum (PES)

The energy distribution can be determined by summing all the partial photoelectron spectra, $P_{l,m}(E)$, as

$$P(E) = \sum_{l,m} P_{l,m}(E) \approx \sum_{l,m,E_\alpha > E_{ion}} |C_\alpha^{(l,m)}|^2/\Delta E. \tag{3.194}$$

An interpolation procedure is performed for each channel l, m in order to evaluate $P_{l,m}(E)$ and subsequently $P(E)$. With respect to all possible photoelectron angular geometries, the photoelectron energy spectrum (PES) can also determined by integrating $P(E, \Omega)$

$$P(E) = \int |A(E,\Omega)|^2 \mathrm{d}\Omega = k \sum_{l,m} |A_{lm}(k)|^2. \tag{3.195}$$

3.9.3 LOPT Calculation of Distributions

Although the TDSE is considered to be very accurate in calculating photoelectron distributions, it does not give clear physical insights as to why particular types of behaviour occur in physical systems [85]. This limitation of the TDSE can be mitigated by using various analytical or perturbative methods. In particular, the perturbation theory has been very useful in interpreting numerical results. In the lowest-order perturbation theory (LOPT), the single-photon ionization amplitude for the case of an initial s state ($l = 0$) is given explicitly as [115]

$$A(E, \mathbf{n}) = \beta_1(k) \cos\theta + \beta_2(k) \sin\theta \cos\theta \cos\phi \tag{3.196}$$

where θ and ϕ are the polar and azimuthal angles of the direction $\mathbf{n}$. The coefficients $\beta_{1,2}$ are functions of energy and they are related to the partial amplitudes A_{10} and A_{21}. That is, $\beta_1 = \sqrt{3/4\pi} A_{10}(k)$ and $\beta_2 = \sqrt{15/2\pi} A_{21}(k)$. Using equation (3.191), the angular distribution takes the form

$$P(\mathbf{n}) = (\lambda_1 + \lambda_2 \sin\theta\cos\phi + \lambda_3 \sin^2\theta\cos^2\phi)\cos^2\theta \tag{3.197}$$

where the real coefficients λ_i are constant. Their values can be determined from the exact numerical values of $P(\mathbf{n})$ by a fitting procedure.

The energy spectrum can be obtained as

$$P(E) \approx k(|A_{1,0}(k)|^2 + 2|A_{2,1}(k)|^2). \tag{3.198}$$

Within the perturbative regime, cross sections can be evaluated from the TDSE calculations using a simple relation with the calculated ionization probability P_N. For the absorption of N photons it takes the form

$$\sigma_N = C(N) \left(\frac{\omega}{I}\right)^N \frac{P_N}{\tau} \tag{3.199}$$

where the cross section is given in $\mathrm{cm}^{2N}\mathrm{s}^{N-1}$, the intensity I in Wcm^{-2}, the photon energy ω in joules, and the total pulse duration τ in seconds. The weighting coefficients $C(N)$ takes into account the effective pulse duration, which depends on the pulse envelope. For a $\cos^2$ pulse, $C(1) = 8/3$, $C(2) = 128/35$, $\cdots$ are the values of the weighting coefficients for the corresponding photon orders [115].

3.10 Asymmetry Parameters

The experimental measurement of the asymmetry parameters provide a stringent test for theory. Within the dipole approximation, the ionization probability is known to exhibit an asymmetric distribution with respect to the polar angles θ but a symmetric one in the azimuthal angle distribution. It is common practice [119] to express the distributions from multipolar interactions in the form

$$\frac{dP}{d\Omega} = \frac{P_{\mathrm{tot}}}{4\pi} \sum_{l,m} B_{n,m} P_l^m(\cos\theta) \cos m\phi \tag{3.200}$$

where P_{tot} is the total ionization probability, θ is the angle between the electric field vector of the incident photon and the ejected-electron directions, and $B_{n,m}$ are the asymmetry parameters, with $B_{0,0} = 1$ and all other asymmetry parameters are generally functions with complex dependence on polar angle θ, radial transition matrix elements, and phase-shifts [116].

The non-dipole interactions, on the other hand, result in photoelectron distributions with a dependence on both polar and azimuthal angles. The non-dipole effects can therefore be seen by examining the deviation from the dipolar distributions in the polar plane. The forward-backward asymmetry in the azimuthal plane is also remarkable and quite instrumental in the experimental detection of the non-dipole effects. Here, the probability distribution in the direction of the laser propagation in the azimuthal plane is different from the distribution in the opposite direction, while the left-right distribution is symmetric. The forward-backward asymmetry parameter A_{f-b} can be defined as the ratio [93]

$$A_{f-b} = \frac{P_f - P_b}{P_f + P_b} \tag{3.201}$$

where P_f is the probability of forward photoelectron ejection ($\hat{k} \cdot \hat{r} > 0$) and P_b is the probability of backward photoelectron ejection ($\hat{k} \cdot \hat{r} < 0$).

3.11 Numerical Errors

As in any numerical process, errors are generated in the computation of the time-dependent matrix elements and subsequently in the calculation of probabilities. Approximations and random errors usually contribute more in the lack of desired accuracy. The orthonormalization process of the B spline basis set may be another likely source of the errors if it is not achieved with reasonable accuracy. These errors cumulatively may lead to a deviation from the normalization condition of all probabilities as required by the statistical theory of quantum mechanics. The magnitude of the errors increase with the field amplitude, the number of states included in the TDSE, the order of the multipole expansion evaluated, and the number of iterations used for full convergence at every time step.

In the vector calculation from the coupled integro-differential equations, the coefficient of the i^{th} state is determined from the equation

$$i\dot{C}_i(t) = C_i(t)E_i + \sum_j^n C_j[V_{ij} + \delta_{ij}(t)] \tag{3.202}$$

where E_i is the eigenvalue corresponding to the field-free i^{th} eigenstate, C_j is the coefficient of the j^{th} eigenstate connected to the i^{th} state by the earlier defined selection rules, and $\delta_{ij}(t)$ is the numerical noise. For the implementation of the multipole expansion, the total accrued error

$$\delta_i(t) = A(t)\sum_j^n \delta_{ij} + \frac{A^2(t)}{2}\sum_{j'}^n \delta_{ij'} \tag{3.203}$$

arises from the partial evaluation of the time dependent transition matrix elements and are amplified by the field magnitude as seen in the above equation. The first term on the right is a sum of errors contributed by the $\mathbf{A}\cdot\mathbf{p}$ transitions while the second term is the sum of errors generated from the $\mathbf{A}\cdot\mathbf{A}$ transitions. The effect of these errors at lower field intensities and at the lowest-order of the multipole expansion may be negligible. But at higher intensities and/or higher orders of the multipole expansion requiring the inclusion of several states for convergence, the impact of the errors on the numerical convergence of probabilities can be very large leading to inaccuracies in the calculated probabilities as well as time-demanding time propagation to achieve full convergence in every time-step. The numerical noise can be reduced to a greater extent by using accurate basis-set diagonalization routines and by taking advantage of symmetry as well as analytical simplification of the numerical processes involved where possible.

3.12 Implicit Time Propagation Routine

A fully implicit scheme is implemented in the extended BEYDPIP code. The implicit scheme is preferred because it is known to offer a high degree of stability as compared to the explicit schemes, although they generally involve more iterations per time-step.

This section provides some insight into the implicit time-propagation routine.

The fully implicit coupled integro-differential equations

$$i\dot{C}_\alpha(t) = C_\alpha(t)\, E_\alpha + \sum_{\alpha'} C_{\alpha'}(t)\, V_{\alpha\alpha'}(t) \tag{3.204}$$

obtained from the solution of the TDSE with the initial conditions

$$C_\alpha(t_0) = \begin{cases} 1 & \text{if } \alpha = \alpha_i \\ 0 & \text{if } \alpha \neq \alpha_i \end{cases} \tag{3.205}$$

defined at $t = t_0$ and a particular initial state α_i can be re-expressed as

$$i\frac{\dot{C}_\alpha}{C_\alpha} = E_\alpha + V_{\alpha\alpha}(t) + \sum_{\alpha'\neq\alpha} \gamma_{\alpha'}(t)\, V_{\alpha\alpha'}(t); \quad \gamma_{\alpha'} = \frac{C_{\alpha'}}{C_\alpha}. \tag{3.206}$$

The total probability for an electron described by the wave packet to be found at any point in space at any instant of time is unity. This means that the amplitude of one state

$$\sum_\alpha |C_\alpha|^2 = 1 \quad \text{or} \quad |C_{\alpha'}| = \sqrt{1 - \sum_{\alpha''\neq\alpha'} |C_{\alpha''}|^2} \tag{3.207}$$

can be expressed in terms of all the other amplitudes, but the phase information is lost in this process. If the phase information is neglected , the coupled integro-differential equation (3.206) in integral form can then be written as

$$\begin{gathered} \ln\frac{C_\alpha(t)}{C_\alpha(t_0)} = -i\int_{t_0}^{t} \mathrm{d}t\, [E_\alpha + V_{\alpha\alpha}(t) + \sum_{\alpha'\neq\alpha} \gamma_{\alpha'}(t)\, V_{\alpha\alpha'}(t)] \\ \text{or} \\ C_\alpha(t) = C_\alpha(t_0)\exp\{-i\int_{t_0}^{t} \mathrm{d}t\, [E_\alpha + V_{\alpha\alpha}(t) + \sum_{\alpha'\neq\alpha} \gamma_{\alpha'}(t)\, V_{\alpha\alpha'}(t)]\} + \kappa \end{gathered} \tag{3.208}$$

Alternatively, equation (3.204), together with the predetermined initial conditions, can be solved iteratively by the numerical time-propagation routines using suitable time steps. The integral can be numerically formulated as

$$C_\alpha(t_{n+1}) = C_\alpha(t_n) + \int_{t_n}^{t_{n+1}} \dot{C}_\alpha(t_n)\, \mathrm{d}t \tag{3.209}$$

where n is the number of time steps used in the integration process. In this work, the numerical advantage of the variable Adams-Bashforth-Moulton predictor-corrector adaptive routine [120] is exploited for the time integration but the possibility of using the Runge-Kutta methods is also implemented.

3.13 Five-State Model Including Non-Dipole Corrections

In order to get a simple picture of the interaction dynamics in the TDSE, the integro-differential equations for the ground ($1s_0$) state and the first four lowest excited states of the hydrogen atom is generated. These excited states are explicitly chosen to be $2s_0$, $2p_0$, $2p_{-1}$ and $2p_1$. The subscripts denote the index of the magnetic quantum numbers for each symmetry. We consider the $1s$ state as the initial state. The selection rules are embedded in the time-dependent transition matrices $M_{\alpha\alpha'}(t)$. The coefficients of the initial state can be written as

$$C_\alpha = \delta_{1s,\alpha} \tag{3.210}$$

where the Kronecker delta has value 1 for the initial state and zero otherwise. The coupled integro-differential equations for each of the five states can then be written as

$$\begin{aligned}
\dot{C}_{1s_0} &= -i\{C_{1s_0}E_{1s_0} + C_{1s_0}M_{1s_01s_0} + C_{2s_0}M_{1s_02s_0} + C_{2p_0}M_{1s_02p_0} \\
&\quad + C_{2p_1}M_{1s_02p_1} + C_{2p_{-1}}M_{1s_02p_{-1}}\} \\
\dot{C}_{2s_0} &= -i\{C_{2s_0}E_{2s_0} + C_{1s_0}M_{2s_01s_0} + C_{2s_0}M_{2s_02s_0} + C_{2p_0}M_{2s_02p_0} \\
&\quad + C_{2p_1}M_{2s_02p_1} + C_{2p_{-1}}M_{2s_02p_{-1}}\} \\
\dot{C}_{2p_0} &= -i\{C_{2p_0}E_{2p_0} + C_{1s_0}M_{2p_01s_0} + C_{2s_0}M_{2p_02s_0} + C_{2p_0}M_{2p_02p_0} \\
&\quad + C_{2p_1}M_{2p_02p_1} + C_{2p_{-1}}M_{2p_02p_{-1}}\} \\
\dot{C}_{2p_1} &= -i\{C_{2p_1}E_{2p_1} + C_{1s_0}M_{2p_11s_0} + C_{2s_0}M_{2p_12s_0} + C_{2p_0}M_{2p_12p_0} \\
&\quad + C_{2p_1}M_{2p_12p_1} + C_{2p_{-1}}M_{2p_12p_{-1}}\} \\
\dot{C}_{2p_{-1}} &= -i\{C_{2p_{-1}}E_{2p_{-1}} + C_{1s_0}M_{2p_{-1}1s_0} + C_{2s_0}M_{2p_{-1}2s_0} + C_{2p_0}M_{2p_{-1}2p_0} \\
&\quad + C_{2p_1}M_{2p_{-1}2p_1} + C_{2p_{-1}}M_{2p_{-1}2p_{-1}}\}.
\end{aligned} \tag{3.211}$$

The variable t has been omitted in this fully implicit implementation only for convenience. It is clear that each of the state coefficients at the end of each time step will have a unique value. This value depends on the initial conditions, the transition matrix elements between the state and each of the states if allowed by the selection rules, the field-free energy of the state itself. Due to the dependence of the transition matrix elements on the quantum numbers defining the geometry of the initial state, the symmetric population distribution of the degenerate levels is likely to be broken for transitions of any multipole order.

Focussing on the $2p$ degenerate states in equation (3.211), making use of the known symmetry properties of the transition matrices, and removing the non-interacting components as defined by the dipole term and its leading-order correction $(1 + i\mathbf{k}\cdot\mathbf{r})$, one obtains

$$\begin{aligned}
\dot{C}_{2p_0} &= -i\{C_{2p_0}E_{2p_0} + C_{1s_0}M_{2p_01s_0} + C_{2s_0}M_{2p_02s_0} + C_{2p_0}M_{2p_02p_0} \\
&\quad + C_{2p_{+1}}M_{2p_02p_1} + C_{2p_{-1}}M_{2p_02p_{-1}}\} \\
\dot{C}_{2p_{+1}} &= -i\{C_{2p_{+1}}E_{2p_{+1}} + C_{1s_0}M_{2p_{+1}1s_0} + C_{2s_0}M_{2p_{+1}2s_0} + C_{2p_0}M_{2p_12p_0}\} \\
\dot{C}_{2p_{-1}} &= -i\{C_{2p_{-1}}E_{2p_{-1}} - C_{1s_0}M_{2p_{+1}1s_0} - C_{2s_0}M_{2p_{+1}2s_0} - C_{2p_0}M_{2p_{+1}2p_0}\}.
\end{aligned} \tag{3.212}$$

If the first time-step Δt_1 only is considered, the equation simplifies to

$$\begin{aligned}
\dot{C}_{2p_0} &= -i\{M_{2p_0 1s_0} + \delta_{1s,\alpha}(E_{2p_0} + M_{2p_0 2s_0} + M_{2p_0 2p_0} \\
&\qquad + M_{2p_0 2p_{+1}} + M_{2p_0 2p_{-1}})\} \\
\dot{C}_{2p_{+1}} &= -i\{M_{2p_{+1} 1s_0} + \delta_{1s,\alpha}(E_{2p_{+1}} + M_{2p_{+1} 2s_0} + M_{2p_{+1} 2p_0})\} \\
\dot{C}_{2p_{-1}} &= -i\{-M_{2p_{+1} 1s_0} + \delta_{1s,\alpha}(E_{2p_{+1}} - M_{2p_{+1} 2s_0} - M_{2p_{+1} 2p_0})\}.
\end{aligned} \tag{3.213}$$

For $\delta_{1s,\alpha} = 0$ then it can be seen that $C_{nl_+} = -C_{nl_-}$ and the population distribution of the magnetic sublevels of opposite parity would be symmetric at the end of the interaction. But if $\delta > 0$ (as a possible case study) regardless of its magnitude, it breaks the symmetry property of the magnetic sublevels of opposite parity by introducing equal Zeeman type splitting of energy levels of the sublevels of opposite parity. This leads to an asymmetric population distribution of the sublevels of opposite parity at the end of the laser pulse. The possible sources of asymmetry could be the contribution of random processes like flourescence and spontaneous emissions [121] or the process of optical pumping [122] where a circularly or elliptically polarized coherent pulse can only allow transitions in m in a specific direction.

3.14 Analytical Comparison of Hydrogen Transition Matrix Elements

The hydrogen time-independent wavefunction $\Psi(r)$ can analytically be expressed as a product of three functions $F(\phi)$, $P(\theta)$, and $R(r)$, which depend on the indicated angular and radial co-ordinates. The analytically calculated transition matrix elements are compared with the ones evaluated numerically in radiation gauge. This was necessary for checking the correctness of the implementation and the accuracy of the results given that the wavefunctions of hydrogen atom are analytically known. If the implementation is correct, the accuracy of the numerically calculated transition matrix elements would depend further on the quality of the numerically generated orbitals. The quality of orbitals obtained using the B splines increase with the box radius $r_{\max}$, number of B splines, the order of B splines, and the type of knot sequence employed as already discussed in section 3.1.6. The transition matrix elements are calculated based on the Taylor expanded multipole interaction Hamiltonian in equation (3.172). Table 3.2 lists the first few solutions of the hydrogen atom specified by the quantum numbers n, l, and m.

n	l	m	$F(\phi)$	$P(\theta)$	$R(r)$
1	0	0	$\frac{1}{\sqrt{2\pi}}$	$\frac{1}{\sqrt{2}}$	$\frac{2}{a_0^{\frac{3}{2}}}\mathrm{e}^{\frac{-r}{a_0}}$
2	0	0	$\frac{1}{\sqrt{2\pi}}$	$\frac{1}{\sqrt{2}}$	$\frac{1}{2\sqrt{2}a_0^{\frac{3}{2}}}[2-\frac{r}{a_0}]\mathrm{e}^{\frac{-r}{2a_0}}$
2	1	0	$\frac{1}{\sqrt{2\pi}}$	$\frac{\sqrt{6}}{2}\cos\theta$	$\frac{1}{2\sqrt{6}a_0^{\frac{3}{2}}}\frac{r}{a_0}\mathrm{e}^{\frac{-r}{2a_0}}$
2	1	± 1	$\frac{1}{\sqrt{2\pi}}\mathrm{e}^{\pm i\phi}$	$\frac{\sqrt{3}}{2}\sin\theta$	$\frac{1}{2\sqrt{6}a_0^{\frac{3}{2}}}\frac{r}{a_0}\mathrm{e}^{\frac{-r}{2a_0}}$

Table 3.2: Table showing the first few solutions of the hydrogen atom separated in the radial $R(r)$ and spherical $(P(\theta), F(\phi))$ parts for the states specified by the quantum numbers n, l, and m. The table entries is taken from [123] .

3.14.1 Dipole Transition Matrix Elements

The dipole transition matrix elements between two hydrogen states is given by

$$\langle\psi_b \mid \mathbf{A}\cdot\mathbf{p} + \frac{1}{2}\mathbf{A}\cdot\mathbf{A} \mid \psi_a\rangle = \langle\psi_b \mid \mathbf{A}\cdot\mathbf{p} \mid \psi_a\rangle + \frac{1}{2}\langle\psi_b \mid \mathbf{A}\cdot\mathbf{A} \mid \psi_a\rangle. \tag{3.214}$$

The two terms of the non-relativistic interaction Hamiltonian $\mathbf{A}\cdot\mathbf{p}$ and $\mathbf{A}\cdot\mathbf{A}$ have different selection rules leading to different final states and different symmetry for corresponding multipole orders. For example, within the dipole approximation the l quantum number changes by ± 1 for the $\mathbf{A}\cdot\mathbf{p}$ transition while there is no change for the $\mathbf{A}\cdot\mathbf{A}$ transition. In both cases the m quantum number remains conserved for this lowest multipole-order expansion in case of a linearly polarized radiation with the electric field vector along the $+z$ direction.

The transitions of both terms from the ground state to the lowest states coupled by the multipole terms of the interaction Hamiltonian are considered. The polarization direction of the laser pulse is chosen to be along the $+z$ axis and the propagation direction to be along the $+x$ axis. Starting with the $\mathbf{A}\cdot\mathbf{p}$ transition matrix elements, one obtains

$$\langle\psi_{2p} \mid \mathbf{A}\cdot\mathbf{p} \mid \psi_{1s}\rangle = \langle\psi_{2p} \mid A_1(t)p_z \mid \psi_{1s}\rangle = A_1(t)\langle\psi_{2p} \mid p_z \mid \psi_{1s}\rangle. \tag{3.215}$$

The time independent part can be evaluated as

$$\psi_{n_b,l_b,m_b} \mid p_z \mid \psi_{n_a,l_a,m_a}\rangle = -\beta_{l_a,m_a} \times \int_0^\infty \mathrm{d}r\, r^2\, R_{n_b,l_b}\left\{\frac{\partial R_{n_a,l_a}}{\partial r} - l_a\frac{R_{n_a,l_a}}{r}\right\} \tag{3.216}$$

where β_{l_a,m_a}

$$\beta_{l_a,m_a} = \sqrt{\frac{(l_a+1)^2 - m_a^2}{4(l_a+1)^2 - 1}} \tag{3.217}$$

is an angular factor equivalent to the pre-factor of the first part of equation (3.121). It simplifies to $l_b/\sqrt{4l_b^2 - 1}$ if $m_a = 0$ and $l_b = l_a + 1$. Therefore, substituting the radial parts of ψ_{2p} and ψ_{1s}, one obtains

$$
\begin{aligned}
&\langle \psi_{2p} \mid p_z \mid \psi_{1s} \rangle \\
&\quad = -\beta_{0,0} \times \int_0^\infty \mathrm{d}r\, r^2\, R_{2,1} \left\{ \frac{\partial R_{1,0}}{\partial r} - l_a\, \frac{R_{1,0}}{r} \right\} \\
&\quad = -\beta_{0,0} \times \left\{ \int_0^\infty \mathrm{d}r\, r^2\, R_{2,1}\, \frac{\partial R_{1,0}}{\partial r} - l_a \int_0^\infty \mathrm{d}r\, r R_{2,1} R_{1,0} \right\} \\
&\quad = -\beta_{0,0} \times \left\{ \int_0^\infty \mathrm{d}r\, r^2\, \frac{1}{2\sqrt{6}}\, r\, e^{\frac{-r}{2}} \times -2\, e^{-r} - l_a \int_0^\infty \mathrm{d}r\, r \frac{1}{2\sqrt{6}} r e^{\frac{-r}{2}} \times 2\, e^{-r} \right\} \\
&\quad = -\beta_{0,0} \times \frac{1}{\sqrt{6}} \left\{ - \int_0^\infty \mathrm{d}r\, r^3\, e^{\frac{-3r}{2}} - l_a \int_0^\infty \mathrm{d}r\, r^2\, e^{\frac{-3r}{2}} \right\} \\
&\quad = -\beta_{0,0} \times \frac{1}{\sqrt{6}} \{ -\frac{3!}{1.5^4} - l_a \times \frac{2!}{1.5^3} \} \\
&\quad = -\beta_{0,0} \times \frac{1}{1.5^3 \times \sqrt{6}} \{ -\frac{3!}{1.5} - 0 \times 2! \} = 0.279350827
\end{aligned}
\tag{3.218}
$$

This analytical value (0.279350827) is compared to a numerically calculated value (−0.279350827) evaluated using a maximum box radius of 200 a.u. and 600 B splines with a non-linear knot sequence. The numerical value is an agreement with the analytical value up to 9 significant digits. The difference in sign could be a consequence of the phase of the numerically calculated radial orbitals which is not present in the analytical solutions used. Similarly, from the $\mathbf{A} \cdot \mathbf{A}$ transition matrix elements one obtains

$$
\begin{aligned}
\frac{1}{2} \langle \psi_{1s} \mid \mathbf{A} \cdot \mathbf{A} \mid \psi_{1s} \rangle &= \frac{1}{4} \langle \psi_{1s} \mid [A_1^2(t) - A_2^2(t)] \mid \psi_{1s} \rangle \\
&= \frac{1}{4}\, [A_1^2(t) - A_2^2(t)]\, \langle \psi_{1s} \mid \psi_{1s} \rangle .
\end{aligned}
\tag{3.219}
$$

The angular factor for this problem is unity for identical l and m quantum numbers and zero otherwise. Thus the time independent integral reduces to

$$
\begin{aligned}
\langle \psi_{1s} \mid \psi_{1s} \rangle &= \int_0^\infty \mathrm{d}r\, r^2\, R_{1s}\, R_{1s} \\
&= \int_0^\infty dr\, r^2\, 4\, e^{-2r} \\
&= 4 \times \frac{2!}{2^3} \quad = 1
\end{aligned}
\tag{3.220}
$$

This analytical value (1.000000000) is compared to a numerically calculated value (1.0000000000) evaluated using a maximum box radius of 200au and 600 B splines with a non-linear knot sequence. The numerical value is in exact agreement with the analytical value.

3.14.2 Quadrupole Transition Matrix Elements

The quadrupole transition matrix elements between two hydrogen states is given by

$$\langle\psi_b \mid A_2(t)\frac{2\pi x}{\lambda}p_z + \frac{1}{4}\left[A_1^2(t) - A_2^2(t)\right]\frac{4\pi x}{\lambda} \mid \psi_a\rangle \tag{3.221}$$

where $A_1(t)$ and $A_2(t)$ are the corresponding time-dependent functions predefined in equation (3.168). The first term of the equation (3.221) contains the electric quadrupole and the magnetic dipole transitions. Inclusion of the magnetic dipole transition yields the effect of the magnetic field produced by the radiation and it should incorporate the effect of spin-magnetic field interaction for completeness [18]. This is because the interactions are of the same order $\sim 1/c$ of the fine structure constant. The interaction Hamiltonian is modified further by interaction between the spin magnetic moment and the resultant magnetic field. The second term in equation (3.221) contains only the effect of the diamagnetism present in the $\mathbf{A}^2$ term.

By re-writing the quadrupole transition matrix in spherical co-ordinates, one can express the variable x as

$$x = \frac{4\pi}{3}\,r \sum_{m=-1,1} Y_1^{m*}(\hat{x})\,Y_1^m(\hat{r}). \tag{3.222}$$

The quadrupole transition matrix element therefore becomes

$$\begin{aligned}
&\langle\psi_b \mid A_2(t)\frac{2\pi x}{\lambda}p_z + \frac{1}{2}\,A_{sq}(t)\,\frac{4\pi x}{\lambda} \mid \psi_a\rangle \\
&= \langle\psi_b \mid A_2(t)\frac{2\pi x}{\lambda}p_z \mid \psi_a\rangle + \frac{1}{2}\,A_{sq}(t)\langle\psi_b \mid \frac{4\pi x}{\lambda} \mid \psi_a\rangle \\
&= A_2(t)\,\frac{8\pi^2}{3\lambda}\sum_{m=-1,1} Y_1^{m*}\,(\hat{k}_x)\langle\psi_b \mid r\,Y_1^m(\hat{r})\,p_z \mid \psi_a\rangle \\
&\quad + \frac{A_{sq}(t)}{2}\,\frac{16\pi^2}{3\lambda}\sum_{m=-1,1} Y_1^{m*}(\hat{k}_x)\,\langle\psi_b \mid r\,Y_1^m(\hat{r}) \mid \psi_a\rangle.
\end{aligned} \tag{3.223}$$

where $A_{sq}(t) = [A_1^2(t) - A_2^2(t)]/4$.

3.14.3 Electric Quadrupole Transition Matrix Element

The time independent part of the electric quadrupole transition from the ground ($1s$) state of hydrogen atom to the excited ($3d$) state with the $m = 1$ and $m = -1$ quantum numbers is first evaluated. The electric quadrupole transition matrix element between the two states can be expressed as

$$\begin{aligned}
&\frac{8\pi^2}{3\lambda}\, Y_1^{1*}(\hat{k}_x)\, \langle \psi_b \mid r\, Y_1^m(\hat{r})\, p_z \mid \psi_a \rangle \\
&\qquad = -\beta_{l_b,m_b,l_a,m_a} \times \int_0^\infty \mathrm{d}r\, r^2\, r\, R_{n_b,l_b} \left\{ \frac{\partial R_{n_a,l_a}}{\partial r} - l_a \times \frac{R_{n_a,l_a}}{r} \right\} \\
&\qquad = -\beta_{l_b,m_b,l_a,m_a} \times \int_0^\infty \mathrm{d}r\, r^2\, r\, R_{n_b,l_b} \frac{\partial R_{n_a,l_a}}{\partial r} \\
&\qquad = -\beta_{l_b,m_b,l_a,m_a} \times \int_0^\infty \mathrm{d}r\, r^2\, \frac{4r}{81\sqrt{30}} r^2 e^{\frac{-r}{3}} \times -2e^{-r} \\
&\qquad = -\beta_{l_b,m_b,l_a,m_a} \times \frac{-8}{81\sqrt{30}} \int_0^\infty \mathrm{d}r\, r^5\, e^{\frac{-4r}{3}} \\
&\qquad = \beta_{l_b,m_b,l_a,m_a} \times \frac{8}{81\sqrt{30}} \frac{5!}{(4/3)^6}
\end{aligned} \tag{3.224}$$

with the pre-factor β_{l_b,m_b,l_a,m_a} containing the spectral information and the angular factor evaluated as

$$\begin{aligned}
\beta_{l_b,m_b,l_a,m_a} &= \frac{8\pi^2}{3\lambda} Y_1^{1*}(\hat{k}_x) \times \sqrt{\frac{(l_a+1)^2 - m_a^2}{4(l_a+1)^2 - 1}} \times \int \mathrm{d}\Omega\, Y_{l_b}^{m_b*}(\hat{r})\, Y_1^1(\hat{r})\, Y_{l_a+1}^{m_a}(\hat{r}) \\
&= \frac{8\pi^2}{3\lambda}\, Y_1^{1*}(\hat{k}_x) \times \sqrt{\frac{(l_a+1)^2 - m_a^2}{4(l_a+1)^2 - 1}} \times \sqrt{\frac{(2l_b+1) \times 3 \times (2l_a+3)}{4\pi}} \\
&\times \begin{pmatrix} l_b & 1 & l_a+1 \\ -m_b & 1 & m_a \end{pmatrix} \begin{pmatrix} l_b & 1 & l_a+1 \\ 0 & 0 & 0 \end{pmatrix} \times (-1)^{m_b} \\
\beta_{2,1,0,0} &= \frac{8\pi^2}{3\lambda} Y_1^{1*}(\hat{k}_x) \times \sqrt{\frac{1}{3}} \times \sqrt{\frac{5 \times 3 \times 3}{4\pi}} \begin{pmatrix} 2 & 1 & 1 \\ -1 & 1 & 0 \end{pmatrix} \begin{pmatrix} 2 & 1 & 1 \\ 0 & 0 & 0 \end{pmatrix} \times (-1)^1 \\
&= -\frac{1.147147441}{\lambda}
\end{aligned} \tag{3.225}$$

The electric quadrupole matrix element between the $1s$ state and the $3\,d_1$ resonant state corresponding to 13 nm wavelength radiation therefore simplifies to

$$\begin{aligned}
\frac{8\pi^2}{3\lambda} Y_1^{1*}(\hat{k}_x) \langle \Psi_{3d} \mid r Y_1^1(\hat{r}) p_z \mid \Psi_{1s} \rangle &= -\frac{1.147147441}{13 \times 18.897261} \times \frac{8}{81\sqrt{30}} \frac{5!}{1.33333^6} \\
&= -0.1798332837E - 02
\end{aligned} \tag{3.226}$$

This analytical value ($-0.1798333333E - 02$) is in agreement with our numerically calculated value ($0.17990571552055E - 02$) up to 4 significant figures. The factor $E - 02 = 10^{-2}$.

3.14.4 Magnetic Dipole Transition Matrix Element

Magnetic dipole transitions are also embedded in the 1st order corrections to the $\mathbf{A} \cdot \mathbf{p}$ term of the interaction Hamiltonian just like the electric quadrupole transition. The difference between them comes in the selection rules. In the magnetic dipole transitions, the orbital angular momentum quantum number is conserved ($\Delta l = 0$) while the projection quantum number can change by a unit value ($\Delta m = \pm 1$).

The magnetic dipole transition matrix element between $2p_0$ and $2p_{-1}$ resonant states is

$$\begin{aligned}
&\frac{8\pi^2}{3\lambda}\, Y_1^{1*}(\hat{k}_x)\, \langle \psi_{2p_0} \mid r\, Y_1^1(\hat{r})\, p_z \mid \psi_{2p_{-1}} \rangle \\
&\qquad = -\beta_{1,1,1,0} \times \int_0^\infty \mathrm{d}r\, r^3\, R_{2,1} \left\{ \frac{\partial R_{2,1}}{\partial r} - 1 \times \frac{R_{2,1}}{r} \right\} \\
&\qquad = -\beta_{1,1,1,0} \times \int_0^\infty \mathrm{d}r\, r^3\, R_{2,1}\, \frac{\partial R_{2,1}}{\partial r} - \frac{R_{2,1}}{r} \\
&\qquad = -\beta_{1,1,1,0} \times \int_0^\infty \mathrm{d}r\, r^3\, \frac{1}{2\sqrt{6}}\, r\, e^{\frac{-r}{2}} \times [\frac{\partial}{\partial r}(\frac{1}{2\sqrt{6}}\, r\, e^{\frac{-r}{2}}) - \frac{1}{2r\sqrt{6} r e^{\frac{-r}{2}}}] \\
&\qquad = -\beta_{1,1,1,0} \times \frac{1}{24} \times \{ \int_0^\infty \mathrm{d}r\, r^4\, e^{\frac{-r}{2}} [\frac{-1}{2} r e^{\frac{-r}{2}} + e^{\frac{-r}{2}} - e^{\frac{-r}{2}}] \} \\
&\qquad = -\beta_{1,1,1,0} \times \frac{-1}{48} \times \int_0^\infty \mathrm{d}r\, r^5\, e^{-r} \\
&\qquad = \beta_{1,1,1,0} \times \frac{5!}{48}.
\end{aligned} \tag{3.227}$$

The pre-factor $\beta_{1,0,1,1}$ yields

$$\begin{aligned}
\beta_{1,1,1,0} &= \frac{8\pi^2}{3\lambda}\, Y_1^{1*}(\hat{k}_x) \times \sqrt{\frac{4}{15}} \times \sqrt{\frac{3 \times 3 \times 5}{4\pi}} \begin{pmatrix} 1 & 1 & 2 \\ -1 & 1 & 0 \end{pmatrix} \begin{pmatrix} 1 & 1 & 2 \\ 0 & 0 & 0 \end{pmatrix} \times (-1)^1 \\
&= \frac{0.592383186}{\lambda}
\end{aligned} \tag{3.228}$$

The magnetic dipole matrix element between the $2p_0$ state and the $2p_{-1}$ state for the 13 nm wavelength radiation therefore simplifies to

$$\frac{8\pi^2}{3\lambda}\, Y_1^{1*}(\hat{k}_x) \langle \psi_{2s} \mid r\, Y_1^1(\hat{r})\, p_z \mid \psi_{2p_{-1}} \rangle = \frac{0.592383186}{13 \times 18.897261} \times \frac{5!}{48} \quad = 0.6028378589E - 02 \tag{3.229}$$

This analytical value ($0.6028378589E - 02$) is compared to our numerically calculated value ($0.6030817225167E - 02$) yielding an agreement up to 3 significant digits. The difference between the magnetic dipole transition matrix element evaluated and the electric quadrupole transition matrix element evaluated in subsection 3.14.3 comes from the angular integral as well as the sizes of the different orbitals coupled.

3.14.5 Quadrupole $\mathbf{A}\cdot\mathbf{A}$ Term Transition Matrix Element

The transition matrix element corresponding to the $\mathbf{A}\cdot\mathbf{A}$ quadrupole interaction Hamiltonian can in general be expressed as

$$\begin{aligned} T^{A\cdot A}_{b\leftarrow a} &= \frac{16\pi^2}{3\lambda}\, Y_1^{1*}(\hat{k}_x)\, \langle \psi_b \mid r\, Y_1^1(\hat{r}) \mid \psi_a \rangle \\ &= \beta^{II}_{l_b,m_b,l_a,m_a} \times \int_0^\infty \mathrm{d}r\, r^2\, R_{n_b l_b}\, r\, R_{n_a l_a} \end{aligned} \tag{3.230}$$

where the pre-factor

$$\begin{aligned} \beta^{II}_{l_b,m_b,l_a,m_a} &= \frac{16\pi^2}{3\lambda}\, Y_1^{m*}(\hat{k}_x) \int \mathrm{d}\Omega\, Y_{l_b}^{m_b*}\, Y_1^{m} Y_{l_a}^{m_a} \\ &= \frac{16\pi^2}{3\lambda}\, Y_1^{m*}(\hat{k}_x) \sqrt{\frac{(2l_b+1)\times 3\times(2l_a+1)}{4\pi}} \\ &\quad \times \begin{pmatrix} l_b & 1 & l_a \\ -m_b & m & m_a \end{pmatrix} \begin{pmatrix} l_b & 1 & l_a \\ 0 & 0 & 0 \end{pmatrix} \times (-1)^{m_b} \end{aligned} \tag{3.231}$$

contains both the angular and spectral information. Here $m = -1$ or 1 correspond to the allowed magnetic quantum numbers. We consider the transition from the $1s$ state to the $2p_1$ state as an example of the allowed transition for this interaction term.

The transition matrix element for this transition is

$$\begin{aligned} T^{A\cdot A}_{2p\leftarrow 1s} &= \frac{16\pi^2}{3\lambda}\, Y_1^{1*}(\hat{k}_x)\, \langle \psi_{2p} \mid r\, Y_1^1(\hat{r}) \mid \psi_{1s} \rangle \\ &= \beta^{II}_{1,1,0,0} \times \int_0^\infty \mathrm{d}r\, r^2\, R_{2p}\, r\; R_{1s} \\ &= \beta^{II}_{1,1,0,0} \times \int_0^\infty \mathrm{d}r\, r^2\, r\, \frac{1}{2\sqrt{6}}\, r\, e^{\frac{-r}{2}}\, 2e^{-r} \\ &= \beta^{II}_{1,1,0,0} \times \frac{2}{2\sqrt{6}} \int_0^\infty \mathrm{d}r\, r^4\, r\, e^{\frac{-3r}{2}} \\ &= \beta^{II}_{1,1,0,0} \times \frac{1}{\sqrt{6}} \times \frac{4!}{1.5^5} \end{aligned} \tag{3.232}$$

The pre-factor $\beta^{II}_{1,1,0,0}$ simplifies to

$$\begin{aligned} \beta^{II}_{1,1,0,0} &= \frac{16\pi^2}{3\lambda}\, Y_1^{1*}(\hat{k}_x) \sqrt{\frac{3\times 3\times 1}{4\pi}} \begin{pmatrix} 1 & 1 & 0 \\ -1 & 1 & 0 \end{pmatrix} \begin{pmatrix} 1 & 1 & 0 \\ 0 & 0 & 0 \end{pmatrix} \times (-1)^1 \\ &= -\frac{5.130194545}{\lambda} \end{aligned} \tag{3.233}$$

and the transition matrix element evaluated analytically for the 13 nm radiation wavelength becomes

$$T^{A\cdot A}_{2p\leftarrow 1s} = -\frac{5.130194545}{13\times 18.897261}\times\frac{1}{\sqrt{6}}\times\frac{4!}{1.5^5} \quad = -0.2694455E-01 \tag{3.234}$$

This analytical value $-0.2694455E-01$ agrees with our numerically calculated value $(0.26955420602E-01)$ up to 4 significant figures. Except for the 0^{th} multipole-order terms, the agreement between the analytically determined transition matrix elements is not very good. The source of this lower precision needs to be investigated further.

Chapter Summary

In this chapter, the theoretical and the mathematical background of the method employed in the study is discussed. The details of implementation adopted in the extended BEYDIP code and the method of determination of the physical observables is also discussed. A comparison between some analytically and numerically determined multipole-order transition matrix elements is also presented. Chapter 4 can be seen as an extension of this chapter since it compares the Rayleigh and the Taylor plane-wave multipole expansion series which incorporate the beyond-dipole effects, being the theme of this study.

4 Taylor versus Rayleigh Plane-wave Expansion

As experimentalists explore new opportunities in strong-field physics offered by current generation light sources, new theoretical tools become inevitable in dealing with the challenging strong-field non-linear dynamics. In this chapter, the Rayleigh plane-wave multipole expansion series which offers a viable alternative to the conventional Taylor expansion of the spatial phase retardation term $e^{i\mathbf{k}\cdot\mathbf{r}}$ is tested. A reasonable comparison of the expansions of the retardation term, $e^{i\mathbf{k}\cdot\mathbf{r}}$ between the Rayleigh and Taylor plane-wave multipole expansion methods is made. This is done by first approximating the real and the imaginary components of the exponential function with the angle between the radial vector and the direction of propagation chosen to be 45°. The second level of comparison involves the use of the various approximation orders in the numerical solution of the TDSE. The other goal of this chapter is to give insights into the most optimal method of solving the TDSE beyond the dipole approximation whose validity is questionable in the strong-field regime.

It is verified that the Rayleigh plane wave multipole expansion, employing the regular spherical Bessel functions as the radial functions of the partial waves, provides a larger validity range in comparison to the widely used Taylor multipole expansion. It is also noted that the Taylor expansion of the plane wave up to a given order reproduces the lower kr limits of the Rayleigh expansion series, but deviates strongly in the asymptotic regime. It can be concluded that the use of the Rayleigh plane-wave expansion provides the most accurate contribution of any given order of the plane-wave multipole transitions. Some discrepancy in the dipole and non-dipole photoelectron energy spectra as predicted by the Taylor and the Rayleigh approximations is shown using intense short wavelength laser pulses interacting with hydrogen atom in its ground state. The discrepancy arises from the higher-order multipole terms which are absent in the finite order Taylor expansion series.

Most strong field theoretical studies have been concentrated on the spatially independent dipole approximation to predict the interaction dynamics between matter and radiation fields. However, there have been some previous efforts to incorporate the non-dipole effects [12, 13, 87–93, 95, 96, 99, 100, 124] in the interaction dynamics. The results of the work done incorporating the non-dipole effects have already predicted certain effects like total breakdown of the dipole approximation for hard x-rays [88, 89], new structures in the photoelectron angular distribution, and a distortion of the dipole photoelectron energy spectra for the XUV and soft x-ray wavelengths with intensities greater than unity (in atomic units) [90, 92], a small distortion of the dipolar angular distribution for very small wavelengths and intensities of ~ 1 a.u. [93], and even a breakdown of stabilization for intense high frequency laser pulses[13]. From a theoretical point of view, the contribution of the non-dipole effects arising from the $\mathbf{A}^2$ term relative to the $\mathbf{A} \cdot \mathbf{p}$ term in the strong-field regime has been a subject of contradicting viewpoints [90–93, 95, 96, 124].

Although diverse theoretical approaches have been used to analyze these strong-field effects, one of the ingredients that has apparently been employed in common is the use of the Taylor approximation of the spatial phase retardation term, $e^{i\mathbf{k}\cdot\mathbf{r}}$, to include the non-dipole effects[18]. But in the plane-wave description of electromagnetic radiation, despite being usual, it is not necessary to expand the electric field in a Taylor series [125]. The expansion of electromagnetic plane waves in terms of Bessel functions and spherical harmonics dates back to theoretical works of the 1930s [126, 127] and this expansion in twisted beams allows a very direct connection to be made between the angular momentum of the photon and the terms of the expansion. The multipole expansion of the plane wave spatial phase retardation term as a function of the spherical Bessel functions and spherical harmonics in itself is credited to the very old works of Lord Rayleigh.

In this chapter, as already briefly introduced, the expansion of the plane-wave spatial phase retardation term using the Rayleigh approximation series employing the regular spherical Bessel functions (SBA) [103] and using the Taylor series approximations (TA) is done. The strategy involves rewriting the Taylor expanded terms of the retardation as a function of the Legendre polynomials. From the coefficients of these Legendre polynomials, unique analytical functions which are correlated with each of the regular spherical Bessel functions $j_l(x)$ are obtained. These unique analytical functions are referenced as the Taylor approximated spherical Bessel functions, $\tilde{j}_l(x)$. The Taylor-approximated spherical Bessel functions are then used alongside the regular spherical Bessel functions to model the retardation term. The effects of the two alternative expansion methods in the photoelectron energy (PE) spectrum of a strongly-driven hydrogen atom are further analyzed. The interactions are considered up to the hexadecapole terms of the interaction Hamiltonian, that is, from the 0^{th} order up to the 3^{rd} order terms in the nomenclature of Taylor multipole expansion of the plane-wave phase retardation term. A comparison is then made between the Taylor-plane wave multipole expansion series and their corresponding orders of interaction in the Rayleigh plane-wave multipole expansion series. In this section, only the $\mathbf{A} \cdot \mathbf{p}$ terms of the interaction Hamiltonian is focussed on. A comprehensive treatment of the non-dipole interaction terms including the effects of both the $\mathbf{A} \cdot \mathbf{p}$ and $\mathbf{A} \cdot \mathbf{A}$ induced transitions is considered in the subsequent sections.

4.1 Taylor-approximated Spherical Bessel Functions

The non-relativistic dynamics of atoms interacting with a classical electromagnetic field is governed by the time-dependent Schrödinger equation

$$i\frac{\partial \Psi(\mathbf{r},t)}{\partial t} = [\mathrm{H}_0 + \mathrm{V}(t)]\Psi(\mathbf{r},t) \tag{4.1}$$

where H_0 is the unperturbed Hamiltonian corresponding to the field-free atom, $\mathrm{V}(t)$ is the radiation-gauge interaction potential expressed in terms of the momentum operator $\mathbf{p}$ and the vector potential $\mathbf{A}(\mathbf{r}, t)$ as

$$\mathrm{V}(t) = -q\mathbf{A} \cdot \mathbf{p} + \frac{1}{2}q^2\mathbf{A}^2 \tag{4.2}$$

The vector potential $\mathbf{A}(\mathbf{r}, t)$ satisfies the Coulomb-gauge condition, $\nabla \cdot \mathbf{A} = 0$. In all the cases discussed in this work, a linearly polarised pulse is considered with the vector potential

$$\mathbf{A}(\mathbf{r}, t) \approx A_0\, f(t) \sin(\mathbf{k} \cdot \mathbf{r} - \omega t + \delta)\, \hat{z} \tag{4.3}$$

in the $+z$ direction and the wave vector $\mathbf{k}$ oriented in the $+x$ direction. Here, $A_0 = E_0/\omega$ is the amplitude of the vector potential, E_0 is the peak electric field strength, ω defines the laser frequency, $f(t)$ describes the laser pulse carrier envelope with δ as the carrier envelope phase shift. The spatial dependence of the carrier envelope function $f(t)$ is assumed to be ignorable for the sake of mathematical convenience. The envelope itself may be chosen as a $\cos^2$, Gaussian, or any other pulse-shape. The $\cos^2$ pulse shape is used entirely in this study, although the other pulse-shapes implementations also exist in the code. The $\cos^2$ pulse is periodic and only non-zero when the time t is enclosed within the set $(0, \tau)$ with $\tau = (2\pi N/\omega)$ as the total pulse duration for a laser pulse containing N cycles. This expression for the vector potential can be expanded as

$$\mathbf{A}(\mathbf{r}, t) \approx A_0\, f(t)\, [\sin(\mathbf{k} \cdot \mathbf{r}) \cos(\omega t) - \cos(\mathbf{k} \cdot \mathbf{r})\sin(\omega t)]\, \hat{z} \tag{4.4}$$

with the phase $\delta = 0$ chosen for the sake of convenience. The spatial components can then be expressed in terms of the spatial phase-retardation term $e^{i\mathbf{k}\cdot\mathbf{r}}$ and its conjugate as

$$\begin{aligned} \cos(\mathbf{k} \cdot \mathbf{r}) &= \frac{1}{2}[e^{i\mathbf{k}\cdot\mathbf{r}} + e^{-i\mathbf{k}\cdot\mathbf{r}}] \\ \sin(\mathbf{k} \cdot \mathbf{r}) &= \frac{1}{2i}[e^{i\mathbf{k}\cdot\mathbf{r}} - e^{-i\mathbf{k}\cdot\mathbf{r}}] \end{aligned} \tag{4.5}$$

The spatial phase retardation term can be expanded in Taylor series

$$e^{i\mathbf{k}\cdot\mathbf{r}} = 1 + (i\mathbf{k} \cdot \mathbf{r}) + \frac{(i\mathbf{k} \cdot \mathbf{r})^2}{2!} + \cdots + \frac{(i\mathbf{k} \cdot \mathbf{r})^l}{l!} \tag{4.6}$$

or equivalently in terms of the well known Rayleigh plane-wave multipole expansion using the regular spherical Bessel functions j_l and the spherical harmonics Y_l^m [19, 20]

$$e^{i\mathbf{k}\cdot\mathbf{r}} = 4\pi \sum_{l}^{\infty} \sum_{m=-l}^{+l} i^l\, j_l(kr)\, Y_l^{m*}(\hat{\mathbf{k}})\, Y_l^m(\hat{\mathbf{r}}) \tag{4.7}$$

with the order of the multipole expansion defined by $l = 0, 1, 2, 3, \cdots$ as the dipole, quadrupole, octupole, hexadecapole, and other higher order multipole terms in case of the Taylor series expansion. An equivalent representation of the plane-wave in the vector spherical harmonics also exists[126].

To compare the two expansions, we consider only the first six terms of the Taylor series expansion,

$$\begin{aligned} e^{i\mathbf{k}\cdot\mathbf{r}} &= 1 + ikr\cos\theta - \frac{k^2r^2\cos^2\theta}{2} - i\frac{k^3r^3\cos^3\theta}{6} \\ &+ \frac{k^4r^4\cos^4\theta}{24} + i\frac{k^5r^5\cos^5\theta}{120} \end{aligned} \tag{4.8}$$

and express them as a function of the Legendre polynomials $P_l(\cos\theta)$ of order l [128]

$$\begin{aligned} e^{i\mathbf{k}\cdot\mathbf{r}} =& P_0(\cos\theta) + ikrP_1(\cos\theta) \\ &- \frac{k^2r^2}{6}[P_0(\cos\theta) + 2P_2(\cos\theta)] \\ &- \frac{ik^3r^3}{30}[3P_1(\cos\theta) + 2P_3(\cos\theta)] \\ &+ \frac{k^4r^4}{24\times 35}[7P_0(\cos\theta) + 20P_2(\cos\theta) + 8P_4(\cos\theta)] \\ &+ \frac{ik^5r^5}{120\times 63}[27P_1(\cos\theta) + 28P_3(\cos\theta) + 8P_5(\cos\theta)] \end{aligned} \tag{4.9}$$

in order to take a similar form as equation (4.7) to allow for a direct comparison. By arranging the terms in the orders of the Legendre polynomials, the retardation term can then be written as

$$e^{i\mathbf{k}\cdot\mathbf{r}} = \sum_l i^l\, h_l(kr)\, P_l(\cos\theta) \tag{4.10}$$

where

$$h_l(kr) = \frac{(kr)^l}{a_l} - \frac{(kr)^{l+2}}{2a_l(2l+3)} + \frac{(kr)^{l+4}}{8a_l(2l+3)(2l+5)} + \cdots \tag{4.11}$$

is a polynomial in kr. The l-dependent term a_l is defined recursively by the relation $a_{l+1} = (2l+1)\,a_l$, with $a_0 = 1$ being the first term. Using these functions, the corresponding Taylor-approximated spherical Bessel functions $\tilde{j}_l(kr)$ can then be constructed using the partial-wave decomposition

$$\tilde{j}_l(kr) = \frac{1}{2l+1}\, h_l(kr) \tag{4.12}$$

The function a_l can be shown to be equal to $(2l-1)!!$. If substituted in the equation (4.12), one obtains the well known power series expansion of the regular spherical Bessel functions [109, 110]

$$\lim_{n_{max}\to\infty} \tilde{j}_l^{(l_{max})}(kr) = (kr)^l \sum_{n=0}^{n_{max}} \frac{(-1)^n\,(kr)^{2n}}{2^n\, n!\,(2n+2l+1)!!} \tag{4.13}$$

where the integer n is a summation index, l denotes the order of the spherical Bessel functions, and n_{max} is the maximum value of the summation index. If only a finite number of terms are used in the series, then the value of n_{max} depends on the maximum order l_{max} of the multipole expansion in equation (4.6). The Taylor approximated functions $\tilde{j}_l^{(l_{max})}(kr)$ can then be used to express the retardation term $e^{i\mathbf{k}\cdot\mathbf{r}}$ in three dimensions using spherical harmonics expansion as

$$e^{i\mathbf{k}\cdot\mathbf{r}} \approx 4\pi \sum_{l}^{\infty} \sum_{m=-l}^{+l} i^l\, \tilde{j}_l^{(l_{max})}(kr) Y_l^{m*}(\hat{\mathbf{k}})\, Y_l^m(\hat{\mathbf{r}}) \tag{4.14}$$

having made use of the known

$$\sum_{m=-l}^{+l} Y_l^{m*}(\hat{\mathbf{k}}) Y_l^m(\hat{\mathbf{r}}) = \frac{(2l+1)\mathrm{P}_l(\cos(\theta))}{4\pi} \tag{4.15}$$

spherical harmonics [20] relation in equation (4.10) with θ being the angle between the vectors $\mathbf{k}$ and $\mathbf{r}$ and P_l as the l^{th} order Legendre polynomial, This expansion is similar to the Rayleigh plane-wave multipole expansion using the regular spherical Bessel functions $j_l(kr)$ in equation (4.7) but different in the corresponding Taylor-approximated spherical Bessel functions $\tilde{j}_l^{(l_{max})}(kr)$. It may be of importance to note that the regular spherical Bessel functions $j_l(kr)$ are related to the ordinary Bessel functions of the first kind $J_m(kr)$ [103] by

$$j_l(kr) = \sqrt{\frac{\pi}{2kr}}\, J_{l+\frac{1}{2}}(kr) \tag{4.16}$$

with $m = l + 1/2$ as the order of the ordinary Bessel function.

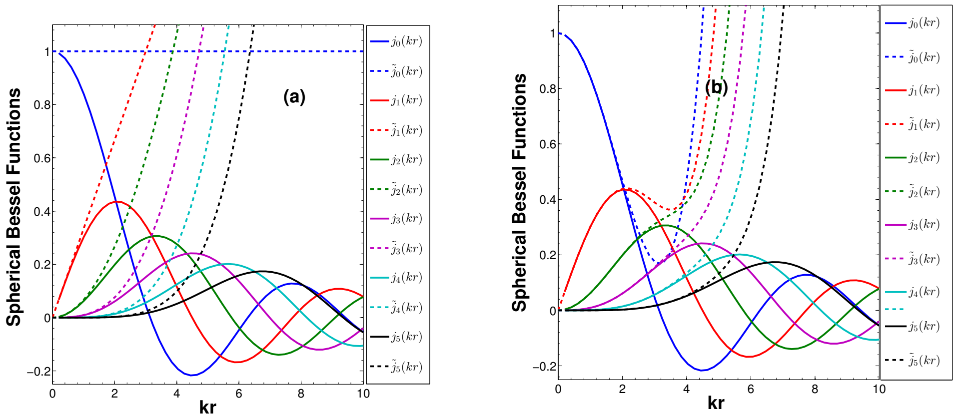

Figure 4.1: Taylor approximated Bessel functions $\tilde{j}_l^{(l_{max})}(kr)$ (broken lines) in comparison with the spherical Bessel functions $j_l(kr)$ (solid lines). Blue are 0^{th} order, red are 1^{st} order, green are 2^{nd} order, violet are 3^{rd} order, cyan are the 4^{th} order, and black are the 5^{th} order. The Taylor approximated spherical Bessel functions $\tilde{j}_l^{(l_{max})}(kr)$ are constructed from the (a) $n_{max} = 0$ and (b) $n_{max} = 2$ degrees of approximation of the $h_l(kr)$ functions.

In making a useful comparison between the two different approaches in simulating nonlinear dynamics, one can start by comparing directly the correlation between $j_l(kr)$ and $\tilde{j}_l^{(l_{max})}(kr)$, and then subsequently compare the components of the spatial retardation term by evaluating the trigonometric ratios $\cos(\mathbf{k}\cdot\mathbf{r})$ and $\sin(\mathbf{k}\cdot\mathbf{r})$ as

$$\begin{aligned} \cos(\mathbf{k}\cdot\mathbf{r}) &= \sum_{l=0,2,\cdots,even} i^l\, j_l'(kr)\,(2l+1)\mathrm{P}_l(\cos(\theta)) \\ \sin(\mathbf{k}\cdot\mathbf{r}) &= \sum_{l=1,3,\cdots,odd} i^{l-1}\, j_l'(kr)\,(2l+1)\mathrm{P}_l(\cos(\theta)) \end{aligned} \tag{4.17}$$

with $j_l' = j_l$ for the regular spherical Bessel functions and $j_l' = \tilde{j}_l^{(l_{max})}$ for the n_{max}^{th} degree of the Taylor-approximated spherical Bessel functions.

4.2 Approximation of the Spatial Retardation Terms

Figure 4.1 is a plot of the graphs of the first six of the Taylor-approximated spherical Bessel functions, $\tilde{j}_l^{(l_{max})}(kr)$, defined in equation (4.14), and their corresponding regular spherical Bessel functions $j_l(kr)$. The difference between the two figures is that in figure 4.1 (a) the summation in equation(4.13) is truncated after the first term ($n_{max} = 0$) while in figure 4.1 (b), the summation is truncated after three terms ($n_{max} = 2$) . While both spherical Bessel functions are in excellent agreement in the limit $kr \to 0$, certain key differences exist. First, it can be seen that the regular spherical Bessel functions are in general convergent towards a zero value as $kr \to \infty$ whereas the functions $\tilde{j}_l^{(l_{max})}(kr)$ are divergent beyond a certain critical point in kr. This could already be an indication of a possible breakdown in the Taylor approximation [129] of any given order beyond that critical point in kr. Second, the Taylor-approximated spherical Bessel functions approach the limit defined by regular spherical Bessels of comparable order as the degree (n_{max}) of the approximation is increased. This basically means that when more higher-order terms are used in the Taylor expansion, the agreement between the two approximations become better and the validity regime of the Taylor approximation increases.

Figure 4.2 and 4.3 show the approximation of $\cos(\mathbf{k}\cdot\mathbf{r})$ and $\sin(\mathbf{k}\cdot\mathbf{r})$ respectively using the regular spherical Bessel functions in comparison to those constructed from the Taylor approximated spherical Bessel functions of up to (a) $n_{max} = 0$ degree and (b) $n_{max} = 2$ degree of the expansion in equation (4.13). The angle between the vectors $\mathbf{k}$ and $\mathbf{r}$ was arbitrarily chosen and here only the case where the angle is $\pi/4$ radians are reported. In the figure legends the functions

$$\begin{aligned} \mathrm{SBA}_N(kr) &= \sum_{l=\text{even, odd, or both}}^{N\le l_{max}} i^{l'}\,\alpha_l(r,t)\,j_l(kr)\,(2l+1)\,\mathrm{P}_l(\cos(\theta)) \\ \mathrm{TA}_N^{(l_{max})}(kr) &= \sum_{l=\text{even, odd, or both}}^{N\le l_{max}} i^{l'}\,\alpha_l(r,t)\,\tilde{j}_l^{(l_{max})}(kr)\,(2l+1)\,\mathrm{P}_l(\cos(\theta)) \end{aligned} \tag{4.18}$$

are used to denote the order of approximation of the trigonometric ratios according to equation (4.17), as well as the ionization probability distributions, and to distinguish between the use of the regular spherical Bessel functions in Rayleigh (SBA) and the Taylor approximated spherical Bessel functions in Taylor approximation (TA) series respectively. In the approximation of $\cos(\mathbf{k}\cdot\mathbf{r})$ only even terms are added with $l' = l$, while for $\sin(\mathbf{k}\cdot\mathbf{r})$ only odd terms are in the summation with $l' = l - 1$. Both even and odd terms are used in the ionization probabilities calculations. The integer N defines the upper limit in the summation and it is related to the order of spherical Bessel functions used in the approximation by $l \leq N$. In the example cases discussed in this chapter, TA_N and SBA_N also specify the inclusion of matrix element evaluated up to a particular order and in this case all the contributions, regardless of even or odd, would be part of this sum. The value of the factor α_l in equation (4.18) is unity when approximating the trigonometric functions but for the ionization probabilities, it is determined by the laser as well as the system parameters making it quite complex. The degree n_{max} of the Taylor approximated spherical Bessel functions $(\tilde{j}_l^{(l_{max})})$ refers to the number of terms included in the Taylor approximated series of the spherical Bessel function of order l and it is defined in terms of the maximum order l_{max} by $n_{max} = \mathrm{tr}\{(l_{max} - l)/2\}$ with n_{max} taking only truncated integral values. In the Taylor approximated spherical Bessel functions, the degree varies with l and l_{max} as already shown in the relation.

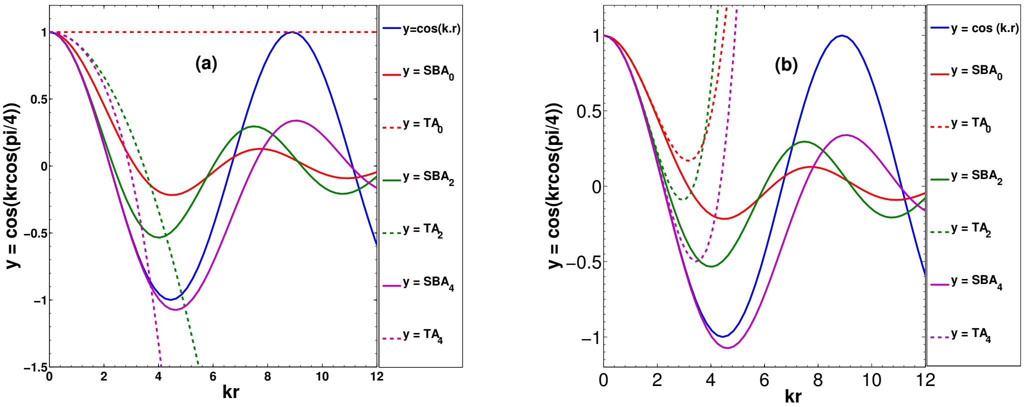

Figure 4.2: The approximation of the function $y = \cos(\mathbf{k}\cdot\mathbf{r})$ for the first six orders of the multipole expansion using the Taylor-approximated spherical Bessel functions in TA_N and the regular spherical Bessel functions expansion in SBA_N. Blue curve is the correct cosine function, while red, green, and violet are the 0^{th}, 2^{nd}, and 4^{th} multipole-order approximations, respectively. The solid lines are the regular spherical Bessel function approximation while broken lines are the corresponding Taylor approximated spherical Bessel functions, with $n_{max} = 0$ degree is used in (a) and $n_{max} = 2$ degree in (b) respectively.

From figures 4.2 and 4.3, it can also be seen that both Taylor and Rayleigh approximations of the trigonometric functions agree in the limit $kr \to 0$ and lower orders of the multipole expansion are sufficient for convergence in that regime. At large kr, the Rayleigh expansion series, using the regular spherical Bessel functions, seem to be a better approximation for the trigonometric functions. The Taylor approximation would match the Rayleigh approximation only when higher degrees (n_{max}) is used.

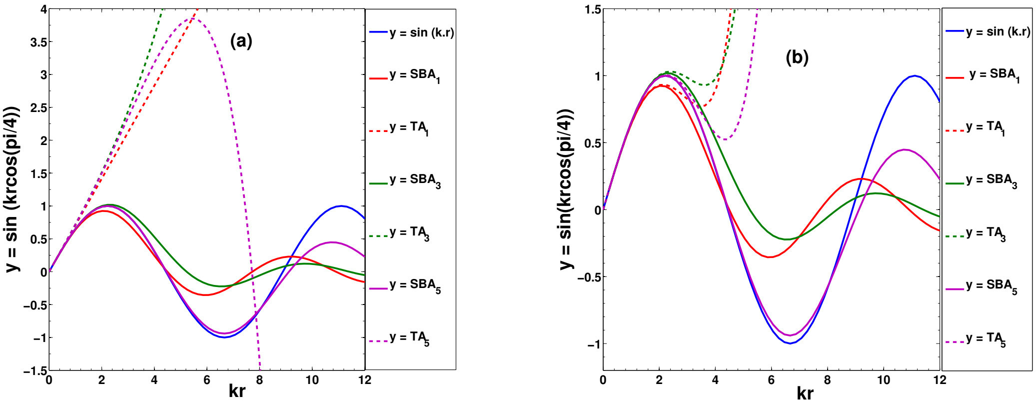

Figure 4.3: Same as figure 3 but for the function $y = \sin(\mathbf{k} \cdot \mathbf{r})$ with blue curve as the correct sine function and red, green, and violet as the 1^{st}, 3^{rd}, and 5^{th} multipole-order approximations respectively.

This confirms further that the validity regime of the Taylor approximation increases with the order of the summation and in the infinite limit, it can only match the corresponding orders of the regular spherical Bessel functions. In figure 4.4, the stringent validity condition, $\cos^2(\mathbf{k} \cdot \mathbf{r}) + \sin^2(\mathbf{k} \cdot \mathbf{r}) = 1$, that needs to be satisfied by the various orders of the approximations, is plotted. The condition helps to visualize the range of validity of the various orders of the approximation. The inclusion of higher order terms in both expansions series, as is expected, improves the satisfaction of the validity condition leading to a better approximation of the retardation.

On a one-to-one comparison, it is evident from figure 4.4 that both series approximation of the plane-wave yield comparable validity range for lower orders of the multipole expansion. At higher orders, the Rayleigh series performs better in comparison to the Taylor series approximation of the same order. At multipole orders $l \leq 1$, the gain in the efficiency of the Rayleigh series seems not to be significant but from the 2^{nd} multipole order onwards, the gain is obvious. As kr increases, both fail with the Rayleigh series under-approximating the functions whereas the Taylor series over-approximating. It can also be seen that the Taylor series are likely to break down at some point. In cases of such breakdown, their use would cause numerical convergence issues resulting in very long durations of computation. It is important to note that even though the usual dipole approximation where $\cos(\mathbf{k} \cdot \mathbf{r})$ is approximated by unity is quite basic, it satisfies fully the validity condition. This makes it quite stable against any breakdown in comparison to other orders of the Taylor approximation although its inherent inaccuracies remain embedded in the photoelectron energy spectrum or the photoelectron angular distribution. The critical point at which the higher order Taylor expansion series are likely to break down is expected to be conspicously manifested in the photoelectron energy resolved probability distribution. The breakdown of such perturbative methods is well known and has been discussed in non-linear dynamics [129].

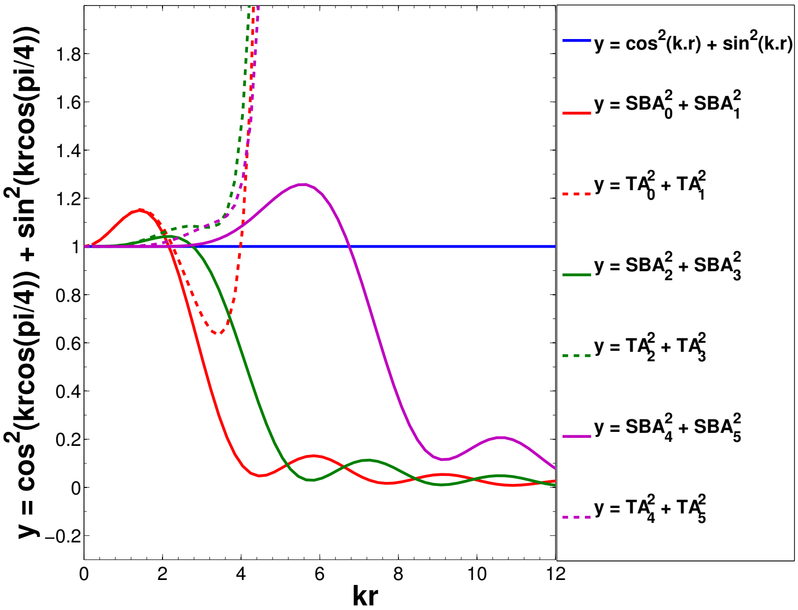

Figure 4.4: Validity constraint function $y = \cos^2(\mathbf{k}\cdot\mathbf{r}) + \sin^2(\mathbf{k}\cdot\mathbf{r})$. $n_{max} = 2$ degree Taylor-approximated spherical Bessel functions are used. Blue is the correct condition while red, green, and violet give the 1^{st}, 3^{rd}, and 5^{th} multipole order approximations respectively.

In a real calculation, the box radius r_{max} together with the radiation wavelength λ can be used to approximate the multipole order required for the results to be valid. As a rule of thumb, it is always required that the radius of the box be at least three times the radiation wavelength to avoid spurious reflections [14]. This therefore means that the product $2\pi\, r_{max}/\lambda$ can be used to estimate the required number of multipole orders using figure 4.4 for better convergence of the calculated observables. However, the convergence usually depends on many other parameters, like intensity of the radiation, and therefore the appropriate multipole orders should also be checked separately by convergence tests.

4.3 Multipole $\mathbf{A}\cdot\mathbf{p}$ Interactions Photoelectron Spectra

In this section, a comparison is made between the Raleigh and the Taylor series expansions in a strong-field calculation of the multiphoton above threshold ionization of a hydrogen atom initially in its ground state irradiated by super-intense free-electron x-ray laser fields. A radiation wavelength of 9.11 nm and the field intensity of 50 a.u. consistent with the parameters of reference [92] is chosen. In the calculations, the first four orders ($N = 3$) of the multipole expansion in $\mathbf{A}\cdot\mathbf{p}$ transitions only is implemented using both Taylor and Rayleigh plane-wave expansion series. The goal was to clearly see the disparity, arising from the different approaches, in the multipole photoelectron energy spectra without incorporating too many interactions and also to compare the computational advantages between them.

Figure 4.5 shows the photoelectron energy spectrum evaluated using both the Rayleigh and the Taylor multipole expansions for transitions from 0^{th} order of up to the 3^{rd} order interactions in the $\mathbf{A}\cdot\mathbf{p}$ transition matrix elements as defined in equations (4.2) and (4.18). In the calculations, a peak electric field strength of 50 a.u. and a pulse duration of 10 optical cycles is considered. The numerical parameters include: $L_{max} = M_{max} = 5$, Box radius = 200 a.u., B splines = 600, velocity gauge, cut-off energy = 20 a.u., tolerance $= 10^{-10}$, and a fully implicit time propagation scheme. In evaluating the transition matrix elements for this figure, the Taylor expansion of the first four terms of the plane wave retardation term from which the Taylor approximated spherical Bessel functions $\tilde{j}_0^{(3)}(kr)$, $\tilde{j}_1^{(3)}(kr)$, $\tilde{j}_2^{(3)}(kr)$, and $\tilde{j}_3^{(3)}(kr)$ in equation (4.13) is derived, and from which the N^{th} order Taylor-approximated ($\text{TA}_N^{(l_{max})}$) spectra as expressed in equation (4.18) are drawn. These are then compared with the corresponding orders of the Rayleigh multipole (SBA_N) expansion.

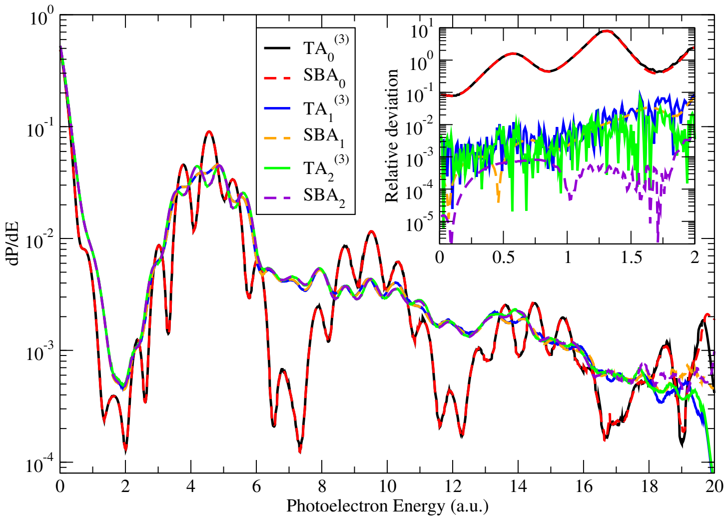

Figure 4.5: Photoelectron energy spectrum of multiphoton ionization of a hydrogen atom using a 9.11 nm radiation field with a peak electric field amplitude of $E_0 = 50$ a.u. corresponding to an intensity of 8.77×10^{19} Wcm^{-2} and the Reiss intensity scaling parameter $z = 4.9956$. Solid lines correspond to the Taylor ($\text{TA}_N^{(l_{max})}$) series: $\text{TA}_0^{(3)}$ (black), $\text{TA}_1^{(3)}$ (blue), and $\text{TA}_2^{(3)}$ (dark green). Broken lines correspond to the Rayleigh (SBA_N) series : SBA_0 (red), SBA_1 (orange), and SBA_2 (violet). Inset: The relative deviation with respect to the preceding lower multipole-order.

Beginning with the $N = 0$ order spectra, one sees clearly distinct multiphoton ATI peak structure. The position of the peak corresponds to the number of photons absorbed with the first multiphoton located at about 5 a.u. The separation between the multiphoton peaks is equivalent to a single-photon energy. The low-energy structure (LES) below the 2 a.u. is a peak whose origin can be attributed to either tunnelling, over-the-barrier tunnelling, or to a two-photon resonant Compton scattering process in which one photon is absorbed by a Stark-shifted eigenstate followed by a one-photon emission process. It therefore does not correspond to any of the multiphoton peaks. Since the LES is enhanced by the peak electric field strength, the over-the-barrier tunnelling effect seems to be a more appropriate explanation for the near-threshold peak. The higher multipole-orders ($N > 0$) can be seen to introduce a destructive interference to the observed ATI peak structure with more significant effects at higher photoelectron energies. The distortion of the ATI structures are similar to the observations in the literature data [92] although they evaluated the TDSE in momentum-space where as position-space is used in this work.

It is evident that for the photoelectron energy window specified in figure 4.5, the second-order multipole terms (TA_2 and SBA_2) are already sufficient for perfect convergence. The comparison between $\mathrm{TA}_N^{(l_{max})}$ and SBA_N spectra can be seen to be very good for the chosen level of Taylor expansion. However, when $l_{max} < 3$ is used as the maximum order of the Taylor expansion (figure not shown for the sake of clarity), it is realized that the agreement between the two approaches for the same laser and numerical parameters is not very good except for the dipole approximation. This means that higher orders of the Taylor expansion are necessary to obtain a very good agreement with the Rayleigh plane-wave multipole expansion as already shown in the mathematical analysis in section 4.1. The caption in figure 4.5 includes the Reiss intensity scaling parameter which shows the ratio of the ponderomotive energy to the photon energy and as a consequence, it measures the degree of applicability of the perturbation theory.

In general, it can be observed that non-dipole corrections may provide significant disparities in the spectra depending on the method of expanding the retardation term. The effect of including the 1^{st} and the 2^{nd} order $\mathbf{A}\cdot\mathbf{p}$ multipole terms as corrections to the leading 0^{th} order term already shows some significant modification of the ATI structures. The side bands are apparently levelled out, the valleys disappear, and the multiphoton peaks flattened by this partial inclusion of non-dipole effects. In the photoelectron energy spectrum, it is observed that tiny higher multipole-order effects also manifest slightly at very low photoelectron energies. As photoelectron energies increase, the disparity in the spectra between various multipole-orders become more pronounced necessitating the need for higher-order corrections to obtain convergence. The dominant non-dipole effects can be attributed to the quadrupole transitions and the higher multipole-order terms above the quadrupole only produce tiny modifications to the quadrupole effects. This is further confirmed in figure 4.7 (left) showing relative deviations of the total ionization yield from the lowest-order spectra with the biggest deviation emanating from the 1^{st} order correction.

The non-dipole effects are spread in the entire photoelectron energy spectrum and the magnitude of these effects is observed to increase generally with the photoelectron energy. The discrepancy between the methods of expanding the retardation is also clearly visible. The objective of introducing the octupole and hexadecapole transitions was to actually test convergence between the spectra by increasing the order of the multipole expansion within the photoelectron energy regime displayed in figure 4.5. A nearly perfect convergence between the TA_N and SBA_N expansions only in the $N = 3$ multipole-order approximation but the relative deviations in the differential ionization probability shown in the inset of figure 4.5 and in the total ionization probability from the zero order spectra shown in figure 4.7 (left) suggests that there always exist a tiny deviation between the corresponding TA_N and SBA_N orders in the total ionization yield. The relative deviation was obtained by dividing the absolute difference between two successive orders of the multipole yields by the lower order yield. This discrepancy in the relative deviation accounts for the contributions of the higher multipole-order terms which are not present in the corresponding Taylor expansion.

Figure 4.6 shows a similar comparison of the photoelectron spectrum at a much shorter wavelength of 0.3 nm. The spectrum shows a series of side bands, which are signatures of the dynamic Stark effect [130, 131], and three multi-photon resonance peaks are also visible. The figure was generated using similar basis-set parameters as in figure 4.5 except that the number of B splines were increased to 5000 (for the left figure) in order to reproduce reliable probabilities at higher photoelectron energies up to the specified range. The inset in figure 4.6 (left) focusses on the lower energy regime where the non-dipole effects are apparent. This regime is probed further in figure 4.6 (right) by considering two additional multipole-orders and zooming into the differences as presented in the inset.

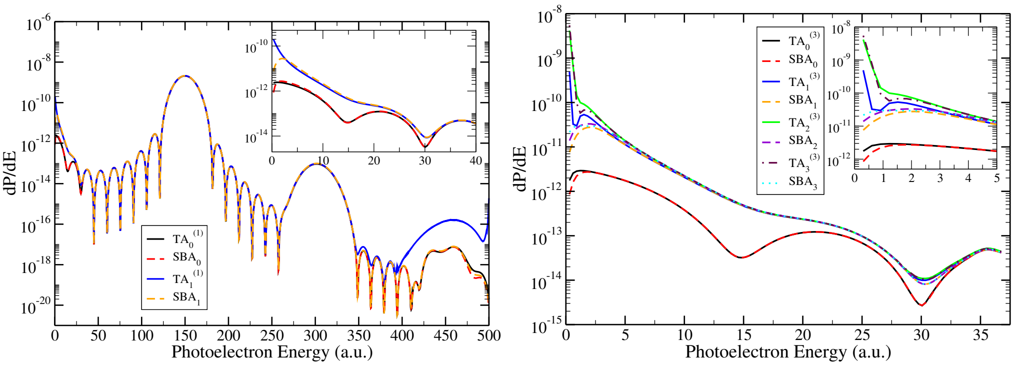

Figure 4.6: Left: Same as figure 4.5 but for a 0.3 nm wavelength and Reiss intensity scaling parameter $z = 1.784 \times 10^{-4}$. Inset: Lower photoelectron energy regime showing some dicrepancy between the $\text{TA}_N^{(1)}$ and SBA_N approximations and the manifestation of first-order correction effects. Right: Zoom into the inset in the left figure and including the effect of higher multipole-orders up to the order $\text{TA}_3^{(3)}$ (cyan) and SBA_3 (light green).

The discrepancy between the TA_N and SBA_N spectra are more pronounced for the lowest-order corrections and also at lower photoelectron energies for this wavelength. The deviations from the dominant 0^{th} order (TA_0 and SBA_0) terms manifesting at the lower photoelectron energies are supported by both approaches even though the estimated magnitude differs. At highest photoelectron energies, there appears to be some slight spatial effect in SBA_1 prediction but the TA_1 predicted non-dipole effect is quite huge. Considering that the Rayleigh plane-wave multipole expansion series give the expected contribution from a mathematical perspective, one can argue that the non-dipole structure observed at the higher end of photoelectron energies when Taylor expansion is used seems to be more of an artefact. This reasoning is quite logical based on the fact that Taylor expansion is valid only when $2\pi r/\lambda \ll 1$. For 0.3 nm, $2\pi r/\lambda \sim 1$ which definitely does not satisfy the validity requirement. This potentially suggests that the Taylor approximation breaks down at this wavelength and its use may yield unreliable results. The inset of figure 4.6 (left) zooms into the low-energy window showing some non-dipole effects. The energy range shown is within the single-photon ionization regime. The deviation between the TA_N and SBA_N expansions is probed further by considering the contribution of higher multipole-order terms in the lower photoelectron energy regime where the difference is larger.

Figure 4.6 (right) shows the spectra evaluated up to the 3^{rd} multipole-order for the energy regimes shown in the inset of figure 4.6 (left). Although the intensity and wavelength of the radiation used can qualify the interactions to be classified under the dipole oasis [132] by the scaling laws, it is surprising that the effects of the additional higher multipole-order terms are quite significant in the lower photoelectron energy regime displayed. In the figure, the discrepancy between TA_N and SBA_N at very low photoelectron energies persists despite the involvement of many orders of the multipole expansion. This shows that several higher multipole-order terms may make a significant contribution in the near-threshold photoelectron energy regime, and many more of the higher-order terms are necessary for perfect agreement between the Taylor and the Rayleigh series approximated spectra. In figure 4.6 (right), a small bending in the TA_0 and $\mathrm{TA}_1^{(3)}$ spectra in the near-threshold region is noticeable because of the Taylor approximated spherical Bessel function ($\tilde{j}_0^{(3)}$ and $\tilde{j}_1^{(3)}$) used incorporates the $n_{max} = 1$ degree correction. This makes the Taylor approximated spectra to be slightly like the regular spherical Bessel functions generated spectra in the Rayleigh plane-wave multipole series expansion.

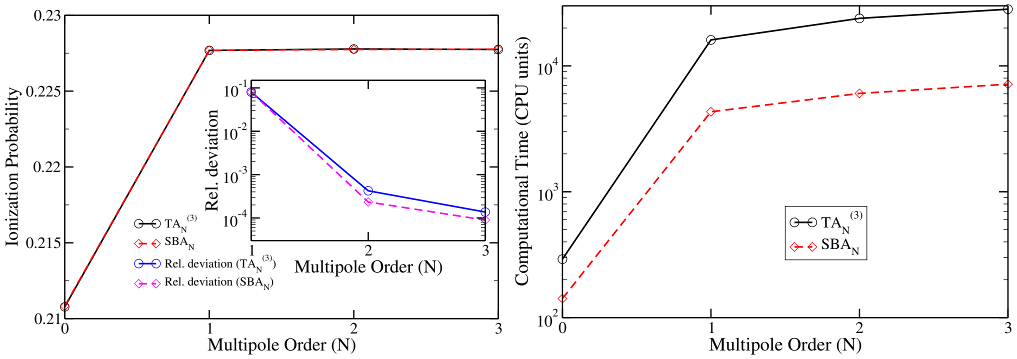

Figure 4.7: Left: Total ionization probability and relative deviation (inset) of the ionization yield with respect to the lowest-order terms. Right: Computational run-time as a function of the multipole order of the retardation expansions in Taylor or in spherical Bessel function series. The numerical and laser parameters are similar to those used in figure 4.5 (right).

From the observations, there appears to be some numerical gain with the use of the Rayleigh plane-wave expansion series as compared to the Taylor series not only in accuracy but also in terms of the computational run-time for the time propagation. The computation run time of 9.11 nm wavelength laser pulse interaction calculated for up to N^{th} order approximation in Taylor and spherical Bessel functions respectively consistent with the numerical parameters used in the calculations of figure 4.5 is illustrated in figure 4.7 (right). In the beyond-the-dipole approximation, the computational run-time shows a logarithmic time dependence as the multipole-orders increase. It can be seen that the SBA_N calculations are more efficient in time. The gain in time when SBA_N is used is observed to be even more significant for shorter wavelengths ($\sim$ 0.3 nm and below) at higher radiation intensities.

From the mathematical relationship between the Taylor and the Rayleigh expansions of the spatial retardation term shown in this chapter, one can conclude that the Rayleigh plane-wave multipole expansion provides the ideal contribution of any given order of the multipole terms of the interaction Hamiltonian. In the example calculations of the ionization probability distributions, it has been shown that the 0^{th} multipole-order terms of the interaction compare very well in both Taylor and Rayleigh expansion series. That essentially means that the dipole approximation would be justified when the importance of the non-dipole corrections is not necessary. When non-dipole effects are of interest, the discrepancy manifesting between the TA_N and SBA_N expansions show that both have slight differences in accuracy for the corresponding orders when used in the evaluation of quantum observables. For the cases considered in this study, the discrepancy between the two expansion methods accounts for the role of higher multipole-order terms which are not present in the Taylor expansion.

For very short wavelengths and very low photoelectron energies, the structure of the photoelectron distibution spectrum varies slightly depending on the method of expansion employed signifying that the inclusion of many higher-order non-dipole effects may be crucial to predict correctly the photoelectron spectrum in the lower-energy regime for extremely short wavelengths. It may be important to note that the validity condition of Taylor approximations requiring the correction terms to be of the order $2\pi r/\lambda \ll 1$ fails in the very short wavelength domain. This could explain the reason why the Taylor corrections are badly behaved in the case of 0.3 nm shown in figure 4.6 as compared to the case of 9.11 nm shown in figure 4.5. Using the Rayleigh plane-wave multipole series expansion is observed to be practically more efficient in terms of the computational time and the accuracy desired for any given multipole-order of the interaction, with the assumption that the other numerical convergence parameters are sufficient.

Chapter Summary

In summary, the multipole expansion of the spatial retardation term $e^{i\mathbf{k}\cdot\mathbf{r}}$ is compared using both Taylor and Rayleigh plane-wave expansion series approximations in this chapter. The Rayleigh plane-wave expansion series, which make use of the regular spherical Bessel functions, are found to a better approximation of the spatial retardation term than the Taylor series when a finite number of multipole orders is considered. Moreover, the Taylor approximated spherical Bessel functions $\tilde{j}_l^{(l_{max})}(kr)$ are shown to converge to the regular spherical Bessel functions in the limit $kr \to 0$ although at large kr values there are larger deviations between the regular and the approximated spherical Bessel functions leading to a possible divergence between the two methods of approximating the plane-wave. Using a larger n_{max} in the summation series of the Taylor-approximated spherical Bessel functions $\tilde{j}_l^{(l_{max})}(kr)$ as defined in equation (4.13) reduce their disparity with the corresponding orders of the Rayleigh plane-wave expansion series.

5 Spatial Correlation Effects in the Lowest-order Interaction Potential Terms

The comparison between Taylor and Rayleigh plane-wave expansion in multipole-order terms is already discussed in chapter 4. In the lowest-order terms of the expansion, the Taylor expansion yields the conventional dipole approximation where the spatial dependence of the vector potential describing the interaction between the photon and the active electron in the system is lost. On the other hand, the Rayleigh expansion introduces the spatial variation of the vector potential even in the lowest-order term of the expansion. In this chapter, the effect of the spatial dependence of the lowest-order term of the vector potential in the Rayleigh plane-wave expansion is investigated. The dipole approximation is expected to be valid if the radiation intensity is low or if the radiation wavelength is longer.

The discussions in this chapter is supposed to be helpful as a preliminary check for the relativistic effects in the strong-field processes in an economical sense. The presence of the relativistic effects can also be a good indicator of the potential radiation pressure effects not testable by the lowest-order term of the plane-wave multipole expansion. The motivation for this chapter is based on the fact that the current generation light sources have made it possible to produce intense laser pulses with short duration and tunable wavelengths which characterise light-matter interactions to be in the strong-field regime. In the strong-field regimes, the validity of the dipole approximation is questionable. Also, the ponderomotive potential (U_p) associated with such strong-fields scales with intensity and wavelength making it comparable to or even dominant over the Coulombic interactions.

In the radiation gauge picture, the U_p shifts the ionization potential and energy levels of the system interacting with the radiation [61]. The length-gauge picture on the other hand explains the effect of the U_p in terms of the Stark shifts of the field-free states of a system dressed by the radiation field. The consideration of the U_p has led to a great success in the understanding of various strong-field features like tunneling ionization and multiphoton ionization [34], barrier-suppression ionization [2], channel closing [55, 133–135] in above threshold ionization (ATI) , atomic stabilization [78, 136], higher-order harmonic generation (HHG) [9, 81] in atomic and molecular physics, and the radiation pressure [85].

This study would therefore give some insight into the intensity limits at which non-dipole corrections may become important while utilizing the cylindrical symmetry applicable in the dipole approximation, in the cases where an atomic system interacts with a pulse which is linearly polarized in the z direction. It is indeed found that at higher strong-field intensities, beyond the perturbative regime, a photoelectron spectrum and ionization yields results without an explicit inclusion of a spatially resolved $\mathbf{A}\cdot\mathbf{p}$ and $\mathbf{A}^2$ interactions may not be valid. The cylindrical symmetry makes it possible for one to use a basis set resolved in n and l quantum numbers only leading to a better optimization of the computational resources. The possibility of extracting the spatial correlation effects due to intense long-wavelength radiation interactions where a full numerical solution of the multipole TDSE would be quite demanding, because of the large box radius requirements and the broken cylindrical symmetry, is an additional benefit derived from the lowest-order term of the Rayleigh plane-wave multipole-order expansion.

In the beyond-the-dipole approximation, the spatial corrections by the higher multipole-order terms with the dipole selection rules in the Taylor plane-wave expansion series may be introduced. These are the correction terms brought into play by the 0^{th} order term of the Rayleigh plane-wave expansion. These terms have an explicit spatial dependence and therefore the contribution of the $\mathbf{A}^2$ term can not be ignored on the basis of a phase transformation in this framework. The additional advantage offered by the Rayleigh plane-wave expansion is the ability to incorporate some of the effects of the higher-order correction terms using the cylindrical symmetry.

A 10-cycle 800 nm light pulse, usually generated by the Titanium-Sapphire laser source, with intensities ranging from 1.0×10^{13} Wcm^{-2} to 5.0×10^{16} Wcm^{-2} is used in the numerical calculations. The hydrogen atoms in their ground or $10f$ states have been selected as a system of choice as it presents a simple system where the influence of the electron correlation effects are absent. The interaction dynamics of the ground ($1s$) state and the $10f$ Rydberg states of the atom with intense linearly polarized laser pulses is considered particularly because of their relative differences in the ionization potential, and consequently their Keldysh adiabaticity parameters. These differences make the systems appealing to study since, for the same laser parameters, the two initial states may classify the interactions to correspond to different processes based on the Keldysh classification scheme. For example, at an intensity of 1.0×10^{14} Wcm^{-2} the interaction of the radiation with the ground state would be classified to be in the multiphoton regime while for the Rydberg state, it would be deep in the tunnelling or over-the-barrier ionization regime.

The relative contribution of the lowest-order spatial corrections have been analyzed in this chapter. The spatial effect on the $\mathbf{A}\cdot\mathbf{p}$ interaction is analyzed first and then the effect of the $\mathbf{A}^2$ term is considered next. The relative deviation is calculated with respect to the dipole approximation spectrum, that is, the absolute deviation from the dipole approximation yield divided by the dipole approximation yield. The numerical solution uses a spectral expansion method employing B splines with a mixed knot sequence, that is, a non-linear geometric sequence from 0 up to 40 a.u. and thereafter, a linear sequence. Reasonable convergence is obtained using a box radius $r_{\max}=2000$, 4000 B splines, a basis size of $L=50$, and a photoelectron cut-off energy of 3 a.u. for intensities up to $\sim 1.0\times10^{16}$ Wcm^{-2}. These convergence parameters, unless otherwise specified, are used for all the intensities considered in the calculations in this chapter.

5.1 Spatial Effect in the Lowest-Order $\mathrm{A} \cdot \mathrm{p}$ Interaction Term

Figure 5.1 shows a comparison of a photoelectron spectrum for the $\mathbf{A} \cdot \mathbf{p}$ interaction only generated using the lowest-order terms for the different intensities of a short Ti:Sa laser field. In this figure and throughout this chapter, SBA_0 refers to the 0^{th}-order terms in the Rayleigh plane-wave expansion series defined by the first two terms in equation (3.173) and TA_0 refers to the 0^{th}-order Taylor plane-wave expansion series defined as the first term of equation (3.172).

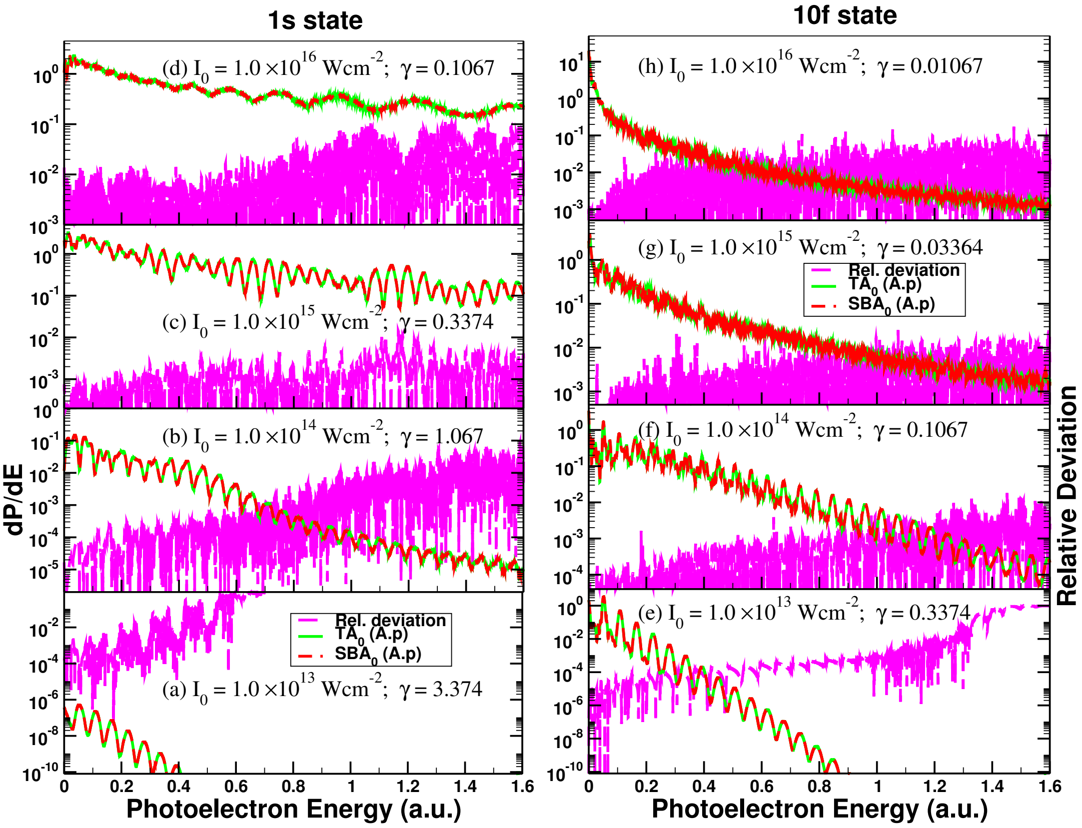

Figure 5.1: PE spectrum for a 10 cycle 800 nm wavelength multiphoton ionization of hydrogen atom in its (a-d) ground and (e-h) $10f$ state corresponding to the intensities 1.0×10^{13} Wcm^{-2}, 1.0×10^{14} Wcm^{-2}, 1.0×10^{15} Wcm^{-2},and 1.0×10^{16} Wcm^{-2}: SBA_0 ($\mathbf{A} \cdot \mathbf{p}$ only, Red dashed lines), TA_0 (the dipole approximation, green solid lines). The relative deviation of SBA_0 with respect to A_0 (magenta long dash lines) in equivalent units to the left vertical scale.

In this chapter, TA_0 is equivalent to the standard dipole approximation where the spatial retardation term is approximated by unity. On the other hand, the lowest-order Rayleigh plane-wave expansion using the spherical Bessel functions (SBA_0) gives the spatial modification to the dipole approximation. The respective Keldysh adiabaticity parameters γ which characterise the regime of various strong field processes by comparing the ponderomotive potential and the ionization potential are also specified in the figures.

The energy resolved differential probabilities of the two approaches as well as a relative deviation between them are shown. The SBA_0 results can be used as the absolute theoretical limit for the transitions with the dipole selection rules in the regions where the spectra is considered converged. The ATI structures are clearly separated in the $1s$ state up to an intensity of order $\sim 1.0 \times 10^{15}\,\mathrm{Wcm}^{-2}$. In the $10f$ state, the ATI structures are well resolved up to the intensities of order $\sim 1.0 \times 10^{14}\,\mathrm{Wcm}^{-2}$. For the Rydberg state, the differential probabilities decay like the static field ionization rates at intensities above $\sim 1.0 \times 10^{15}\,\mathrm{Wcm}^{-2}$.

Significant spatial corrections effects are observable in the spectra. The magnitude of the spatial effects increase with the radiation intensity, the photoelectron energy, and to some extent with a decrease in the ionization potential of the system. The relative deviations are highly oscillatory showing that the contributions seem to only modify the spectra in the regions where the dipole-approximation interactions are weak. The relative deviation on the $1s$ and the $10f$ states do not compare one-to-one, but comparable wiggles in the spectrum can be seen in figure 5.1 (d) and 5.1 (f), having the same Keldysh parameter but different intensities. A similar observation in the spectrum is also evident in figure 5.1 (c) and 5.1 (e). For the $1s$ state, the spatial effects become visible in the PE spectrum at the intensities of order $\sim 1.0 \times 10^{16}\,\mathrm{Wcm}^{-2}$ where as for the $10f$ state, the effects become visible at the intensities of order $\sim 1.0 \times 10^{14}\,\mathrm{Wcm}^{-2}$.

5.2 Spatial Effect in the Lowest-Order A^2 interaction Term

Within the minimal coupling formalism, the light-matter interaction has been adequately described by the dipole approximation which ignores the contribution of $\mathbf{A}^2$ term since it is taken to be spatially independent and therefore contributes a zero force in the interaction dynamics. The treatment is well justified within the dipole approximation since the effect of a fully time-dependent $\mathbf{A}^2$ term can be removed by a simple transformation reducing its effect to a mere phase shift of the transition amplitude. In that case, the ionization probability would be insensitive to whether or not the coupling moments of the $\mathbf{A}^2$ terms are included [137, 138]. However, Ivanov and Kheifets [139] note that the use of a Hamiltonian without the $\mathbf{A}^2$ term contribution alters interpretation of the shift, which both continuum threshold and bound states undergo in the presence of electromagnetic field. Reiss, on this argument, adds that physical descriptions like channel closing are altered when A^2 term is removed by a gauge transformation [135].

In this section, the effect of the spatial variation of the vector potential in the lowest-order $\mathbf{A}^2$ term is investigated using the Rayleigh plane-wave multipole expansion. The dipole approximation results are also provided for comparison purposes. In this case, the spatially dependent lowest-order $\mathbf{A}^2$ term is explicitly included in the interaction Hamiltonian and the resulting non-relativistic Schrödinger equation is solved in three dimensions using the radiation gauge interaction potential. The use of the spatially varying lowest-order $\mathbf{A}^2$ term has an added advantage of bringing into play the otherwise forbidden same symmetry transitions (for example, $(1s - 2s)$ transitions) as corrections to the dipole approximation.

Figure 5.2 shows the effect of the inclusion of the lowest-order $\mathbf{A}^2$ interaction term on the photoelectron energy spectra for the hydrogen atom in its ground and $10f$ Rydberg states and for the same laser parameters as in figure 5.1. The use of SBA$_0$ allows for additional transitions due to the the $\mathbf{A}^2$ interaction term which are otherwise forbidden within the dipole approximation.

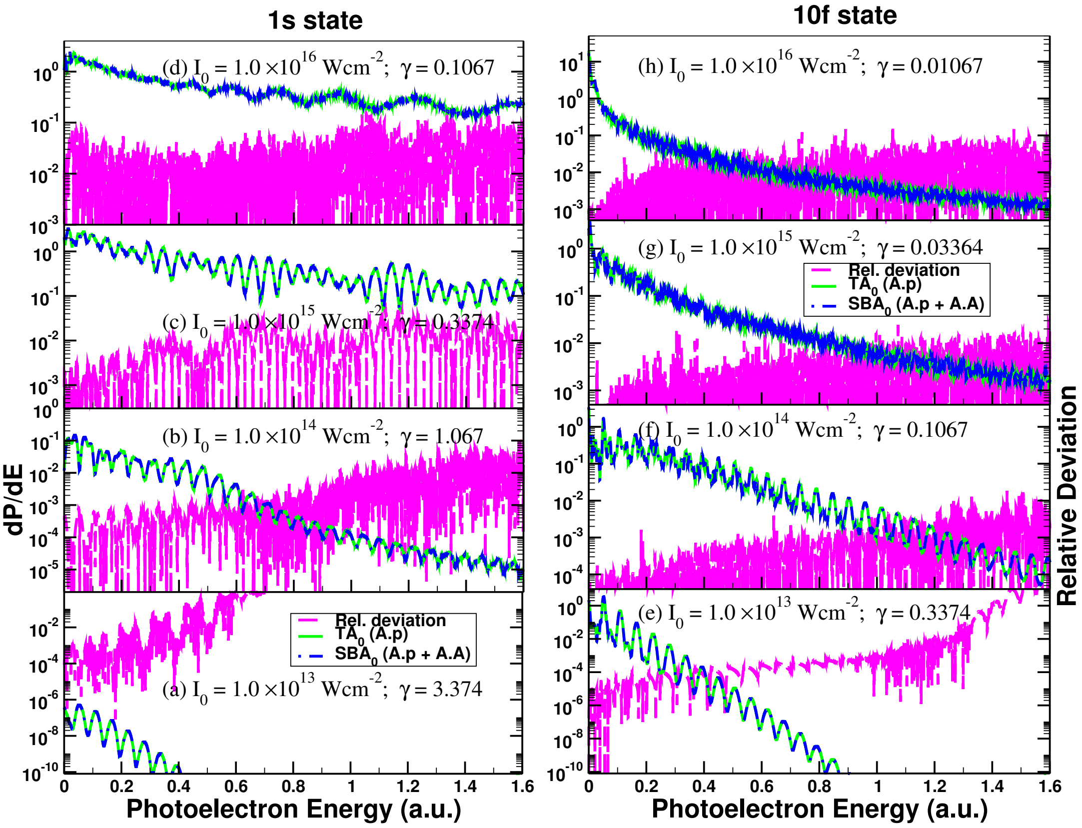

Figure 5.2: Same as figure (5.1) but with the SBA$_0$ including both $\mathbf{A} \cdot \mathbf{p}$ and $\mathbf{A}^2$ terms (blue dash dot lines).

The relative deviation from the dipole approximation in this case is comparable to the cases discussed in section 5.1 in which the $\mathbf{A}^2$ interaction term is not included. This effectively means that the additional effects that come into play with the spatial consideration of the two interaction terms are of the comparable order in the strong-field regime. The terms should therefore be considered together especially in the deep tunnelling regime where significant effects in the spectrum become visible. The relative change in the deviations between figures 5.1 (d) and 5.2 (d) is explicitly visible and it can be attributed to be a consequence of the lowest-order $\mathbf{A}^2$ term only. But for the other corresponding figures, it is quite difficult to isolate the additional effects of the lowest-order $\mathbf{A}^2$ term only.

The peak spatial modulation can be up to ~ 1 percent of the ionization probability for intensities less than 1.0×10^{15} Wcm^{-2} and up to ~ 10 percent for intensities of the order $\sim 10^{16}$ Wcm^{-2} in the photoelectron energy regime capable of contributing significantly to the total ionization yield. The relative change in the total ionization yield is discussed later in section 5.4. Generally, it can be observed that the relative spatial contributions are rather comparable for both the ground and the excited Rydberg state and for both terms of the interaction potential.

In figure (5.3), the additional effect of the lowest-order $\mathbf{A}^2$ term only is investigated by obtaining the relative deviation as a ratio of the absolute difference between the SBA_0 $(\mathbf{A}\cdot\mathbf{p})$ and SBA_0 $(\mathbf{A}\cdot\mathbf{p}+\mathbf{A}^2)$ probabilities, and the dipole approximation (TA_0) differential probabilities. The relative deviation in this case can be used as a measure of the relative importance of the spatial variation of the lowest-order $\mathbf{A}^2$ term only with respect to the dipole approximation. Just like in the other figures, it can be seen that the importance of this term increases with intensity, photoelectron energy, and decrease in the ionization potential. At the intensity of the 1.0×10^{16} Wcm^{-2}, one can easily see that contributes a probability of $\sim 10\%$ of the dipole approximation value in the $1s$ state but in the $10f$ state, the contribution can be up to $\sim 100\%$. Bearing in mind that the effects discussed in this chapter are actually relativistic corrections, one may conclude that at the ponderomotive pressure effects are likely to show up at relatively lower intensities.

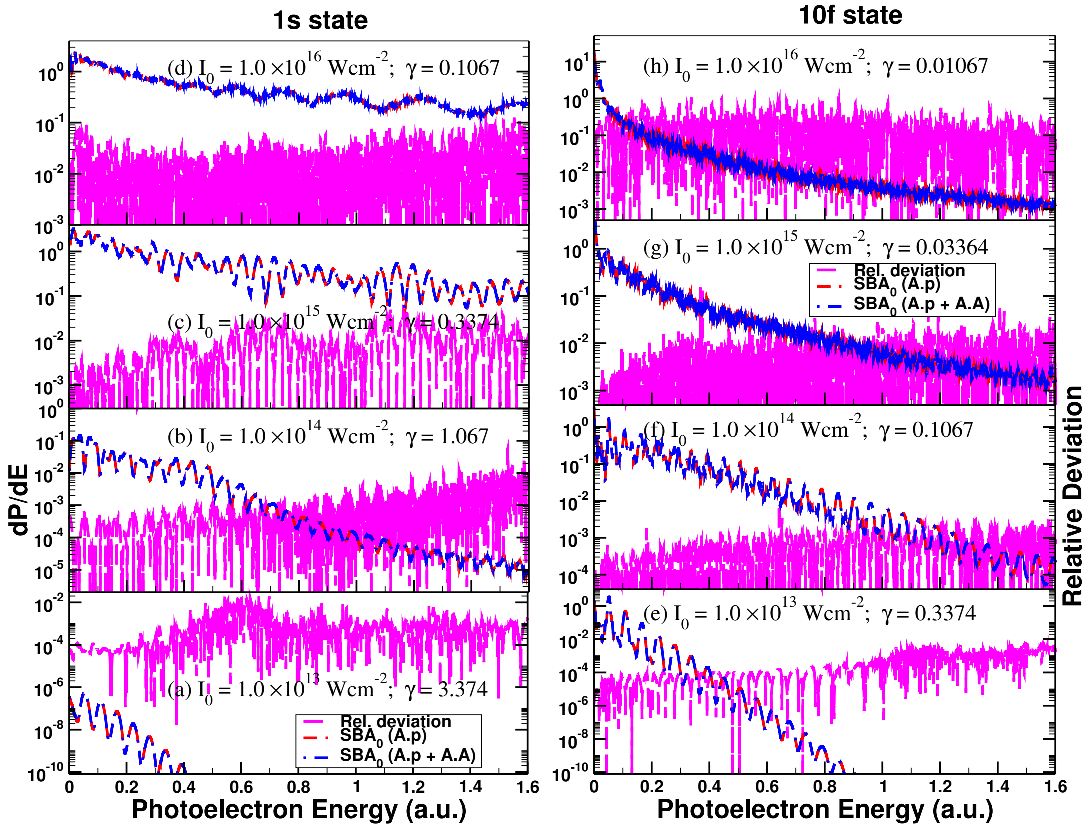

Figure 5.3: Same as figure (5.1) but comparing SBA_0 ($\mathbf{A}\cdot\mathbf{p}$, red dashed lines) and SBA_0 ($\mathbf{A}\cdot\mathbf{p}+\mathbf{A}^2$, blue dash dot lines). The relative deviation is the absolute difference divided by the TA_0 differential probabilities.

The peak relative effect of this interaction appears to be slowly varying for the excited Rydberg state while it increases at a higher rate with the photoelectron energy for the ground state for all the intensities considered. It is important to note that the modifications in the spectra observed emanate from the spatial variation of **A** and are therefore not observable if dipole approximation is employed in the calculations. The spatial modulation can be seen to be highly oscillatory in general. Figures 5.4 (a)-5.4 (c) and 5.4 (d)-5.4(f) focus on the photoelectron energies below 0.2 a.u. for the ground and $10f$ states respectively for the laser intensity regimes where visible effects in the photoelectron energy spectrum are expected. It can be seen that the (very) low-energy structures [(V)LES] [73, 74, 140] and zero energy structures (ZES) [75] observed in recent experiments are modified significantly at higher intensities by the inclusion of the spatially resolved $\mathbf{A}^2$ interaction term. Significant enhancement of these low-energy structures is observable for the ground state at an intensity of 2.0×10^{16} Wcm^{-2} showing that indeed the relativistic effects could partly explain the origin of the (V)LES/ZES. It is noted that structures similar to VLES (< 30 meV) had been observed in an earlier experiment [141] but was suspected to be resulting from multiphoton ionization of impurities in the interacting helium atoms.

The origin of these low-energy structures is still a subject of current debate with several theoretical studies attributing the effect to soft recollisions modified by the interaction of the outgoing electron with the ion's Coulomb field [74, 77, 142] or multiple scattering of the photoelectron in the Coulomb field of the parent ion [52].

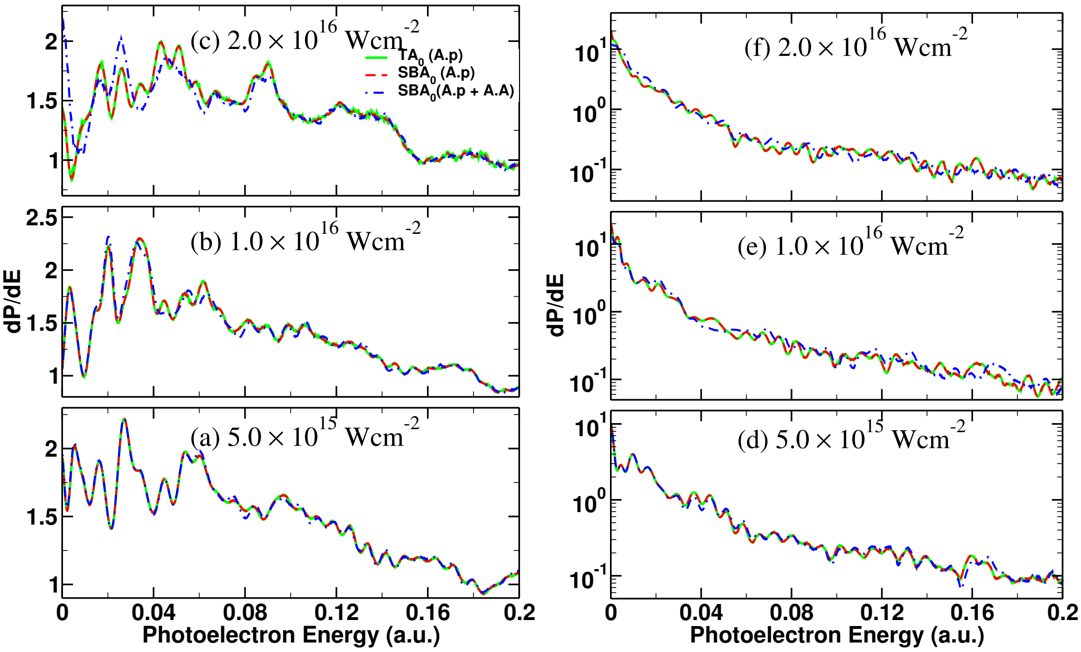

Figure 5.4: Same as figure (5.2) but for lower photoenergies up to 0.2 a.u..for the (a-c) ground state and (d-f) $10f$ state respectively.

To the best of my knowledge, none of the previous studies have so far considered explicitly a possibility of the low-energy structures being modified by the gradient force due to a spatially resolved lowest-order $\mathbf{A}^2$ term. The laser-driven soft-recollisions prediction of [142] illustrate the formation of the structures using non-Coulombic Gaussian potential which induces energy bunching for low-energy photoelectrons. The similarity between the Gaussian potential described and the $\mathbf{A}^2$ kind of potential could be a hint towards their prediction.

5.3 Spatial effects in the Long Wavelength Interactions

Repeat calculations done using a spatially independent $\mathbf{A}^2$ term verified as expected that if the spatial dependence is ignored, the induced shifts in the dipole spectrum at all the intensities investigated vanish. For consistency purposes, the radiation wavelength has been varied to 3100 nm corresponding to mid-infrared wavelengths for which the experimental evidence [75] for the very low-energy structures have been reported. Figures 5.5(a) -5.5(f) shows the numerical results obtained for an intensity of 1.0×10^{13}Wcm^{-2}, 1.0×10^{14} Wcm^{-2}, and 1.0×10^{15} Wcm^{-2} for the longer wavelength laser pulses interacting with the hydrogen atom in its ground state at a wider (left) and at a narrower (right) photoelectron energy window. It is clear from figure 5.5 that the spatial effects are more pronounced at relatively lower intensities compared to the 800 nm case. This means that the spatial effects due to the $\mathbf{A}^2$ interaction term increase with the ponderomotive energy which is significantly higher for such relatively low laser frequencies. The modification of the low-energy photoelectron structures is clearly visible and grows with intensity. Figures 5.4 (c) and 5.5 (f) having comparable Keldysh parameters, despite the difference in intensities and wavelengths, show how large the low-energy structures can be modified by the lowest-order $\mathbf{A}^2$ interaction term.

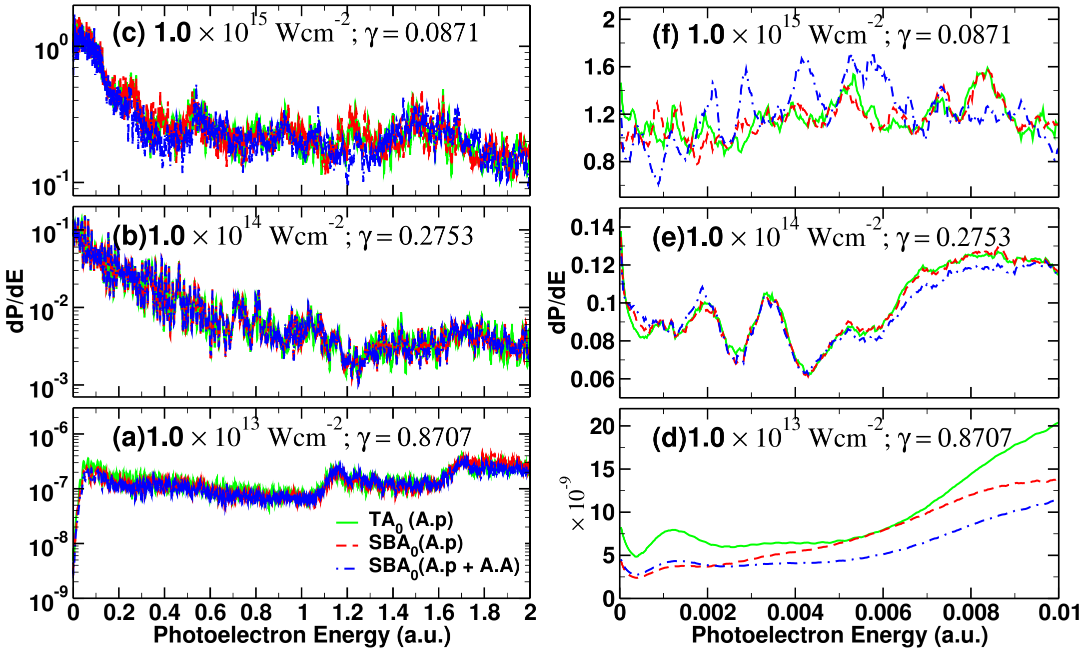

Figure 5.5: Photoelectron energy spectrum for a 3100 nm, 10 cycle, 1.0×10^{13}, 1.0×10^{14} and 1.0×10^{15} Wcm^{-2} intense laser pulse interacting with a hydrogen atom in its ground state. (a-c) Energy range up to 2 a.u. (d-f) lower energy regime from threshold up to 0.01 a.u. The modification of the photoelectron spectrum by the $\mathbf{A}^2$ term is clearly visible.

A possible explanation for the spatial modification of the low- and very low-energy structures would be that the ionization potential of the ground state and low-energy excited states are strongly modified as the magnitude of the $\mathbf{A}^2$ term increases with intensity. This would lead new resonances with the highly excited Rydberg states which were previously out of resonance. The resonant peaks corresponding to these Rydberg states show up as the LES or VLES structures.

From a classical perspective, the $\mathbf{A}^2$ term introduces a dipole force resulting from its spatial dependence. This dipole force pushes the electrons in the direction of laser propagation thereby reducing the electron binding force along the propagation axis. Additional electrons are likely to leak out along this line of weakness. The enhancement of the low energy structures when the $\mathbf{A}^2$ term is incorporated can therefore be seen as a consequence of over-the-barrier tunneling resulting from an additional shift in the potential barrier and that explains their prominence at higher intensities. In the multiphoton regime where physical effects like above threshold ionization structures and channel closing are observed, the explicit inclusion of the $\mathbf{A}^2$ term may lead to the observed modification of the peak positions and amplitude.

5.4 Lowest-Order Spatial Effects in the Total Yields

The total ionization and excitation yields for a 10 cycle 800 nm laser pulse corresponding to different intensities are presented in figure 5.6 (a) for the ground state and in figure 5.6 (b) for the excited $10f$ Rydberg state. The ground state excitation yields have been multiplied by factor 10 to enhance their visibility in the graph. An numerical accuracy of 10^{-6} is used in the time propagation in all the calculations reported in this chapter. The effect of the spatially dependent $\mathbf{A}^2$ term on the total ionization and excitation yields appear to be at variance for both the ground and the Rydberg states. For the ground state, it can be observed that at the highest intensities considered, the inclusion of the $\mathbf{A}^2$ term leads to a slight decrease in the ionization yields and a slight increase in excitation yields. This could be interpreted to signify some slight stabilization effect for the ground-state. On the other hand, there is some enhancement of the ionization probability of the Rydberg state and some decline of the excitation yield at the corresponding intensities where $\mathbf{A}^2$ term become important and thus the stability of this Rydberg state is reduced.

The relative change in the excitation and ionization yields if the $\mathbf{A}^2$ interaction term is included suggests that this interaction classically varies the critical intensity at which the Barrier-Suppression Ionization (BSI) [2, 71] comes into play. The stabilization [78, 143] effect of neutral species at high intensities can be said to be partially a consequence of the $\mathbf{A}^2$ term as predicted in figure 5.6. However, the observed effects on stability of the ground and Rydberg states of hydrogen atom, may not be conclusive because at high radiation intensities, the other higher-order non-dipole terms not considered in this chapter become significant and their inclusion in the interaction Hamiltonian may lead to a breakdown of the stabilization effects [13, 144]. Actually, the observed spatial effects are relativistic in nature emanating predominantly from the octupole term of the Taylor expansion. Other finer adjustments to this spatial correction originate from the even multipole order terms in the Taylor expansion series. If these spatial effects become noticeable in the probability distributions, the quadrupole-order contributions, not captured in this work because of the inherent non-cylindrical symmetry, may actually be quite significant at much lower laser-field intensities as was already shown in a recent experimental observation [132]. The intensity-wavelength thresholds where the non-dipole effects manifest has been discussed by Reiss [85, 86]. The spatial effects observed in this study fits within the lower-dipole limits highlighted [85].

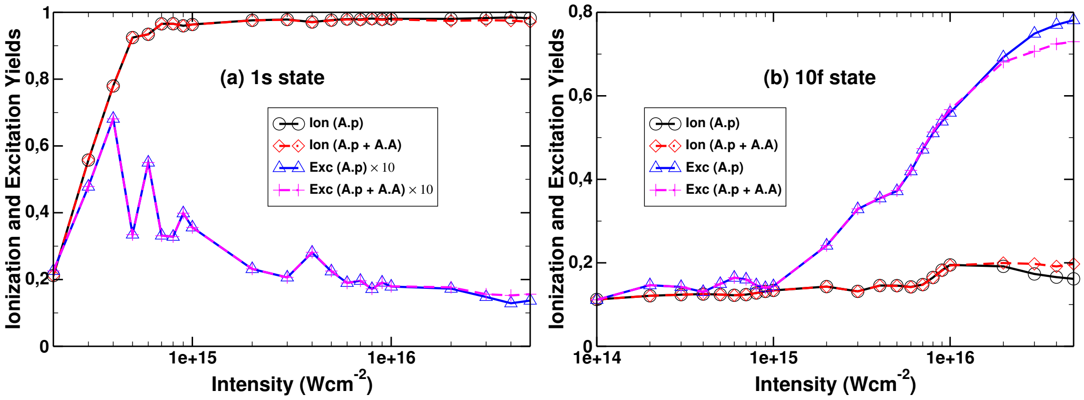

Figure 5.6: Intensity-dependent photoionization and photoexcitation yields corresponding to the 800 nm 10-cycle laser pulses interacting with a hydrogen atom in (a) its ground state and (b) in the $10f$ state. The symbols denote the data points and the continuous lines connect these data points as a guide for the eye. The excitation probability in (a) have been multiplied by factor 10 to increase visibility.

Chapter Summary

The effects of the spatial dependence of the $\mathbf{A} \cdot \mathbf{p}$ interaction on the photoelectron energy spectrum become visible not only with the increase of the photoelectron energy and the radiation field intensity , but also with the decrease in the ionization threshold. The spatial dependence of the ionization probabilities is quite non-linear. The aspect definitely requires further investigation. The recently observed zero- or very low-energy structures [73–75, 140] are seen to be enhanced by the inclusion of the spatially resolved lowest-order approximation of the $\mathbf{A}^2$ interaction. These observations are confirmed by repeating the ground state calculations with a 3100 nm wavelength laser pulse with intensities of 1.0×10^{13} Wcm^{-2} , 1.0×10^{14} Wcm^{-2}, and 1.0×10^{15} Wcm^{-2}. An enhancement of the ionization yield of the Rydberg state at radiation intensities of order $\sim 10^{16}$ Wcm^{-2} and above for the 800 nm radiation wavelength is also predicted.

At the intensities where the spatial effects are important, the effect of including spatially resolved $\mathbf{A}\cdot\mathbf{p}$ and $\mathbf{A}^2$ interactions play a crucial role in the ionization and excitation dynamics leading to shifts in the probability amplitudes. Classically, the dependence of the $\mathbf{A}^2$ term on the spatial coordinates creates a radiation dipole force which increases with intensity of radiation. This force modifies the Coulombic force in the direction of the laser propagation leading to a change in the ionization and excitation dynamics.

6 Non-dipole Effects in the Photoionization of Hydrogen Atoms

In this chapter, the non-dipole effects in the ionization probabilities of hydrogen atoms interacting with short intense laser pulses is discussed in relation to the their dependence on intensity, wavelength, pulse duration, and the initial state. The focus is mainly on the changes arising in the physical observables due to the higher multipole-order terms of the interaction, in comparison with the observables evaluated using the lowest-order terms of the interaction Hamiltonian. The physical observables considered are the energy and angle resolved differential ionization probability distributions, total ionization and excitation yields, as well as the non-dipole asymmetry parameter. The effects considered specifically include the dependence of physical observables on the: intensity, wavelength, pulse duration, and the initial state. For computational convenience and accuracy as already discussed in chapter 4, the spatial retardation $e^{i\mathbf{k}\cdot\mathbf{r}}$ term is expressed in terms of the Rayleigh plane-wave multipole expansion series in this chapter except in the cases in which the ionization dependence on radiation wavelength is investigated or where a further comparison between the Taylor and the Rayleigh expansions is made. In the exceptional case, the implementation of the first-order correction of the spatial retardation term in the Taylor plane-wave multipole expansion series is more convenient.

In solving the non-relativistic TDSE, the relative importance of the various beyond-dipole terms of the interaction Hamiltonian in the strong-field regime is checked. The importance of the various terms is a subject of current debate. In this debate, one group associate the dominant corrections to be emanating from the $\mathbf{A}\cdot\mathbf{p}$ interaction terms [92, 93, 96, 124] while the other group associate the dominant corrections to the $\mathbf{A}\cdot\mathbf{A}$ interaction terms [12, 90, 91, 95, 98, 99]. The chapter begins with the consideration of the beyond-dipole interactions from a classical perspective in order to give an insight into the factors that quantify the magnitude of the non-dipole effects. The results obtained by solving the TDSE numerically using an implicit variable Adamms time-propagation routine are then presented and discussed.

Because of the recent developments in the current generation light sources which allows the production of intense short wavelength short pulse lasers [8], this chapter focusses on the beyond-the-dipole effects for such relatively short wavelength regime. For the sake of comparison with available literature data [91], it has been found favourable to work with a laser wavelength of 13 nm ($\omega = 3.5$ a.u.) and peak electric field strength ranging from 1 to 45 a.u. with finite pulse durations of 10 and 15 cycles. The non-dipole effects corresponding to this wavelength have already been reported by Morten Førre [91] for peak electric field strengths ranging from 1 to 60 a.u. for a 15 cycle pulse. For completeness, the results for a fixed peak electric field strengths but with varying wavelengths or pulse durations are also reported. The 10-cycle pulse is chosen in this case to supplement the already existing knowledge for other pulse durations. The results reported here involve a spectral expansion of the time-independent transition matrix elements first in a B spline basis set and then using the calculated matrix blocks for implicit time propagation. Reasonable convergence is found for the following basis parameters: $r_{\max} = 200$, $L; M_{\max} = 25$, 600 B splines of order $k = 10$, and a geometric knot sequence for a varying r up to 40 a.u. followed by a linear knot sequence. This knot distribution has been found to yield a good probability distribution of both bound and continuum states [95].

The calculation of the multipole transition matrix elements is implemented in both the Taylor and the Rayleigh plane-wave series expansion. The comparison between the two approaches is discussed in section 4. In brief, the Rayleigh plane-wave multipole expansion series is found to be more accurate and efficient, as predicted by Bugacov [12], in comparison to the Taylor plane-wave multipole expansion series. Except for comparison purposes, all the results are based on the Rayleigh plane-wave multipole expansion series. The usual multipole nomenclature, that is, dipole, quadrupole, octupole, etc. is avoided in the discussion because of the use of the Rayleigh plane-wave multipole expansion series for which this terminology may be confusing. Instead reference is made to the various orders of expansion using natural numbers as subscripts beginning from 0 as one progresses to higher-orders in the summation series.

In the reported results, the non-dipole effects are observed in the energy and angle resolved differential probabilities as well as in the total ionization and excitation yields. The magnitude of these non-dipole effects increase with the intensity and wavelength of radiation, the pulse duration, as well as the ionization potential of the initial state. In the multiphoton regime, the non-dipole effects are relatively smaller as compared to the dipole effects. However in the tunneling regime, the non-dipole effects may become dominant as can be verified in the photoelectron angular distributions (PADs) presented in this chapter. All the interactions, both the dipole and beyond, are also observed to be dependent on the projection quantum number m of the initial state. Three different non-dipole asymmetry parameters are discussed as possibilities for further experimental verification of the predicted physical observables.

6.1 Classical Perspective of Non-dipole Interactions

For a linearly polarized laser field propagating in the $+x$ direction with its electric field component aligned in the $+z$ direction, the total non-relativistic interactions evaluated up to the first-order corrections beyond the dipole term in the Taylor expansion is given by

$$H_I = A_1(t)p_z - k\,x\,A_2(t)\,p_z + \tilde{A}(t) - k\,x\,A_1(t)\,A_2(t) \tag{6.1}$$

where

$$\begin{aligned} A_1(t) &= A_0\, f(t)\, \sin(\omega t + \delta) \\ A_2(t) &= \frac{1}{\omega}\dot{A}_1(t) = -\frac{E(t)}{\omega} \\ \tilde{A}(t) &= A_0^2\, f^2(t)\, \frac{1}{4}\,[1 - \cos(2\omega t + 2\delta)] \end{aligned} \tag{6.2}$$

k is the wave number, $A_0 = E_0/\omega$ is amplitude expressed in terms of the peak electric field strength E_0, ω is the radiation frequency, $f(t) = \sin^2(\pi t/\tau)$ is the function describing the carrier envelope, τ is the pulse length, and δ is the carrier-envelope phase. Classically, the z component of linear momentum can be defined as $p_z = m_e v_z$ with $m_e = 1$ in atomic units. With this classical definition, the interaction in equation (6.1) therefore takes the form

$$\begin{aligned} H_I &= A_1(t)\, p_z - k\, x\, A_2(t)\, \frac{dz}{dt} - k\, x\, A_1(t)\, A_2(t) \\ &= A_1(t)\, p_z + k\, x\, z\, \frac{dA_2(t)}{dt} - k\, x\, A_1(t)\, A_2(t) \\ &\approx A_1(t)\, p_z - \omega\, k\, x\, z\, A_1(t) - k\, x\, A_1(t)\, A_2(t) \\ &\approx A_1(t)\, \{p_z - k\, x\, [\omega\, z + A_2(t)]\} \\ &\approx A_1(t) \left\{ p_z - \frac{x}{c}\, [\omega^2\, z + \omega\, A_2(t)] \right\} \\ &\approx A_1(t) \left\{ p_z - \frac{x}{c}\, [\omega^2\, z - E(t)] \right\} \end{aligned} \tag{6.3}$$

where the relation

$$A_2(t)\frac{dz}{dt} = \frac{d(A_2\, z)}{dt} - z\, \frac{dA_2(t)}{dt} \tag{6.4}$$

is used together with an assumption that the first-term on the right-hand side is vanishing because the product $A_2(t)\, z$ is slowly varying in time. Here, it is argued that $A_1(t) \propto z$ and consequently, $1/A_2(t) \propto z$. In the framework of the centre of mass and relative coordinates being adopted, the product $A_2(t)\, z$ would actually be a constant in time, for an electron considered to be initially free, resulting into a zero value in its first derivative and hence the assumption would be justified. From the simplified classical picture, one can see that the non-dipole interactions have two-fold dependence. That is, one part of it depends quadratically on the frequency of radiation and linearly with the electron displacement in the direction of polarization of the electric field vector, and the other part depends on the magnitude of the electric field. The field dependent part indirectly varies with pulse duration. For very short pulse durations, the dependence is inverse while for very long pulse durations, it can be shown that the dependence tends to be linear. Both parts vary linearly with the displacement in the propagation direction. This displacement is caused by the radiation pressure and it induces some ellipticity in the interaction dynamics.

From the classical consideration, the excursion radius of a free-electron oscillating in an electric field is $|z| = |E(t)|/\omega^2$. If one substitutes for z in the equation (6.3), it is found that the two non-dipole interactions are actually comparable (or equal) to each other and should therefore be considered all together. The superposition of the two would lead to a destructive interference if they have opposite relative phases and a constructive interference for similar relative phases. Because of the difference in the selection rules for each of the non-dipole interactions, the final state would be different for each case assuming a transition from the same initial state. The difference between the two interactions can therefore be attributed to the geometry (size and shape) of the states involved in the transitions other than the magnitude of the transitions themselves, as well as the relative interference of each with the dipole interactions. Considering both $A_1(t)$ and $E(t)$ in equation (6.3), it can also be observed that the dipole interactions increase linearly with the magnitude of the electric field whereas the non-dipole interactions increase quadratically with the electric field amplitude.

6.2 Definitions and Terminology

The multipole-order interaction Hamiltonian can be expanded in terms of the Taylor (TA) or the Rayleigh series, using spherical Bessel functions (SBA) approximations, as

$$V(\mathbf{r},t) = \sum_l \mathbf{A}\cdot\mathbf{P}_l + \frac{1}{2}\mathbf{A}\cdot\mathbf{A}_l \tag{6.5}$$

with the subscripts l denoting the orders of the orbital angular momentum of the photon-field included in the multipole expansion. Equation (6.5) is the radiation gauge interaction Hamiltonian introduced in equation (3.83) of section 3.4. The first few interaction terms of the Taylor plane-wave multipole expansions series(TA) have been specifically defined as

$$\begin{aligned}
\mathbf{A}\cdot\mathbf{P}_0 &= A_1(t)\,p_z \\
\mathbf{A}\cdot\mathbf{P}_0 + \mathbf{A}\cdot\mathbf{A}_0 &= A_1(t)\,p_z + \tilde{A}(t) \\
\mathbf{A}\cdot\mathbf{P}_{0,1} &= A_1(t)\,p_z - \frac{\omega x}{c}\,A_2(t)\,p_z \\
\mathbf{A}\cdot\mathbf{P}_0 + \mathbf{A}\cdot\mathbf{A}_1 &= A_1(t)\,p_z - \frac{\omega x}{c}\,A_1(t)\,A_2(t) \\
\mathbf{A}\cdot\mathbf{P}_{0,1} + \mathbf{A}\cdot\mathbf{A}_{0,1} &= A_1(t)\,p_z - \frac{\omega x}{c}\,A_2(t)\,p_z + \tilde{A}(t) - \frac{\omega x}{c}\,A_1(t)\,A_2(t)
\end{aligned} \tag{6.6}$$

and of the corresponding Rayleigh plane-wave multipole expansion series (SBA) as

$$\begin{aligned}
\mathbf{A}\cdot\mathbf{P}_0 =& A_1(t)\, j_0(kr)\, p_z \\
\mathbf{A}\cdot\mathbf{P}_0 + \mathbf{A}\cdot\mathbf{A}_0 =& A_1(t)\, j_0(kr)\, p_z + \tilde{A}(t)\, j_0(2kr) \\
\mathbf{A}\cdot\mathbf{P}_{0,1} =& A_1(t)\, j_0(kr)\, p_z - \sum_{m=-1,1} 4\pi\, j_1(kr)\, A_2(t)\, p_z\, Y_1^{m*}(\hat{k})\, Y_1^m(\hat{r}) \\
\mathbf{A}\cdot\mathbf{P}_0 + \mathbf{A}\cdot\mathbf{A}_1 =& A_1(t)\, j_0(kr)\, p_z - \sum_{m=-1,1} \frac{4\pi}{2}\, j_1(2kr)\, A_1(t)\, A_2(t)\, Y_1^{m*}(\hat{k})\, Y_1^m(\hat{r}) \\
\mathbf{A}\cdot\mathbf{P}_{0,1} + \mathbf{A}\cdot\mathbf{A}_{0,1} =& A_1(t)\, j_0(kr)\, p_z - \sum_{m=-1,1} 4\pi\, j_1(kr)\, A_2(t)\, p_z\, Y_1^{m*}(\hat{k})\, Y_1^m(\hat{r}) \\
& + \tilde{A}(t)\, j_0(2kr) - \sum_{m=-1,1} \frac{4\pi}{2}\, j_1(2kr)\, A_1(t)\, A_2(t)\, Y_1^{m*}(\hat{k})\, Y_1^m(\hat{r})
\end{aligned} \tag{6.7}$$

with the functions $A_1(t)$, $A_2(t)$ and $\tilde{A}(t)$as defined in equation (6.2). The summation over the projection quantum number m does not include $m = 0$ as specified in equation (6.7) and in the selection rules discussed in section 3.6. The definitions of the interaction terms in equations (6.6) and (6.7) are used in all the figure legends in this chapter. The double indices used in the subscripts of some of these equations show the orders of the interaction terms defined in that interaction Hamiltonian.

6.3 Validation of Results

Having extended the BEYDIP code to incorporate the higher multipole-order interactions with the transition matrix elements evaluated using the multipole expansion in either Taylor or Rayleigh series, it was quite necessary to validate the results using reliable data. The code, in its initial form before the non-dipole extension, was developed by Yulian Vanne [14] and optimised by Johann Föster (members of AMO group at Humboldt-Universität zu Berlin) to solve the time-dependent Schrödinger equation for single-active-electron systems within the dipole approximation. The extension process involved restructuring the code from the dipole interactions which obey the cylindrical symmetry relations, enabling the use of a reduced basis size resolved in only n and l quantum numbers, to a non-cylindrical symmetry of higher multipole-order interactions. The extension required the use of a complete basis-set resolved in the entire non-relativistic n, l and m quantum numbers. The task in itself is quite involved and prone to minute programming errors which may compromise the results if careful attention is not paid to the tiny details while programming. Other than the diagonalization part of the program, the entire code was amended while trying to retain the structure of the original code for portability reasons.

While developing the code, emphasis was paid to the optimization with a view of maximizing the computational resources and enhancing computer efficiency. In achieving this goal, the use of established symmetry relations governing the transition matrices was of great value. Despite the already implemented optimizations, the strong-field dynamics for wavelengths above the optical regime still present a significant challenge with regards to computational capacity. This can be viewed as an opportunity for further development.

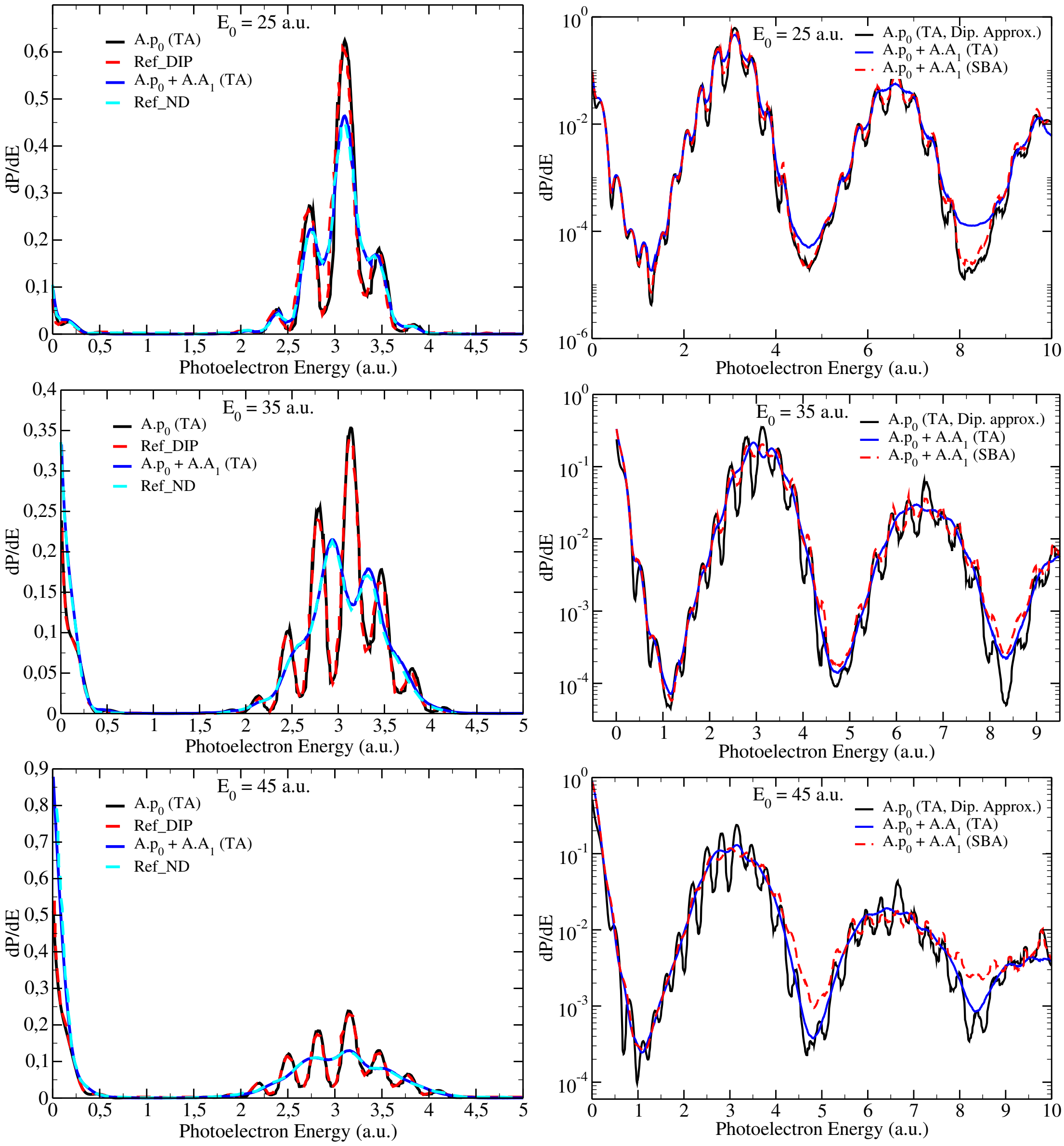

Figure 6.1: Dipole and non-dipole photoelectron energy spectra for a 15 cycle 13 nm laser pulse with peak electric field strengths $E_0 = 25, 35$ and 45 a.u. in the top, middle, and bottom respectively. Left: comparison of present and reference data [91]. Right: comparison of the dipole to the Taylor and Rayleigh non-dipole spectra.

The validation of results in itself has also been quite a challenge since there is not so much published work extending beyond the dipole approximation and the computations are tedious in time. The available literature data is used for both quantitative and qualitative comparison with the results discussed in this work.

The results of Morten Førre et al. [91] were of natural preference for the validation process because in the preliminary results of the BEYDIP code, their dipole results were reproduced exactly . Also, their willingness and actual collaboration in the benchmarking and troubleshooting of the current results with the inclusion of the non-dipole interactions was an added advantage. Figure (6.1) compares the non-relativistic results reported in this work, for a 15 cycle 13 nm laser pulse at the three different peak electric field strengths $E_0 = 25, 35$ and 45 a.u., with the results presented in the literature data [91]. They used an interaction Hamiltonian equivalent to the third interaction term in equation (6.6). On the left is a comparison of the present values against the literature values for both dipole and non-dipole results evaluated using Taylor expansion only. On the right is a comparison of the dipole results to the non-dipole results evaluated using both Taylor and Rayleigh plane-wave expansions from the 0^{th} order up to the 1^{st} order terms of the plane-wave multipole expansion series.

Figure 6.1 (left) shows a comparison of the present work with the results extracted from the literature data [91]. The terms of the interaction Hamiltonian adopted are expressed in equations (6.6) and (6.7). The 13 nm wavelength corresponds to a photon energy of 3.5 a.u. (or 95.2 eV). For hydrogen atom with the ground state energy of -0.5 a.u., the absorption of one photon is sufficient to liberate a bound electron to the continuum state with a kinetic energy of 3.0 a.u., corresponding to the first-photon peak. In the strong-field regime, the absorption of multiple photons is possible with the n^{th}-photon peak expected at $\approx (n\omega - I_p)$ a.u. in the photoelectron energy spectrum (PES). The ionization potential I_p can be modified by the dynamic Stark shifts (or ponderomotive shifts) which correspondingly shift the position of the expected peak in the energy spectrum. Shorter wavelengths, where a single photon is sufficient to cause ionization, have the tendency to shift the photon-peak towards the higher photoelectron energy regime as can be verified in figure 6.1 while longer wavelengths shift the photon-peak towards the lower regime [130]. The peak at the zero energy in the PES does is not the first photon peak. It corresponds to either tunnelling or over-the-barrier tunnelling ionization peak or a two-photon stimulated Compton scattering peak resulting from absorption of a photon by a dressed initial state followed by the emission of a photon of similar frequency from a dressed intermediate state.

The good agreement of the dipole and non-dipole results with the reference spectra using the Taylor expansion series can be used as a validation of the present results. Figure 6.1 (right) compares the results in the left figure evaluated using the Taylor series as well as the Rayleigh series. As already discussed in section 4, the Rayleigh and the Taylor predictions of the non-dipole effects are comparable but not exactly equal. The discrepancy between the two methods for the spectral parameters considered in this case increase with photoelectron energies. In the regions where the discrepancy manifests especially in the higher photoelectron energy regime, the higher multipole-order corrections present in the Rayleigh plane-wave expansion series are quite significant. The Rayleigh plane-wave expansion, as opposed to the Taylor expansion, can be seen to preserve the structural effects present in the dipole spectrum.

6.4 Convergence of Results

In this subsection, the convergence of results with respect to the number of angular momenta as well as the box radius is tested. This is because the quality of the eigenvectors and eigenvalues intrinsically depend on the box radius and density of states. A bigger box size is necessary to describe the states more accurately and this would also reflect in the quality of transition matrices and the measurable observables by extension. The quality of the states can further be improved by increasing the density of states for a fixed box size. In principle, a complete basis set requires the number of states to be defined with an infinite set of quantum numbers. A computation with an infinite number of states is not only demanding but also impossible. Unless a new trick is found, only a finite set is usually used depending on the laser parameters and the system geometry. A suitable choice can then be made after a proper convergence test catering for the wavepacket spreading during the laser-matter interaction using the extreme laser parameters in the regimes of interest. The effect of numerical convergence parameters is adequately described in Yulian's PhD thesis [14].

The convergence is tested in this case by varying the box radius and the number of angular momenta while keeping the number of B splines fixed at 600. This in principle meant that the density of states is varied simultaneously with the radius of the box. It is observed that the ionization dynamics is poorly described if the box radius is reduced and the density of states kept constant by fixing the number of B splines to be three times the box radius. The convergence calculations have been done by using the Rayleigh plane-wave multipole expansion of the spatial retardation term. This choice is made due to its inherent accuracy and efficiency over the Taylor plane wave expansion. In general, the multipole calculations are too demanding in terms of memory capacity and computational time.

Using some of the symmetry relations discussed in section 3.6.1, the BEYDIP code is optimized to reduce on the memory demand by more than a factor of two. It is also established that for the same memory requirements, the implementation in the Rayleigh multipole expansion is in many orders of magnitude faster, besides providing a higher degree of accuracy. The only limitation seems to stem from the use of wavelength specific transition matrix elements as opposed to the Taylor multipole plane-wave expansion where the dipole and quadrupole matrix elements can be generalized for any wavelength, but considering the wavelength effects as pre-factors to be considered only during time propagation.

Figure 6.2 shows the convergence spectra for the multipole-order terms of the interaction Hamiltonian as a function of angular momenta and peak electric field strengths of the laser pulse. The lowest-order $\mathbf{A}\cdot\mathbf{p}$ terms within the Rayleigh plane-wave expansion are shown on the left while all the $\mathbf{A}\cdot\mathbf{p}$ and $\mathbf{A}\cdot\mathbf{A}$ terms up to the first-order in the Rayleigh series are shown on the right-hand side.

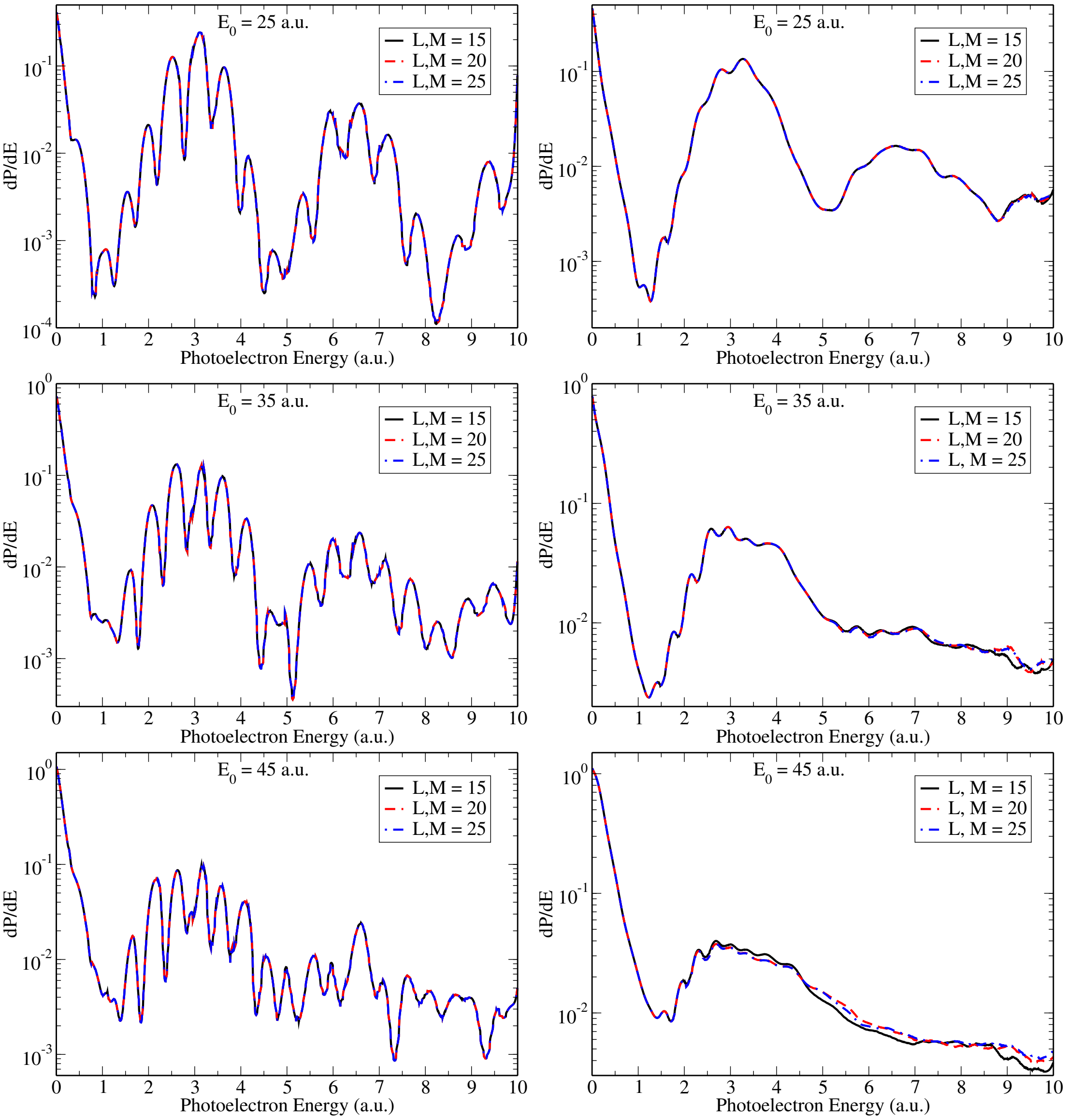

Figure 6.2: Multipole-order photoelectron energy convergence spectra for a 10 cyle 13 nm laser pulse as a function of angular momenta and peak electric field strengths $E_0 = 25, 35$ and 45 a.u. in the top, middle, and bottom respectively. The box radius and the number of B spines was fixed at 200 a.u and 600 respectively. Left: Lowest-order $\mathbf{A} \cdot \mathbf{p}_0$ interaction spectra in the Rayleigh approximation. Right: Multipole $\mathbf{A} \cdot \mathbf{p}_{0,1} + \mathbf{A} \cdot \mathbf{A}_{0,1}$ interactions spectra up to the first-order in the Rayleigh plane-wave series expansion.

The box radius is fixed at $r_{\max} = 200$ and the number of B splines fixed at 600. The lowest-order $\mathbf{A} \cdot \mathbf{p}$ interaction terms spectra show perfect convergence with only $L, M_{\max} = 15$ angular momenta for all the peak electric field strengths considered. On the other hand, in the multipole-order terms spectra it can be seen that $L, M_{\max} = 15$ angular momenta are sufficient for $E_0 = 25$ a.u. only, while $E_0 = 35$ a.u., and $E_0 = 45$ a.u. require $L, M_{\max} = 20$ and $L, M_{\max} = 25$ angular momenta respectively for sufficient convergence. The multipole-order terms spectra show that higher-order electron-photon interactions involving exchange of angular momenta enhance wave packet spreading and therefore a higher dimension, scaling with intensity and photoelectron energies, of angular momenta is necessary for full convergence.

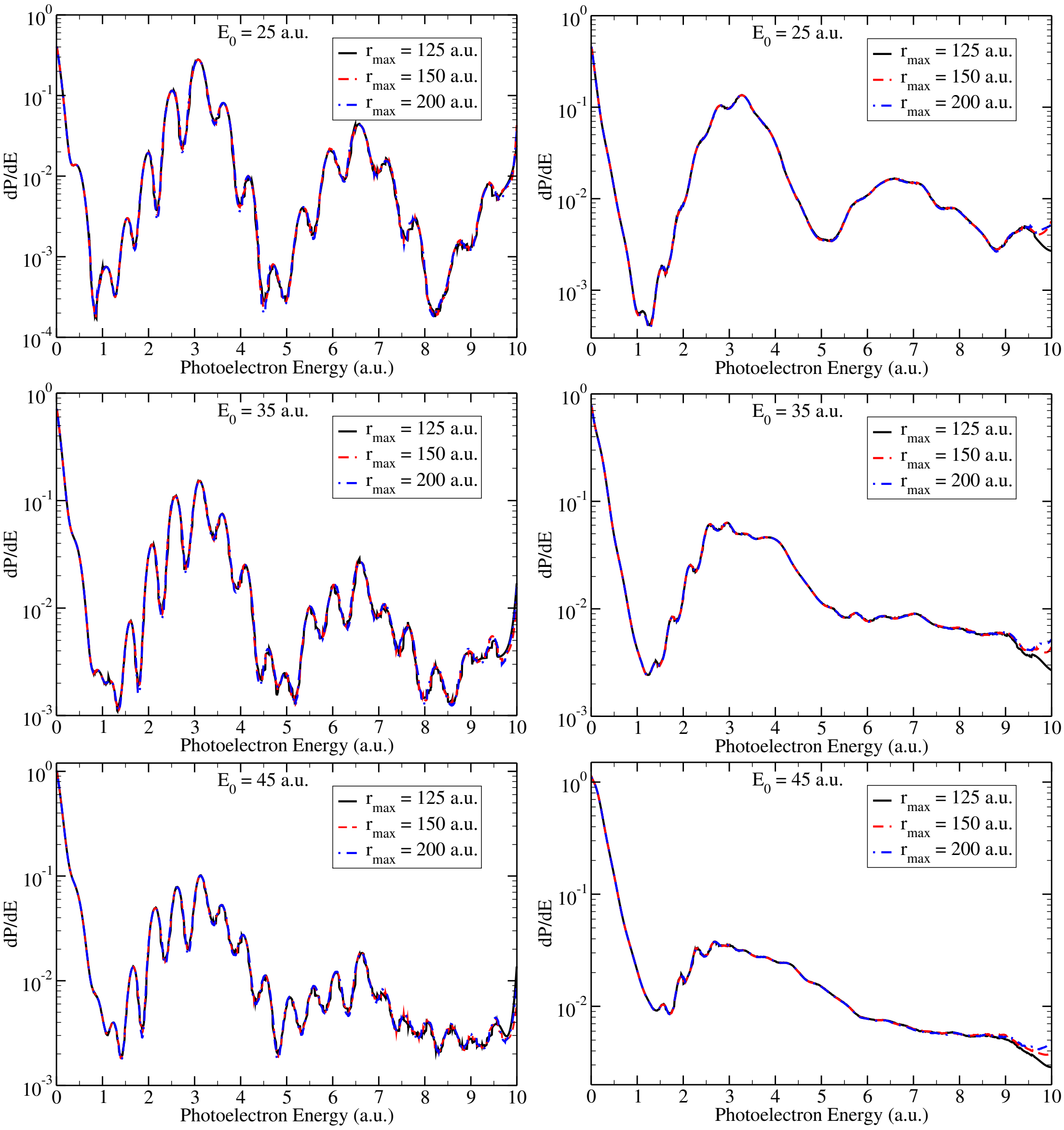

Figure 6.3: Multipole-order photoelectron energy convergence spectra for a 10 cyle 13 nm laser pulse as a function of box radius $r_{\max}$ and peak electric field strengths $E_0 = 25, 35$ and 45 a.u. in the top, middle, and bottom respectively. The number of B splines was kept constant at 600. Left: Lowest order $\mathbf{A} \cdot \mathbf{p}_0$ interaction spectra in Rayleigh approximation. Right: multipole $\mathbf{A} \cdot \mathbf{p}_{0,1} + \mathbf{A} \cdot \mathbf{A}_{0,1}$spectra for all the interactions upto the first-order in the Rayleigh plane-wave expansion.

The convergence of spectra as a function of box radius $r_{\max}$, while keeping the number of B splines constant at 600 and angular momenta at a maximum of 25 for both L and M, shows a marginal increase in the convergence of spectra as the box radius increases. In this case, both the lowest-order $\mathbf{A}\cdot\mathbf{p}$ interaction term and the multipole-order terms spectra shows convergence for all the three values of r_{max} shown in figure 6.3 up to about 9 a.u. photoelectron energies for the three intensity values. Having fixed the number of B splines at 600 implies that the smaller box radii have a higher density of states compared to the larger box radius. Prior to these box radius convergence parameters, calculations with smaller box radii were tried while keeping the density of states constant at 3 but the results obtained could not converge. Subsequent calculations, keeping the box radius constant at $r_{\text{max}} = 200$ and varying the density by factor 2.5 and 3.5 using 500 and 700 B splines did not reveal any further change in the spectrum.

6.5 Dependence of Ionization on Intensity

It is already discussed in chapter 2 that beyond the perturbative regime, ionization is characterized by strong-field processes which can be classified as multiphoton, tunneling or barrier-suppression ionization depending on the magnitude of the Keldysh adiabaticity parameter. The ionization yield in this non-perturbative regime exhibits non-linear dependence on the pulse intensity owing to the intensity- and wavelength-dependent ponderomotive potential which becomes comparable to the ionization potential. As the ponderomotive potential increases, it is expected that the corresponding effects like radiation pressure also increases in the direction of the laser propagation, relativistic effects come into play, as well as the quantum electrodynamic (QED) effects. The radiation pressure is an effect of the force derived from the ponderomotive potential. The relativistic and quantum electrodynamic effects on the other hand become significant as the photoelectron velocity approach the speed of light. The spin-dependent features like spin-orbit coupling, spin-spin interactions are examples of the relativistic effects whereas the Lamb shift is an example of a QED effect. These non-linear effects are non-dipole in nature and they may be observable in the photoelectron energy and angular distributions. They can possibly lead to a change in the total ionization yields relative to the yields predicted by the dipole approximation.

Figure 6.4 shows the ionization probability on the left and the excitation probability on the right, as a function of peak electric field strength, for a hydrogen atom initially in the ground ($1s$) state interacting with a linearly polarized laser pulse whose wavelength and pulse duration are fixed at 13 nm and 10 cycles respectively. The orders of the respective multipole interaction terms are specified by the subscripts (i.e. 0 and 1) in the legends according to equation (6.7). The effect of various multipole-order terms of interaction Hamiltonian on the total ionization and excitation probability are compared. From the ionization probability, it can be seen that all the interaction terms predict the atomic stabilization beyond a saturation point at about $E_0 = 12$ a.u. During stabilization, the ionization probability decreases as the intensity increases up to some minimum value before beginning to rise again. Within the lowest-order (or 0^{th} order) interaction terms, the minimum value is located around $E_0 = 30$ a.u. If all the higher multipole-order interactions considered in this work are included, the minimum drifts towards a lower value, that is $E_0 = 25$ a.u. This effect was already noted and discussed earlier as a possible breakdown of atomic stabilization [12, 13].

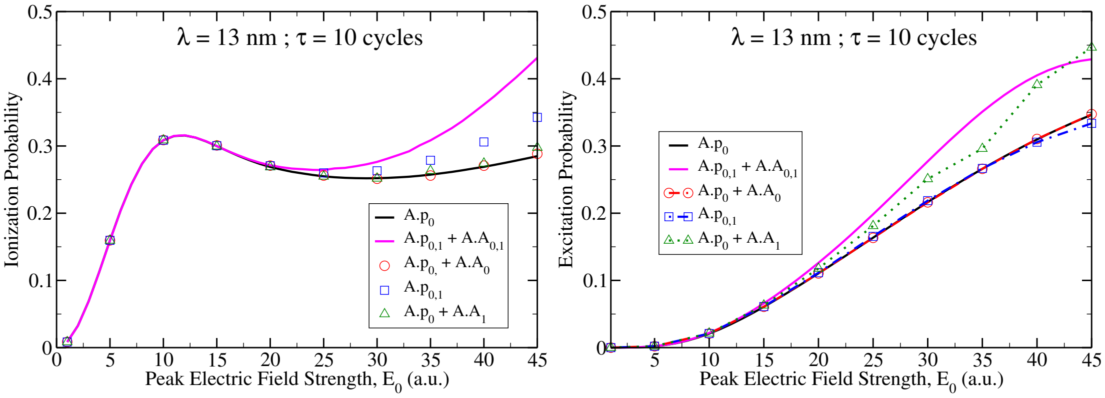

Figure 6.4: Ionization (left) and excitation (right) probability dependence on the multipole-order terms of the interaction Hamiltonian and peak electric field strength for a 13 nm linearly polarized laser pulse with a fixed pulse duration, $\tau = 10$ cycles.

In this work, it is observed that atomic stabilization persists, but with the stabilization window narrowed for the laser parameters considered. Indeed, it has been shown with an approximated non-dipole interaction potential that the non-dipole effects may lead to the narrowing or enhancement of the stabilization window depending on the laser parameter regimes in question [145]. The relative importance of the non-dipole terms of the interaction Hamiltonian can also be observed with the dominant ionizing non-dipole interaction stemming from the non-dipole $\mathbf{A} \cdot \mathbf{p}_1$ followed by the non-dipole $\mathbf{A} \cdot \mathbf{A}_1$ interaction. If all the multipole-order interaction terms up to 1^{st} order are considered, the overall increase in the ionization probability is higher than the gains of each individual corrections beyond the dipole approximation.

The excitation probability on the other hand also increases with the peak electric field strength for the laser parameters considered. The non-dipole $\mathbf{A} \cdot \mathbf{A}_1$ interaction appears to be significant in enhancing excitation probability as compared to the other corrections. In fact, at higher peak electric field strengths, the non-dipole $\mathbf{A} \cdot \mathbf{p}_1$ interaction seems to suppress the excitation probability. When all the corrections are put together, the overall excitation probability also increases to a maximum point around the highest peak electric field strength considered. The role of $\mathbf{A} \cdot \mathbf{A}_1$ interaction in enhancing the excitation probability can be a big boost to resonant excitation and ionization processes, thereby resulting to the catalysis of the narrowing of the stabilization window. From the observations in figure 6.4, it can be seen that the dominant non-dipole corrections are comparable in magnitude and should therefore be considered simultaneously.

Intensity a.u.	1	3	5	10	15	25	35	45
U_p a.u.	0.02	0.18	0.51	2.04	4.58	12.72	24.93	41.21
γ	3.50	1.17	0.70	0.35	0.23	0.14	0.10	0.08

Table 6.1: Table showing the variation of the U_p and γ with intensity.

Table 6.1 shows the variation of the ponderomotive potential U_p and the Keldysh adiabaticity parameter γ with the intensity regimes considered in this section. The Keldysh parameter is typically used for the characterisation of the interactions with long-wavelength radiation where $\gamma > 1$ corresponds to the multiphoton regime and $\gamma < 1$ corresponds to the tunneling regime. In this case, the intensities above ~ 3 a.u. for the 13 nm wavelength can be classified to be in the tunneling regime while lower intensities can be considered to be in the multiphoton regime.

Figure 6.5 shows the energy-resolved photoelectron ionization probability distribution for the five different atom-laser multipole interaction terms at various peak electric field strengths. As already explained in the introduction, a 13 nm wavelength laser field with a pulse duration of 10 optical cycles is used predominantly in this chapter unless otherwise specified. The goal in this case is to make an explicit comparison of the relative importance of each of the interaction terms with respect to the dominant zero-order $\mathbf{A}\cdot\mathbf{p}_0$ (dipole) interaction term. The discussion is restricted to the first two multipole-orders for which it is already shown in chapter 4 to be the most significant. From this figure, several key features of the non-dipole effects are manifested. First, the non-dipole $\mathbf{A}\cdot\mathbf{A}_1$ interaction is the first to manifest at 1 a.u. peak electric field strength beyond the one-photon peak. But its effect seems to have a weaker dependence on intensity. It can be seen that it generally gives a weak modulation of the dipole spectrum except at higher intensities (beyond 25 a.u.) where some of its observable effects show up.

The effects of non-dipole $\mathbf{A}\cdot\mathbf{p}_1$ interaction on the other hand shows up at about 5 a.u. and remains dominant, with a strong intensity dependence, for the remaining peak field strengths. The effect of the lowest-order $\mathbf{A}\cdot\mathbf{A}_0$ interaction term remains negligible except at higher photoelectron energies and at higher intensities where its effects become significant. In the Taylor expansion series, this term does not lead to any transition and therefore it is usually ignored based on a phase-transformation. But within the Rayleigh expansion series, this term is dependent on the spatial radial co-ordinates and therefore its contribution is non-vanishing. It actually leads to the same symmetry (e.g. $1s-2s$) transitions considered to be of higher multipole-order effects.

In general, the non-dipole effects in the energy spectrum are similar regardless of the interaction. The effects include the enhancement of probability at valleys, the suppression of probability at the peaks, the disappearance of side-bands, the enhancement of the short-pulse energy-bandwidth generated low-energy photoelectrons, and the distortion of the ATI structure by levelling the higher-order multiphoton peaks first. In deed in the experimental results of reference [146], it was already observed that spatial averaging washes out the single-atom ATI structures in the tunneling regime due to the large ponderomotive shift of the ionization potential and the relatively weak dependence of the ionization rate.

In terms of the relative importance, it is again observed from photoelectron energy spectrum that for the laser parameters under consideration, the non-dipole $\mathbf{A}\cdot\mathbf{p}_1$ interaction term is the most dominant term. It is followed by the non-dipole $\mathbf{A}\cdot\mathbf{A}_1$ interaction term, and then the non-dipole zero order $\mathbf{A}\cdot\mathbf{A}_0$ interaction term which provides a higher order correction to the dipole approximation (if expanded in the Taylor series) in comparison to $\mathbf{A}\cdot\mathbf{p}_1$ and $\mathbf{A}\cdot\mathbf{A}_1$ interactions.

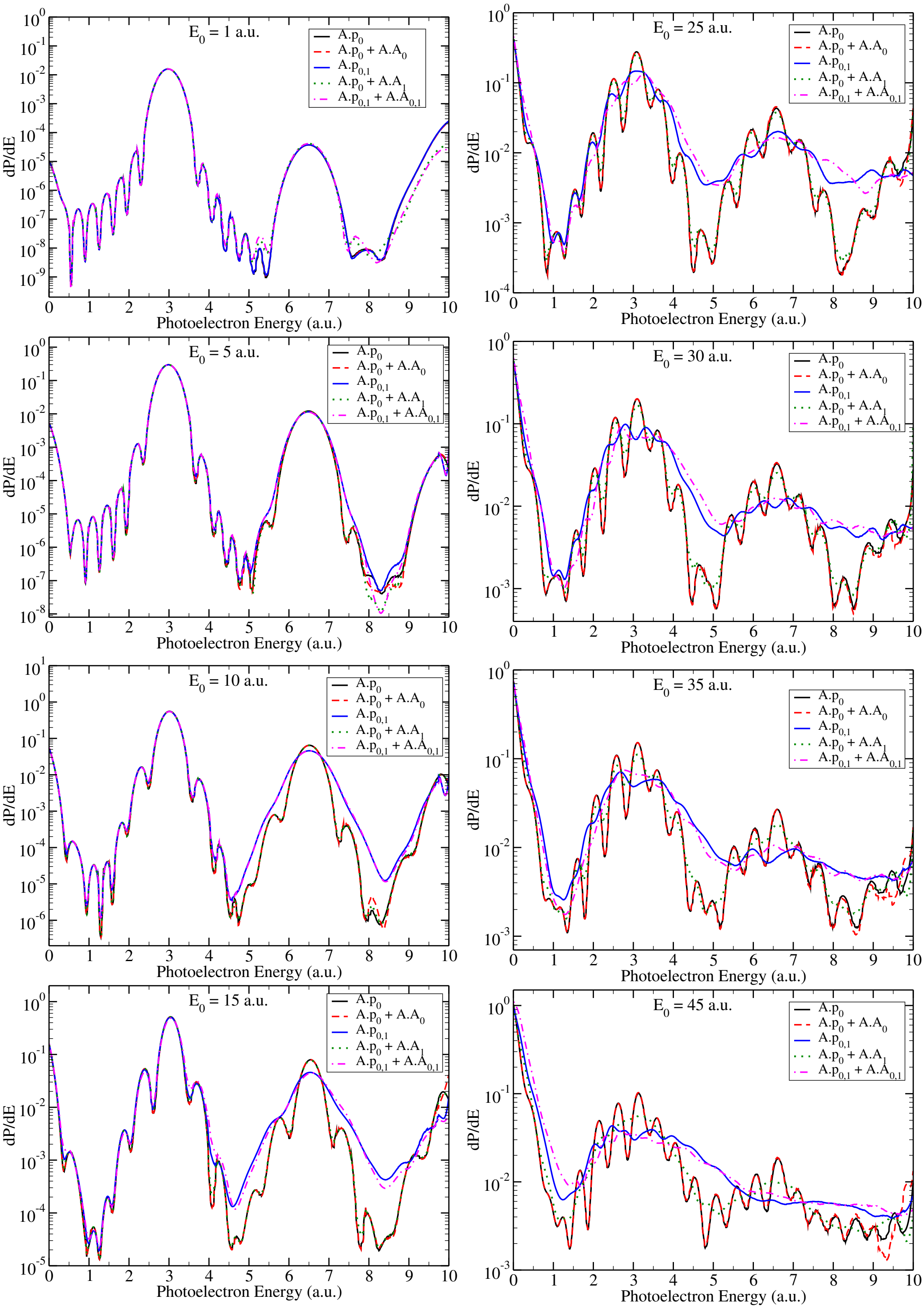

Figure 6.5: Comparison of the effect of the various multipole-order interaction terms in the photoelectron energy spectra for varying peak electric field strength ranging from $1 - 45$ a.u. The other pulse parameters are as specified in figure (6.4).

The relative importance of the leading multipole-order corrections is supported by figure 6.6 in which the relative deviation from the dominant $\mathbf{A} \cdot \mathbf{p}_0$ interaction term, at a peak electric field strength of $E_0 = 25$ a.u. on the left and at $E_0 = 45$ a.u. on the right, is plotted. The relative importance determined is found to be consistent for the other peak electric field strengths where the non-dipole effects are more pronounced. These results agree with the observations of the references [92, 93, 96, 124] as well as the predictions of quantum physics which attributes the paramagnetic effects to be of leading importance in comparison with the diamagnetic effects [18].

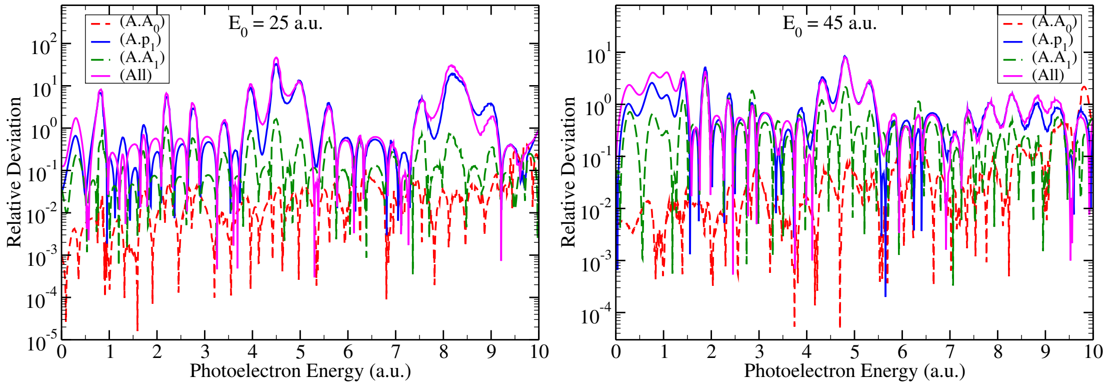

Figure 6.6: Relative deviation of the multipole spectra from the lowest order $\mathbf{A} \cdot \mathbf{p}$ (dipole) interaction spectrum at a peak electric field strength, $E_0 = 25$ a.u. (left) and $E_0 = 45$ a.u. (right).

The effects of non-dipole $\mathbf{A} \cdot \mathbf{p}_1$ interaction are associated with the radiation induced paramagnetism whereas those of the non-dipole $\mathbf{A} \cdot \mathbf{p}_1$ interaction are related to the radiation induced diamagnetism. In reference to the relative deviations in figure 6.6 shown, it can be seen that role of non-dipole interactions is not limited to higher photoelectron energies, as it is always assumed, but cut across the entire energy regime. Even in the near-zero regime, a relative deviation greater than 1 can be observed signifying that the non-dipole dynamics dominate at those points.

Figures 6.7 and 6.8 are 3-dimensional colour plots showing the energy resolved photoelectron probability distribution of the lowest-order $\mathbf{A} \cdot \mathbf{p}_0$ term of the interaction on the left and that of the multipole-order $\mathbf{A} \cdot \mathbf{p}_{0,1} + \mathbf{A} \cdot \mathbf{A}_{0,1}$ terms of the interaction on the right at various peak electric field strengths, E_0, ranging from $1 - 45$ a.u. Several interesting phenomena can already be observed from these figures. First, there is an enhancement of photoelectrons probability in the near-zero energy regime on both spectra as intensity increases. These correspond to the high-frequency low-energy structures already featured in literature [91].

Second, the probability distribution corresponding to the multiphoton peaks increase with intensity up to a peak value at about $E_0 = 12$ a.u before beginning to decrease gradually. Coincidentally, this peak value corresponds to the critical intensity demarcating the onset of stabilization.

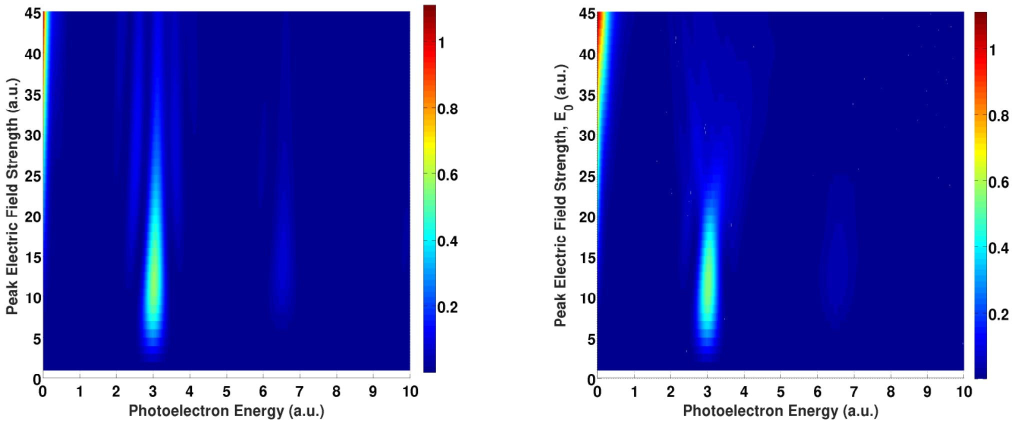

Figure 6.7: $3D$-colour plot showing the energy resolved photoelectron probability distribution of the lowest-order $\mathbf{A}\cdot\mathbf{p}_0$ term interaction spectrum on the left and multipole $\mathbf{A}\cdot\mathbf{p}_{0,1}+\mathbf{A}\cdot\mathbf{A}_{0,1}$ term interaction spectrum on the right at various peak electric field strengths, E_0, ranging from $1-45$ a.u.

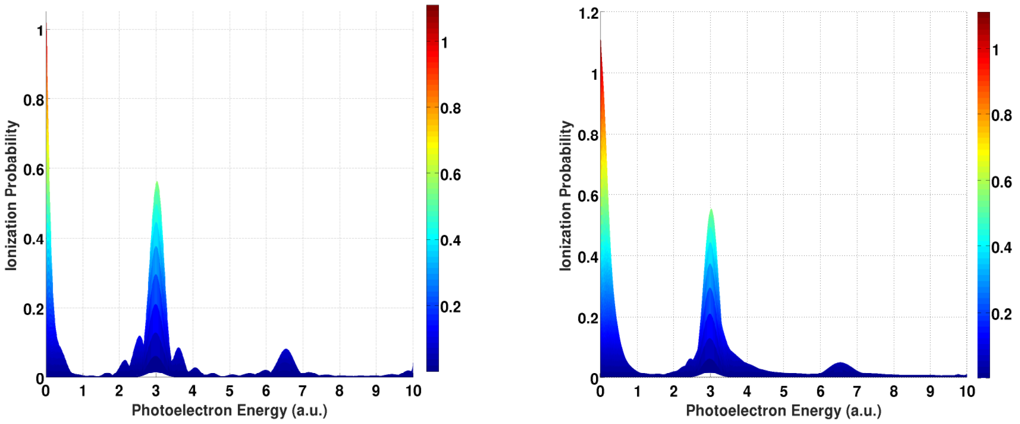

Figure 6.8: Same as figure 6.7 but from a different plane.

The stabilization effect breaks down at the point $E_0 = 30$ a.u. for the dipole spectrum, and $E_0 = 25$ a.u. for the multipole spectrum. The population of the low-energy photoelectrons begin to increase at about the peak value $E_0 = 12$ a.u. for both spectra although these low-energy electrons' probabilities are enhanced by the higher multipole-order effects. As the low-energy electron probabilities increase, the multiphoton ionization peaks decrease in amplitude as intensity rises after the onset of stabilization.

Key differences are also observable in the photoelectron energy spectra between the lowest-order interaction term only and the multipole interaction terms. In the lowest-order $\mathbf{A}\cdot\mathbf{p}_0$ term spectrum, the multiphoton peaks remain clearly resolved even at higher intensities. The above-the-threshold ionization (ATI) structures can also be observed by noticing that the second-photon peak is suppressed relative to the first-photon peaks for fixed valued intensity. The side bands are clearly resolved around the first photon peak and the number of side bands observable increases with intensity. One can argue that the enhancement of probability at lower energies and the suppression of probability at the multiphoton peaks as the radiation intensity increases correspond to an interplay of different ionization mechanisms where the former can be attributed to be a barrier-suppression ionization effect [71] and the latter to be a multiphoton ionization effect [41].

In the multipole-order terms spectra, there are less side bands which are not clearly resolved in the multipole spectrum. The disappearance of peaks and dips is also prominent. As an example, the second photon peak in figure 6.7 is more resolved in the lowest-order spectrum than in the multipole-order spectrum at higher intensities. Higher order interactions present in the multipole-order spectrum can also be seen to enhance the (very) low-energy structures, (V)LES, even in the relatively short-wavelength regime considered. The differences between the lowest-order $\mathbf{A} \cdot \mathbf{p}_0$ and multipole-order terms spectra could be a consequence of destructive interference of the amplitude between the different multipole interactions.

Despite the fact that the Rayleigh plane-wave multipole expansion has been employed in the calculations, the results are qualitatively similar to the findings of Morten [91]. In table 6.1, the Keldysh parameter regimes for which the non-dipole structures are magnified can be seen to be in the deep tunnelling regime. This means that the non-dipole interactions can be said to enhance tunnelling or over-the-barrier ionization.

Figures 6.9-6.10 show the variation of the photoelectron angular distribution with intensity. The distributions have been calculated using a generalized relation

$$I(\theta, \phi) = \sum_m B_m(\theta) \cos(m\phi) \tag{6.8}$$

obtained from equation (3) of reference [116]. In this equation I is the probability distribution which varies with the polar angle θ and the azimuthal angle ϕ and $B_m(\theta)$ are complex functions of $\sin\theta$, $\cos\theta$, the radial matrix elements, and the phase shifts. The relation successfully reproduced the experimental measurement of azimuthal dependence of the photoelectron angular distribution from $13^2D_{3/2}-$state sodium atoms aligned transversely to the direction of propapagation, and parallel to the direction of linear polarization, of $532-$nm ionizing radiation [116]. A similar distribution function, $I(\phi) = 1 + (2/3)^{1/2}(\delta + \gamma)\cos\phi$ with δ and γ as defined non-dipole fitting parameters, was also used to successfully reproduce the experimental measurements of the azimuthal angle dependence of 2000 eV Argon $1s$ photoelectrons at a fixed polar angle $\theta = 54.7°$ [117].

The expected dipolar probability angular distribution (PAD) as a function of intensity is well reproduced by the lowest-order $\mathbf{A} \cdot \mathbf{p}_0$ interaction term as shown in figure 6.9. It has the typical two maxima at 0 and 180° polar angles and a minimum at 90° polar angle. The probabilities generally increase with intensity and at higher intensities, an additional sub-peak forms at the 90° polar angle and two minima form at about 60° and 120° polar angles. The multipole angular probability distribution on the other hand can be seen to also vary with the radiation intensity. At lower intensities, the multipole PADs takes the symmetric doughnut-type distribution with the maxima at 0° and 180° polar angles and the minimum at 90° polar angle, just like the dipole PAD.

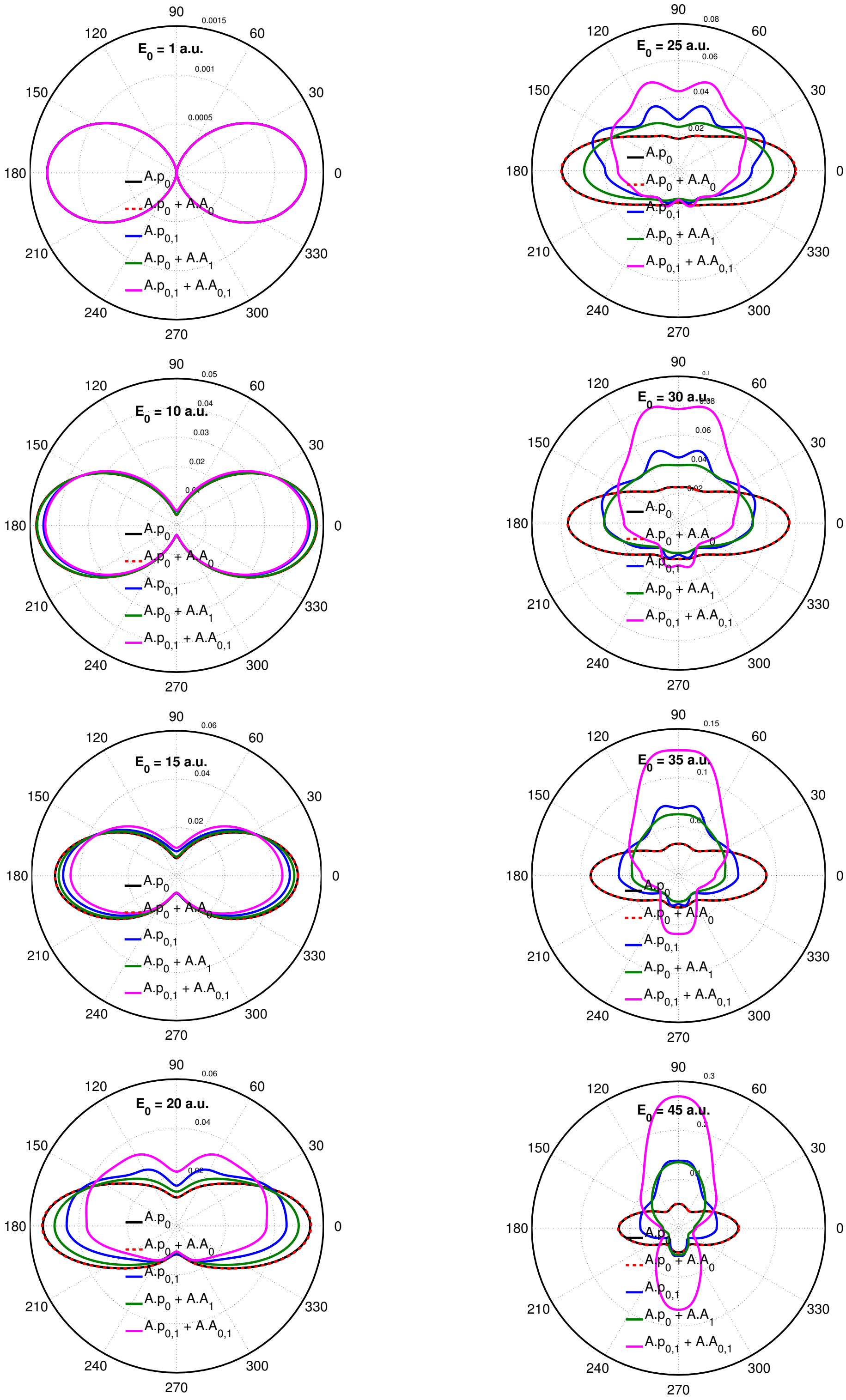

Figure 6.9: Comparison of non-dipole interactions effects in the photoelectron angular distributions for various peak electric field strengths ranging from $1 - 45$ a.u. The upper half-circle correspond to forward angle ($\phi = 0^\circ$) while the lower half-circle correspond to backward angle ($\phi = 180^\circ$) with respect to the propagation direction.

As the intensity increases, the non-dipole effects manifest first by tending to suppress the probability at angles less than 30° with the horizontal axis and thereafter by also enhancing the probability at angles greater than 30° with the horizontal axis along the direction of the laser propagation. At the peak field strength $E_0 = 25$ a.u., two maxima appear at about 70° and 110° polar angles corresponding to the effect of the first order $\mathbf{A} \cdot \mathbf{p}$ interaction. Further increase in intensity leads to a complete reversal of the multipole PADS with the predicted minimum becoming a maximum and the maxima becoming minima. In general, the multipole PADs observed can be described using two axes, the major and the minor axis.

At lower intensities, the major axis is oriented parallel to the electric field polarization axis (considered in this study to be in the $+z$ direction) and the minor oriented parallel to the laser propagation axis. As radiation intensity rises, the axis parallel to the polarization direction shortens as the other axis parallel to the propagation direction (considered in this study to be in the $+x$ axis) is elongated. At higher intensities, the picture is completely reversed. The major axis is shifted to be along the propagation direction while the minor axis is shifted along the polarization direction. The crossing point between the dipole and the non-dipole distributions at high intensities range between 38° and 44° relative to the horizontal axis.

The effect of first-order $\mathbf{A} \cdot \mathbf{p}_1$ correction term is generally higher, as already discussed, but comparable to that of the first order $\mathbf{A} \cdot \mathbf{A}_1$ correction term. This means that they should always be treated together in order to reproduce accurate non-dipole results since the overall change in ionization seems to be bigger than a cumulative sum of the change corresponding to each individual non-dipole interaction. The 0° and 180° polar angles correspond to parallel and anti-parallel alignment of the electron to the electric field $\mathbf{E}$ while the 90° polar angle correspond to the parallel alignment of the electron to the radiation propagation vector $\mathbf{k}$.

Similar to experimental observations, the probability angular distributions show the forward-backward asymmetry with respect to the azimuthal angle ϕ when non-dipole interactions manifest. The non-dipole PADs have distorted lobes which are enhanced in the direction of radiation propagation and suppressed in the reverse direction [116, 117]. The PADs show that as the radiation intensity rises, the photoelectrons are more likely to be emitted in the plane of radiation propagation. The sharp contrast with the lowest-order distributions further show that above some critical intensity (above 1 a.u.), higher multipole-order interactions need to be considered. Figure 6.10 shows the lowest-order $\mathbf{A} \cdot \mathbf{p}_0$ (left) and the multipole $\mathbf{A} \cdot \mathbf{p}_{0,1} + \mathbf{A} \cdot \mathbf{A}_{0,1}$ (right) PAD in the forward-backward directions of propagation integrated for all the peak elecric field strengths considered. In the lowest-order interaction term, the PADs are symmetric and concentrated parallel or counter-parallel to the polarization direction.

At higher intensities, a sub-maximum is formed along the propagation direction for the lowest-order PAD. The picture formed by the multipole PAD, on the other hand, shows the transversal cusp-like distribution [147] as the field intensity increases with a major lobe in the propagation direction and a minor lobe in the counter-propagation direction. These cusp-like distributions are concentrated, as can be seen in the $3D$ photoelectron spectrum at near-threshold energies. One can attribute the cusps to be a consequence of tunneling and the barrier-suppression ionization (BSI) since they appear only at higher radiation intensities. It is noted that the concepts of tunneling and barrier suppression are usually discussed only for low-frequency fields with the explanation that at the high-frequencies, the ejected electron does not have enough time to tunnel before the electric field changes. By observing the present ejected electron distributions, one can conclude that at very high intensities, even the high-frequency fields display similar strong-field traits like ATI, HHG, tunneling, BSI, etc. Indeed Delone and Krainov [72] discuss the possibility of observing BSI at high frequency with the increasing radiation field strength.

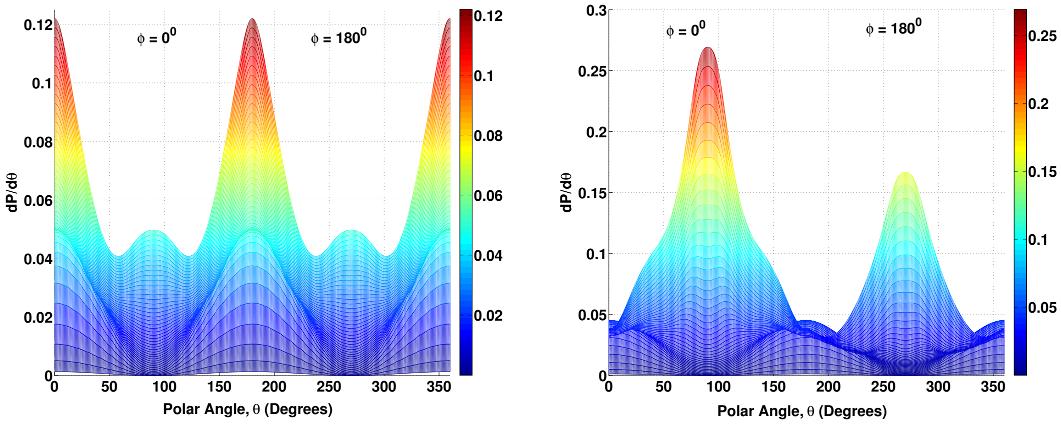

Figure 6.10: $3D$-colour plots showing the photoelectron angular probability distribution of the lowest-order $\mathbf{A}\cdot\mathbf{p}_0$ (left) and multipole $\mathbf{A}\cdot\mathbf{p}_{0,1}+\mathbf{A}\cdot\mathbf{A}_{0,1}$ (right) interaction spectra at various peak electric field strengths, E_0, ranging from $1-45$ a.u.

Figures 6.11 shows additional 3−D PADs for the lowest-order $\mathbf{A}\cdot\mathbf{p}_0$ interaction term compared to the multipole $\mathbf{A}\cdot\mathbf{p}_{0,1}+\mathbf{A}\cdot\mathbf{A}_{0,1}$ interaction term in figure 6.12 and 6.13. The $x-y$ and $x-z$ plane side views are shown for both interaction potential terms, but for the multipole interaction potential term, an additional $y-z$ view is included because of the asymmetry in its azimuthal distribution. For the lowest-order interaction term, the $x-z$ and the $y-z$ plane side views are exactly symmetric since there is no asymmetry in the azimuthal angle dependence in the interaction Hamiltonian. The multipole distribution is quite different for each of the side views as can be seen in the plots. Except for the $y-z$ plane side view which has two lines of symmetry in the multipole distribution, the other planes have only one line of symmetry. At lower intensities (less than 15 a.u.), the interactions seem to be the perturbative regime (although this is apparently contrary to the characterization using the Keldysh parameter) where only the dipole interactions are sufficient to describe the ionization dynamics. This can be confirmed by the dipole type doughnut PAD distributions in the multipole spectrum for the ~ 15 a.u. intensity regimes. The multipole PADs in the 3−D figures illustrate the self-focussing behaviour of the photoelectron cloud as the laser intensity increases, that is, the two polar maxima drift towards the propagation direction as intensity rises and finally converge into one spot at the maximum intensity considered.

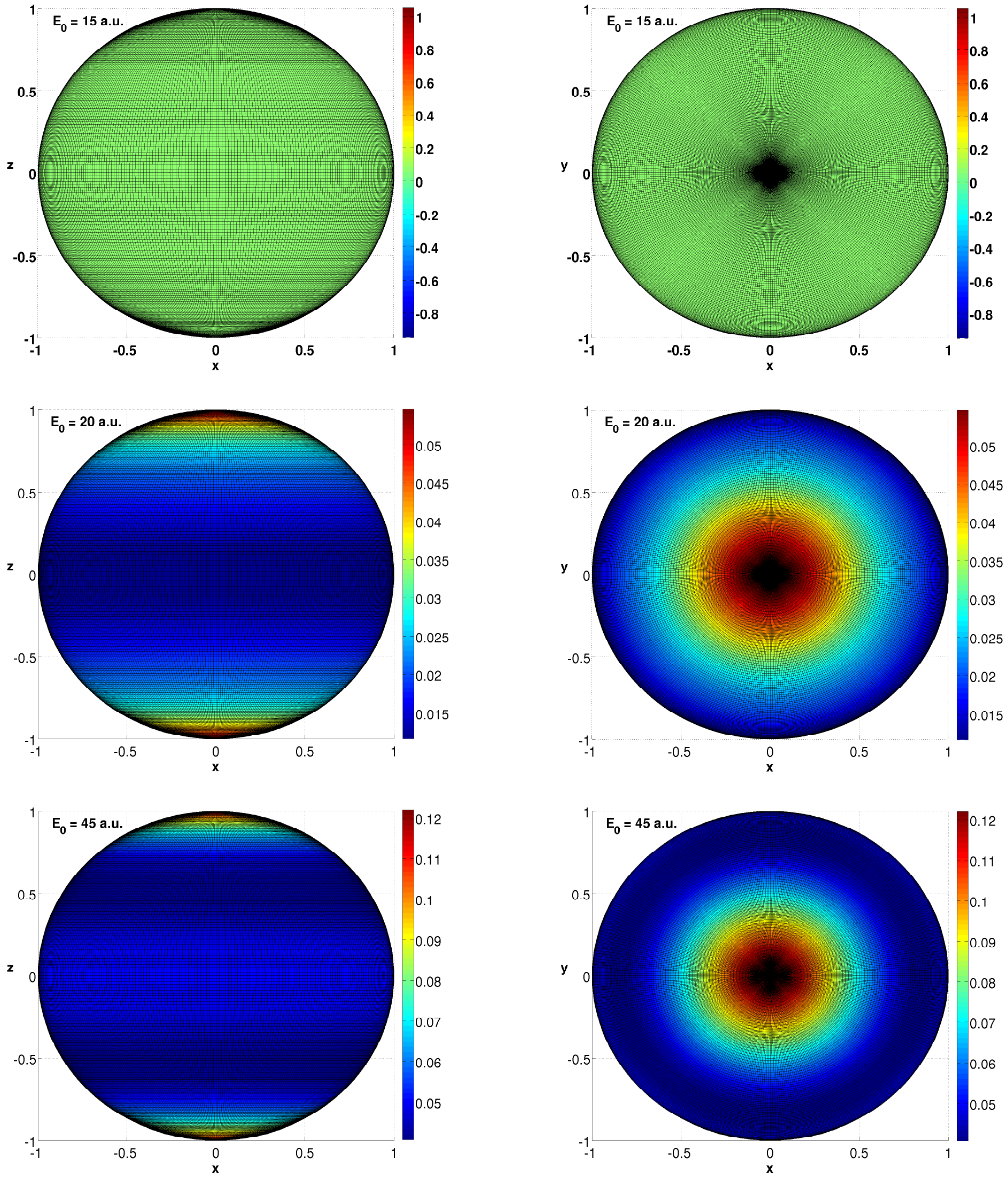

Figure 6.11: $3D-$ lowest-order $\mathbf{A} \cdot \mathbf{p}_0$ photoelectron angular distribution for the intensities of $15, 20$, and 45 a.u. Left: the $x-z$ plane view showing the polar probability variation. Right: the $x-y$ plane view showing the azimuthal probability variation.

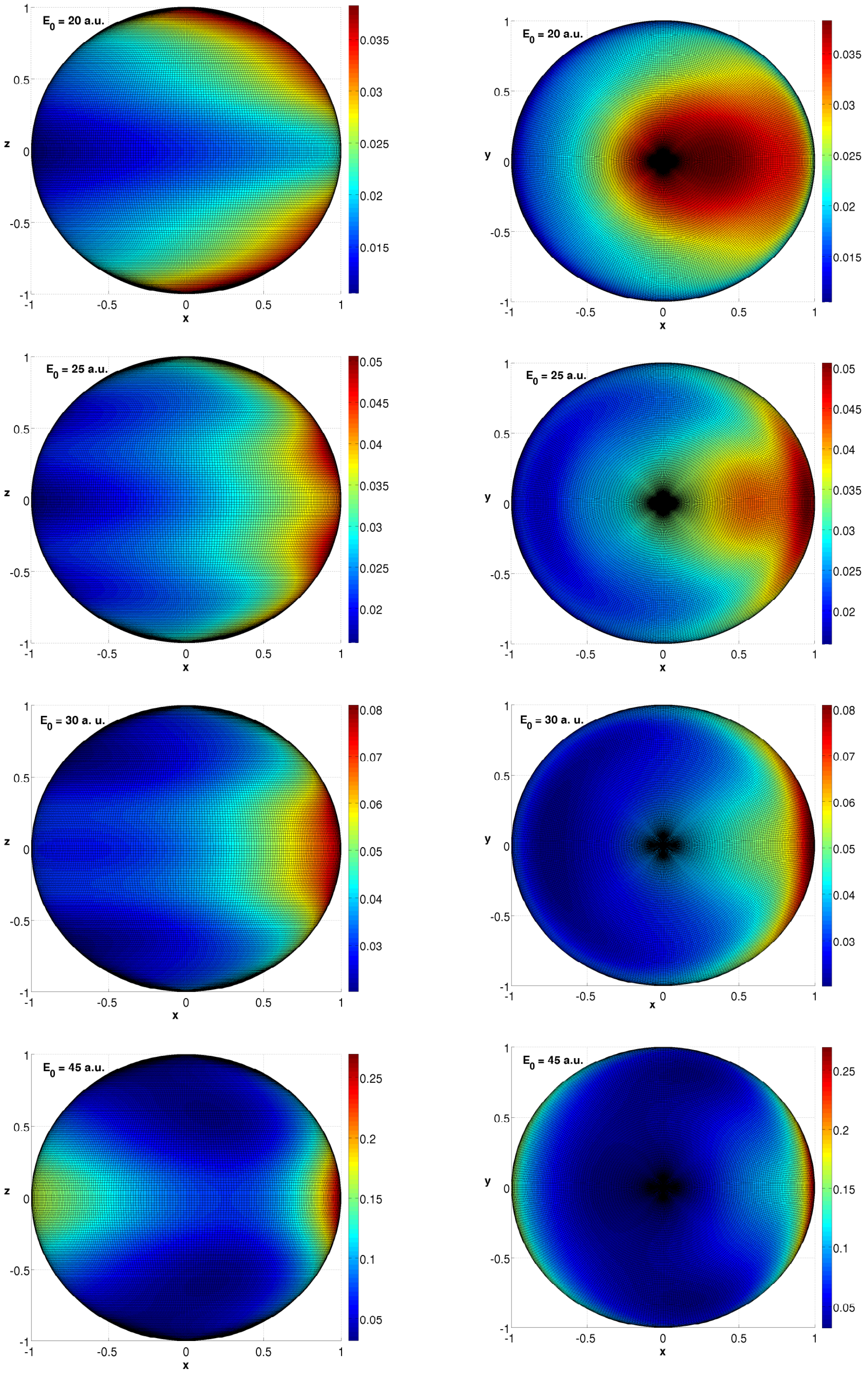

Figure 6.12: Same as figure 6.11 but for the multipole $\mathbf{A}\cdot\mathbf{p}_{0,1}+\mathbf{A}\cdot\mathbf{A}_{0,1}$ PADs for the intensities of $20, 25, 30$, and 45 a.u.

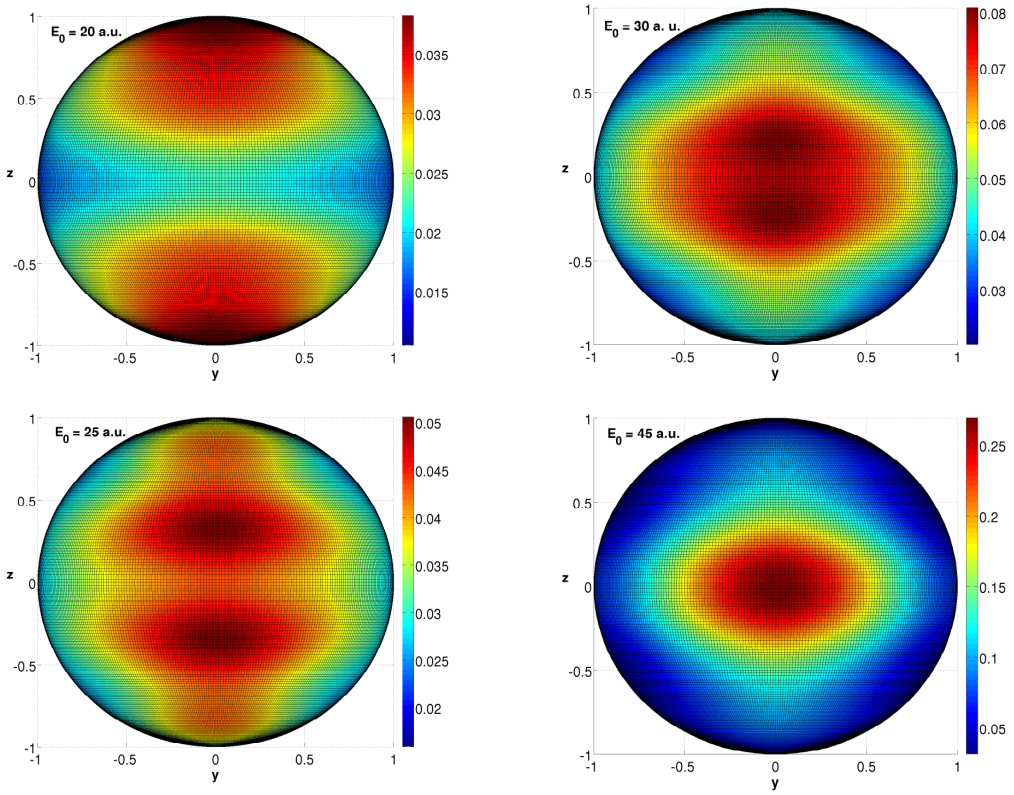

Figure 6.13: Same as figure (6.12) but showing the polar probability variation for the $y - z$ plane view .

6.6 Dependence of Ionization on Wavelength

In this section, the wavelength dependence of the multipole-order multiphoton ionization of hydrogen atom in its ground state is investigated using a 10 cycle linearly polarized laser pulses with peak electric field strengths of 1 a.u. and 45 a.u. The Taylor plane-wave expansion series is exclusively used in the investigation for computational convenience only. The Taylor expansion series, as opposed to the Rayleigh plane-wave expansion series, are advantageous if the focus is solely on the dipole and quadrupole terms of interactions without considering the effect of higher order interactions . The basis-set parameters used in the calculations include: $r_{\max} = 200$, $L_{\max}, M_{\max} = 25$, 600 B splines of order $k = 10$, and a geometric knot sequence.

Figure 6.14 shows the variation of ionization probability with wavelength for a 10 cycle linearly polarized laser pulse with its peak electric field strength fixed at 1 a.u. The symbols indicate the data points while the lines joining them are merely for guiding the eye. The range of the ponderomotive potential U_p and Keldysh parameters γ corresponding to some of the wavelengths is presented in table 6.2. As the wavelength increases, γ decreases in value characterising the interactions to be in the tunneling regime. The non-dipole effects can be visualized by looking at the relative deviation from the lowest-order $\mathbf{A}\cdot\mathbf{p}_0$ spectrum. From the magnitude of the relative deviation, it can be seen that the total ionization probability manifests some tiny non-linear non-dipole dependence at the peak intensity considered. The total ionization probability increases non-linearly with increase in wavelength up to some point before it reaches saturation. The excitation probability also shows saturation behaviour and a saddle point with a sub-minimum as the radiation wavelength increases. The non-dipole induced changes in the probability distribution, on the other hand, rise abruptly and then decreases on this ionization rising edge upto a minimum at the onset of saturation before it begins to rise again with some resonant-like enhancements at various points as the wavelength increase. This observation is also true for excitation except for the initial abrupt rise.

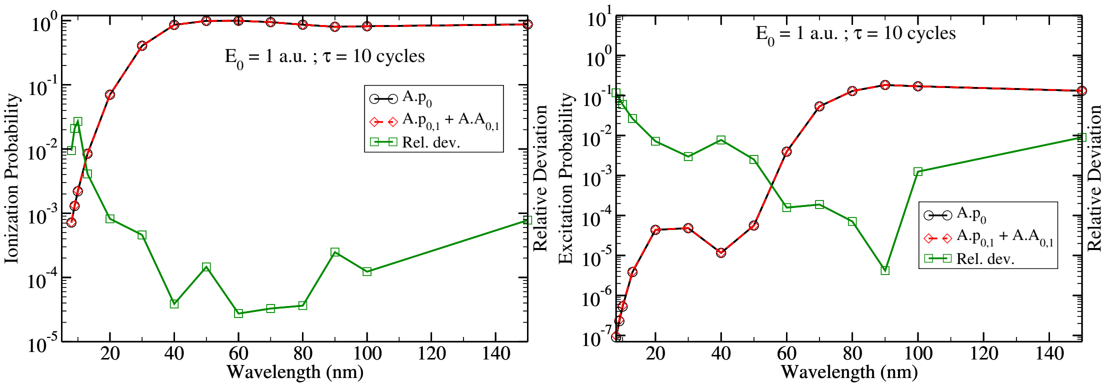

Figure 6.14: Multipole ionization (left) and excitation (right) probability dependence on wavelength for a linearly polarized laser field with a peak electric field strength of 1 a.u. and pulse duration of 10 cycles.

Figure 6.15 shows multipole multiphoton photoelectron energy spectra for various laser field wavelengths at a fixed peak electric field strength, $E_0 = 1$ a.u. and a fixed pulse duration of 10 cycle pulses. The corresponding wavelength, in nm, for each graph is specified inside the graph. The black solid lines correspond to the lowest-order $\mathbf{A}\cdot\mathbf{p}_0$ term spectra while the red dashed lines correspond to the dipole plus quadrupole spectra. The multipole $\mathbf{A}\cdot\mathbf{p}_{0,1}+\mathbf{A}\cdot\mathbf{A}_{0,1}$ spectra consists in this case the $0^{\text{th}}-$ and the $1^{\text{st}}-$ order transitions in both $\mathbf{A}\cdot\mathbf{p}$ and $\mathbf{A}\cdot\mathbf{A}$ interaction terms. In all the wavelengths considered, it can be observed that non-dipole effects manifest significantly at higher photoelectron energies. At lower photoelectron energies, the non-dipole effects become visible as the wavelength increases. For example, non-dipole effects become visible at 0.2 a.u. photoelectron energy for 100 nm while for 8 nm the effects become visible at about 7 a.u. photoelectron energy for the intensity considered. In general, one can conclude that at a constant intensity the non-dipole effects increase with the wavelength as well as the photoelectron energies.

Wavelength (nm)	8	10	20	30	50	70	100	150
U_p a.u.	0.01	0.01	0.05	0.12	0.30	0.59	1.20	2.71
γ	5.70	4.56	2.28	1.52	0.91	0.65	0.46	0.30

Table 6.2: Table showing the variation of the U_p and γ with wavelength.

Figure 6.16 shows the wavelength dependence of the photoelectron polar angular distribution corresponding to the dipole (black solid line) and the non-dipole (red dashed line) spectra at a fixed peak electric field strength, $E_0 = 1$ a.u. and a fixed pulse duration, $\tau = 10$ cycles. For wavelengths less than or equal to 10 nm, it can be observed that there is a symmetric enhancement of the ionization probability which one can attribute to be an effect of the lowest-order $\mathbf{A} \cdot \mathbf{A}_0$ term. Between $10 - 30$ nm, the non-dipole effect in the angular distribution is not explicitly visible in the angular distribution. As the wavelengths increase beyond 30 nm, the non-dipole forward-backward asymmetry sets in and increases with wavelength. The photoelectron probability along and opposite the polarization direction also decrease simultaneously. From this figure, it is also quite evident that non-dipole effects at a fixed intensity increase with wavelength.

Based on the Keldysh classification scheme as depicted in table 6.2 and in figures 6.15 and 6.16, the wavelength dependent non-dipole effects in the PES show up at the Keldysh parameter of order $\gamma \sim 1$. The effects increase as $\gamma \to 0$. In the PADs on the other hand, the effects only manifest at $\gamma < 1$ and become more significant as the Keldysh parameter decreases further. The observation is also true for the intensity dependence already discussed in section 6.5. The significance of the non-dipole effects can be seen to be more in the tunneling and in the barrier-suppression regime.

The dipole photoionization probabilities have been shown in previous studies [148] to increase monotonically as the laser wavelength decreases. In the present multipole probabilities in which the spatial effects embedded in the correlation $\sim kr$ are included, the non-dipole probabilities are also seen to increase with wavelengths. At the peak electric field strength considered, the dipole interactions are dominant but as wavelength increases, the significance of the non-dipole effects in the total ionization and excitation yields is observed to increase.

Despite the fact that the total ionization probabilities shown in figure 6.14 are not as sensitive to the wavelength-dependent non-dipole effects as the angular and energy differential probabilities at non-varying intensities. The relative importance of the non-dipole effects as the radiation wavelength increase seems to contradict the reasoning behind the dipole approximation. The dipole approximation assumes that at longer wavelengths, the excursion radius at the peak of the field amplitude is far much less than the radiation wavelength ($r \ll \lambda$) and therefore $e^{i\mathbf{k}\cdot\mathbf{r}} \approx 1$ is justified. From the observations, it is seen that the dipole approximation is likely to breakdown as the wavelength increases (and not the reverse) and the intensity remains invariant. A similar argument has been presented by Reiss [85, 86] where the dipole oasis, the lower and upper dipole limits, and the laser parameter regimes where the non-dipole effects are likely to manifest are illustrated. According to these references, the lower-dipole limit beyond which the dipole approximation breaks down manifests at relatively low intensities for longer wavelengths whereas the upper-dipole limit is sharply defined at a wavelength of about 0.3 nm regardless of the intensity.

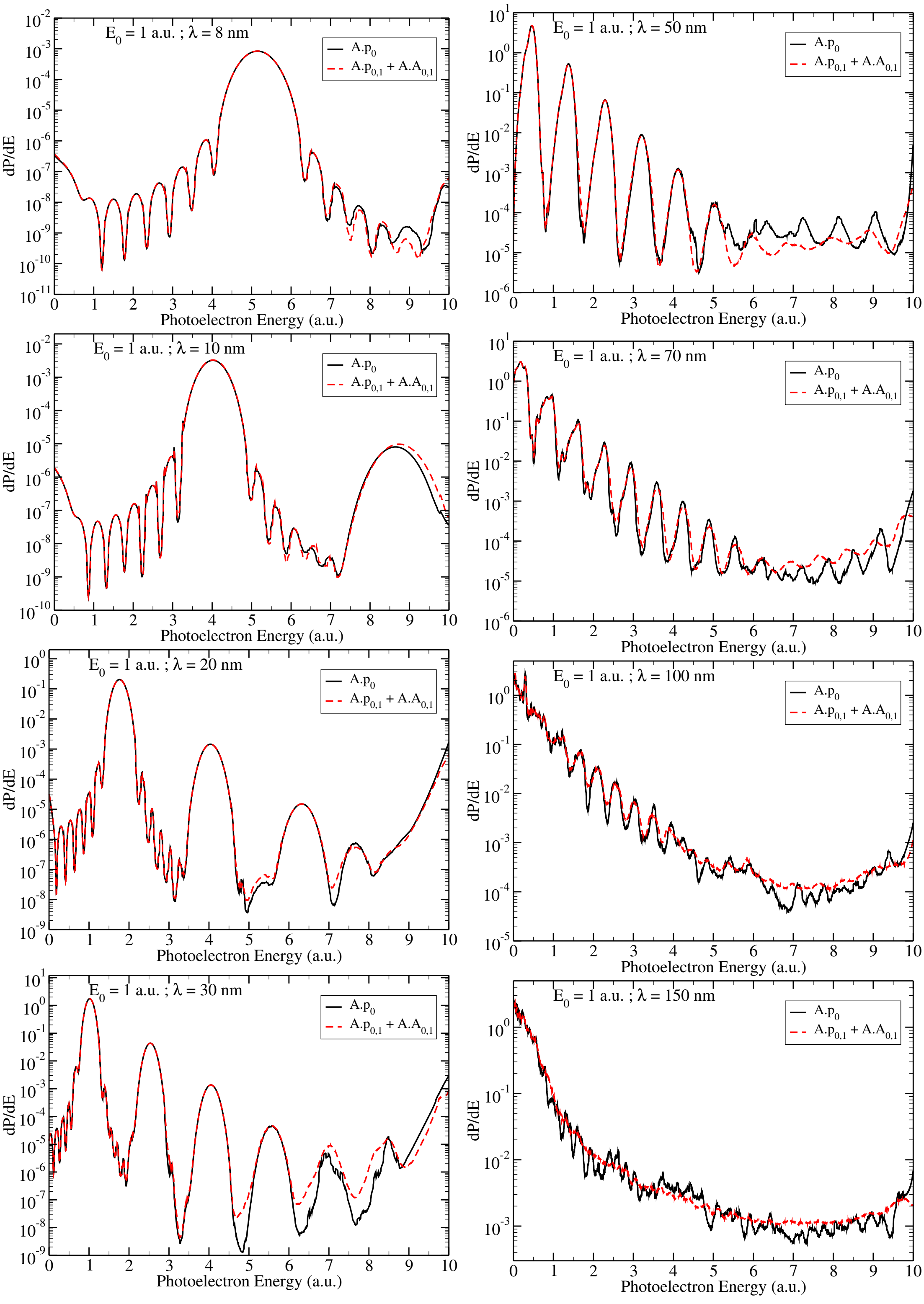

Figure 6.15: Wavelength dependence of the lowest-order $\mathbf{A}\cdot\mathbf{p}_0$ and multipole $\mathbf{A}\cdot\mathbf{p}_{0,1}+\mathbf{A}\cdot\mathbf{A}_{0,1}$ multiphoton photoelectron energy spectra for a 10 cycle linearly polarized laser field with a peak electric field strength, $E_0 = 1$ a.u.

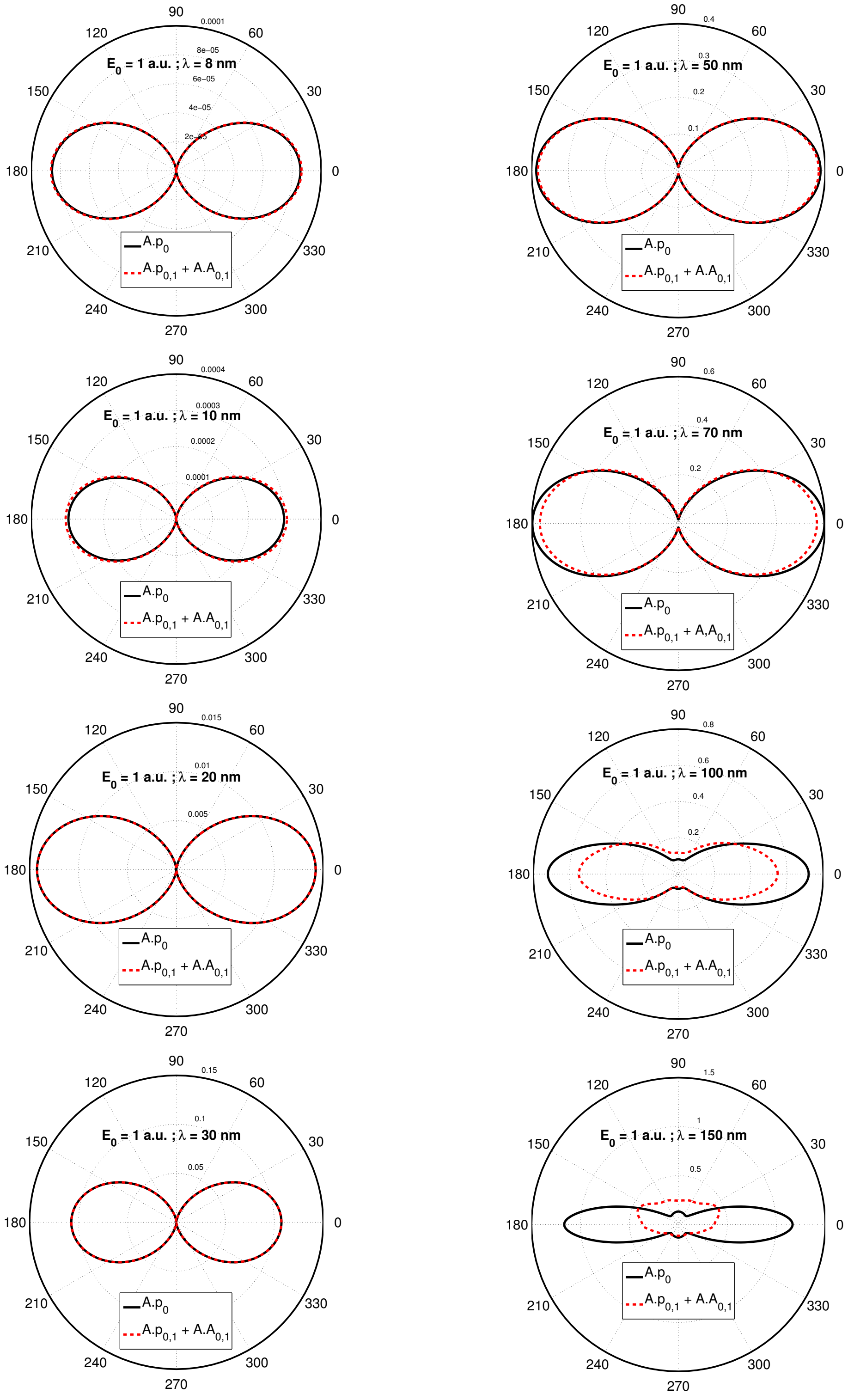

Figure 6.16: Wavelength dependence of the lowest-order $\mathbf{A} \cdot \mathbf{p}_0$ and multipole $\mathbf{A} \cdot \mathbf{p}_{0,1} + \mathbf{A} \cdot \mathbf{A}_{0,1}$ multiphoton PAD for a 10 cycle linearly polarized laser field with a fixed peak electric field strength of $E_0 = 1$ a.u. The upper half-circle correspond to forward angle ($\phi = 0°$) while the lower half-circle correspond to backward angle ($\phi = 180°$) with respect to the propagation direction.

6.7 Dependence of Ionization on Pulse Duration and Interaction Time

In the perturbative regime, the ionization probability has a linear dependence with increasing pulse duration [149]. At higher intensities, Horbatsch [150] observed in the numerical calculation of ATI of hydrogen atom at $\sim 10^{14} - 10^{20}$ Wcm^{-2} intensities and 0.4 a.u. wavelength that the total ionization yield shows little dependence on pulse duration at short laser pulses. At longer pulse durations ranging from $100 - 20,000$ cycles, reference [151] observes an increase in ionization yield with pulse duration and a non-linear wavelength dependence at very high intensities. In this section, the ionization dependence on pulse duration if the non-dipole terms are included in the interaction Hamiltonian is investigated.

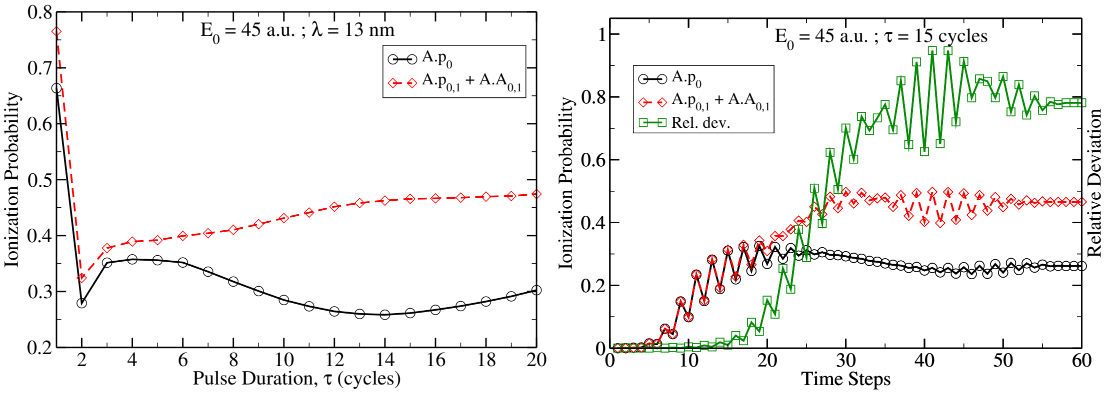

Figure 6.17: Ionization probability dependence on the pulse duration (left) and interaction time (right) for a 13 nm laser pulse with a fixed peak electric field strength, $E_0 = 45$ a.u.

Figure 6.17 shows the total ionization probability as a function of pulse duration on the left and as a function of time (during interaction) on the right for a laser pulse with definite wavelength of 13 nm and peak electric field strength of $E_0 = 45$ a.u. The dependence of ionization probability on time during the interaction process should be interpreted with caution because the picture is gauge-dependent, but one can get some insights even within the gauge-dependent picture. In the perturbative regime, where the non-dipole effects are expected to be vanishingly small, the evolution of ionization probability has linear dependence with pulse duration. The non-perturbative regime considered in this case already shows non-linear dependence of the ionization probability with pulse duration in the lowest-order ($\mathbf{A} \cdot \mathbf{p}_0$) interaction term. It can be seen that the ionization probability of a single-cycle pulse is very high, but it falls sharply for a two-cycle pulse. It then rises at three cycles where it saturates and then gradually falls to a minimum at about 14 cycles before begining to rise gradually.

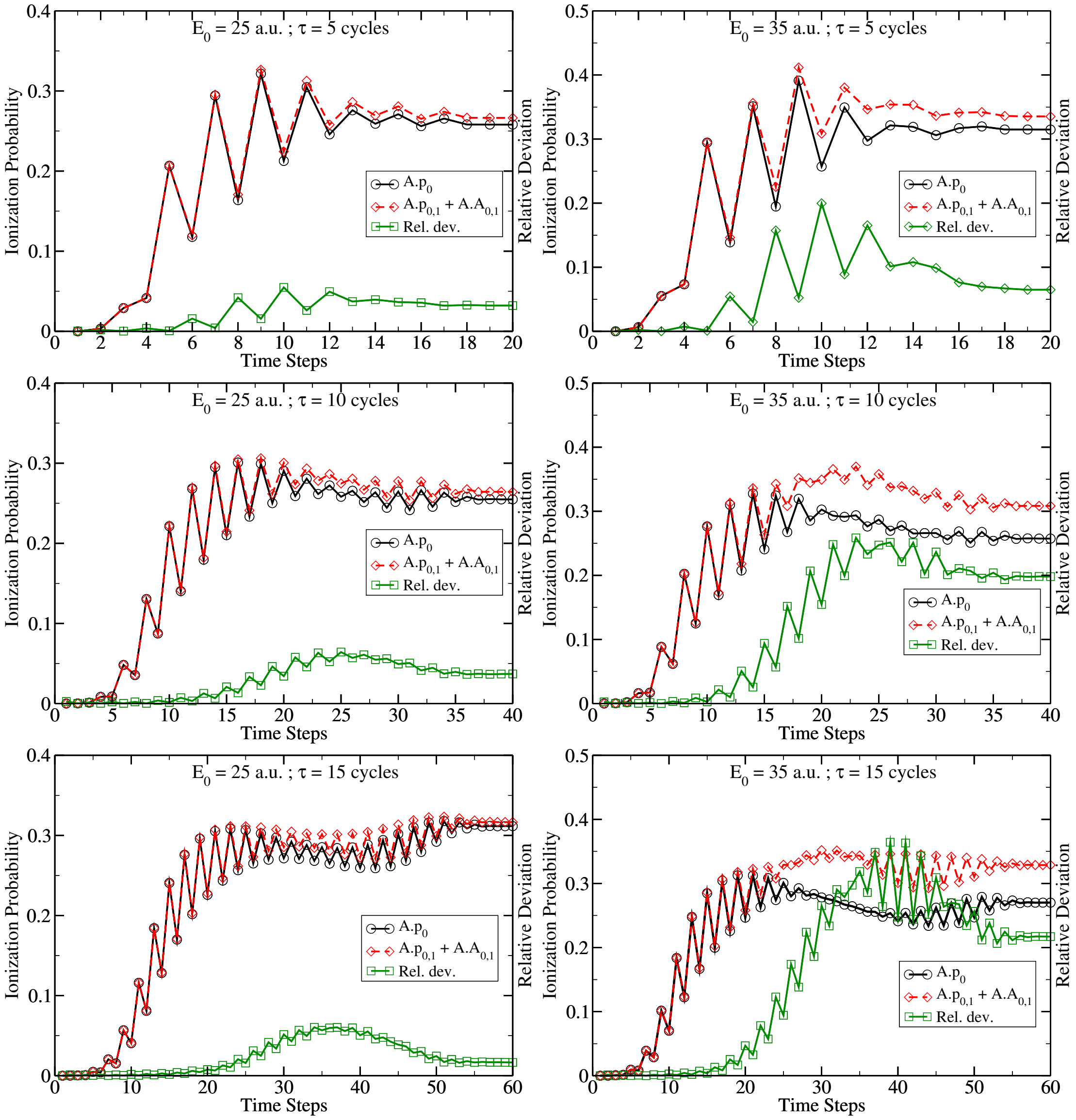

Figure 6.18: Multipole-order ionization probability variation with interaction time for a 5, 10, and 15 cycle laser pulse, arranged from top to bottom respectively, with 13 nm wavelength and peak electric field strengths $E_0 = 25$ a.u. on the left and 35 a.u. on the right. The relative deviation is the difference between the spectra divided by the zero order $\mathbf{A} \cdot \mathbf{p}$ distribution.

The dependence of the multipole-order ionization probability with pulse duration is on the other hand quite different. Below three-cycle pulse duration, the trend is similar with that of the lwest-order interaction but there after, the ionization probability increases almost linearly with the pulse duration. On can argue that the non-dipole corrections increase the adiabatic response to laser-matter interactions. For the lowest-order ($\mathbf{A} \cdot \mathbf{p}_0$) interactions, one can observe that the non-adiabatic short pulse response lasts for relatively longer pulse durations as compared to the multipole-order interactions.

The effect of the non-dipole interactions as a function of time during the interaction is viewed in terms of the relative deviation of the multipole-order ionization probability from the lowest-order probability during the time evolution. It can be observed that, just like ionization process itself, the non-dipole effects possess exponential dependence on time evolution similar to a charging capacitor.

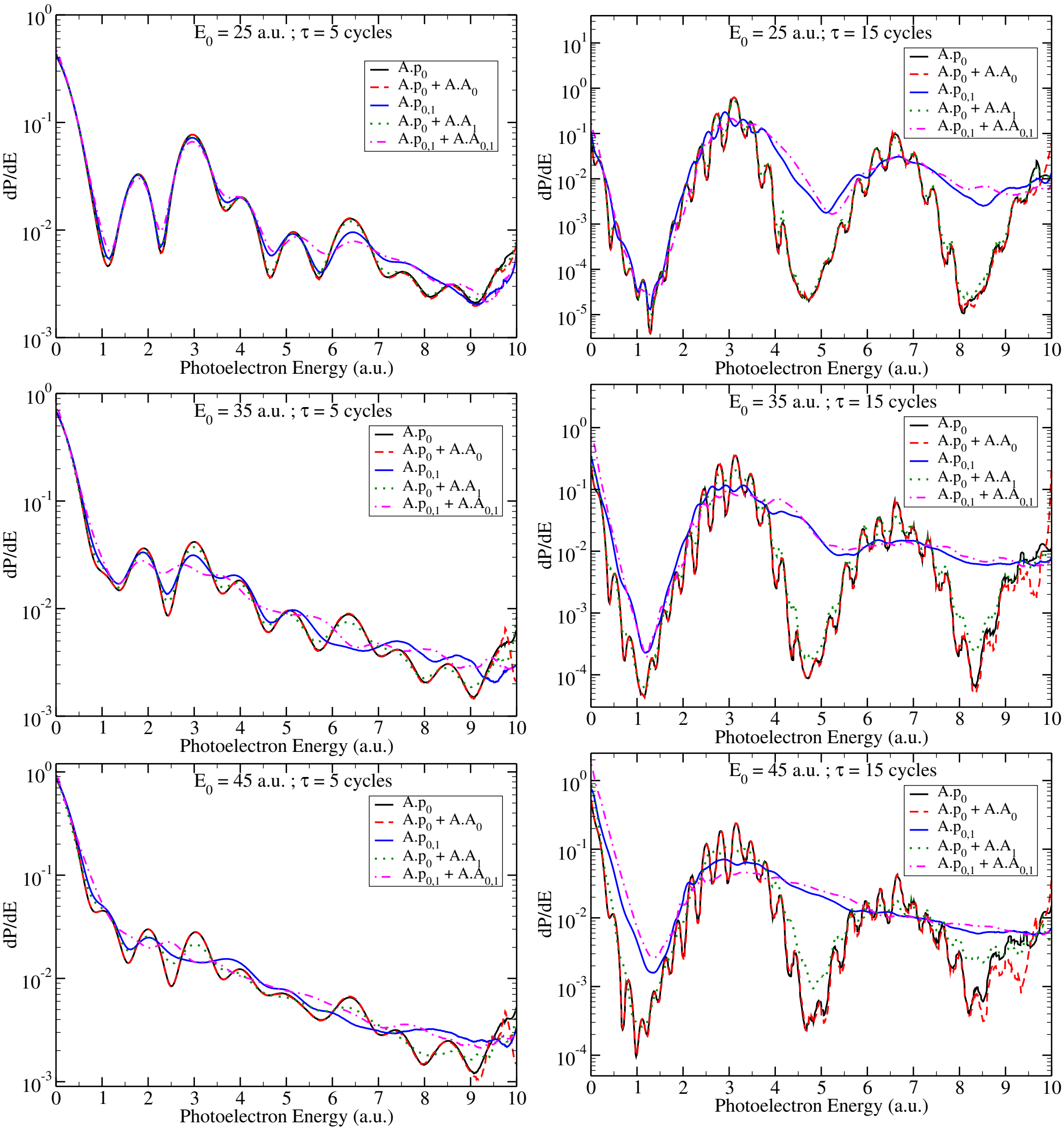

Figure 6.19: Multipole-order photoelectron energy spectra for a 5 cycle (left) and a 15 cycle (right) laser pulse with a wavelength of 13 nm and peak electric field strengths $E_0 = 25, 35$ and 45 a.u. in the top, middle, and bottom respectively.

The influence of the carrier-wave oscillations embedded within the carrier envelope are also apparent. Figure 6.18 further shows ionization probability variation with time during the interaction process for different field strengths and pulse durations. It can be concluded also from this figure that non-dipole effects increase with the laser pulse duration, electric field strength, and with time during interaction up to some saturation point . Figure 6.19 shows the variation of the ATI peak structure with the total pulse duration for different peak electric field strengths. The ATI peaks are well resolved for longer pulse durations as compared to the shorter pulse durations.

6.8 Peak Suppression and Peak Shifting

It is discussed in section 2.2.3 that the use of short intense pulses in strong-field ionization embed a unique signature of peak shifting and peak suppression, a feature which longer pulse durations do not possess. In this section, the additional effect of the non-dipole interactions on these short pulse characteristic features is analyzed.

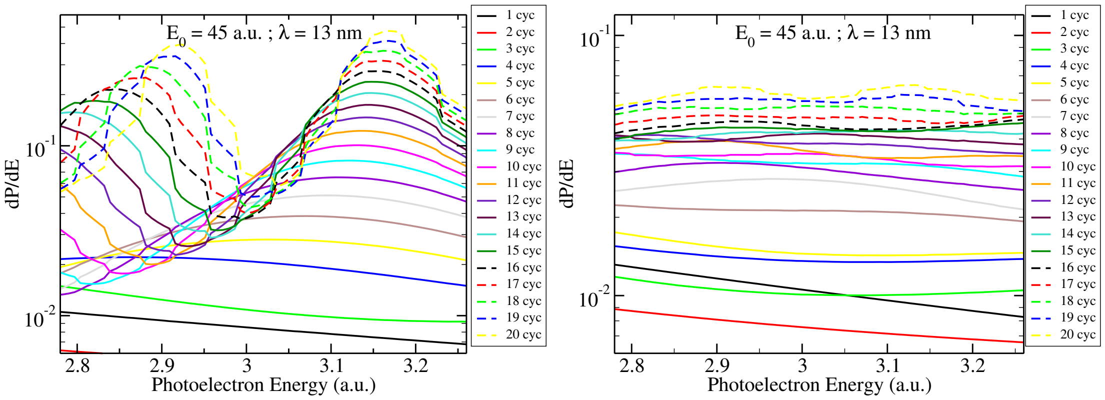

Figure 6.20: First photon peak position and amplitude as a function of the pulse duration for the lowest-order $\mathbf{A}\cdot\mathbf{p}_0$ term (left) and the multipole $\mathbf{A}\cdot\mathbf{p}_{0,1}+\mathbf{A}\cdot\mathbf{A}_{0,1}$ term (right) for a 13 nm laser pulse with a fixed peak electric field strength, $E_0 = 45$ a.u.

Figure 6.20 shows the first-photon peak position and amplitude as a function of the laser pulse duration for the lowest-order $\mathbf{A}\cdot\mathbf{p}_0$ interaction term (left) and the multipole $\mathbf{A}\cdot\mathbf{p}_{0,1}+\mathbf{A}\cdot\mathbf{A}_{0,1}$ interaction term (right) for a 13 nm laser pulse with a fixed peak electric field strength, $E_0 = 45$ a.u. It can be considered that at the longer pulse durations, the effect of the pulse bandwidth is minimal and therefore the position of the peak relative to the expected photoelectron energy position, 3 a.u. in this case, indicates the magnitude of the dynamic Stark shift at this intensity [130]. The lowest-order $\mathbf{A}\cdot\mathbf{p}_0$ interaction term captures the expected observation as the pulse duration decreases. The peak position shifts to the left and the peak amplitude is suppressed. This implies that there is an carrier-envelope induced energy shift that increases inversely with pulse duration, an effect already known for ionization with few-cycle pulses [152]. This shift appears to be out of phase with the dynamic Stark shift changing the resonance position towards the left and reducing the amplitude consequently.

If the multipole interaction terms are considered, the shifting of peaks is less resolved with the broadening of the peaks and the levelling of the valleys. This property is similar to the disappearance of the ATI structure observed at higher intensities for optical wavelengths, an effect attributed to be a consequence of the spatio-temporal intensity distribution of the laser focus [152]. That is, the peak structure washes out if volume averaging is taken into account for gas jet atoms exposed to different peak intensities resulting into different light shifts [152, 153]. The vanishing of the ATI structure with the inclusion of the multipole interaction terms can also be a consequence of the absence of rescattering, induced by the elliptical polarization of the higher multipole-order interaction components, which prevent electrons from returning to the ion core [152].

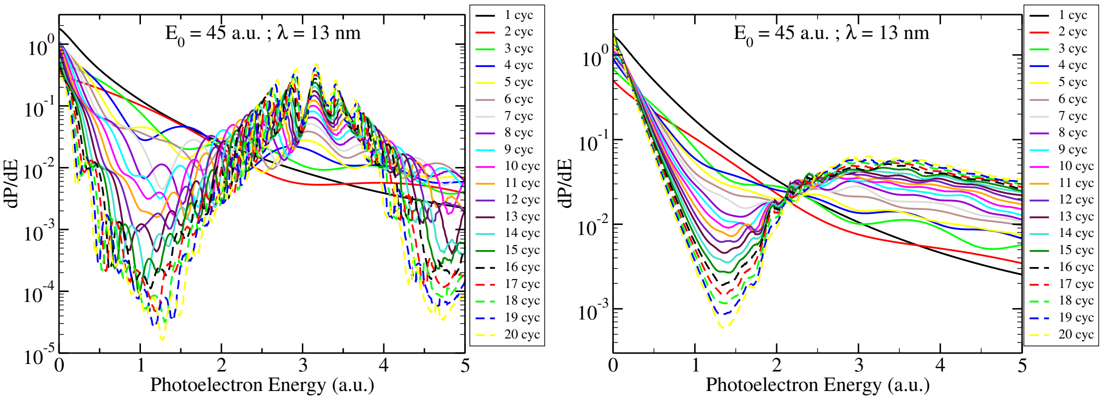

Figure 6.21: Same as figure (6.20) but for a larger photoelectron energy window.

If the window of photoelectron energy within this first-photon peak is widened as in figure 6.21, a new unique feature emerges from the multipole-order spectra. There are two distinct crossings which are absent in the lowest-order $\mathbf{A}\cdot\mathbf{p}_0$ term spectra. These crossings show little dependence on pulse duration. We can infer from the carrier-envelope function that these are the photoelectrons born at time $t = 0.25\tau$ and $t = 0.75\tau$ when the value of the cosine function $\cos 2\pi t/\tau$ in the pulse envelope is zero. The photoelectron energy corresponding to those times are completely free from the pulse duration induced widths. The non-adiabatic short pulse interactions show some small deviations at these points because of their inverse dependence on pulse duration originating from the electric field correction term.

Figure 6.22 shows the energy shifts extracted from the deviation of the first-photon peak position in the energy spectrum relative to the expected 3 a.u. value as a function of pulse duration. The values have been extracted for only the lowest-order $\mathbf{A}\cdot\mathbf{p}_0$ term spectra shown in figure (6.20). Plotted along side is a fitting function

$$\Delta\omega_\tau = 0.115\left(1 - \exp\left[\frac{2\pi}{\tau} - 0.24 \times \frac{4\pi^2}{\tau^2}\right]\right) + 0.21 \tag{6.9}$$

which successfully reproduces the pulse duration dependence for pulse widths greater than four cycles. The intercept value 0.21 could be equivalent to the magnitude of the dynamic Stark shift corresponding to the peak electric field strength of 45 a.u. The other constants, 0.115 and 0.24 are the additional fitting parameters which may be related to the pulse or system characteristic features. The strong deviation from this fitting function for lower pulse durations can indicate the role of non-adiabatic interactions at the shorter pulse widths. The point of deviation, $\tau = 5$ cycles, is closer to the 4 cycles value considered to be the threshold of short pulses where the phase of the carrier-envelope function becomes physically important [154].

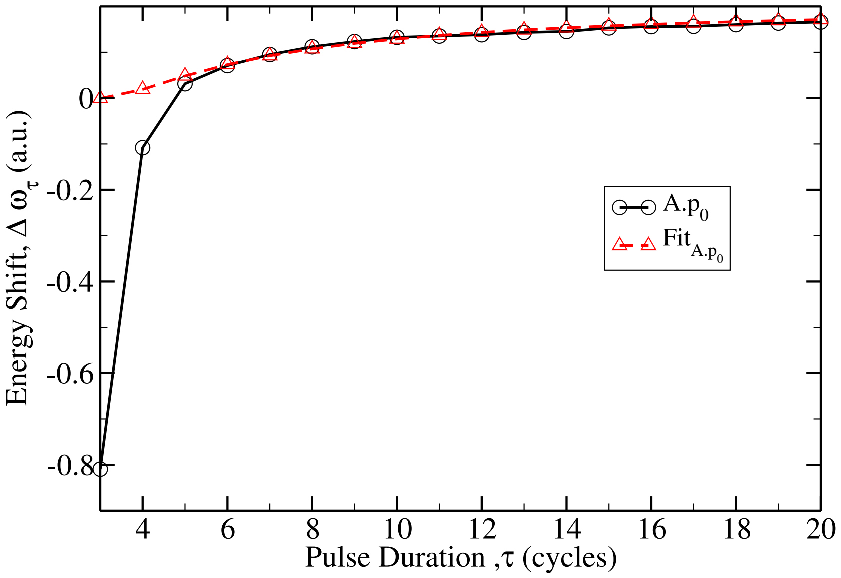

Figure 6.22: Energy shift of the first-photon peak as a function of pulse duration for the lowest-order $\mathbf{A} \cdot \mathbf{p}_0$ interaction in figure (6.20). Black solid line are the extracted values and the red dashed line is a fitting function.

6.9 Dependence of Ionization on the Initial State

The Ionization dynamics is not only sensitive to the laser parameters but also to the structural effects like the ionization potential and the initial state geometry. The ionization potential and the quality of the eigenvectors can be greatly improved by testing for convergence of eigenvalues while adjusting the numerical parameters like the box radius, the number and density of B splines, the order of B splines, and the knot sequence. Sensitivity to the initial state is a characteristic that is made use of in spectroscopy. Each state has its unique properties like ionization potential and line shifts in the presence of electric, magnetic, and optical fields. These features manifest in the energy spectrum making them useful in characterizing the system properties.

Figure 6.23 shows the photoelectron energy spectra for the hydrogen atom at different initial states for two different intensities. For both intensities, $E_0 = 25$ a.u. and $E_0 = 45$ a.u., the effect of the higher multipole-order terms is quite similar regardless of the initial state. These effects, as already discussed in previous sections, include: the flattening of peaks, the disappearance of side bands and ATI structures, and the enhancement of probabilities at higher photoelectron energies. However, unique differences of the initial states can also be seen. For example, the $1s - 2s$ comparison shows that at near-threshold region, the probabilities are nearly equal. But at higher photoelectron energies, the probabilities for the $1s$ initial state are higher than that of the $2s$ initial state. Besides, the positions of the $2s$ peaks are aligned to the positions of the $1s$ valleys. The difference in the total ionization yields could be as a result of the different ionization potentials as well as their difference in relative sizes.

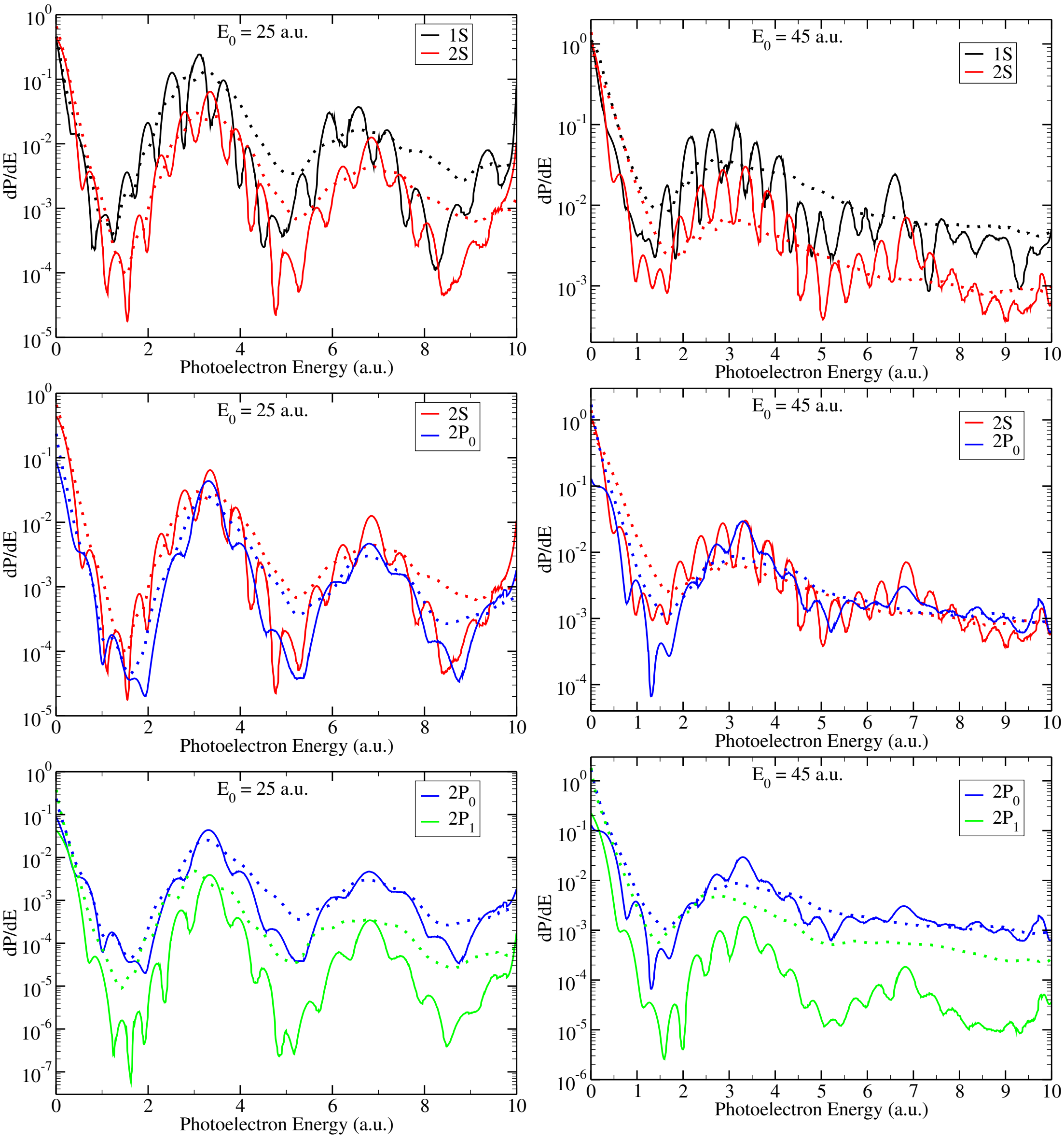

Figure 6.23: The Rayleigh multipole-order photoelectron energy spectra for a 10 cyle 13 nm laser pulse as a function of the initial state of a system and peak electric field strengths $E_0 = 25$ and 45 a.u.: $1S - 2S$ (top), $2S - 2P_0$ (middle), and $2P_0 - 2P_1$ (bottom) respectively. Solid lines: Lowest-order $\mathbf{A} \cdot \mathbf{p}_0$ term. Dotted lines of corresponding colour: Multipole $\mathbf{A} \cdot \mathbf{p}_{0,1} + \mathbf{A} \cdot \mathbf{A}_{0,1}$ terms. Left: $E_0 = 25$ a.u., right: $E_0 = 45$ a.u.

The ionization probabilities from the $2s$ and $2p_0$ as the initial states are also almost equal in magnitude owing to their energy degeneracy in the absence of fields. But the $2s$ spectrum displays a lot of wiggles and has slightly higher probabilities at almost the entire photoelectron energy regime. The $2p_0$ and $2p_1$ states on the other hand are perfectly degenerate in the absence of the electromagnetic fields. But because of the difference in projection quantum numbers, this degeneracy is removed by the magnetic field component of the radiation through the Zeeman splitting. The difference in energy in their dressed states can explain the difference in their spectra. It can be seen that $2p_0$ has a higher probability than $2p_1$ but the enhancement of probability as a result of the multipole-order interaction terms is higher in the $2p_1$ initial state than in the $2p_0$ initial state.

6.10 Taylor Versus Rayleigh Expansion

In this section, the Taylor versus Rayleigh expansion series are compared. The multipole-order interaction terms include both $\mathbf{A}\cdot\mathbf{p}$ and $\mathbf{A}\cdot\mathbf{A}$ up to the 1^{st} order terms. The 0^{th} order spectrum in the Taylor series is equivalent to the usual electric dipole approximation (EDA) while the the 0^{th} order spectrum in the Rayleigh series, as already discussed earlier, provides a spatial correction to the dipole spectrum. This section can be seen as a supplementary to the discussion in chapter 4 which did not include the effect of the $\mathbf{A}\cdot\mathbf{A}$ terms. The interactions compared are also discussed in equations (3.172) and (3.173) in section 3.7.

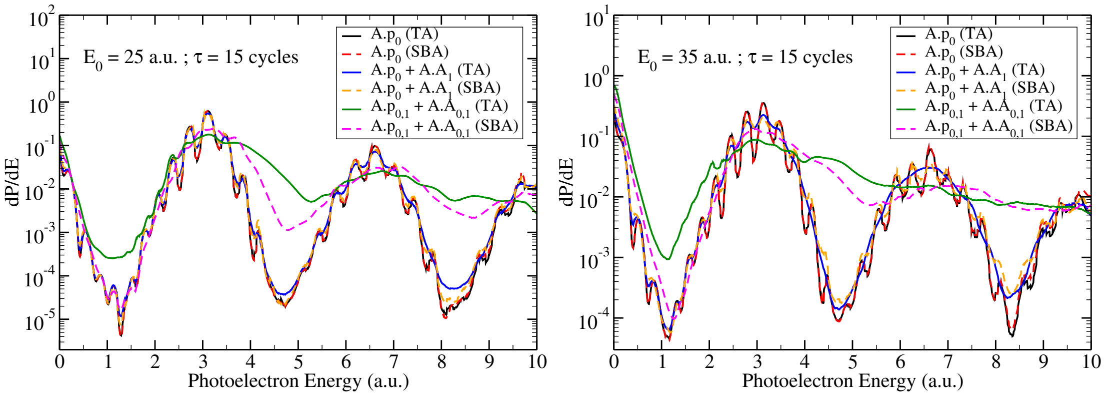

Figure 6.24: Comparison of Taylor (solid lines) and Rayleigh (dashed lines) multipole photoelectron energy spectra up to first order for a 13 nm wavelength 15 cycle linearly polarized laser field with peak electric field strengths of 25 and 35 a.u. on the left and right respectively.

Figure 6.24 shows the multipole-order photoelectron energy spectra for different terms of the interaction Hamiltonian in both Taylor and Rayleigh plane-wave expansions for a 13 nm wavelength 15 cycle linearly polarized laser field with peak electric field strengths of $E_0 = 25$ a.u. (left) and $E_0 = 35$ a.u. (right) respectively. The legends show the type and the order of interactions considered in the calculation of the transition matrix elements. The $\mathbf{A}\cdot\mathbf{p}_0$ in the Taylor approximation (TA) correspond to the standard dipole approximation. Within the energy regime of interest and considering only the lowest-order terms of the interaction, it can be seen that the effect of the $\mathbf{A}\cdot\mathbf{A}_0$ correction is negligible except at photoelectron energies above 8.0 a.u. where the spatial effects slightly modify the lowest-order ionization probabilities. If the 1^{st} order corrections of type $\mathbf{A}\cdot\mathbf{A}_1$ are included, the spatial effects show a slight modification of the 0^{th} order spectra. That is, the wiggles in the 0^{th} order spectra vanish with the inclusion of this correction within the Taylor approximation while in the Rayleigh approximation, the wiggles are non-vanishing. If all the multipole interactions up to the first-order are considered, the results are qualitatively similar with the wiggles vanishing both in the Taylor and Rayleigh approximations but lacking agreement in the quantitative comparison. The discrepancy between the two approximations is enhanced by the number of multipole-order terms included, the magnitude of the peak electric field strength, and the photoelectron energy. The differences between the two approximations for the same multipole order show the necessity of higher multipole-order terms (not present in the current order of the Taylor expansion) in resolving the discrepancies.

6.11 Non-Dipole Asymmetry Parameters, γ

The non-dipole effects, as already discussed in subsection 3.10, can be observed in the laboratory set up by measuring the forward-backward asymmetry in the photoelectron angular distributions (PADs). The non-dipole asymmetry stems from the fact that probability distribution of ionization is enhanced in the direction of the laser field propagation and suppressed in the opposite direction [155]. In this section, a theoretical calculation of three types of asymmetry parameters , $\gamma_{i=1,2,3}$, is presented. The first two (γ_1 and γ_2) require at least two detectors to be measured while the third asymmetry parameter (γ_3) requires at least three detectors. The asymmetry parameters are defined as

$$\gamma_1 = P_\mathrm{f}(\theta = 90^\circ, \phi = 0^\circ) - P_\mathrm{b}(\theta = 90^\circ, \phi = 180^\circ), \tag{6.10}$$

$$\gamma_2 = \frac{P_\mathrm{f}(\theta = 90^\circ, \phi = 0^\circ) - P_\mathrm{b}(\theta = 90^\circ, \phi = 180^\circ)}{P_\mathrm{f}(\theta = 90^\circ, \phi = 0^\circ) + P_\mathrm{b}(\theta = 90^\circ, \phi = 180^\circ)}, \tag{6.11}$$

and,

$$\begin{aligned}\gamma_3 &= \frac{P_\mathrm{f}(\theta = 90^\circ, \phi = 0^\circ) - P_\mathrm{b}(\theta = 90^\circ, \phi = 180^\circ)}{P_\mathrm{pol}(\theta = 0^\circ, \phi = 0^\circ)} \\ &= \frac{P_\mathrm{f}(\theta = 90^\circ, \phi = 0^\circ) - P_\mathrm{b}(\theta = 90^\circ, \phi = 180^\circ)}{P_\mathrm{pol}(\theta = 180^\circ, \phi = 0^\circ)}\end{aligned} \tag{6.12}$$

where P_f, P_b, and P_pol refer to probabilities in the forward propagation direction, backward (or counter) propagation diection, and electric field polarization directions respectively.

The asymmetry parameter γ_2 is already established in literature [93, 147] and the asymmetry parameter γ_1 is implied in the definition. On the other hand, the asymmetry parameter γ_3 is suggested in this work based on the theoretical observation of the shift in angular distribution as the non-dipole effects become significant. Figure 6.25 shows the three asymmetry parameters plotted as a function of peak electric field strength for a 13 nm laser pulse on the left and as a function of wavelength for a laser pulse with its peak electric field strength fixed at $E_0 = 1$ a.u.. In both cases, a 10 cycle linearly polarized laser field is used. Both γ_1 and γ_3 show that the forward-backward asymmetry, and by extension the significance of non-dipole effects, increase with the wavelength and the peak electric field strength. The asymmetry parameter γ_3 is actually an amplification of the signal in γ_1 based on the fact that as the photoelectron distribution tends towards the propagation direction, the lobe along the polarization direction shrinks proportionately.

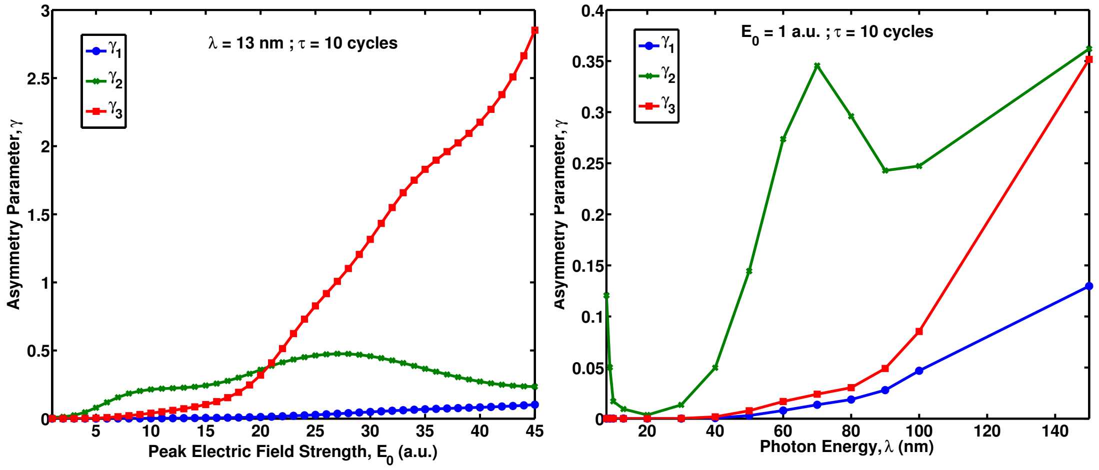

Figure 6.25: Various forward-backward non-dipole asymmetry parameters as a function of peak electric field strength for 13 nm wavelength laser field (left) and as a function of wavelength for a peak electric field strength,$E_0 = 1$ a.u., laser field (right). In both cases, the pulse is linearly polarized with a finite pulse duration of 10 cycles.

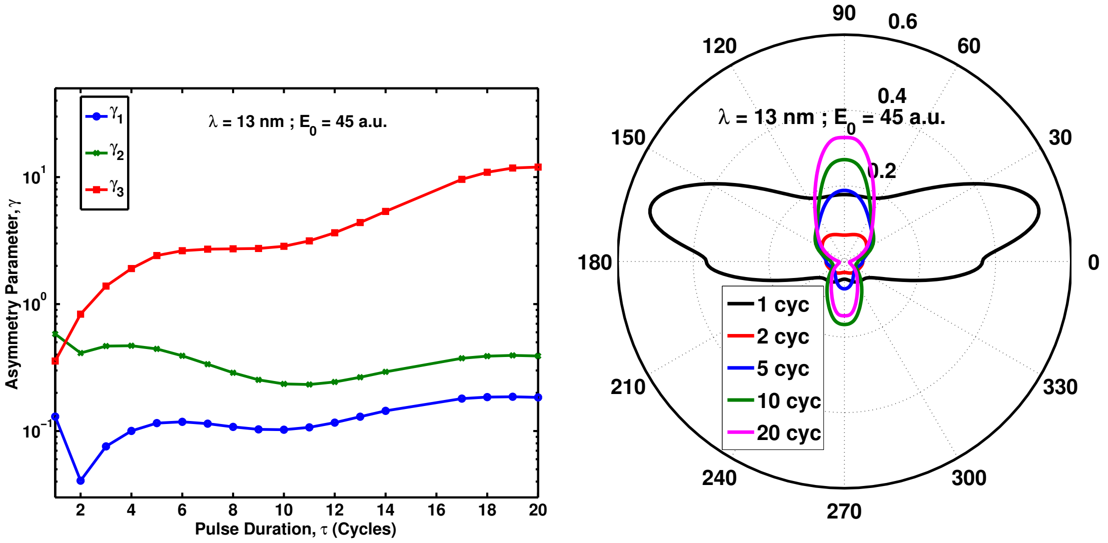

Figure 6.26: The three forward-backward asymmetry parameters as a function of the total pulse duration for 13 nm wavelength laser field with a peak electric field strength,$E_0 = 45$ a.u. (left) and the corresponding photoelectron polar angular distributions for selected pulse durations (right).

The asymmetry parameter γ_2 on the other hand technically measures the relative magnitude of the asymmetry in relation to the total probability transverse to the polarization direction. It depicts a rather complex correlation between the non-dipole effects and the peak electric field strength as well as the radiation wavelength. By examining the variation of the ionization probability in figure 6.4 with peak electric field strength, it can be seen that the critical intensities defining the onset and offset of stabilization are captured in γ_2 in form of saddle points at about $E_0 = 10$ and $E_0 = 25$ a.u. respectively. Beyond the offset of stabilization, γ_2 becomes a decreasing function of peak electric field strength because of the increasing backward lobe, leading to a decreasing ratio of increasing asymmetry in the forward-backward direction.

In figure 6.26, the variation of the different asymmetry parameters with the total pulse duration in semi-logarithmic plots and the corresponding PADs for selected pulse durations are shown. Each of the asymmetry parameters presents a different picture, although γ_1 shows a similar trend just like γ_3 except for one cycle pulse where the non-dipole effect is overrated in one and not the other.

6.12 Higher Multipole-Order Effects

Only the multipole interactions of order 0 and order 1 have been considered so far. In this subsection, the effects of additional multipole interactions of order 2 and 3 are investigated. These calculations are heavily demanding in terms of the computational resources and the computational time. In order to visualize the higher multipole-order effects, a slight compromise on the number of angular momenta used for convergence has been made by limiting $L_{\max} = 15$ and $-L_{\max} \leq M \leq L_{\max}$. This compromise is expected to have minimal impact on the accuracy of the photoelectron distributions especially at peak electric field strengths less than $E_0 = 25$ a.u.

Figures 6.27 and 6.28 show the multipole-order photoelectron energy spectra and the corresponding PADs respectively if the additional orders are included in both $\mathbf{A} \cdot \mathbf{p}$ and $\mathbf{A} \cdot \mathbf{A}$ interactions of the 13 nm linearly polarized laser pulse with electric field strengths $E_0 = 25,\ 35$ and 45 a.u. in the top, middle, and bottom positions respectively. The figures on the left correspond to a pulse duration of 10 cycles, while on the right correspond to a pulse duration of 15 cycles. The subscripts in the figure legends denote the range of multipole-terms included in the interaction Hamiltonian.

From the figures it is very clear that at the intensities considered, the contributions of the 2nd order terms of interaction Hamiltonian are also quite significant both in the photoelectron energy spectra and in the photoelectron angular distributions. The distributions are modified further by the inclusion of these higher multipole-order terms. Just like the 1st order corrections, the 2nd order corrections raise the ionization probability at the valleys and lower the peaks slightly. The impact of the additional corrections are higher at the valleys than at the peaks. This probably because the dipole effects are significantly smaller at the valleys as compared to the non-dipole interactions. The effects also increase with the peak field strengths.

The 3rd order terms can be considered negligible if the results are compared by eye. This confirms the expectation that when extremely high intensities, tending to the relativistic regime, are used then higher multipole-order terms become extremely necessary for accurate description of the laser-matter dynamics [18]. Only the intensity dependence has been considered for the higher multipole-order interactions beyond the first-order term. But it has been shown that the non-dipole effects also increase with wavelength and pulse duration.

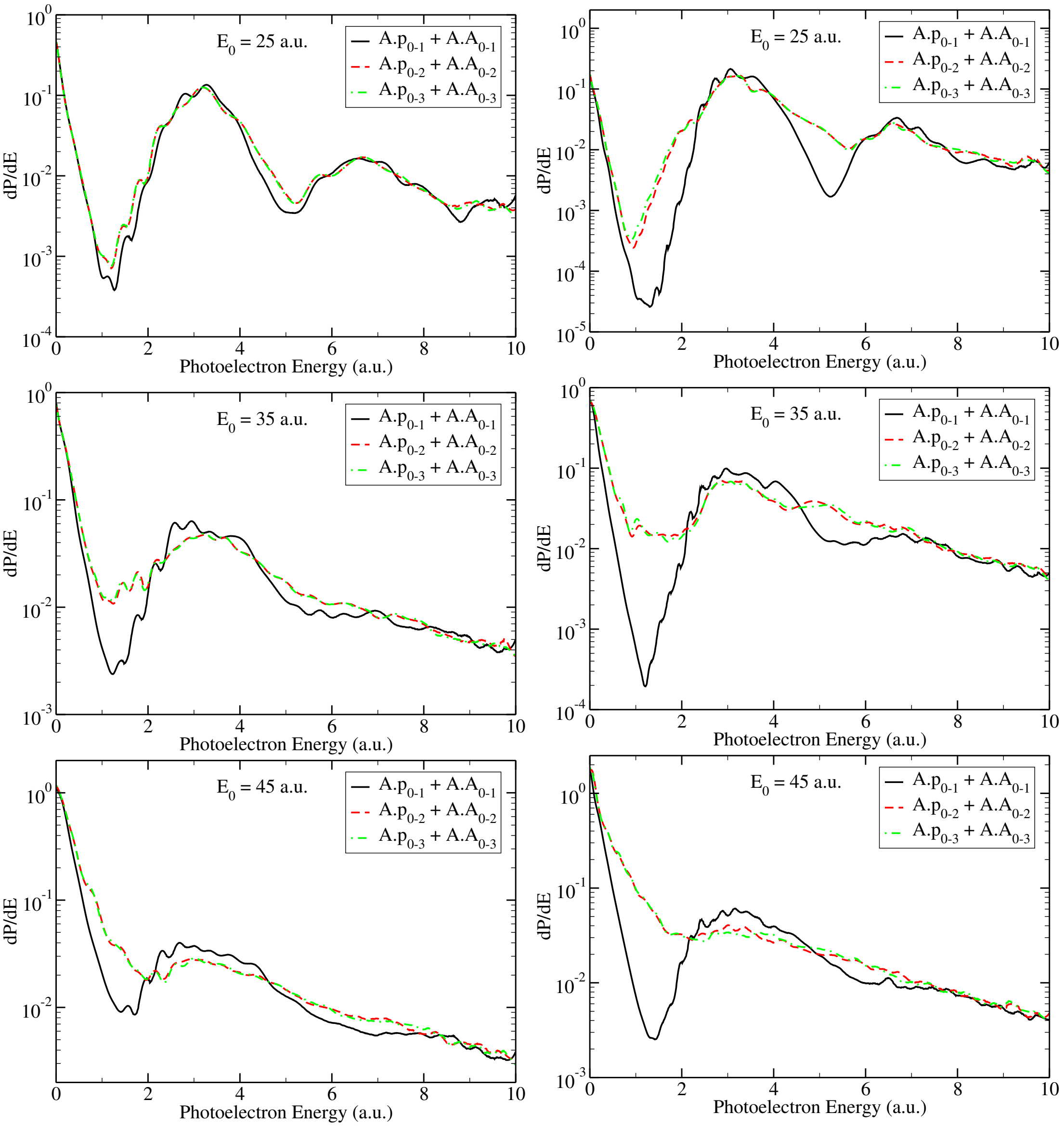

Figure 6.27: Multipole photoelectron energy spectra for a 13 nm laser pulse as a function of the multipole order for electric field strengths $E_0 = 25$, 35 and 45 a.u. The $L_{\max}$ and $M_{\max}$ are fixed at 15. The legends indicate the interactions considered with the subscripts specifying the range of multipole orders in the Rayleigh plane wave expansion included. Left: results for $\tau = 10$ cycle pulse, right: results for $\tau = 15$ cycle pulse.

The longer wavelengths stretch the computational limits further by demanding larger basis-sets. The increasing relative importance of this interactions as the radiation intensities and wavelengths continue to grow, as expected from the new generation light sources, pose a great theoretical challenge. The calculations would definitely require more computational resources and longer computational times for valid results to be generated. This calls for better approximation methods to cope with the challenge. It is hoped that the progress being made with the complex scaling methods would help in resolving the computational problems associated with longer wavelengths. The developments in the computational facilities is also expected to increase the efficiency required especially in the time propagation which usually take longer durations in the simulations.

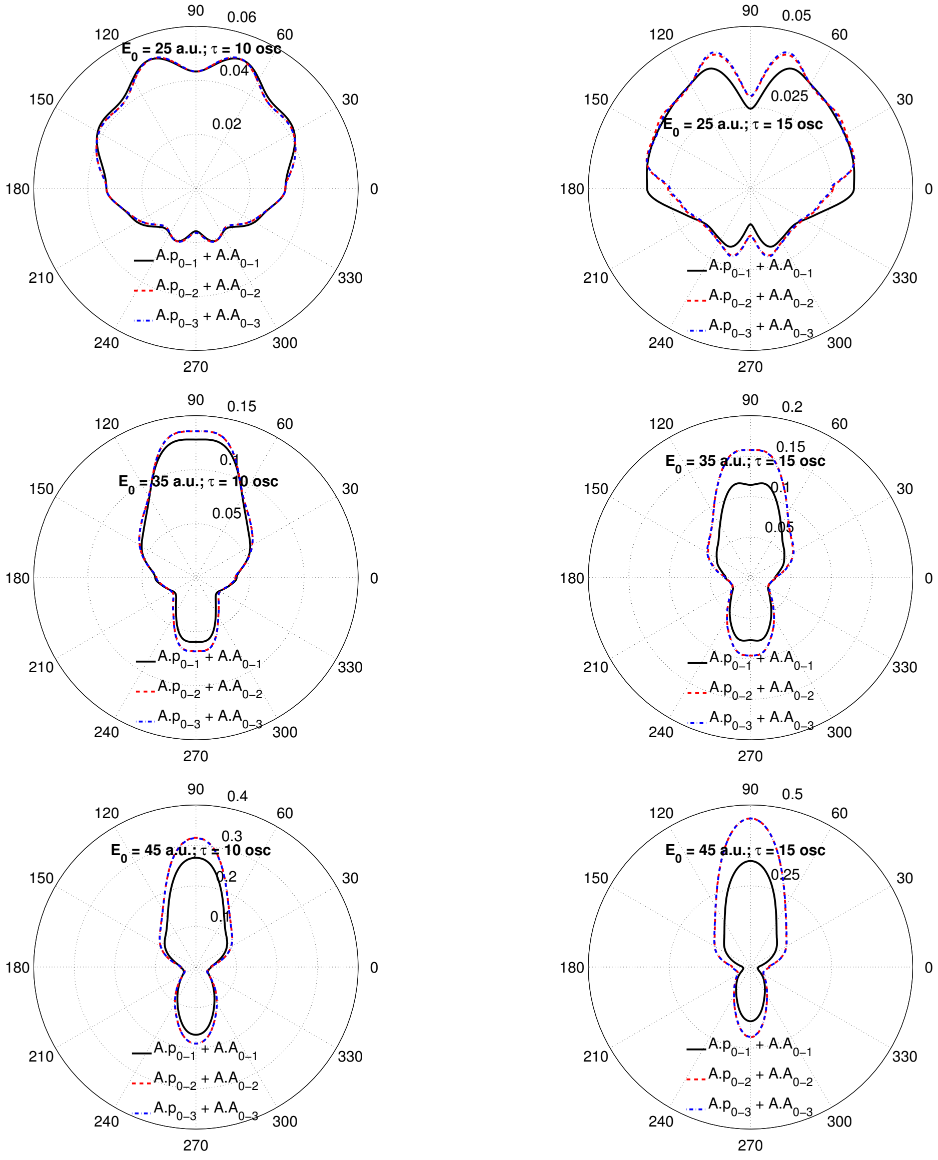

Figure 6.28: The multipole-order photoelectron angular distributions (PADS) corresponding to the laser parameters defined in figure 6.27. The upper half-circle correspond to forward angle ($\phi = 0^\circ$) while the lower half-circle correspond to backward angle ($\phi = 180^\circ$) with respect to the propagation direction. Left: 10 cycle pulse, right: 15 cycle pulse.

Chapter Summary

In this chapter, the effects of higher multipole-order interaction terms are discussed relative to the lowest-order interaction terms. The non-dipole effects are evaluated with the Rayleigh plane-wave expansion with the exception of cases where an explicit comparison with the Taylor plane-wave expansion is done or in the cases where the wavelength dependence of the non-dipole effects is discussed. Other than wavelength of radiation, the dependence on: intensity of radiation, pulse duration, and the initial state of hydrogen atom is discussed. The non-dipole effects are looked at in terms of the changes in the calculated energy-resolved, angle-resolved, and total ionization probabilities, as well as the asymmetry parameters. Besides the first-order correction terms, the effect of second- and the third- multipole order correction terms is also discussed. Significant non-dipole effects have been observed in the differential and total ionization probabilities. The non-dipole effects increase with intensity, pulse duration, wavelength, and photoelectron energy. The effects also further dependence on the structural properties like the ionization potential, the geometry and the symmetry of the initial states. Based on the observations in the angular distribution, a new asymmetry parameter has been suggested in this chapter.

7 Helium Model Potential

7.1 Introduction

Helium atom contains two electrons which interact among themselves in addition to their interaction with the nucleus. It is therefore the simplest many-body system and this makes it an ideal candidate for studying the electron correlation effects. The major problem in the many-body interaction potential is the electron-electron interaction terms which complicate the reduction to a single-particle equation . In this chapter, the effective model potentials for a two-electron system is presented. Reasonable eigenvalues for the helium atom are obtained using these model potentials.

The field-free Hamiltonian of a two-electron system with a nuclear charge Z is given by

$$H = -\frac{Z}{r_1} - \frac{Z}{r_2} + \frac{1}{|\mathbf{r}_1 - \mathbf{r}_2|} \tag{7.1}$$

where the first two terms correspond to the interaction between each of the electrons and the nucleus and the last term is the electron correlation term corresponding to the interaction between the two electrons. If this Hamiltonian is used to solve the time-independent Schrödinger equation

$$H\Phi_n(\mathbf{r}_1, \mathbf{r}_2) = E_n \Phi_n(\mathbf{r}_1, \mathbf{r}_2) \tag{7.2}$$

for any eigenstate $\Phi_n(\mathbf{r}_1, \mathbf{r}_2)$ of the system, the eigenenergies E_n for the particular state are obtained. The major problem in many-body systems is the correlation term coupled with the fact that the wavefunction of the system is never exactly known making the solution to the eigenvalue problem difficult. One has to therefore rely on some approximation methods in trying solve such a problem in order to obtain the correct eigenenergies and eigenvectors which may be useful for further estimation of many physical parameters like the transition matrix elements, expectation values, and polarizabilities.

Some of the theoretical approaches used in the past to deal with difficulties resulting from the electron correlation term includes the independent particle model, the Hylleraas method [156], coupled channels method [157], the configuration interaction method [158], and the explicitly correlated basis and complex scaling method [159]. Many of these methods have proved to be quite accurate but they are also quite expensive computationally. To overcome this computational challenge especially for really large systems, single active electron (SAE) methods based on a central effective potential formalism become advantageous to use, but they also require some approximation to derive a model (or pseudo) potential which can further be used to generate the eigenvectors and energies.

The development of the SAE models has been an active field of study for several decades. The differences in the variety of SAE models are based on different approximations of the non-local exchange correlation radial integral. Other than the SAE models, the single and multi-configurational Hartree-Fock (HF) method, density functional theory (DFT) method, random phase approximation (RPA), and other variants [160] have also been of great computational advantage.

The major limitation of SAE approximations is their inability to explain multiple-electron features like multiple excitation, simultaneous excitation and ionization, and multiple ionization. However, progress is being made towards the realization of these features. The strengths and limitations of various SAE models have been investigated [161–165] by directly comparing SAE predictions with those of more sophisticated two-electron models. On the flip side, the very high intense laser sources currently available with a short or long wavelength radiation are already probing dynamics beyond the dipole and into the relativistic regime. Investigation of these features even for the hydrogen atom is computationally demanding [91, 92] in terms of resources and the time required for full convergence. This makes such studies quite impractical for a fully correlated multi-electron systems and therefore the SAE models remain attractive. In deriving the SAE models, the mean value of the electron-electron correlation can be decomposed into two parts: the Coulomb charge density (J) correlation integral which is local, and the exchange density (K) integral which is non-local. The Coulomb part can be evaluated exactly while the exchange part usually involves different degrees of approximations.

7.2 Derivation of the Model Potentials

The starting point for deriving a model is based on the assumption that each of the electrons occupy the $1s$ state when the system is in its ground ($1s^2$) state. It is further assumed that the single electron orbital for the $1s$ state is hydrogenic. The $1s$ orbital is used to further derive the model potential extensible to any general quantum state of the system.

The general wavefunction for a two-electron system with its quantum numbers specified by a set $\alpha = \{n, l, m_l, m_s\}$

$$\Phi_\alpha(\mathbf{r}_1, \mathbf{r}_2) = \frac{1}{\sqrt{2}} \sum_{n,l} c_{n,l} [\phi_{1s}(\mathbf{r}_1)\phi_{nl}(\mathbf{r}_2) + \phi_{1s}(\mathbf{r}_2)\phi_{nl}(\mathbf{r}_1)] \tag{7.3}$$

is considered as a symmetric superposition of the product of the orbitals but with one of the electrons frozen in the $1s$ state. The anti-symmetrization of the wavefunction is considered to be determined by the spin states. This is justified for the ground state which is a singlet state and therefore the anti-symmetric part is limited to the spin component of the ground state vector. This assumed wavefunction is then used to determine the general expectation value of the potential function of the Hamiltonian as,

$$
\begin{aligned}
&\langle \Phi_\alpha(\mathbf{r}_1,\mathbf{r}_2)|V(\mathbf{r}_1,\mathbf{r}_2)|\Phi_\alpha(\mathbf{r}_1,\mathbf{r}_2)\rangle \\
&\quad = -\langle \Phi_\alpha(\mathbf{r}_1,\mathbf{r}_2)|\frac{Z}{r_1}|\Phi_\alpha(\mathbf{r}_1,\mathbf{r}_2)\rangle - \langle \Phi_\alpha(\mathbf{r}_1,\mathbf{r}_2)|\frac{Z}{r_2}|\Phi_\alpha(\mathbf{r}_1,\mathbf{r}_2)\rangle \\
&\quad + \langle \Phi_\alpha(\mathbf{r}_1,\mathbf{r}_2)|\frac{1}{|\mathbf{r}_1-\mathbf{r}_2|}|\Phi_\alpha(\mathbf{r}_1,\mathbf{r}_2)\rangle \\
&\quad = \sum_{n,l}|c_{n,l}|^2[-\frac{1}{2}\langle\phi_{n,l}(\mathbf{r}_1)|\frac{Z}{r_1}|\phi_{n,l}(\mathbf{r}_1)\rangle - \frac{1}{2}\langle\phi_{1s}(\mathbf{r}_2)|\frac{Z}{r_2}|\phi_{1s}(\mathbf{r}_2)\rangle \\
&\quad - \frac{1}{2}\langle\phi_{n,l}(\mathbf{r}_2)|\frac{Z}{r_2}|\phi_{n,l}(\mathbf{r}_2)\rangle - \frac{1}{2}\langle\phi_{1s}(\mathbf{r}_1)|\frac{Z}{r_1}|\phi_{1s}(\mathbf{r}_1)\rangle \\
&\quad + \frac{1}{2}\langle\phi_{n,l}(\mathbf{r}_1)\phi_{1s}(\mathbf{r}_2)|\frac{1}{|\mathbf{r}_1-\mathbf{r}_2|}|\phi_{1s}(\mathbf{r}_2)\phi_{n,l}(\mathbf{r}_1)\rangle \\
&\quad + \frac{1}{2}\langle\phi_{n,l}(\mathbf{r}_2)\phi_{1s}(\mathbf{r}_1)|\frac{1}{|\mathbf{r}_1-\mathbf{r}_2|}|\phi_{1s}(\mathbf{r}_1)\phi_{n,l}(\mathbf{r}_2)\rangle \\
&\quad + \frac{1}{2}\langle\phi_{n,l}(\mathbf{r}_1)\phi_{1s}(\mathbf{r}_2)|\frac{1}{|\mathbf{r}_1-\mathbf{r}_2|}|\phi_{1s}(\mathbf{r}_1)\phi_{n,l}(\mathbf{r}_2)\rangle \\
&\quad + \frac{1}{2}\langle\phi_{n,l}(\mathbf{r}_2)\phi_{1s}(\mathbf{r}_1)|\frac{1}{|\mathbf{r}_1-\mathbf{r}_2|}|\phi_{1s}(\mathbf{r}_2)\phi_{n,l}(\mathbf{r}_1)\rangle]
\end{aligned}
\tag{7.4}
$$

where the single-electron functions have been considered to be ortho-normalized. The last two terms arise from the exchange integral where some approximations need to be considered as well. We can reduce this problem, using the orthogonality of eigenstates argument, to

$$
\begin{aligned}
&\langle \Phi_\alpha(\mathbf{r}_1,\mathbf{r}_2)|V(\mathbf{r}_1,\mathbf{r}_2)|\Phi_\alpha(\mathbf{r}_1,\mathbf{r}_2)\rangle \\
&\quad = \sum_{i,n,l}|c_{n,l}|^2[-\frac{1}{2}\langle\phi_{n,l}(\mathbf{r}_i)|\frac{Z}{r_i}|\phi_{n,l}(\mathbf{r}_i)\rangle - \frac{1}{2}\langle\phi_{1s}(\mathbf{r}_j)|\frac{Z}{r_j}|\phi_{1s}(\mathbf{r}_j)\rangle \\
&\quad + \frac{1}{2}\langle\phi_{n,l}(\mathbf{r}_i)\phi_{1s}(\mathbf{r}_j)|\frac{1}{|\mathbf{r}_i-\mathbf{r}_j|}|\phi_{1s}(\mathbf{r}_j)\phi_{n,l}(\mathbf{r}_i)\rangle \\
&\quad + \frac{1}{2}\langle\phi_{n,l}(\mathbf{r}_i)\phi_{1s}(\mathbf{r}_j)|\frac{1}{|\mathbf{r}_i-\mathbf{r}_j|}|\phi_{1s}(\mathbf{r}_i)\phi_{n,l}(\mathbf{r}_j)\rangle]
\end{aligned}
\tag{7.5}
$$

where the i index represents either electron 1 or electron 2 and j index represents the other electron. The second term is exactly known, and the inner integral of the direct correlation term can be evaluated reducing the problem to only one radial co-ordinate. The major challenge in evaluating the electron correlation term as already stated is the method of integrating the exchange integral. In this work, a local approximation to the exchange integral is made by considering its effect as a small correction to the Coulomb part of this electron-electron interaction. As usual with many body problems, the potential function of the two-electron system can be expressed as

$$V(\mathbf{r}_1, \mathbf{r}_2) = -\frac{Z}{r} + V_{\text{screen}}(r) \tag{7.6}$$

where one of the electrons is considered to be the active electron and the other electron is frozen in the $1s$ orbital of the ground state with a task of shielding the active electron from experiencing the full nuclear potential with a screening potential $V_{\text{screen}}(r)$. r is the mean field radial position of the active electron from the nucleus.

The correlation term $\frac{1}{|\mathbf{r}_1-\mathbf{r}_2|}$ can be expanded in Legendre polynomials as

$$\frac{1}{|\mathbf{r}_1 - \mathbf{r}_2|} = \sum_{l=0}^{\infty} \frac{r_<^l}{r_>^{l+1}} P_l(\cos\theta) \tag{7.7}$$

where $P_l(\cos\theta)$ are the Legendre polynomials of order l, $r_<(_>)$ corresponds to the lesser (greater) electronic radial distance between the two electrons, and θ is the relative azimuthal angle between the electrons or equivalently in spherical harmonics as

$$\frac{1}{|\mathbf{r}_1 - \mathbf{r}_2|} = \sum_{l=0}^{\infty} \sum_{m=-l}^{+l} \frac{4\pi}{2l+1} \frac{r_<^l}{r_>^{l+1}} Y_l^{m*}(\hat{r_<}) Y_l^m(\hat{r_>}) \tag{7.8}$$

with the terms as already predefined. If the two electrons are in their ground state, then one can approximate the correlation term with only the first term of the series in equation (7.7). With this approximation, the inner part of the direct correlation term can then be evaluated using an assumed hydrogenic $1s$ orbital as

$$\begin{aligned}
\langle \phi_{1s}(\mathbf{r}_2) | \frac{1}{|\mathbf{r}_1 - \mathbf{r}_2|} | \phi_{1s}(\mathbf{r}_2) \rangle &= \frac{1}{r_1} \int_0^{r_1} \mathrm{d}r_2\, r_2^2\, |R_{1s}|^2 + \int_{r_1}^{\infty} \mathrm{d}r_2\, r_2\, |R_{1s}|^2 \\
&= 4Z^3 [\frac{1}{r_1} \int_0^{r_1} \mathrm{d}r_2\, r_2^2\, \exp(-2Zr_2) + \int_{r_1}^{\infty} \mathrm{d}r_2\, r_2\, \exp(-2Zr_2) \\
&= 4Z^3 [-\{\frac{r_1}{2Z} + \frac{2}{(2Z)^2} + \frac{2}{(2Z)^3 r_1}\} \exp(-2Zr_1) + \frac{2}{(2Z)^3 r_1}] \\
&+ \{\frac{r_1}{2Z} + \frac{1}{(2Z)^2}\} \exp(-2Zr_1)] \\
&= 4Z^3 [-\{\frac{1}{(2Z)^2} + \frac{2}{(2Z)^3 r_1}\} \exp(-2Zr_1) + \frac{2}{(2Z)^3 r_1}] \\
&= \frac{\{1 - (1 + Zr_1)\exp(-2Zr_1)\}}{r_1}
\end{aligned} \tag{7.9}$$

In principle one can be able to use any assumed trial function with proper normalization to evaluate the inner integral and then a variational procedure can be used to optimize the ground state energy [161, 166]. Likewise, the integral

$$\begin{aligned}\langle\phi_{1s}(\mathbf{r}_2)|\frac{Z}{r_2}|\phi_{1s}(\mathbf{r}_2)\rangle &= 4Z^4\int_0^\infty \mathrm{d}r_2\, r_2\,\exp(-2Zr_2)\\ &= 4Z^4\frac{1}{(2Z)^2}\\ &= Z^2\end{aligned} \tag{7.10}$$

Using equations (7.9) and (7.10) and excluding the exchange term, the model potential V_{pot} can be given by

$$V_{\mathrm{pot}} = \frac{1}{2}\frac{\{1 - Z^2r - Z - (1+Zr)\exp(-2Zr)\}}{r}. \tag{7.11}$$

If the exchange correlation interaction potential is added, assuming equivalence with the direct part, one obtains the total effective central potential as

$$\begin{aligned}V_{\mathrm{eff}}(r) &= \frac{1}{2}\frac{\{2 - Z^2r - Z - 2(1+Zr)\exp(-2Zr)\}}{r}\\ &\approx -\frac{Z}{r} + \frac{\{1 - \frac{Z^2}{2}r - (1+Zr)\exp(-2Zr)\}}{r}\end{aligned} \tag{7.12}$$

where the normalization constant is taken to be unity and a further approximation which neglects factor 1/2 of the nuclear interaction is assumed. The second term on the right hand side can be considered as the screening potential $V_{screen}(r)$. This central potential does not give the correct ground-state value. An adjustable core polarization potential is considered to set the ground-state. The final effective model potential for a two-electron system can then written as

$$V_{\mathrm{model}_1} \approx -\frac{Z}{r} + \frac{\{1 - \frac{Z^2}{2}r - (1+Zr)\exp(-2Zr)\}}{r} + V_{\mathrm{pol}}(r) \tag{7.13}$$

where the last term is the one particle core polarization potential which gives the ground state static adiabatic dipole polarizability correction. Here the value of the cut-off function [167]

$$V_{\mathrm{pol}}(r) = -\frac{\alpha_d}{2r^4}[1 - \exp(-(\frac{r}{r_c})^4)] \tag{7.14}$$

is numerically fitted with the exact value of the static dipole polarizability of helium $\alpha_d = 1.38376079$ [168] and $r_c = 1.6375$ in order to obtain a reasonable ground state eigenvalue of -2.90368 for the helium atom.

In order to optimize the model potential further, the parameters in equation (7.13) were adjusted stochastically until the quality of eigenstates and eigenenergies improved significantly. A reasonable description of the eigenstates and eigenvalues with the potential of the form

$$\begin{aligned} V_{\text{model}_2}(r) &= -\frac{2Z + Z^2 r - 2 + [1 + 3Zr]\exp(-2Zr)}{2r} + V_{\text{pol}}(r)\delta_{1s} \\ &= -\frac{Z}{r} + \frac{1 - \frac{Z^2 r}{2} - \frac{1}{2}[1 + 3Zr]\exp(-2Zr)}{r} + V_{\text{pol}}(r)\delta_{1s} \end{aligned} \tag{7.15}$$

was obtained with the static dipole polarization potential $V_{\text{pol}}(r)$

$$V_{\text{pol}}(r) = \frac{1 - \exp(-[\frac{r}{r_c}]^4)}{2r^4} \tag{7.16}$$

having an adjustable cut-off parameter r_c set at $r_c = 1.25$ for $r_{max} = 300$ a.u. added to it in order to reproduce the ground state eigenvalue for helium. This additional polarization potential is purely an estimation of the higher-order contributions of the non-local exchange potential. The justification for using the polarization potential for the ground state alone is based on the fact that the ground state experiences an additional confinement since the screening electron also occupies the $1s$ state and therefore the higher-order terms resulting from the exchange correlation would be non-vanishing as opposed to the excited states where these terms may be negligible because of the large spatial separation between the two electrons.

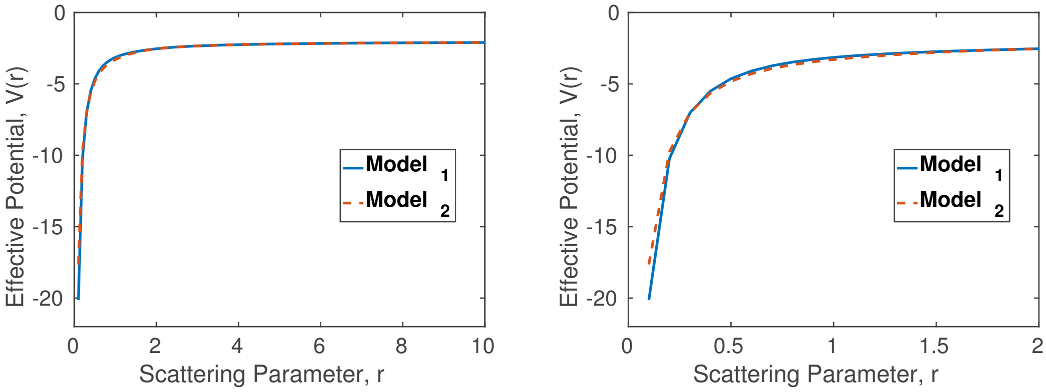

Figure 7.1: Variation of the model potentials with the scattering parameter r. Left: long range limit. Right: Short range limit.

Figure 7.1 shows the variation of the two model potentials with the scattering parameter r. In the limit of a large r, one can see that the effective potential approaches a value $V(r) \to -2$ which is corresponds to a single-electron ionization threshold in a frozen-core model potential. In the limit $r \to 0$, the screening potential due to the electron-electron correlation approaches the short-range limit in which the active-electron feels the presence of the full nuclear change resulting into a deeper effective potential. The difference between the two model potentials clearly manifests in the short-range limit. Actually, this could be the regime in which the validity of the mean-field approximations used in modelling the effective potentials fails. The accuracy in this short range limit can only be improved by tackling the complicated non-local exchange potential integral. The density functional theory research is focussed in this direction.

S. No.	**model$_1$**	**model$_2$**	**Ref. values**	**I.P**
$\mathbf{L = 0}$				
1.	-2.9037165053	-2.9035233717	-2.903724377	-0.9035705688
2.	-2.1576481314	-2.1477891839	-2.145974037	-0.1573692781
3.	-2.0644680097	-2.0618954237	-2.0612719	-0.0644057390
4.	-2.0348796243	-2.0338534642	-2.033586	-0.0348561014
5.	-2.0218221184	-2.0213131765		-0.0218107484
$\mathbf{L = 1}$				
1.	-2.1274580764	-2.1262784705	-2.12384308	-0.1279843895
2.	-2.0563508111	-2.0559881432	-2.05514637	-0.0565276620
3.	-2.0315942853	-2.0314398674	-2.0310696	-0.0316710698
4.	-2.0201782110	-2.0200988916	-2.0199059	-0.0202179423
5.	-2.0139925948	-2.0139466316		-0.0140156982
$\mathbf{L = 2}$				
1.	-2.0555778603	-2.0555597268	-2.05562071	-0.0555761912
2.	-2.0312624312	-2.0312524585	-2.0312798	-0.0312618752
3.	-2.0200070618	-2.0200014311	-2.0200158	-0.0200068385
4.	-2.0138931919	-2.0138897722	-2.0138989	-0.0138930856
5.	-2.0102068730	-2.0102046591		-0.0102068155
$\mathbf{L = 3}$				
1.	-2.0312502247	-2.0312500085	-2.0312551444	-0.0312501060
2.	-2.0200001819	-2.0200000072	-2.0200029370	-0.0200000884
3.	-2.0138890169	-2.0138888941	-2.0138906837	-0.0138889521
4.	-2.0102041713	-2.0102040853	-2.010205246	-0.0102041263
5.	-2.0078125641	-2.0078125027		-0.0078125321

Table 7.1: Numerically calculated eigenvalues using the present model potentials at $r = 0$ versus the reference [159] eigenvalues and the ionization potentials evaluated using another model potential [169]. A box radius $r_{\max} = 300$ a.u. and 600 B splines is used in the calculations. Model$_1$ values are evaluated using equation (7.13) and model$_2$ values using equation(7.15).

S. No.	**model$_1$**	**model$_2$**	**Ref. values**	**I.P**
L = 4				
1.	-2.0200000018	-2.0200000000	-2.0200007108	-0.0200000003
2.	-2.0138888908	-2.0138888888	-2.0138893453	-0.0138888893
3.	-2.0102040832	-2.0102040816	-2.0102043836	-0.0102040820
4.	-2.0078125012	-2.0078124999		-0.0078125003
5.	-2.0061728405	-2.0061728395		-0.0061728397
L = 5				
1.	-2.0138888889	-2.0138888889	-2.0138890346	-0.0138888889
2.	-2.0102040816	-2.0102040816	-2.0102041827	-0.0102040816
3.	-2.0078125000	-2.0078125000	-2.0078125737	-0.0078125000
4.	-2.0061728395	-2.0061728395		-0.0061728395
5.	-2.0049999944	-2.0049999944		-0.0049999944
L = 6				
1.	-2.0102040816	-2.0102040817	-2.0102041204	-0.0102040816
2.	-2.0078124999	-2.0078125000	-2.0078125284	-0.0078125000
3.	-2.0061728395	-2.0061728395	-2.0061728509	-0.0061728395
4.	-2.0049999977	-2.0049999977		-0.0049999977
5.	-2.0041316082	-2.0041316082		-0.0041316082
L = 7				
1.	-2.0078125000	-2.0078125000	-2.0078125124	-0.0078125000
2.	-2.0061728395	-2.0061728396	-2.0061728489	-0.0061728395
3.	-2.0049999994	-2.0049999993	-2.0049999968	-0.0049999993
4.	-2.0041319543	-2.0041319544		-0.0041319543
5.	-2.0034579633	-2.0034579633		-0.0034579633

Table 7.2: Continuation of table 7.1 for higher angular momenta.

The difference between model$_1$ and model$_2$ potentials can be accounted for by the difference in the screening potential of the frozen electron on to the active electron. The table 7.1 and 7.2 below shows some of the eigenvalues calculated using the model potentials defined in equations(7.13) and (7.15), hereby referred to as model$_1$ and model$_2$

respectively, in comparison with those calculated using correlated basis set and complex scaling [159] and the ionization potentials evaluated using the model potential of reference [169].

It can be seen from tables 7.1 and 7.2 that the model$_2$ values are in very good agreement with the eigenvaues of reference [159] for all the states considered while the model$_1$ values are also in very good agreement with the relative ionization potentials generated using the model of [169]. In comparison, one can say that model$_2$ performs better than model$_1$ potential. The advantage of the current model potentials is that, other than the polarization potential term which is adjustable to obtain a good fit for the ground state energy, the screening potential is entirely dependent on the nuclear charge and the screening radius without any additional fitting.

7.3 Non-Orthogonality of the s States

The application of the Hamiltonian operator given in equation (7.15) numerically leads to non-orthogonality between the ground state and other s states. This ensuing non-orthogonality has to be carefully treated since orthogonality and normalization (orthonormalization) are some of the fundamental principles upon which quantum mechanics is founded. The non-orthogonality of the ground state can fortunately be corrected by applying the Gram-Schmidt orthonormalization procedure which is an established method for orthonormalizing a set of vectors in an inner product space, most commonly, the Euclidean space R^n.

The Gram-Schmidt orthonormalization process takes a finite, linearly independent sets $S = \{\mathbf{v}_1, \mathbf{v}_2, \cdots, \mathbf{v}_k\}$ for $k \leq n$ and generates an orthogonal set $S' = \{\mathbf{u}_1, \mathbf{u}_2, \cdots, \mathbf{u}_k\}$ that spans the same k-dimensional subspace of R^n as S. The application of the Gram-Schmidt process to the column vectors of a full column rank matrix yields the QR (orthogonal and triangular matrix) decomposition.

In the Gram-schmidt orthogonalization process, the projection operator is defined by

$$\mathrm{Proj}_{\mathbf{u}}(\mathbf{v}) = \frac{\langle \mathbf{v}, \mathbf{u} \rangle}{\langle \mathbf{u}, \mathbf{u} \rangle} \mathbf{u} \tag{7.17}$$

where $\langle \mathbf{v}, \mathbf{u} \rangle$ denotes the inner product of the vectors $\mathbf{v}$ and $\mathbf{u}$. This operator projects the vector $\mathbf{v}$ orthogonally onto the line spanned by vector $\mathbf{u}$. If vector $\mathbf{u} = 0$, then $\mathrm{Proj}_{\mathbf{0}}(\mathbf{v}) := 0$ is the projection mapping every vector to zero and it is referred to as a zero map.

The Gram-Schmidt process can be expressed as a recursive routine that generates an orthogonal vector as follows

$$\begin{aligned}
\mathbf{u}_1 &= \mathbf{v}_1 \\
\mathbf{u}_2 &= \mathbf{v}_2 - \mathrm{Proj}_{\mathbf{u}_1}(\mathbf{v}_2) \\
\mathbf{u}_3 &= \mathbf{v}_3 - \mathrm{Proj}_{\mathbf{u}_1}(\mathbf{v}_3) - \mathrm{Proj}_{\mathbf{u}_2}(\mathbf{v}_3) \\
\mathbf{u}_4 &= \mathbf{v}_4 - \mathrm{Proj}_{\mathbf{u}_1}(\mathbf{v}_4) - \mathrm{Proj}_{\mathbf{u}_2}(\mathbf{v}_4) - \mathrm{Proj}_{\mathbf{u}_3}(\mathbf{v}_4) \\
&\vdots \\
\mathbf{u}_k &= \mathbf{v}_k - \sum_{j\neq k}^{n-1} \mathrm{Proj}_{\mathbf{u}_j}(\mathbf{v}_k) = \mathbf{v}_k - \sum_{j\neq k}^{n-1} \frac{\langle \mathbf{v}_k, \mathbf{u}_j\rangle}{\langle \mathbf{u}_j, \mathbf{u}_j\rangle}\mathbf{u}_j
\end{aligned} \tag{7.18}$$

with a corresponding orthonormalized vector defined as

$$\mathbf{e}_k = \frac{\mathbf{u}_k}{||\mathbf{u}_k||} \tag{7.19}$$

where $||\mathbf{u}_k||$ is the modulus of the vector. The sequence $S' = \{\mathbf{u}_1, \mathbf{u}_2, \cdots, \mathbf{u}_k\}$ is the required system of orthogonal vectors, and the vectors $S" = \{\mathbf{e}_1, \mathbf{e}_2, \cdots, \mathbf{e}_k\}$ form an orthonormal set.

7.4 Helium Multiphoton Ionization Probability

As a test of model$_2$ potential, the wavelength dependent ionization probability of helium atoms is evaluated at an intensity of 2.97×10^{14} Wcm^{-2} reported in the works of Armin Scrinzi [159]. The reference data were evaluated by solving the TDSE for atoms with two active electrons in a strong laser field using an accurate method which employs complex scaling and an expansion in an explicitly correlated basis. In this method, they could capture both single and double electron transition dynamics where as in our model potential, one of the electrons is frozen in its ground state and therefore dynamics is only possible with the active electron. All the present calculations including the non-dipole corrections in the helium atom are evaluated using the Taylor plane-wave multipole expansion series of the spatial retardation term. Figure 7.2 (left) shows the total ionization probability results generated with model$_2$ potential in comparison with the reference results.

It can be seen that the present results compare well with the literature data and the discrepancy between them may be associated with the contribution of the double excitation and double ionization dynamics not captured in the present model potential but present in the literature data. At photon energies above the ground state ionization threshold, only a single photon is sufficient to cause ionization from the ground state. The equivalence of our results to the reference probabilities in this regime show that the ionization dynamics is governed dominantly with single electron transitions.

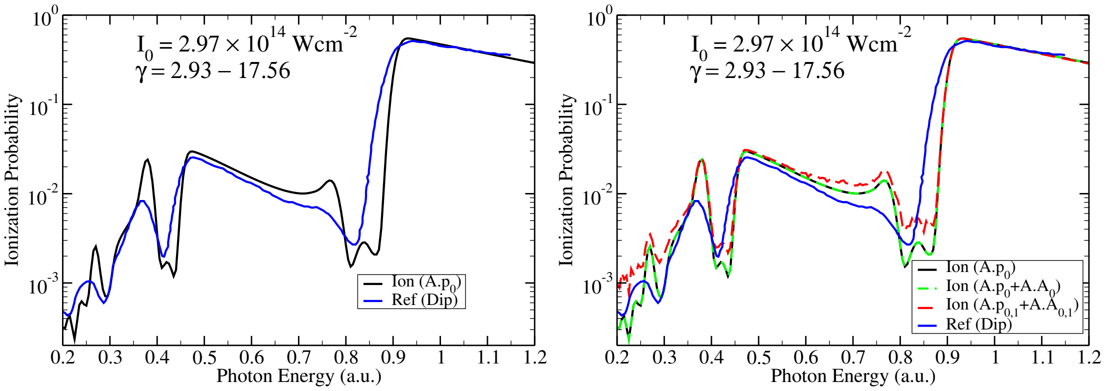

Figure 7.2: Left: The wavelength dependent dipole ionization probability calculated using the present model potential (black) in comparison the reliable ionization probability in literature [159] (blue). Right: Similar as the probability distribution on the left figure but with additional non-dipole interaction potentials.

At photon energies below the ground state ionization threshold, multiple photon absorption is necessary for ionization and in this regime the contribution of double ionization may be seen to be quite significant. Figure 7.2 (right) shows the additional contribution of the non-dipole interactions to the ionization probability. The goal in this case was to determine the photon energy regimes at the defined intensity where the non-dipole effects may be manifested.

The non-dipole enhancement of probability at various photon energy ranges in the multiphoton regime are clearly visible. In the single-photon ionization window, the non-dipole effects in the total ionization probability are insignificant. The contribution of the non-dipole effects at these relatively low strong field intensity regime may be surprising especially their appearance in the total ionization yield for a broad spectrum of wavelengths.

In figure 7.3 (left), the multipole ionization and excitation probability calculated using model$_2$ potential are compared with the reference dipole ionization probability. The black solid line shows the lowest-order results in $\mathbf{A}\cdot\mathbf{p}$ interaction, the green dashed line shows the zero order results in $\mathbf{A}\cdot\mathbf{p}$ plus $\mathbf{A}\cdot\mathbf{A}$ interactions, and the red dash dot line shows the $\mathbf{A}\cdot\mathbf{p}$ plus $\mathbf{A}\cdot\mathbf{A}$ interaction terms up to the 1^{st} order. The resonant structures in the reference data are successfully reproduced by the model$_2$ potential.

As expected within the dipole approximation, the effect of the $\mathbf{A}\cdot\mathbf{A}$ interaction vanishes. This justifies the use of the phase transformation in moving from the radiation gauge to velocity gauge within the dipole approximation. In figure 7.3 (right), the non-dipole effects in the excitation probabilities only is examined. It is found that the non-dipole effect in the excitation probability is negligible at the laser parameters considered. It is not clear whether difference between the dipole ionization plus excitation probabilities generated using the present model$_2$ potential and the literature values only emphasize the role of double ionization and double excitation or otherwise.

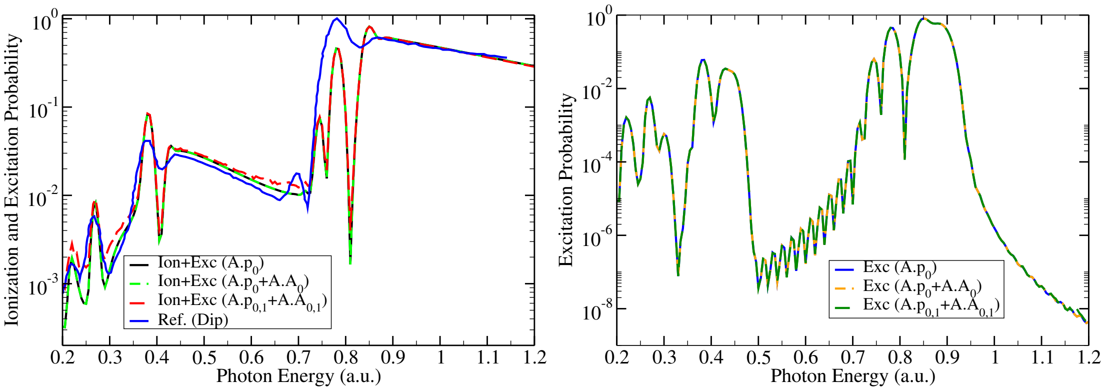

Figure 7.3: Left: The wavelength dependent multipole ionization plus excitation probability calculated using the present model potential (black, green, and red) in comparison the reliable ionization probability in literature [159] (blue). Right: Only the multipole excitation probability is presented.

From the results, it may be curious to note that the intensity considered is approximately two orders of magnitude lower than unity (in atomic units), yet at this relatively lower intensity some non-dipole effects causing enhancement of the total ionization probability are already significant in the multiphoton regime. Since the effect of the 0^{th} order quadratic term $\mathbf{A}\cdot\mathbf{A}$ is absent (within the Taylor plane-wave multipole expansion) at the considered laser parameters, it can be concluded that the apparent non-dipole effects emanate from the 1^{st} order corrections in $\mathbf{A}\cdot\mathbf{p}$ and $\mathbf{A}\cdot\mathbf{A}$ interaction terms. At the photon energies where the observed non-dipole effects are significant, they can be seen to be comparable in magnitude with the assumed double excitation and double ionization induced changes in ionization probability distribution of the literature data.

From these preliminary results of helium, it can be suggested that for multiphoton transitions with helium atoms at radiation intensities of $\sim 10^{14}$ Wcm^{-2} and above, the contribution of non-dipole effects need further investigation.

Chapter Summary

In this chapter, two approximate model potentials for helium atom are derived. Reasonable eigenvalues are obtained using the model potentials. One of the model potentials is used further to probe the wavelength-dependent excitation and ionization processes for helium atom in a strong-field regime. The results obtained compare favourably with the literature data. Some non-dipole effects are also reported at the relatively low intensity regime considered showing that at higher intensities, the use of the dipole approximation may not be valid.

8 Conclusion

An existing program has been extended to incorporate the effects of higher multipole-order interaction terms in the solution of the non-relativistic time-dependent Schrödinger equation (TDSE) describing a system interacting with an electromagnetic field. The resulting coupled integro-differential equations are solved within the single active electron (SAE) approximation. The original program was initially developed in our research group for the solution of non-relativistic SAE TDSE using the dipole approximation in a reduced basis-set. The extension exercise involved an entire restructuring of the program to allow for multiple interactions and the broken cylindrical symmetry that come into play with the multipole $\mathbf{A} \cdot \mathbf{p}$ and $\mathbf{A} \cdot \mathbf{A}$ terms of the interaction potential if the m quantum numbers are not conserved.

The non-dipole effects have been included through the multipole expansion of the plane-wave spatial phase retardation term, $\exp(i\mathbf{k} \cdot \mathbf{r})$, using both Taylor and Rayleigh multipole expansions series for comparison purposes. In order to check the correctness of the implementation, the calculations are performed for atomic hydrogen using the laser parameters in [91], that is, for a ground-state hydrogen atom exposed to 13 nm ($\omega = 3.5\,\mathrm{a.\,u.}$) 15 cycle laser pulses with varying peak electric-field strengths ($E_0 = 25$, 35, and 45 a. u.). The numerical parameters used include a box size of $r_{\max} = 200$ a.u., angular momenta up to $L_{max} = 25$, and 600 B splines per angular momentum. Based on the reference [91] interaction potentials, it was possible to reproduce their results exactly using the Taylor plane-wave multipole expansion series. This was a good indication that the implementation in the extended program was correct and therefore the results presented are considered reliable and valid.

The extended BEYDIP code is further used to compare the numerical advantages of using either the Taylor or the Rayleigh plane-wave multipole expansion series of the spatial retardation term. The dependence of total, and differential where applicable, multipole ionization and excitation probabilities of hydrogen atoms on intensity, wavelength, pulse duration, and the initial state is also tested. The TDSE results for different multipole interaction terms are compared while investigating the interaction strength. The possible effects of multipole interaction terms of order 2 and 3 are also included as part of convergence check in the multipole orders. Part of the interest in the research project was to extend the multipole interaction dynamics to the helium atom using the SAE approximation. This required the use of a model potential to incorporate the electron-electron interaction effects for this simple multi-electron system. To achieve the goal, a frozen core two-electron model potential has been developed. The model potential can reproduce the ionization probabilities of helium atom interacting with short pulse intense laser fields with relatively good accuracy. The results obtained are summarized as follows:

- The Rayleigh plane-wave expansion of the spatial retardation term is not only more accurate but also more efficient with regards to computational time than the Taylor plane-wave expansion. Very high orders of Taylor expansion may be necessary to obtain near-perfect convergence with the Rayleigh plane-wave expansion. The Rayleigh plane-wave expansion has the additional advantage of allowing same symmetry transitions in its lowest-order $\mathbf{A} \cdot \mathbf{A}$ interaction term which would ortherwise be forbidden transitions within the dipole approximation.

- The lowest-order term in the Rayleigh plane-wave multipole expansion series, within the cylindrical symmetry, can be instrumental for a rough estimate of the laser parameter regimes where the spatial effects become important and hence the dipole approximation would not be valid. This may be specifically important for longer wavelengths where a broken cylindrical symmetry would not be feasible computationally. It is shown in this work that at intensities $\sim 10^{16}$ Wcm^{-2} corresponding to an 800 nm Ti:Sa laser, the spatial relativistic effects in the vector potential are likely to manifest in the photoelectron energy distribution. This means that the radiation pressure effects, which are an order lower in terms of the fine structure constant, would become significant at relatively lower intensities.

- The dominant correction to the dipole approximation is the quadrupole $\mathbf{A} \cdot \mathbf{p}$ interaction followed by the quadrupole $\mathbf{A} \cdot \mathbf{A}$ interaction for the laser parameter regimes considered in this work. This point has been a subject of debate which to date remains unresolved.

- At the highest intensities considered in this work, the effects of the 2$^{\text{nd}}$-order multipole interaction terms contributing to the octupole transitions are clearly visible in the photoelectron energy spectrum. The effects of the 3$^{\text{rd}}$-order multipole interaction terms contributing to the hexadecapole transitions are negligible. The 3$^{\text{rd}}$-order multipole corrections can then be considered as the limit of convergence of the multipole-orders for the intensity and photoelectron energy regimes specified.

- The non-dipole effects for a fixed wavelength and a fixed pulse duration increase with intensity. At lower intensities, dipole transitions are dominant as can be seen in the corresponding photoelectron energy spectra (PES) and photoelectron angular distributions (PADs) in these regimes. Above some critical intensity, the non-dipole transitions manifest in the electron energy spectrum washing out the ATI peak structures and enhancing the low- and very low-energy peak structures. The alignment of the PADS is also transformed from being oriented in the electric field polarization direction for a linearly polarized laser field to being oriented in the laser propagation direction for intensities where the non-dipole effects dominate.

- The non-dipole effects for a fixed intensity and a fixed pulse duration increase with wavelength. The wavelength-dependence of the non-dipole effects can be sensitively detected in the differential ionization probabilities as opposed to the total ionization probabilities. As wavelength increases, the convergence with respect to the box radius and angular momenta becomes increasingly demanding and the ionization probability is also likely to get into saturation at relatively low intensities.

- The multipole ionization probability for a fixed intensity and a fixed wavelength shows a different pulse duration dependence as compared to the dipole transition ionization probability. In the multipole case, non-adiabatic effects disappear with a much shorter pulse duration where as for the dipole case, they thrive for a longer pulse durations. The dipole transition related effects like multiphoton peak shifting and peak suppression also tend to be washed out when the higher-order multipole interaction terms become dominant. The multipole energy spectra, as opposed to the dipole energy spectra, show two distinct points where the ionization probabilities have weaker dependence on the pulse duration.
- If different initial states are considered, the multipole ionization probability distributions show sensitive dependence on the corresponding ionization potentials, the initial state orbital and projection symmetry. The $m = 1$ initial state seems to experience a larger non-dipole effect as compared to $m = 0$ initial state if other quantum numbers are the same.
- For any laser parameter regime, a new non-dipole backward-forward asymmetry parameter is suggested that can be used in complementary terms with the already established non-dipole asymmetry parameters. It is shown that the asymmetry parameters not only show the relative non-dipole strength but also reveal the critical intensities in the interaction dynamics where change of processes are likely to occur.
- In a bid to extend the multipolar interactions to the two-electron systems, two approximate model potentials that can describe the interaction dynamics of the system interacting with strong laser-fields with relatively good accuracy are developed. This is achieved by adopting a modified Hartree-Fock approximation formalism in the analytical evaluation of the double integral using the hydrogenic orbitals as the trial wavefunctions.
- The wavelength dependent non-dipole effects in the total ionization probabilities for helium at a fixed intensity of 2.97×10^{14} Wcm^{-2} and a pulse duration of 3.8 fs are shown to increase with wavelength just like for the hydrogen atom case. These effects are evaluated using the Taylor plane-wave multipole expansion series of the spatial phase retardation term.

There are opportunities for further development in the extended code. First, one may consider a possible implementation of the multipolar interaction dynamics using exterior complex scaling method. This may have the potential of solving the computationaly demanding long wavelength interaction dynamics with good accuracy, improved efficiency, and reasonable basis size. This is already implemented in part in the BEYDIP code, but it requires further code-testing and validation. Second, an extension into the relativistic interaction dynamics by transforming the non-relativistic time-dependent Schrödinger equation into the time-dependent Pauli equation is straight forward and can be achieved with minimal effort. This has the advantage of treating the spin-dependent interactions on an equal footing with the field-dependent multipolar interactions. The ultimate comparison of the results evaluated using the Schrödinger equation, Pauli equation and the Dirac equation may be a good link between the non-relativistic and the relativistic description of the interaction dynamics. Third, extending the BEYDIP code beyond the single active electron (SAE) approximation for multipolar interactions is an open problem. This would bring in a direct comparison of the relative importance of the non-dipole effects vis a vis the multi-electron effects in a correlated electron-electron interaction dynamics as well as the influence of the nuclear vibrations in molecular dynamics.

Abbreviations

- **TDSE** Time-Dependent Schrödinger Equation
- **SAE** Single Active Electron Approximation
- **SFA** Strong-Field Approximation
- **KFR** Keldysh Faisal Reiss Theories
- **PPT** Peremolov, Popov, and Terentent'eV Tunneling Ionization Model
- **ADK** Ammosov, Delone, and Krainov Tunneling Ionization Model
- **ATI** Above-the-Threshold Ionization
- **MPI** Multi-Photon Ionization
- **REMPI** Resonant Multi-Photon Ionization
- **BSI** Barrier-Suppression Ionization
- **HHG** High Harmonic Generation
- **LOPT** Lowest Order Perturbation Theory
- **PT** Perturbation Theory
- $\mathbf{TA}_n$ n^{th} order Taylor Multipole Expansion Approximation
- $\mathbf{SBA}_n$ n^{th} order Rayleigh Multipole Expansion Approximation employing the spherical Bessel functions
- **PES** Photoelectron Energy Spectrum
- **PAD** Photoelectron Angular Distribution
- $\mathbf{U}_p$ Ponderomotive Energy or Ponderomotive Potential
- $\mathbf{I}_p$ Ionization Energy or Ionization Potential

Bibliography

[1] M. E. Couprie. New generation of light sources: Present and future. *J. Electr. Spectros. Relat. Phenom.*, 196:3, 2014.

[2] A. Scrinzi, M. Yu Ivanov, R. Kienberger, and D. M. Villeneuve. Attosecond physics. *J. Phys. B*, 39, 2006.

[3] Ackermann, W. et al. Operation of a free-electron laser from the extreme ultraviolet to the water window. *Nat. Phys.*, 1:336, 2007.

[4] Ishikawa, T. et al. A compact X-ray free-electron laser emitting in the sub-angstrom region. *Nat. Photon.*, 6:540, 2012.

[5] ESRF. Brilliance. URL `http://www.esrf.eu/Accelerators/`.

[6] G Mourou and T Tajima. Exploring fundamental physics at the highest-intensity-laser frontier. URL `http://spie.org/x88664.xml`.

[7] EXFEL. New EU project: Guiding light for the world's brightest light sources. URL `http://www.xfel.eu/news/2015/`.

[8] Ferenc Krausz and Misha Ivanov. Attosecond physics. *Rev. Mod. Phys.*, 81:163, 2009.

[9] P. B. Corkum. Plasma perspective on strong field multiphoton ionization. *Phys. Rev. Lett.*, 71:1994, 1993.

[10] J. Itatani, J. Levesque, D. Zeidler, Hiromichi Niikura, H. Pépin, J. C. Kieffer, P. B. Corkum, and D. M. Villeneuve. Tomographic imaging of molecular orbitals. *Nature*, 432:867, 2004.

[11] Lotte Holmegaard, Jonas L. Hansen, Line Kalhøj, Sofie Louise Kragh, Henrik Stapelfeldt, Frank Filsinger, Jochen Küpper, Gerard Meijer, , Darko Dimitrovski, Mahmoud Abu-samha, Christian P. J. Martiny, and Lars Bojer Madsen. Photoelectron angular distributions from strong-field ionization of oriented molecules. *Nat. Phys.*, 6:428, 2010.

[12] Alejandro Bugacov, Marcel Pont, and Robin Shakeshaft. Possibility of breakdown of atomic stabilization in an intense high-frequency field. *Phys. Rev. A*, 48:R4027, 1993.

[13] N. J. Kylstra, R. A. Worthington, A. Patel, P. L. Knight, J. R. Vázquez de Aldana, and L. Roso. Breakdown of stabilization of atoms interacting with intense, high-frequency laser pulses. *Phys. Rev. Lett.*, 85:1835, 2000.

[14] Yulian V. Vanne. *Ionization of Molecular Hydrogen in Ultrashort Intense Laser Pulses.* PhD thesis, Institut für Physik, Humbold Universität zu Berlin, Germany, 2009.

[15] Yong-Chang Han and Lars Bojer Madsen. Comparison between length and velocity gauges in quantum simulations of high-order harmonic generation. *Phys. Rev. A*, 81:063430, 2010.

[16] E. Cormier and P. Lambropoulos. Optimal gauge and gauge invariance in non-perturbative time-dependent calculation of above-threshold ionization. *J. Phys. B*, 29:1667, 1996.

[17] A. D. Bandrauk, F. Fillion-Gourdeau, and E. Lorin. Atoms and molecules in intense laser fields: gauge invariance of theory and models. *J. Phys. B*, 46:153001, 2013.

[18] H. A. Bethe and E. E. Salpeter. *Quantum Mechanics of one- and two-electron atoms.* Springer-Verlag, Berlin, 1957.

[19] B. H. Bransden and C. J. Joachain. *Physics of atoms and molecules.* Longman Scientific & Technical, Essex, 1990.

[20] V. Devanathan. *Angular Momentum Techniques in Quantum Mechanics.* Kluwer Academic Publishers, New York, 2002.

[21] S. Svensson. Soft x-ray photoionization of atoms and molecules. *J. Phys. B*, 38: S821, 2005.

[22] H. Hertz. Die kräfte elektrischer schwingungen, behandelt nach der MAXWELL'schen theorie. *Ann. der Phys.*, page 1, 1889.

[23] A. Einstein. Concerning an heuristic point of view towards the emission and transformation of light. *Ann. of Phys.*, 17:132, 1905.

[24] K. Burnett, V. C. Reed, and P. L. Knight. Atoms in ultra-intense laser fields. *J. Phys. B*, 26:561, 1993.

[25] Maria Göppert. Über die Wahrscheinlichkeit des Zusammenwirkens zweier Lichtquanten in einem Elementarakt. *Die Naturwissenschaften*, 48:932, 1929.

[26] M. Göppert-Mayer. Über Elementarakte mit zwei Quantensprüngen. *Ann. der Phys.*, 401:273, 1931.

[27] V. Hughes and L. Grabner. The radiofrequency spectrum of rb^{85}f and rb^{87}f by the electric resonance method. *Phys. Rev.*, 79:314, 1950.

[28] W. Kaiser and C. G. B. Garrett. Two-photon excitation in CaF_2:Eu^{2+}. *Phys. Rev. Lett.*, 7:229, 1961.

[29] I. D. Abella. Optical double-photon absorption in cesium vapor. *Phys. Rev. Lett.*, 9:453, 1962.

[30] J. L. Hall, E. J. Robinson, and L. M. Branscomb. Laser double-quantum photodetachment of i^-. *Phys. Rev. Lett.*, 14:1013, 1965.

[31] G. S. Voronov and N. B. Delone. Many-photon ionization of the xenon atom by ruby laser radiation. *Sov. Phys. JETP*, 23:54, 1966.

[32] P. Agostini, G. Barjot, J. Bonnal, G. Mainfray, C. Manus, and J. Morellec. Multiphoton ionization of hydrogen and rare gases. *IEEE*, 4:667, 1968.

[33] P. Agostini, F. Fabre, G. Mainfray, G. Petite, and N. K. Rahman. Free-free transitions following six-photon ionization of xenon atoms. *Phys. Rev. Lett.*, 42: 1127, 1979.

[34] L. V. Keldysh. Ionization in the field of a strong electromagnetic wave. *Sov. Phys. JETP*, 20:1307, 1965.

[35] Manohar Awasthi. *Molecules in strong laser fields: In depth study of H2 molecule.* PhD thesis, Humboldt-Universität zu Berlin, Germany, 2009.

[36] F. H. M. Faisal. Multiple absorption of laser photons by atoms. *J. Phys. B*, 6:L89, 1973.

[37] Howard R. Reiss. Effect of an intense electromagnetic field on a weakly bound system. *Phys. Rev. A*, 22:1786, 1980.

[38] H. R. Reiss. Theoretical methods in quantum optics: S-matrix and Keldysh techniques for strong-field processes. *Prog. Quant. Electr.*, 16:1, 1992.

[39] E. A. Volkova, V. V. Gridchin, A. M. Popov, and O. V. Tikhonova. Tunneling ionization of a hydrogen atom in short and ultrashort laser pulses. *J. Exp. Theor. Phys.*, 102:40, 2006.

[40] S.-W. Bahk, P. Rousseau, T. A. Planchon, V. Chvykov, G. Kalintchenko, A. Maksimchuk, G. A. Mourou, and V. Yanovsky. Generation and characterization of the highest laser intensities (10^{22} w/cm^2). *J. Opt. Soc. Am.*, 29:2837, 2004.

[41] M. Crance. Multiphoton ionisation towards multiple continua: the role of space charge. *J. Phys. B*, 19:L267, 1986.

[42] L. A. Lompré, G. Mainfray, C. Manus, S. Repoux, and J. Thebault. Multiphoton ionization of rare gases at very high laser intensity (10^{15} w/cm^2) by a 30-psec laser pulse at 1.06 μm. *Phys. Rev. Lett.*, 36:949, 1976.

[43] H. Rottke, B. Wolff, M. Tapernon, K.H. Welge, and D. Feldmann. Resonant multiphoton ionization of xenon in intense sub-ps-laser pulses. *Z. Phys.*, 15:133, 1990.

[44] R. R. Freeman, P. H. Bucksbaum, H. Milchberg, S. Darack, D. Schumacher, and M. E. Geusic. Above-threshold ionization with subpicosecond laser pulses. *Phys. Rev. Lett.*, 59:1092, 1987.

[45] T. Marchenko, H. G. Muller, K. J. Schafer, and M. J. J. Vrakking. Wavelength dependence of photoelectron spectra in above-threshold ionization. *J. Phys. B*, 43: 185001, 2010.

[46] L. A. Lompré, A. L'Huillier, G. Mainfray, and C. Manus. Laser-intensity effects in the energy distributions of electrons produced in multiphoton ionization of rare gases. *J. Opt. Soc. Am. B*, 2:1906, 1985.

[47] A. F. Starace. Electron correlation effects in nonresonant multiphoton ionization processes. *Phys. Scr.*, T17:221, 1987.

[48] Y. Gontier and M. Trahin. Resonat above-threshold ionization of atomic hydrogen. *Phys. Rev. A*, 46:1488, 1992.

[49] P. Kruit, J. Kimman, H. G. Muller, and M. J. van der Wiel. Electron spectra from multiphoton ionization of xenon at 1064, 532, and 355 nm. *Phys. Rev. A*, 28:248, 1983.

[50] P. Agostini, J. Kupersztych, L. A. Lompré, G. Petite, and F. Yergeau. Direct evidence of ponderomotive effects via laser pulse duration in above-threshold ionization. *Phys. Rev. A*, 36:4111, 1987.

[51] P. Agostini, M. Clement, F. Fabre, and G. Petite. Multiphoton ionisation involving multiphoton continuum-continuum transitions. *J. Phys. B*, 14, 1981.

[52] L. Guo, S. S. Han, X. Liu, Y. Cheng, Z. Z. Xu, J. Fan, J. Chen, S. G. Chen, W. Becker, C. I. Blaga, A. D. DiChiara, E. Sistrunk, P. Agostini, and L. F. DiMauro. Scaling of the low-energy structure in above-threshold ionization in the tunneling regime: Theory and experiment. *Phys. Rev. Lett.*, 110:013001, 2013.

[53] G. Petite, P. Agostini, and F. Yergeau. Intensity, pulse width, and polarization dependence of above-threshold-ionization electron spectra. *J. Opt. Soc. Am. B*, 4: 765, 1987.

[54] F. Yergeau, G. Petite, and P. Agostini. Above-threshold ionisation without space charge. *J. Phys. B*, 19:L663, 1986.

[55] G. Petite, P. Agostini, and H. G. Muller. Intensity dependence of non-perturbative above-threshold ionisation spectra: experimental study. *J. Phys. B*, 21:4097, 1988.

[56] Patrick Kaminski, Rolf Wiehle, Vincent Renard, Anne Kazmierczak, Bruno Lavorel, Olivier Faucher, and Bernd Witzel. Wavelength dependence of multiphoton ionization of xenon. *Phys. Rev. A*, 70:053413, 2004.

[57] P. Kruit, J. Kimman, and M. J. Van der Wiel. Absorption of additional photons in the multiphoton ionisation continuum of Xenon at 1064, 532 and 440 nm. *J. Phys. B*, 14:L597, 1981.

[58] P. H. Bucksbaum, M. Bashkansky, R. R. Freeman, T. J. McIlrath, and L. F. DiMauro. Suppression of multiphoton ionization with circularly polarized coherent light. *Phys. Rev. Lett.*, 56:2590, 1986.

[59] R. R. Freeman, T. J. McIlrath, P. H. Bucksbaum, and M. Bashkansky. Pondermotive effects on angular distributions of photoelectrons. *Phys. Rev. Lett.*, 57:3156, 1986.

[60] M. H. Mittleman. Intensity dependence of the ionisation potential of an atom in a resonant laser field. *J. Phys. B*, 17:L351, 1984.

[61] P. H. Bucksbaum, R. R. Freeman, M. Bashkansky, and T. J. McIlrath. Role of the ponderomotive potential in above-threshold ionization. *J. Opt. Soc. Am.*, 4:760, 1987.

[62] G. Wentzel. Eine verallgemeinerung der quantenbedingungen für die zwecke der wellenmechanik. *Z. Phys.*, 38:518, 1926.

[63] H. A. Kramers. Wellenmechanik und halbzahlige quantisierung. *Z. Phys.*, 39:828, 1926.

[64] L. Brillouin. La mécanique ondulatoire de schrödinger: une méthode générale de resolution par approximations successives. *Comptes Rendus de l'Academie des Sciences*, 183:24, 1926.

[65] L. D. Landau and E. M. Lifshitz. *Quantum Mechanics Non-Relativistic Theory*, volume 3. Butterworth-Heinemann, 1981.

[66] A. M. Perelomov, V. S. Popov, and M. V. Terent'ev. Ionization of atoms in an alternating electric field. *Sov. Phys. JETP*, 23:924, 1966.

[67] A. M. Perelomov and V. S. Popov. Ionization of atoms in an alternating electric field. ii. *Sov. Phys. JETP*, 24(1):207, 1967.

[68] A. M. Perelomov and V. S. Popov. Ionization of atoms in an alternating electric field. iii. *Sov. Phys. JETP*, 25(2):336, 1967.

[69] M. V. Ammosov, N. B. Delone, and V. P. Krainov. Tunnel ionization of complex atoms and of atomic ions in an alternating electromagnetic field. *Sov. Phys. JETP*, 64:1191, 1986.

[70] V. P. Krainov. Theory of barrier-suppression ionization of atoms. *JNOPM*, 4:775, 1995.

[71] S. Augst, D. D. Meyerhofer, D. Strickland, and S. L. Chin. Laser ionization of noble gases by coulomb-barrier suppression. *J. Opt. Soc. Am.*, 8:858, 1991.

[72] N. B. Delone and V. P. Krainov. Tunneling and barrier-suppression ionization of atoms and ions in a laser radiation field. *Phys. -Usp.*, 41:469, 1998.

[73] C. I. Blaga, F. Catoire, P. Colosimo, G. G. Paulus, H. G. Muller, P. Agostini, and L. F. DiMauro. Strong-field photoionization revisited. *Nat. Phys.*, 5:335, 2009.

[74] W. Quan, Z. Lin, M. Wu, H. Kang, H. Liu, X. Liu, J. Chen, J. Liu, X. T. He, S. G. Chen, H. Xiong, L. Guo, H. Xu, Y. Fu, Y. Cheng, and Z. Z. Xu. Classical aspects in above-threshold ionization with a midinfrared strong laser field. *Phys. Rev. Lett.*, 103:093001, 2009.

[75] J. Dura, N. Camus, A. Thai, A. Britz, M. Hemmer, M. Baudisch, A. Senftleben, C. D. Schroter, J. Ullrich, R. Moshammer, and J. Biegert. Ionization with low-frequency fields in the tunneling regime. *Sci. Rep.*, 3:2675, 2013.

[76] M. Möller, F. Meyer, A. M. Sayler, G. G. Paulus, M. F. Kling, B. E. Schmidt, W. Becker, and D. B. Milošević. Off-axis low-energy structures in above-threshold ionization. *Phys. Rev. A*, 90:023412, 2014.

[77] H. Liu, Y. Liu, L. Fu, G. Xin, D. Ye, J. Liu, X. T. He, Y. Yang, X. Liu, Y. Deng, C. Wu, and Q. Gong. Low yield of near-zero-momentum electrons and partial atomic stabilization in strong-field tunneling ionization. *Phys. Rev. Lett.*, 109: 093001, 2012.

[78] Mihai Gavrila. Atomic stabilization in superintense laser fields. *J. Phys. B*, 35: R147, 2002.

[79] T. Nubbemeyer, K. Gorling, A. Saenz, U. Eichmann, and W. Sandner. Strong-field tunneling without ionization. *Phys. Rev. Lett.*, 101:233001, 2008.

[80] M. .V Fedorov and A. M. Movsesian. Field-induced effects of narrowing of photoelectron spectra and stabilisation of rydberg atoms. *J. Phys. B*, 21:L155, 1988.

[81] A. L'Huillier, K. J. Schafer, and K. C. Kulander. Theoretical aspects of intense field harmonic generation. *J. Phys. B*, 24:3315, 1991.

[82] S. Baker, J. S. Robinson, C. A. Haworth, H. Teng, R. A. Smith, C. C. Chirilă, M. Lein, J. W. G. Tisch, and J. P. Marangos. Probing Proton Dynamics in Molecules on an Attosecond Time Scale. *Science*, 312:424, 2006.

[83] H. J. Wörner, J. B. Bertrand, D. V. Kartashov, P. B. Corkum, and D. M. Villeneuve. Following a chemical reaction using high-harmonic interferometry. *Nature*, 466:604, 2010.

[84] V. C. Reed and K. Burnett. Loss of harmonic generation in intense laser fields. *Phys. Rev. A*, 46:424, 1992.

[85] H. R. Reiss. The tunnelling model of laser-induced ionization and its failure at low frequencies. *J. Phys. B*, 47:204006, 2014.

[86] H. R. Reiss. Relativistic effects in nonrelativistic ionization. *Phys. Rev. A*, 87:033421, 2013.

[87] M. Y. Amusia, A. S. Baltenkov, Z. Felfli, and A. Z. Msezane. Large nondipole correlation effects near atomic photoionization thresholds. *Phys. Rev. A*, 59:R2544, 1999.

[88] P. V. Demekhin. On the breakdown of the electric dipole approximation for hard x-ray photoionization cross sections. *J. Phys. B*, 47:025602, 2014.

[89] Valery K. Dolmatov and Steven T. Manson. Large nondipole parameters with strong correlation effects in photoelectron angular distributions at kilo-electron-volt energies. *Phys. Rev. A*, 63:022704, 2001.

[90] Morten Førre. Nondipole ionization dynamics of excited atoms in intense femtosecond pulses. *Phys. Rev. A*, 74:065401, 2006.

[91] M. Førre and A. S. Simonsen. Nondipole ionization dynamics in atoms induced by intense xuv laser fields. *Phys. Rev. A*, 90:053411, 2014.

[92] Z. Zhongyuan and C. Shih-I. Multiphoton above-threshold ionization in superintense free-electron x-ray laser fields: Beyond the dipole approximation. *Phys. Rev. A*, 87:023407, 2013.

[93] M. Dondera and H. Bachau. Exploring above-threshold ionization of hydrogen in an intense x-ray laser field through nonperturbative calculations. *Phys. Rev. A*, 85:013423, 2012.

[94] O. Latinne, C. J. Joachain, and M. Dörr. Atomic hydrogen in a superintense high-frequency field: Testing the dipole approximation. *Europhys. Lett.*, 26:333, 1994.

[95] H. R. Varma, M. F. Ciappina, N. Rohringer, and R. Santra. Above-threshold ionization in the x-ray regime. *Phys. Rev. A*, 80:053424, 2009.

[96] V. Florescu, O. Budriga, and H. Bachau. Two-photon above threshold ionization of hydrogen over the photon energy range from 15 ev to 50 kev. *Phys. Rev. A*, 84:033425, 2011.

[97] T. Katsouleas and W. B. Mori. Comment on “packet spreading, stabilization, and localization in superstrong fields”. *Phys. Rev. Lett.*, 70:1561, 1993.

[98] J. R. Vázquez de Aldana, N. J. Kylstra, L. Roso, P. L. Knight, A. Patel, and R. A. Worthington. Atoms interacting with intense, high-frequency laser pulses: Effect of the magnetic-field component on atomic stabilization. *Phys. Rev. A*, 64:013411, 2001.

[99] Morten Førre and Aleksander Skjerlie Simonsen. Generalized velocity-gauge form of the light-matter interaction hamiltonian beyond the dipole approximation. *Phys. Rev. A*, 93:013423, 2016.

[100] Michael Klaiber, Karen Z. Hatsagortsyan, and Christoph H. Keitel. Above-threshold ionization beyond the dipole approximation. *Phys. Rev. A*, 71:033408, 2005.

[101] M. W. Walser, C. H. Keitel, A. Scrinzi, and T. Brabec. High harmonic generation beyond the electric dipole approximation. *Phys. Rev. Lett.*, 85:5082, 2000.

[102] C. C. Chirilă, N. J. Kylstra, R. M. Potvliege, and C. J. Joachain. Nondipole effects in photon emission by laser-driven ions. *Phys. Rev. A*, 66:063411, 2002.

[103] K. F. Riley, M. P. Hobson, and S. J. Bence. *Mathematical methods for Physics and Engineering.* Cambridge University Press, Cambridge, 2006.

[104] L. A. A. Nikolopoulos. A package for the ab-initio calculation of one- and two-photon cross sections of two-electron atoms, using a CI B splines method. *Comp. Phys. Comm.*, 150:140, 2003.

[105] Carl de Boor. *A Practical Guide to Splines.* Springer, New York, 1978.

[106] J Sapirstein and W R Johnson. The use of basis splines in theoretical atomic physics. *J. Phys. B*, 29:5213, 1996.

[107] H. Bachau, E Cormier, P Decleva, J. E. Hansen, and F Martín. Applications of B-splines in atomic and molecular physics. *Rep. Prog. Phys.*, 64:1815, 2001.

[108] B. W. Shore. Use of boundary-condition wavefunctions for bound states, continuum states, and resonances. *J. Phys. B*, 7:2502, 1974.

[109] M. Abramowitz and I. A. Stegun. *Handbook of Mathematical Functions with Formulas, Graphs, and Mathematical Tables.* Dover Publications, Inc., New York, 1970.

[110] E. Weisstein. Spherical Bessel Function of the First Kind. URL http://mathworld.wolfram.com/.

[111] F. H. M. Faisal. *Theory of multiphoton processes.* Plenum Press, New York, 1987.

[112] L. D. Landau and E. M. Lifshitz. *Quantum Mechanics, revised edition.* Pergamon Press, Oxford, 1977.

[113] J. J. Sakurai. *Modern Quantum Mechanics*. Addison-Wesley Publishing Company Inc, USA, 1994.

[114] W. H. Press, S. A. Teukolsky, and W. T. Vetterling. *Numerical Recipes in Fortran 77*. Cambridge University Press, Cambridge, 1992.

[115] M. Dondera. Atomic ionization by intense laser pulses of short duration: Photoelectron energy and angular distributions. *Phys. Rev. A*, 82:053419, 2010.

[116] G. Leuchs, S. J. Smith, S. N. Dixit, and P. Lambropoulos. Observation of interference between quadrupole and dipole transitions in low-energy (2-ev) photoionization from a sodium rydberg state. *Phys. Rev. Lett.*, 56:708, 1986.

[117] B. Krässig, M. Jung, D. S. Gemmell, E. P. Kanter, T. LeBrun, S. H. Southworth, and L. Young. Nondipolar asymmetries of photoelectron angular distributions. *Phys. Rev. Lett.*, 75:4736, 1995.

[118] O. A. Hemmers and D. W. Lindle. Photoelectron spectroscopy and the dipole approximation. *AIP Conf. Proc.*, 576:189, 2001.

[119] J. W. Cooper. Multipole corrections to the angular distribution of photoelectrons at low energies. *Phys. Rev. A*, 42:6942, 1990.

[120] R. L. Burden, D. J. Faires, and A. M. Burden. *Numerical Analysis*. Cengage Learning, Essex, 2005.

[121] X. L. Ruan, S. C. Rand, and M. Kaviany. Entropy and efficiency in laser cooling of solids. *Phys. Rev. B*, 75:214304, 2007.

[122] F. D. Colegrove and P. A. Franken. Optical pumping of helium in the $^3s_1$ metastable state. *Phys. Rev.*, 119:680, 1960.

[123] J. Branson. The Radial Wavefunction Solutions. URL `http://quantummechanics.ucsd.edu/ph130a/130_notes/node233.html`.

[124] V. Florescu, O. Budriga, and H. Bachau. Two-photon ionization of hydrogen-like ions: Retardation effects on differential and total generalized cross sections. *Phys. Rev. A*, 86:033413, 2012.

[125] D. P. Craig and T. Thirunamachandran. *Molecular Quantum Electrodynamics, an Introduction to Radiation Molecule Interactions*. John Wiley and Sons, Inc, New York, Dover, 1998.

[126] R. Grinter. Photon angular momentum: selection rules and multipolar transition moments. *J. Phys. B*, 41:095001, 2008.

[127] W. Heitler. On the radiation emitted by a multipole and its angular momentum. *Proc. Camb. Phil. Soc.*, 32:112, 1936.

[128] M. L. Boas. *Mathematical methods in the Physical Sciences.* John Wiley and Sons, Inc, USA, 2006.

[129] S. H. Strogatz. *Non-linear dynamics and chaos: With applications to Physics, Biology, Chemistry, and Engineering*, pages 216–217. Perseus Books Publishing, LLC, Bloomberg, 2000.

[130] P. V. Demekhin and L. S. Cederbaum. Dynamic interference of photoelectrons produced by high-frequency laser pulses. *Phys. Rev. Lett.*, 108:253001, 2012.

[131] Chuan Yu, Ning Fu, Guizhong Zhang, and Jianquan Yao. Dynamic stark effect on xuv-laser-generated photoelectron spectra: Numerical experiment on atomic hydrogen. *Phys. Rev. A*, 87:043405, 2013.

[132] A. Ludwig, J. Maurer, B. W. Mayer, C. R. Phillips, L. Gallmann, and U. Keller. Breakdown of the dipole approximation in strong-field ionization. *Phys. Rev. Lett.*, 113:243001, 2014.

[133] J. H. Eberly and J. Javanainen. Above-threshold ionisation. *Eur. J. Phys.*, 9:265, 1988.

[134] Rolf Wiehle, Bernd Witzel, Hanspeter Helm, and Eric Cormier. Dynamics of strong-field above-threshold ionization of argon: Comparison between experiment and theory. *Phys. Rev. A*, 67:063405, 2003.

[135] H. R. Reiss and V. P. Krainov. Generalized Bessel functions in tunnelling ionization. *J. Phys. A*, 36:5575, 2003.

[136] U. Eichmann, A. Saenz, S. Eilzer, T. Nubbemeyer, and W. Sandner. Observing rydberg atoms to survive intense laser fields. *Phys. Rev. Lett.*, 110:203002, 2013.

[137] R. Shakeshaft. Multiphoton ionization of an atom; the choice of gauge. *Z. Phys. D*, 8:47, 1998.

[138] Robin Shakeshaft and X. Tang. Integral-equation approach to multiphoton ionization by intense fields. ii. application to h and h^{-}. *Phys. Rev. A*, 36:3193, 1987.

[139] I. A. Ivanov and A. S. Kheifets. Above-threshold-ionization structures in photoelectron momentum distributions for single ionization of he by a strong electromagnetic field. *Phys. Rev. A*, 80:063418, 2009.

[140] Tian-Min Yan, S. V. Popruzhenko, M. J. J. Vrakking, and D. Bauer. Low-energy structures in strong field ionization revealed by quantum orbits. *Phys. Rev. Lett.*, 105:253002, 2010.

[141] H. Helm and M. J. Dyer. Resonant and nonresonant multiphoton ionization of helium. *Phys. Rev. A*, 49:2726, 1994.

[142] A. Kästner, U. Saalmann, and J. M. Rost. Electron-energy bunching in laser-driven soft recollisions. *Phys. Rev. Lett.*, 108:033201, 2012.

[143] A. M. Popov, O. V. Tikhonova, and E. A. Volkova. Strong-field atomic stabilization: numerical simulation and analytical modelling. *J. Phys. B*, 36:R125, 2003.

[144] J. R. Vásquez de Aldana, N. J. Kylstra, L. Roso, P. L. Knight, A. Patel, and R. A. Worthington. Atoms interacting with intense, high-frequency laser pulses: Effect of the magnetic-field component on atomic stabilization. *Phys. Rev. A*, 64:013411, 2001.

[145] Aleksander Skjerlie Simonsen and Morten Førre. Magnetic-field-induced enhancement of atomic stabilization in intense high-frequency laser fields. *Phys. Rev. A*, 92:013405, 2015.

[146] B. Walker, B. Sheehy, L. F. DiMauro, P. Agostini, K. J. Schafer, and K. C. Kulander. Precision measurement of strong field double ionization of helium. *Phys. Rev. Lett.*, 73:1227, 1994.

[147] Coulomb-Volkov approximation for near-threshold ionization by short laser pulses. Arbó, diego g. and miraglia, jorge e. and gravielle, maría silvia and schiessl, klaus and persson, emil and burgdörfer, joachim. *Phys. Rev. A*, 77:013401, 2008.

[148] Fu Yan-Zhuo, Zhao Song-Feng, and Zhou Xiao-Xin. Multiphoton and tunneling ionization of atoms in an intense laser field. *Chin. Phys. B*, 21:113101, 2012.

[149] V. A. Astapenko and V. S. Lisitsa. On the theory of hydrogen atom ionization by ultra-short electromagnetic pulses. *Contrib. Plasma Phys.*, 55:522, 2015.

[150] M. Horbatsch. Numerical calculation of above-threshold-ionization of hydrogen atoms in short intense laser pulses. *J. Phys. B*, 24:4919, 1991.

[151] E. Brunetti, W. Becker, H. C. Bryant, D. A. Jaroszynski, and W. Chou. Laser stripping of hydrogen atoms by direct ionization. *New J. Phys.*, 17:053008, 2015.

[152] F. Grasbon, G. G. Paulus, H. Walther, P. Villoresi, G. Sansone, S. Stagira, M. Nisoli, and S. De Silvestri. Above-threshold ionization at the few-cycle limit. *Phys. Rev. Lett.*, 91:173003, 2003.

[153] Markus Schenk, Michael Krüger, and Peter Hommelhoff. Strong-field above-threshold photoemission from sharp metal tips. *Phys. Rev. Lett.*, 105:257601, 2010.

[154] Szczepan Chelkowski and André Bandrauk. Asymmetries ins strong-field photoionization by few-cycle laser pulses: Kinetic-energy spectra and semiclassical explanation of the asymmetries of fast and slow electrons. *Phys. Rev. A*, 71:053815, 2005.

[155] K. Krajewska and J. Z. Kamiński. Radiation pressure in strong-field-approximation theory: Retardation and recoil corrections. *Phys. Rev. A*, 92:043419, 2015.

[156] G. W. F. Drake. High precision theory of atomic helium. *Phys. Scr.*, 1999:83, 1999.

[157] I. F. Barna and J. M. Rost. Photoionization of helium with ultrshort xuv laser pulses. *Eur. Phys. J. D*, 27:287, 2003.

[158] R. Hasbani, E. Cormier, and H. Bachau. Resonant and non-resonant ionization of helium by xuv ultrashort and intense laser pulses. *J. Phys. B*, 33:2101, 2000.

[159] Armin Scrinzi and Bernard Piraux. Two-electron atoms in short intense laser pulses. *Phys. Rev. A*, 58:1310, 1998.

[160] T. N. Chang and U. Fano. Many-body theory of atomic transitions. *Phys. Rev. A*, 13:263, 1976.

[161] Jonathan S. Parker, Laura R. Moore, Edward S. Smyth, and K. T. Taylor. One- and two-electron numerical models of multiphoton ionization of helium. *J. Phys. B*, 33:1057, 2000.

[162] T. Ishihara, K. Hino, and J. H. McGuire. Photoionization of two electrons in helium. *Phys. Rev. A*, 44:R6980, 1991.

[163] M. S. Pindzola, F. Robicheaux, and P. Gavras. Double multiphoton ionization of a model atom. *Phys. Rev. A*, 55:1307, 1997.

[164] M. S. Pindzola, D. C. Griffin, and C. Bottcher. Validity of time-dependent hartree-fock theory for the multiphoton ionization of atoms. *Phys. Rev. Lett.*, 66:2305, 1991.

[165] D. G. Lappas and van L. Robert. Electron correlation effects in the double ionization of he. *J. Phys. B*, 31:L249, 1998.

[166] Jonathan S. Parker, Edward S. Smyth, and K. T. Taylor. Intense-field multiphoton ionization of helium. *J. Phys. B*, 31:L571, 1998.

[167] J. Mitroy and M. W. J. Bromley. Semiempirical calculation of van der waals coefficients for alkali-metal and alkaline-earth-metal atoms. *Phys. Rev. A*, 68:052714, 2003.

[168] J. Mitroy, M. S. Safronova, and Charles W. Clark. Theory and applications of atomic and ionic polarizabilities. *J. Phys. B*, 43:202001, 2010.

[169] Armin Lühr, Yulian V. Vanne, and Alejandro Saenz. Parameter-free one-center model potential for an effective one-electron description of molecular hydrogen. *Phys. Rev. A*, 78:042510, 2008.